1997

Development of high-Tc superconducting coils and magnets through processing optimization and characterization of Bi(Pb/Ag and Ag-alloy composite tapes

Nghia Van Vo
University of Wollongong

Development of High-T_c Superconducting Coils and Magnets Through Processing Optimization and Characterization of Bi(Pb)-2223/Ag and Ag-Alloy Composite Tapes

A thesis submitted in fulfilment of the requirements
for the award of the degree of
Doctor of Philosophy

from
University of Wollongong

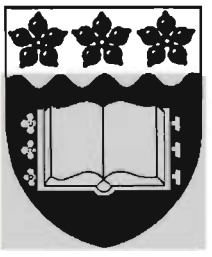

by
Nghia Van Vo
B. Ma. Sc., B. E. (Elec.), B. Sc. (Hon. Phys.)

Department of Materials Engineering
January 1997

Statement of Originality

This thesis contains neither material which has been accepted for the award of any other degree or diploma in any University, nor, to the best of the author's knowledge and belief, any material previously published or written by another person, except where due reference is made.

Signed :-

Nghia Van Vo

January 8th, 1997

Abstract

The extensive research effort in the development of high-T_c superconducting (HTSC) class-II $(Bi,Pb)_2Sr_2Ca_2Cu_3O_{x+10}$ (Bi(Pb)-2223) coils, and magnets, through processing optimization, and characterization of silver, and silver-alloy composite tapes, has been conducted at the Center for Superconducting and Electronic Materials (part of the Institute of Materials Technology and Manufacturing), Department of Materials Engineering, University of Wollongong.

Studies leading up to the production of Bi(Pb)-2223 class-II coils, and magnets include the following investigations in materials processing, and science of Bi(Pb)-2223 composite tapes:-

The processing of Bi(Pb)-2223 short, and long length composite tapes (from the standard procedure of PIT, to the conventional method of CTFF, and the novel format of WIT, or wire-in-tube), and the characterization on their physical, chemical, electrical, and magnetic properties by means of measurements - implemented techniques include; Vickers microhardness tests (H_VT), particle size analysis (PSA), X-ray diffraction (XRD), differential thermal and thermo-gravimetric analysis (DTA/TG), scanning electron microscopy with energy-dispersive spectrometry (SEM/EDS), electrical transport, ac-susceptibility, and the SQUID (superconducting quantum interference device) magnetometry.

The effect of powder packing density, using the conventional method of powder-in-tube (PIT) by various means, on the transport critical current density, J_c, mechanical properties, and high-T_c phase (2223) formation of Bi(Pb)-2223 single filamentary (SF) superconducting tapes - higher initial packing density of PIT monocore short tapes has been found to give higher J_c values, as well as higher rate of 2223 formation, while lower initial packing density samples gave better mechanical performance. Critical strains for bend tests showed a dependence on the core thickness, and silver/oxide volume ratio.

The effect of sintering periods on the microstructure, phase development, and electrical transport and magnetic properties of Bi(Pb)-2223 SF tapes - comparisons have been made between three batches of tapes with the same thermomechanical deformation, and sintering conditions, but with the starting precursor powders being different in their synthesis. It has been found that the volume density of the macroscopic pinning force in fields up to 1T is greater for a particular sintering period, viz. ~ 60 h in duration. Resistivity measurements further showed that the pinning activation energy also reaches a higher value for the same sintering period chosen. Scanning electron microimages of the fractured surfaces indicated that better core morphology, and density can be achieved in SF tapes from using this particular sintering period. Prolong sintering has been found to lead to greater porosity, while short duration sintering inhibits grain growth, which is undesirable for not providing sufficient time for the healing of cracks, induced during the intermediate deformation between sintering periods. The results also showed that longer sintering periods (of duration $\geq$ 100 h) tend to give better grain growth (in terms of grain size), but greater grain misalignment. Prolong sintering however, has been found to facilitate the increase in porosity of the core due to random grain growth. Critical currents in tapes treated with long sintering periods also have been measured to be lower in comparison with the values obtained for samples treated with slightly shorter sintering periods. The tapes made using 'three-to-four-sinter-period' (each period ~ 60 h) showed superior electrical transport properties over the 'two-sinter-period' (each period $\geq$ 100 h) tapes, and revealed less microcracks in comparison with the 'five-to-six-sinter-period' (each period ~ 40 h) tapes. These attributes are the result of higher core density with better connected and aligned grains, owing to sufficient sintering time for each period of heat treatment.

The effect of intermediate rolling reduction on the transport property, microstructure, phase formation and fill factor of Bi(Pb)-2223 composite tapes - well controlled intermediate deformation between sintering stages of Bi(Pb)-2223 composite tapes is crucial in achieving high critical current density. This deformation whether by rolling or pressing, depends on factors such as the compositional phase, the degree of microcracks, sintering periods or duration, and sintering temperature. It has been investigated that there is indeed an optimal 'window' of reduction for intermediate rolling (at room temperature) between sintering stages. For a particular sintering

temperature, this window has been determined to vary depending on the time of sintering and phase composition after a certain sintering period. It has been found that the amount of intermediate deformation controls the transformation rate of 2223, as well as determining the tape's final microstructure and fill factor.

Mechanical property, and filamentary configuration of Bi(Pb)-2223 composite tapes - mutifilamentary (MF) tapes prepared by both methods of oxide-powder-in-tube (OPIT), and continuous-tube-forming-filling (CTFF) technique with reproducible, and scalable transport critical current densities between 15 and 20 kA/cm^2 (77 K, self field, 1μ V/cm) by rolling have been achieved. It has been found that the filament distribution (geometry of filaments), the fill factor (ratio of superconducting ceramic core to the total cross-section of the conductor), and the stacking factor (number of times the filaments are stacked) play a crucial roll in determining the overall mechanical and electrical performance of these tapes.

The determination of stability parameters for Bi(Pb)-2223 composite tapes - with high upper critical fields, HTSC have been recognized as candidate materials for coil and magnet applications. High field devices at one time or another, when operated close to their rated limits, are often faced with instability problems which normally are of electrical, magnetic or mechanical nature. The determination of stability parameters therefore are of interest to the conductor designer which assists in the processing aspect of long length production of wires and tapes. It has been found that Bi(Pb)-2223/Ag tapes are cryostabled, as well as flux-jump stabled. Processing parameters such as intermediate deformation and fill factor, have found to have a direct effect on the stability outcome of these tapes.

Thermal stability of Bi(Pb)-2223 coils at 77 K - it has been found that the degree of thermal stability of Bi(Pb)-2223/Ag pancake-shaped coils at 77 K can be determined by controlling the amount of matrix and superconducting materials during processing. The intermediate deformation step between sintering stages has been found to be crucial in optimizing the performance of the processed composite tapes as well as governing the thermal stability of the subsequently produced pancake-shaped coils. Results obtained from numerical analysis by the finite element method has shown that

monolayer coils produced from Bi(Pb)-2223/Ag composite tapes are thermally very stable, with high values of fill factor. Increasing the number of co-wound tapes however, for reasons of achieving higher current carrying capacity, and improving in mechanical integrity of the coil or magnet system, has been found to require either a reduction in the fill factor or an increase in cooling rate for thermal stability to be sustained as would otherwise be achieved with the metallurgically same single tape.

Development of Bi(Pb)-2223 class-II coils and magnets - once the production of high quality long length Bi(Pb)-2223/Ag tapes have been achieved considerations such as how to fabricate them into practical applications without degrading the performance of the tape becomes the major issues. The main problems concerned are usually related to the winding procedures (e.g. wind-react (W&R) and react-wind (R&W)), the insulating material, the construction or stacking of coils if they are pancake-shaped, and the study of quench propagation parameters.

A novel W&R solenoidal coil (reaching ~ 973 ampere-turns) wound on an alumina ceramic tube generates a dc-field of ~ 19 mT at 77 K has been produced together with five pancake-shaped coils, each generates an average of ~ 5 mT at 77 K, destined for magnet construction with a possible combined calculated field of ~ 0.04 T at 77 K (with liquid nitrogen as a coolant). Critical currents of superconducting silver, and silver-alloy composite double pancake coils of Bi(Pb)-2223 have been measured at liquid nitrogen temperature. A critical current density of ~ 12.5 kA/cm^2 has been measured for a coil fabricated from Bi(Pb)-2223/Ag composite tape of length ~ 2.2 m (~ 342 Ampere-turns) using the WIT method. For coils made from alloys of silver (e.g. ~ 0.02% magnesium), higher critical currents (~ 17 A) have been achieved over those fabricated with tapes processed with pure silver matrix. Transport measurements of normalised J_c *vs* B in fields up to 1T showed encouraging results for WIT, and CTFF composite tapes prepared from intermediate rolling. New methods of joining between double pancake-shaped coils have also been investigated, together with the determination of some quench propagation parameters. The implementation of the superconducting joint with strap has produced a laboratory test magnet constructed from two double pancake-shaped coils (total length of ~ 20 m, or ~ 552 Ampere-turns) giving a self dc-field of ~ 21 mT, at 77 K.

Acknowledgments

During the period of my candidature, numerous people have provided assistance both of a professional and a personal nature. In particular, I would like to thank the following persons: -

My thesis supervisors Professor Shi Xue Dou and Associate Professor Hua Kun Liu for their guidance and willingness to discuss problems. Professor Druce Dunne, Head of the Department of Materials Engineering for his generosity in giving permission to share various equipment with the CSEM (Centre for Superconducting and Electronic Materials) group.

Dr Edward W. Collings at the Ohio State University Department of Materials Science and Engineering of the United States for giving his time over the Internet and upon visiting the University of Wollongong for technical as well as theoretical advice. On behalf of our group I must thank him for providing our Centre, now part of the Institute of Materials Technology and Manufacturing, long lengths of continuous-tube-forming-filling BSCCO wires.

Dr David Yao-Tsung Huang at the Industrial Technology Research Institute, Materials Research Laboratories of Taiwan for his sharing expertise on the heat treatment of composite Bi(Pb)-2223/Ag tapes from which our group has benefited as a result, as well as matters concerning the making of pancake-shaped coils.

Professor Emil Babic and Dr Ivica Kusevic at the University of Zagreb, Department of Physics of Croatia for their enthusiasm in receiving samples for transport and magneto-resistivity measurements at temperatures below and above that of liquid nitrogen.

Mr David Cook and his team at the University of Wollongong, Department of Mechanical Engineering, Bulk Materials Handling Laboratory for their kindness in performing many particle size measurements during the under-developed stages of our Centre.

Mr Jerry Ostenson at the Iowa State University, Department of Energy, Ames Laboratories of the United States for his great effort in getting all the measurements for the samples sent using the technology of SQUID magnetometry.

Professor Antony J. Bourdillon at the National University of Singapore, Department of Physics of Singapore, together with Mr Chee Cheong Neo for conducting the finite elements analysis software which was used to study the thermal stability on one of the pancake-shaped coils.

Dr Nick Savvides at the Commonwealth Scientific and Industrial Research Organisation, Division of Applied Physics for his advice on the use of indium metal for soldering voltage and current taps on the coils.

Dr Ming Xu at the Iowa State University, Ames Laboratories for advice regarding presentations and publications. Dr Mike Sumption at the Ohio State University Department of Materials Science and Engineering for suggestions on the cryogenic properties of certain Hall probes. Professor Harald W. Weber at the Institute of Low Temperature Physics/Superconductivity of Austria for providing a colourful schematic of the crystallographic structure of the Bi(Pb)-2223 during his visit to our Centre.

Mr M. Yavuz for supplying some of his precursor powders during the early stages of my research, and to all colleagues and research fellows as well as members of the Metals Manufactures Ltd. for their contributed discussions throughout my candidature.

The workshop people for their excellent technical assistance which helped me get started in the early stages of my candidature. Mr Graham Hamilton in particular, for his know-how on the construction of several 'home-made' furnaces, Mr Greg Tillman for his expertise in optical microscopy, and Mr Nick Mackie for his SEM training time.

The secretarial team of Ms Rhondalee Cambareri, Ms Joy de Mestre and Ms Nadyne Smith for their tremendous support in matters regarding many aspects including mailing, dissertation preparation advice and the organization of travel to conferences.

I was fortunate to enjoy some of the kind hospitality and benefit a lot from the social aspect of college life during my first four months of stay at Richard Johnson College and about a year and a half at Weerona College in Wollongong as a residential tutor.

Finally, I am grateful to the following persons for the very important contributions that they have made to my work and life in general:- my father, mother, sister, and two brothers for their psychological support and encouragement, and Melissa Scully for her friendship and unfailing patience.

The extensive work performed has been supported in part by the Energy Research and Development Council, the Australian Research Council, and Metals Manufactures Ltd.

Nghia Van Vo
January 8th, 1997

To My Beloved Family

Contents

Chapter 1

Superconductivity Review: Fundamentals, Materials and Applications of High-T_c Superconductors

1.1 Brief History

It could be said that superconductivity owes itself to the study of *Low Temperature Physics*. The theory of superconductivity began when scientists around the world were attempting to liquefy the so-called *permanent gases* - elements that exist on earth only in the gaseous state. Michael Faraday's realization of applying high pressure and Thomas Andrews' discovery of low temperature that made the liquefaction of carbon dioxide (~ 194.7 K) first possible in 1869 [1]. Raoul Pictet and Louis Paul Cailletet independently managed to produce droplets of liquid oxygen (~ 90.2 K) and nitrogen (~ 77.4 K) in 1877, which Zygmunt Wroblewski successfully reproduced in 1883. The greatest challenge then was to liquefy the remaining two permanent gases of hydrogen (~ 20.4 K) and helium (~ 4.2 K), and it took nearly fifteen years later for hydrogen gas to be condensed by James Dewar, in 1898 [2]. The liquefaction of helium gas was first performed by Heike Kamerlingh Onnes in 1908 and it was the pursuit in the study of the effects of impurities on the low-temperature resistance of gold and platinum that led to the discovery of superconductivity. The breakthrough was made on April 28, 1911 when the resistance of mercury was reported by Onnes to have vanished [3].

Being synonymous with its zero resistance state, it took over 20 years until in 1933 when Walther Meissner and his colleague Robert Ochsenfeld performed their landmark experiment that demonstrated the expulsion of magnetic flux density from the interior of a metal cooled below its superconducting, transition or critical temperature, T_c [4] (with the latter term sometimes defined to be the temperature at the midpoint between the onset

temperature of superconductivity and the temperature at which the specimen is in its full superconducting state). This implied that the local magnetic field causes supercurrents to flow, rather than the electric field, as in an ordinary conductor. Maxwell's classical theory of electromagnetism could not predict this perfect diamagnetism [5] and it was now clear that superconductors were not just (lossless) perfect conductors.

Based on the notion of perfect diamagnetism - the Meissner effect - the brothers Heinz and Fritz London formulated two electrodynamic equations, first published in 1935 [6]. The first London equation made an additional claim to the Meissner effect that a current that flows in a superconducting wire is maintained by its own self generating field. The second equation expresses the Meissner result whereby the magnetic flux density must vanish inside a superconductor, not merely remain unchanged. The London theory at the same time importantly established that the magnetic flux density could occupy a shallow region at the surface of a superconductor - now called the *London penetration depth*, λ_L, somewhat analogous to the skin depth, δ, in ordinary conductors. However, unlike δ, λ is not a function of frequency. According to the London theory, the magnitude of λ_L is determined by the mass, charge and density of superelectrons. This last property directly correlates with the two-fluid model (that the electrons which flow in a superconductor can be categorized into two types; the normal electrons and the superconducting electrons - hence the name) of Gorter and Casimir [7] where there is also a parameter that indicates the strength of superconductivity. Like λ_L, this parameter vanishes at the transition temperature and reaches a maximum value at the lowest temperature.

Although essentially classical, the phenomenological picture of superconductivity from the London theory and the two-fluid model from Gorter and Casimir could then be understood from a quantum mechanical view point that the superconducting electrons could somehow only move in unison - a condensation of superelectrons in momentum-space. Further contribution by London includes the prediction of magnetic flux quantization in a superconducting loop in 1950 [8].

In his 1953 paper, Brian Pippard introduced a parameter known as the coherence length, ξ, into his new formulation for the expression relating supercurrents and magnetic field [9]. This concept of nonlocal electrodynamics suggested that the extent of superconductivity is governed by the size of the region set by ξ. The consequence of this idea is that the density of superelectrons (London theory) or degree of superconductivity (two-fluid model) cannot appreciably change over an arbitrary short distance in the superconductor, but vary only a characteristic distance ξ.

Within the same decade (in 1950), Vitaly Ginzburg and Lev Landau developed yet another important phenomenological theory which uses quantum mechanics to predict the electrodynamic behaviour of superconductors [10]. The Ginzburg-Landau (GL) theory expressly makes use of a superconducting wave function whose attributes determine the behaviour of the superconductor. This wave function is termed an *order parameter* in the sense that it measures the extent to which the long-ranged order of the superconducting state exists. This order parameter in the GL theory is essentially equivalent to the London density of superelectrons or the Gorter-Casimir degree of superconductivity. One of the greatest successes of the GL theory was the prediction of the existence of type-II superconductors.

In 1957 John Bardeen, Leon Cooper and Robert Schrieffer developed, now considered as one of the great achievements of modern science, a microscopic theory of superconductivity, in that it provides an explanation of *how* superconductivity comes about at the atomic and sub-atomic level. The core of the problem was to identify a microscopic mechanism that leads to superconductivity.

Herbert Frohlich in 1950 proposed a mechanism for superconductivity whereby he suggested that ions in a superconductor or the crystalline lattice itself must participate in the interactions of the electrons (an electron-phonon interaction) [11]. He claimed the experiment required to do was to look for an isotope effect [12] in superconductors. Based on the ionic motion in solids, and that heavier ions vibrate more slowly than their counterparts (as with protons and neutrons) it was possible to relate the lattice vibration

frequency and the mass of the ions. By making use of the mass spectrographs developed in the 1940s, it was possible to sort elements by their mass. John Bardeen in that same year, duplicated Frohlich's results using a different theoretical technique [13]. Many major groups around the world eventually succeeded in demonstrating the isotopic effect, obtaining conclusive evidence that superconductivity was linked to the electron-phonon interaction.

According to quantum mechanics, it is not possible to form a bound state between any tightly bound particles unless the attractive binding energy is sufficient to overcome the particles kinetic energy. Leon Cooper took the next significant step in developing the theory of superconductivity in 1956 [14] by showing, in the presence of an attractive interaction, no matter how weak, two electrons with equal and opposite momentum added to the Fermi energy level will form a bound pair.

Having layed the ground work, Bardeen, Cooper and Schrieffer (BCS) proceeded to combine the concepts of the attractive electron-phonon interaction and the Cooper pair with the use of a mean-field assumption (by considering pair interactions only), whence the evolution of the BCS theory [15]. In the BCS theory, the transition to the superconducting state is given by

$$k_B T_c = \hbar\omega_0 \exp\left[-1/N_{(0)}V\right] \tag{1.1}$$

where k_B is the Boltzmann constant, η is the Planck constant, h, divided by 2π, ω_0 is the Debye frequency of the lattice, $N_{(0)}$ is the density of states at the Fermi surface, and V is the effective electron-electron attraction potential with $N_{(0)}V$ as the dimensionless electron-phonon coupling parameter. Equation (1.1) yields insight concerning the enhancement of the superconducting transition temperature, T_c. It is dependent on the frequency of the lattice vibrations, the density of states of carrier electrons and the net attractive potential between the paired electrons. The theory shows that the transition to the superconducting state is caused by an attractive interaction between the itinerant charge carriers (electrons

or holes) mediated by the lattice which causes them to form pairs. It enables the calculation of the probability for forming Cooper pairs from electrons of given energy levels in the Fermi sea possible. This calculation reveals an energy distribution complete with an energy gap which corresponds to the binding energy of the Cooper pair. The attractive interaction responsible for pairing is caused by the virtual exchange of phonons, the quantized vibrational modes of the lattice. These are the same lattice vibrations which, when thermally excited, scatter the conduction electrons - a process that results in the temperature-dependent electrical resistance. This theory provides the understanding for why poor metals are good superconductors: a strong electron-phonon interaction gives high resistance above T_c, and strong pairing below. The BCS theory has been successful in explaining essentially all of the phenomena associated with the superconducting state, inlcuding: specific heat, critical fields, tunnelling, and others.

The other major theoretical development in superconductivity came in 1962 with Brian Josephson's prediction of pair tunnelling between weakly linked superconductors [16]. The quantum mechanical process of tunnel junctions had first been studied by Ivar Giaever in 1960 describing that the chances of a particular electron crossing through a tunnelling barrier were slim but nonzero. By 1963, the first Josephson junctions had been made and the theoretical prediction was verified. When pairs carry current, there is no resistance, thus there is zero-voltage current in a Josephson junction. Josephson also predicted an additional effect in these junctions: the so-called *ac Josephson effect*. With an applied voltage across a thin insulating oxide barrier (~ 10 Å) between two superconductors, an alternating current flows whose frequency is set by the magnitude of the voltage.

In 1957, Alexei Abrikosov [17] theoretically predicted the existence of what he coined the *mixed state* in superconductors. This state reduces the amount of energy that a superconductor must expend in expelling magnetic flux densities by letting a partial penetration of the field into the material. In the ordinary Meissner effect, magnetic flux densities are kept at bay by surface diamagnetic screening currents. In the mixed state, the flux lines penetrate the superconductor through a number of cylindrical cores of normal material distributed across the superconducting surface. The cores or *vortices* are

surrounded by tiny circulating currents maintaining a magnetic field. Each vortex contains exactly 1 quantum of magnetic flux. As predicted by Fritz London, any closed loop of superconductor can contain only certain quantized amounts of magnetic flux; a vortex in the mixed state forms just such a closed loop.

Superconductors exhibiting these behaviour are known as *type-II superconductors*, which act like ordinary superconductors in the presence of small magnetic fields (as *type-I superconductors*), but in a sufficiently large field, the mixed state takes over [18]. In this state, the field generated by the current encircling each vortex is interacted with the field of other vortices. This result in an arrangement called *fluxon lattice* due to the repulsive forces that exist between the vortices. To achieve the lowest energy state, the lattice takes on an hexagonal symmetry. The size of the vortices is set by the superconducting coherence length (~ a few 100s Å). The GL theory of superconductivity thus provided a way to predict a type-II behaviour in superconductors. The test involves comparing the magnetic penetration depth, λ, with the superconducting coherence length, ξ [19]. Type-II superconductors always have $\lambda > \xi$, the reason being that ξ determines the characteristic separation between the electrons in a Cooper pair. This separation is normally so large that many pairs can coexist (electrons can 'exchange partners' if you will) in the same region of the superconductor (as with type-I superconductors). When the separation of ξ is small (like in type-II superconductors), the Cooper pairs cannot over lap much and as a result, magnetic flux lines can thread their way between Cooper pairs in discrete channels. Most elemental superconductors have been shown not to have such compact Cooper pairs, whereas niobium and most alloys and compounds do [20].

It turns out that the presence of the vortices in superconductors enables them to cope with magnetic fields in a way that requires the expense of much less energy. As a result, type-II superconductors can sustain superconductivity in far greater magnetic fields making them prime candidates for superconducting wire applications. However, to be useful, the current carrying capacity of any superconductor is also of major concern. For type-II superconductors, their critical currents (I_c, the current at which the onset to the normal state occurs) can be improved by manipulation of the imperfections in the superconductor.

By virtue of the Meissner effect, supercurrents flow only at the surface of type-I superconductors. For type-II superconductors, the mixed state allows supercurrent to flow partially into the superconductor, but according to the law of electromagnetism, moving electrons and magnetic fields exert forces on one another [21], this so-called Lorentz force causes the vortices to move at right angles to the direction of current flow, which give rise to energy dissipation in the form of heat. This dissipation of energy or *flux flow resistance* results in very small I_c for type-II superconductors. Fortunately, flux flow resistance can be overcome by controlling the imperfections of the superconductors by either adding appropriate elements or by means of mechanical deformation of the superconducting wire [22].

So much for the theoretical development in superconductivity. The search for superconducting materials continues on with over a quarter of all the natural elements - and about half the metallic elements found to be superconductors. The applications for the so-called *low temperature superconductors* (LTSC) is another topic of its own and shall be mentioned briefly later on in this chapter. The transition temperature for most alloys and compounds (T_c up to ~ 23.2 K) [23] is usually somewhat higher than for elemental metals (T_c of no more than ~ 9.25 K, that of niobium) [24] such compounds followed certain empirical rules [25] (discovered from experiments, not deduced from theory) which were first reported by Matthias and co-workers [26] in 1953. Synthesizing compounds according to Matthias's rules became a major research activity in the 1960s and 1970s. Soon the quest for the highest possible superconducting transition temperature centred around the niobium compounds and one particular crystal structure known as the beta-tungsten or "A15" structure [27]. The highest T_c recorded for materials with the A15 structure was ~ 23.2 K, that of the binary compound of niobium germanium (Nb_3Ge) reported by John Gavaler in 1973 [28]. This T_c remained the highest for the next 15 years until a breakthrough in an entirely different class of material to surpass the superconductivity of the niobium compounds.

In 1973, the first superconducting oxide was discovered by David Johnston and Bernd Matthias - that of lithium titanate, with a respectable T_c of ~ 13 K [29]. Two years later, Arthur Sleigh discovered another superconducting oxide, barium-lead-bismuth-oxide with a T_c of ~ 14 K. Despite these discoveries the search for *high temperature superconductors* (HTSC) was mainly focussed on intermetallic compounds (formed from metals), organic compounds and thin film materials. The breakthrough came in 1986, when a superconducting oxide in the Ba-La-Cu-O system (or $La_{1.85}Ba_{0.15}Cu_1O_4$) or chemically known as *perovskites* [30], was reported to have a transition temperature of ~ 40 K by Johannes Georg Bednorz and Karl Alex Mueller [31]. This record T_c did not stand for long when within less than a year later, Maw-Kuen Wu and James Ashburn (lead by Ching-Wu Paul Chu) smashed it with the announcement of superconductivity at ~ 90 K (breaking the liquid nitrogen barrier of 77 K) in compounds with the general formula $RBa_2Cu_3O_\delta$ (i.e. RBCO, in which R indicates Y or a rare-earth element) [32]. This fuelled the search for even higher- T_c materials. Two major discoveries followed soon after, again in the copper-oxide system, and as a result have launched HTSC technology with great practical possibilities. The first superconducting system published by Maeda *et al* in 1988 [33] was that in the Bi(Pb)-Sr-Ca-Cu-O (BSCCO) with T_c's as high as ~ 110 K. The second subsequently reported by Herman *et al* [34] also in the same year, was that of Tl-Ba-Ca-Cu-O (TBCCO) system with a T_c of ~ 125 K, second only to Hg-Ba-Ca-Cu-O (HBCCO) with a current T_c record of ~ 135 K [35].

At the present time there are strong indications that the pairing interaction in the so-called high-T_c (to mean anything with $T_c \geq 90$ K) copper oxide superconductors is not due to phonons (unlike conventional superconductors - defined as superconductors that do not contain Cu-O planes, or $T_c \leq 25$ K) but rather other degrees of freedom are responsible [37]. While there is no clear consensus among scientists, most would agree however, that the role of phonons cannot be excluded (at least) up to ~ 50 K and that present theories do not exclude the existence of even higher $T_c > 200$ K. With these cuprates superconductors, both their superconductivity, and *normal state* properties posed the greatest challenge to the existing theory developed so far.

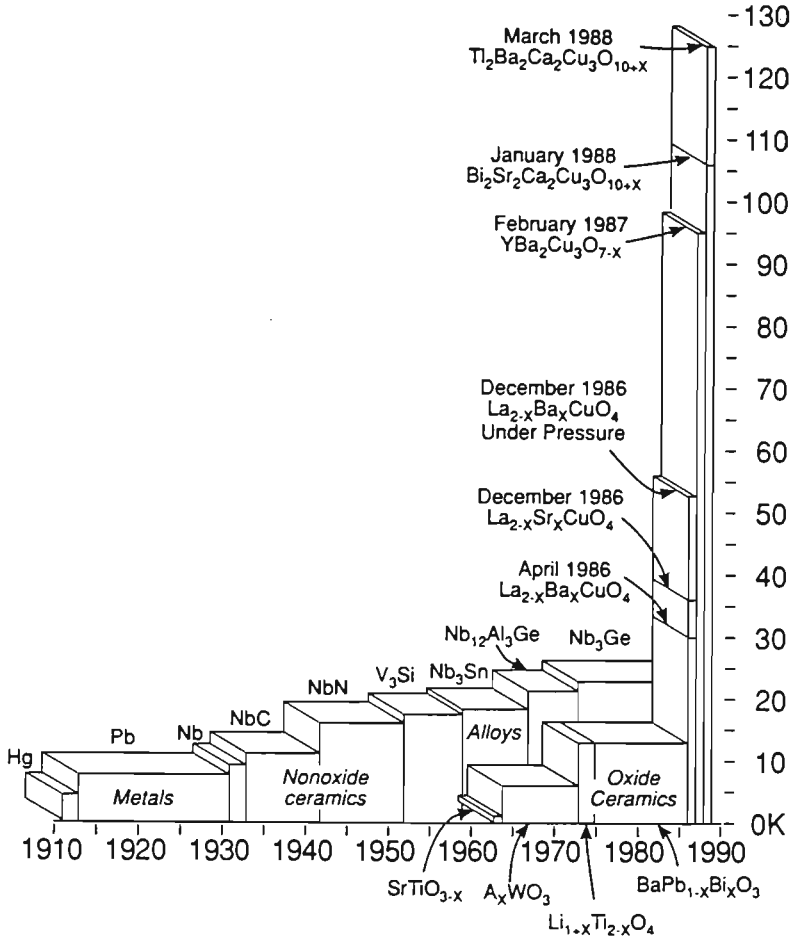

Figure 1.1 *The evolution of critical temperatures since superconductivity was first discovered [36].*

1.2 Fundamentals of Superconductivity

The discussions on the fundamentals of superconductivity in this section focus primarily on type-II and the high-T_c superconducting (HTSC) oxides, with the inclusion of the relevant theories and results established so far for type-I superconductors where necessary. Although the explanation for the mechanism responsible for superconductivity in HTSC cuprates remains to be a topic of theoretical research, the macroscopic behavior of these superconductors however, can be quantified by fundamental physics. Rigorous mathematical treatment on the theory of superconductivity is beyond the scope of this

thesis and can be found in some of the text books and journal articles given in the reference section.

1.2.1 Zero Resistance and Perfect Diamagnetism

It is a known fact that any material which is considered to be a superconductor must exhibit the following two properties: no electrical resistivity and zero internal magnetic induction.

1.2.1.1 No electrical resistivity ($\rho = 0$ for all $T < T_c$)

When the state of superconductivity is reached, scattering between electrons and lattice vibrations ceased to exist. The electrons which form into pairs have opposite momenta (and opposite spins) with zero net momentum. By the de Broglie relation for the Fermi momentum $\boldsymbol{p}_F$ and wave vector $\boldsymbol{k}_F$ [38]

$$\boldsymbol{p}_F = \eta \boldsymbol{k}_F \tag{1.1}$$

where η is the Planck constant, h, divided by 2π, the associated wave of the pair has an infinite wavelength (or in physical terms, the wavelength is the of the order of the size of the sample), since in the *matter waves* equation, $\lambda = h/mv$, with m the mass of the moving particle with a velocity v. Hence the Cooper pairs cannot be scattered by the usual way as normal electrons, i.e. there is no mechanism that could give rise to resistivity. This property can be demonstrated with the percolative nature of a dc-resistivity measurement made on a HTSC multifilamentary $Bi_{1.8}Pb_{0.4}Sr_{2.0}Ca_{2.2}Cu_{3.0}O_x$ silver sheathed (or Bi(Pb)-2223/Ag) tape prepared at the Center for Superconducting and Electronic Materials (CSEM), Institute of Materials Technology and Manufacturing (IMTM), University of Wollongong (UW). The transition temperature curve is shown in Fig. 1.2 below.

In a conventional superconductor, the resistive transition shifts downwards with increasing applied external magnetic field. In HTSC material the same increase in field would cause a

broadening of the transition. This effect is shown in Fig 1.3, that of a Bi(Pb)-2223/Ag superconducting tape.

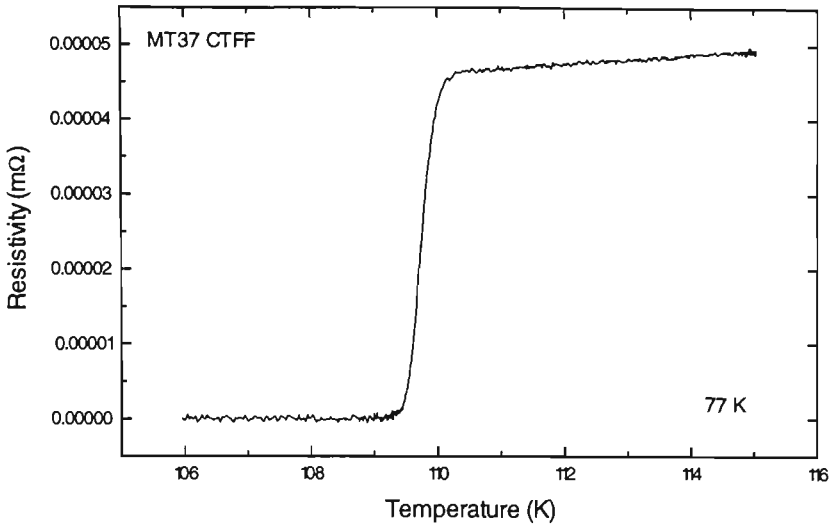

Figure 1.2 *Temperature dependence of electrical dc-resistivity of a 37 filamentary Bi(Pb)-2223/Ag oxide superconducting tape. The measurement was carried out at liquid nitrogen temperature of ~ 77 K with zero applied magnetic field.*

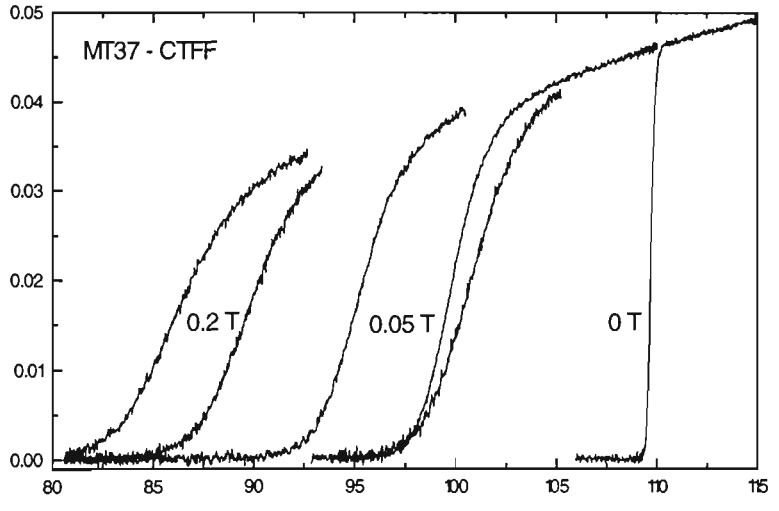

Figure 1.3 *The broadening effect of temperature dependence electrical resistivity measurements due to background field for the same HTSC tape shown in Fig. 1.2.*

The plots of Fig. 1.3 also show the anisotropy of these HTSC oxides, namely with conductivity decreases dramatically in the *c-axis* (normal to the tape plane) in comparison with that in the *ab-plane* (or tape plane). This is attributed to the inherent plate-like crystallites of these layered structure ceramic materials composed of the non-metallic Bi-O layers [39].

In general, dc-resistive measurements are not very sensitive to small amounts of impurity, though magnetic impurities tend to lower the transition temperature [40]. A more informative method would be that of magnetic ac-susceptibility (a volumetric method in nature) where more precise temperature determination, geometrical concerns and the detection of impurity phase (and hence loss mechanism) can be revealed in one measurement [41]. Figure 1.4 depicts one of such measurements performed at the Center.

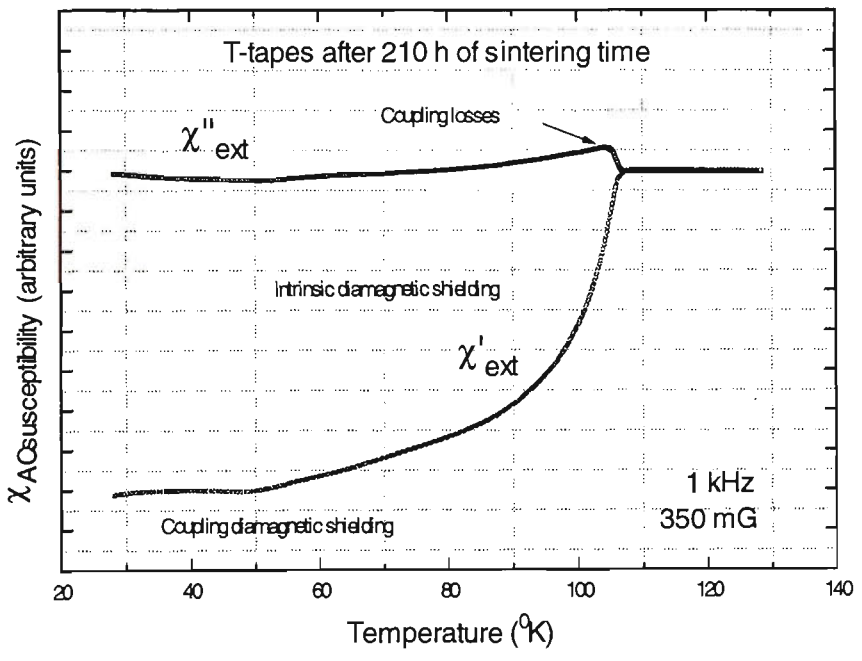

Figure 1.4 *Real and imaginary ac-magnetic susceptibilities, χ' and χ'' as a function of increasing temperature in field of 350 mG at 1kHz, with the intrinsic and coupling segments identified for a monocore Bi(Pb)-2223/Ag tape.*

It must be mentioned that the conditions for superconductivity are different when the superconductor is subjected to an ac-current because of the inertial mass of the superelectrons. The alternating electric field thus causes the supercurrent to lag behind - superconductivity does not occur instantaneously but only at the rate at which the electrons accelerate in the electric field. Hence the superelectrons present and inductive impedance. In addition, since there is now an alternating e.m.f. present, some of the current will be carried by the normal electrons. This also results in an inductive reactance, but is swamped by the resistance resulting from their being scattered in the metal. Hence a representation for a superconductor under ac-resistivity conditions would be a perfect inductance in parallel with a resistance.

1.2.1.2 No magnetic induction ($B = 0$ inside the superconductor)

This behavior is analogous to Lenz's law for electromagnetic induction of normal metals. The screening currents on the surface of the superconductor would generate an internal flux density everywhere equal and opposite to the applied magnetic flux density, $\boldsymbol{B}_a$, and consequently the net flux density is zero. Alternatively, the exclusion of magnetic flux lines in a superconductor can be explained with the assumption that the relative permeability $\mu_r = 0$ (the effect of screening currents is included in this statement), thus $\boldsymbol{B} = \mu_r \boldsymbol{B}_a$ is zero. The magnetic field strength of the applied field is given by

$$\boldsymbol{H}_a = \frac{\boldsymbol{B}_a}{\mu_0}, \tag{1.2}$$

(μ_0, the permeability of free space = $4\pi\times10^{-7}$ H/m) and that the flux density in a magnetic material is related to the strength of the applied field by

$$\boldsymbol{B} = \mu_0 (\boldsymbol{H}_a + \boldsymbol{M}) \tag{1.3}$$

where $\boldsymbol{M}$ is the magnetization, which represents the intrinsic magnetic properties of a medium. The Meissner effect requires $B = 0$ implies that

$$M = - H_a, \tag{1.4}$$

and the magnetic susceptibility, i.e. the ratio of the magnetization to the field strength, must be

$$\chi = -1 \tag{1.5}$$

the negative sign of Eqn. 1.4 and 1.5 indicates that the superconductor becomes a perfect diamagnet that excludes the flux from its interior by means of surface currents.

This second property can be better envisaged from a schematic shown in Fig. 1.5 where perfect diamagnetism is achieved.

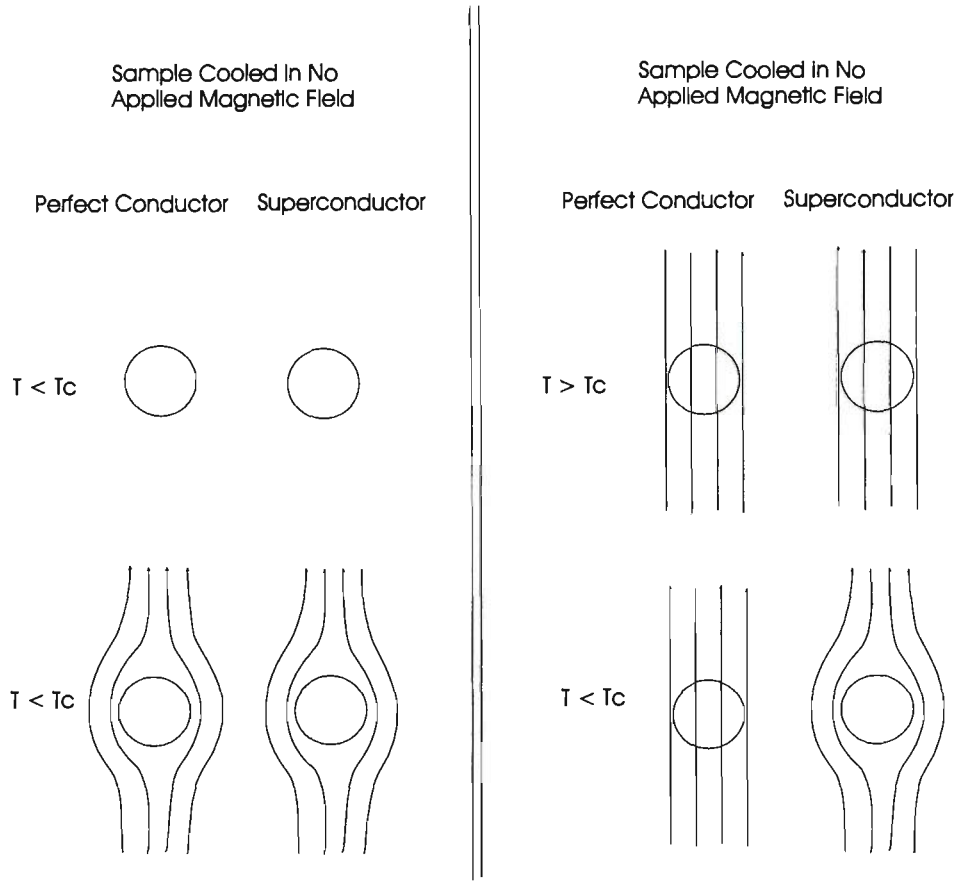

Figure 1.5 *Magnetic behavior between a "perfect conductor" and a superconductor [5].*

Unlike the "perfect conductor", a metal in a superconducting state never allows a magnetic flux density to exist in its interior as shown in Fig. 1.5. The state of magnetization of a "perfect conductor" would depend on the order in which the final conditions of applied magnetic field and temperature were obtained, but the magnetization of a superconductor depends only on the actual value of the applied field and temperature, not on the way they were arrived at.

1.2.2 Characteristic Lengths and Critical Fields

In general, associated with each superconductor is a critical surface of current density, magnetic field and temperature (*J-H-T*) defining the region within which the material is superconducting.

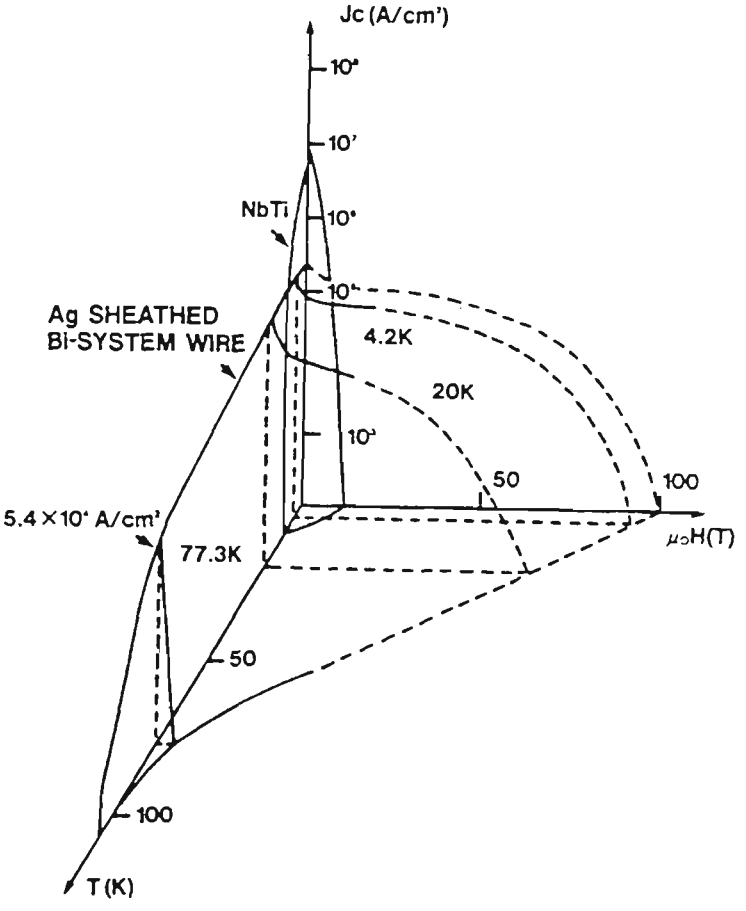

Figure 1.6 *The relationship between temperature (T), magnetic flux density ($\mu_0 H$), and current density (J) in a superconductor. Superconductivity is sustained anywhere inside the surface [42].*

Apart from the intrinsic critical temperature, T_c, and critical field, H_c, superconductors of various types can categorically be grouped according to their characteristic lengths. These are [5]; the wavelength of electromagnetic field, $2\pi c/\omega$ (with c the velocity of light and $\omega/2\pi$ the frequency of the field), the magnetic penetration depth, λ (that thickness of a sample as measured from the surface, through which supercurrents flow), the coherence length, ξ (the characteristic distance that the electrons in the Cooper pair remained correlated) and the mean free path, l_{tr} (being the intrinsic average distance between scattering events given that the average time between each scattering event is τ_{tr}, such that $l_{tr} = v_F \tau_{tr}$, where v_F is the Fermi velocity, order of ~ 10^6 m/s in most metals [43]).

1.2.2.1 Coherence length

The notion of coherence length, ξ, was first introduced in the microscopic theory of BCS and is given by [15]:

$$\xi_0 = 0.18\frac{\eta v_F}{k_B T_c} \tag{1.6}$$

where ξ_0 denotes the BCS coherence length. For a T_c of ~10 K, ξ_0 ~1800 Å. This length is temperature-independent. Note that ξ_0 is much greater than the average distance between electrons in a solid, one Cooper pair overlaps many others. This overlap causes a correlated state over the entire solid and gives rise to a macroscopic wave function or an order parameter, thus creating the superconducting state. The relation to the temperature dependent coherence length $\xi(T)$ of the Ginzburg-Landau (GL) theory, depends on the mean free path l_e of the electrons [10]. The two limiting cases are given here for an isotropic superconductor. For a 'clean' material (where l_e is much greater than ξ_0) the temperature dependent coherence length is given by [5]:

$$\xi(T) = 0.74\xi_0\left(\frac{T_c}{T_c - T}\right)^{1/2}, \quad l_e \gg \xi_0, \tag{1.7}$$

and in the case of the 'dirty' limit, it is given by

$$\xi(T) = 0.85\sqrt{\xi_0 l_e}\left(\frac{T_c}{T_c - T}\right)^{1/2}, \quad l_e \ll \xi_0, \tag{1.8}$$

Equations (1.7) and (1.8) have an important physical interpretation. When the superconductor is being alloyed with non-magnetic impurities, its T_c and v_F remain unchanged, hence ξ_0 is rather insensitive to alloying. However, by decreasing the mean free path with alloying, the GL coherence length of $\xi(T)$ would also decrease.

For an anisotropic superconductor (such as those of HTSC cuprates), the following expressions are better suited in characterizing their coherence lengths, also derived from the GL equations [18]:

$$\xi^c = \frac{h}{\sqrt{2m^c\alpha}}, \tag{1.9}$$

and

$$\xi^{ab} = \frac{h}{\sqrt{2m^{ab}\alpha}}, \tag{1.10}$$

where the electron mass m has been replaced by the tensor mass m^c and m^{ab} along the *c*-axis and *ab*-plane respectively, due to the layered structure of these HTSC oxides, with $\alpha = a(T\text{-}T_c)$, a a constant in the Helmholtz free energy expression in powers of magnetization, close to the transition point [35]. Note that the directions *a* and *b* are taken to lie in the plane of the Cu-O planes while the *c-axis* is taken to be perpendicular to that plane. The results from Eqn. 1.9 and 1.10 indicate that $\xi^c \ll \xi^{ab}$.

1.2.2.2 Penetration depth

For isotropic superconductors, the expressions for the penetration depth, $\lambda(T)$, for two limiting cases in the Ginzburg-Landau analysis is given below [18]

$$\lambda(T) = \frac{1}{\sqrt{2}}\lambda_L\left(\frac{T_c}{T_c - T}\right)^{1/2}, \quad l_e \gg \xi_0, \tag{1.11}$$

where the London penetration depth, $\lambda_L = [m/\mu_0 n e^2]^{1/2}$, ($n$ the number of carriers per unit volume) and

$$\lambda(T) = 0.64\sqrt{\frac{\xi_0}{l_e}}\left(\frac{T_c}{T_c - T}\right)^{1/2}, \quad l_e \ll \xi_0, \tag{1.12}$$

Contrary to the coherence length, which decreases as the mean free path becomes shorter by alloying, the penetration depth increases. As a result the Ginzburg-Landau parameter $\kappa = \lambda/\xi$, is given in the two limits by [18]:

$$\kappa = 0.96\frac{\lambda_L}{\xi_0}, \quad l_e \gg \xi_0, \tag{1.13}$$

and

$$\kappa = 0.715\frac{\lambda_L}{\xi_0}, \quad l_e \ll \xi_0, \tag{1.14}$$

From the Eqn. 1.13 and 1.14, it can be seen that κ increases with decreasing mean free path. Thus it is possible to produce a type-II superconductor by alloying a type-I superconductor. Close to T_c, κ is independent of temperature and it enables the distinction between type-I ($\kappa \leq 1/\sqrt{2}$) and type-II ($\kappa \geq 1/\sqrt{2}$) superconductors.

With HTSC oxides possessing high T_c (some 10 times of that of type-I and some conventional superconductors), it can be expected from Eqn. 1.6 that these cuprates have

much shorter coherence lengths since $\xi \sim v_F/k_B T_c$. In addition, because of the low density of carriers, v_F in the ionic materials of HTSC is also lower than in normal metals. This results in a very short ξ. Again, due to the anisotropy nature, the penetration depths vary depending on the orientation of the superconducting material:

$$\lambda^c = \frac{m^c}{\sqrt{\mu_0 n e^2}}, \tag{1.15}$$

and

$$\lambda^{ab} = \frac{m^{ab}}{\sqrt{\mu_0 n e^2}}, \tag{1.16}$$

which implies that in high-T_c oxides, $\lambda^c \ll \lambda^{ab}$. Tables 1.1(a)-(c) lists some characteristic property and critical field values for the three types of superconductors [18, 35, 37].

The values given in Table 1.1(a) are for clean elements of type-I superconductors while in 1.1(b) they are representative values for type-II superconductors (again depends on how clean or dirty the material is).

TABLE 1.1 *Approximate values of the characteristic parameters and critical fields of type-I and type-II superconductors (T_c values are in zero magnetic field).*

(a) Type-I

Material	T_c (K)	λ_0 (Å)	ξ_{c0} (Å)	Δ_0 (meV)	B_{c0} (mT)
Al	1.18	500	16000	0.18	10.5
In	3.41	650	3600	0.54	23.0
Sn	3.72	500	2300	0.59	30.5
Pb	7.20	400	900	1.35	80.0
Nb	9.25	850	400	1.50	198.0

(b) Type-II (Conventional Superconductors)

Material	T_c (K)	$\lambda_{GL}(0)$ (Å)	$\xi_{GL}(0)$ (Å)	Δ_0 (meV)	$B_{c2,0}$ (T)
Pb-In	7.0	1500	300	1.2	0.2
Pb-Bi	8.3	2000	200	1.7	0.5
Nb-Ti	9.5	3000	40	1.5	13
Nb-N	16	2000	50	2.4	15
$PbMo_6S_8$	15	2000	20	2.4	60
V_3Ga	15	900	20-30	2.3	23
V_3Si	16	600	30	2.3	20
Nb_3Sn	18	650	30	3.4	23
Nb_3Ge	23	900	30	3.7	38

(c) Type-II (High-Temperature Superconductors)

Material	T_c (K)	λ^{ab} (Å)	λ^{c} (Å)	ξ^{ab} (Å)	ξ^{c} (Å)	$B_{c2}^{ab}(T)$	$B_{c2}^{c}(T)$
$La_{1.85}Sr_{0.5}CuO_4$	40	800	4000	40	7	80	15
$YBa_2Cu_3O_7$	95	1500	6000	15	4	150	40
$Bi_2Sr_2CaCu_2O_8$	85	250	5000	40	2	280	32
$Bi_2Sr_2Ca_2Cu_2O_{10}$	110	2000	10 000	13	2	250	30
$Tl_2Ba_2Ca_2Cu_2O_{10}$	125	2000	6000	--	--	120[#]	--

[#] *Thallium based systems exhibit non-micaceous morphology showing less anisotropy in their microstructure [35].*

For type-I and conventional superconductors, the '0' subscript is used to denote values given at zero temperature, e.g. Δ_0 is the gap characteristic given at zero temperature (with $2\Delta(T)$ as the electrons binding energy or 'energy gap' in a Cooper pair). The penetration depth $\lambda_{GL}(0)$ and coherence length $\xi_{GL}(0)$ are coefficients of the Ginzburg-Landau temperature dependence equations [5] similar to that of Eqn. 1.7, 1.8 and 1.11, 1.12. Table 1.1(c) lists the approximated values for some HTSC materials given in their nominal compositions (since the stoichiometric values of these compounds do vary substantially making some of these results not being well established). Apart from the two distinctive

values of upper critical magnetic flux densities of $B_{c2}^{ab}(T)$ and $B_{c2}^{c}(T)$ (discussed next) listed in Table 1.1(c), the measurement of the energy gap parameter is also affected by the anisotropic nature of these HTSC oxides, hence making it only plausible to say that the gap in the *ab*-plane is larger than along the *c*-axis for these materials. For some HTSC oxides however, the superconducting energy gap is ~ 25 meV [37].

1.2.2.3 Critical fields

In a type-I superconductor with a geometry where demagnetization effects can be ignored, Eqn. 1.4 holds up to the critical field $H_c(T)$, which has been experimentally established to be described within an error of a few percent by the following 'parabolic' relation [18]

$$H_c(T) = H_0\left[1-\left(\frac{T}{T_c}\right)^2\right] \tag{1.17}$$

with H_0 the extrapolated value of H_c at absolute zero temperature. Note that the H_c vanishes at T_c, where a change of phase from the perfect diamagnetism state to the normal state takes place.

In a type-II superconductor for which in increasing magnetic field, the Meissner state is followed by the mixed state before the normal state is reached. In the mixed state, single-quantum magnetic flux lines enter the superconductor forming a flux line lattice representing a mixture between the superconducting and the normal phases. The value of magnetic field at which the mixed state starts to form is called the lower critical field H_{c1}. The mixed state extends up to the magnetic field value H_{c2} called the upper critical field. The following relations for H_{c1} and H_{c2}, for isotropic superconductors derived from the Ginzburg-Landau equations [44] (based on the Schrödinger equation from wave mechanics) are given as follows:

$$H_{c1} \approx \frac{\Phi_0}{4\pi\mu_0\lambda^2}\ln\kappa \approx \frac{H_c}{\sqrt{2}\kappa}\ln\kappa \tag{1.18}$$

and

$$H_{c2} = \frac{\Phi_0}{2\pi\mu_0\xi^2} = \sqrt{2}\kappa H_c \tag{1.19}$$

where the quantity $\Phi_0 = h/2e = 2.07 \times 10^{-15}$ Tm^2 represents the magnetic flux quantum.

By applying the Ginzburg-Landau equations, it can be established that the following relation holds true:

$$B_{c2} = \mu_0 H_{c2} = \mu_0 \kappa \sqrt{2} H_c \,. \tag{1.20}$$

Thus this further enables the distinction between the two types of superconducting materials;

- if $\kappa \leq 1/\sqrt{2}$, then $B_{c2} < B_c$, as for a type-I superconductor - by decreasing the field the superconductor state appears at (and below) B_c with total expulsion of the flux.

- If $\kappa \geq 1/\sqrt{2}$, then $B_{c2} > B_c$, as for a type-II superconductor - since the flux expulsion is not complete, the superconducting state appears at and below B_{c2}.

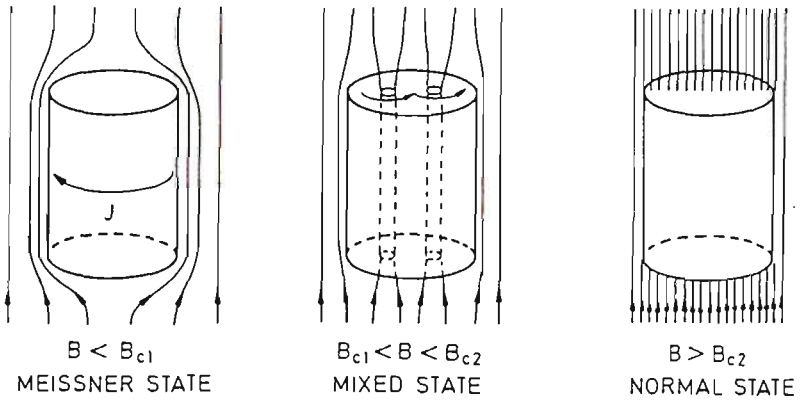

Figure 1.7 *Magnetic flux expulsion in the Meissner state, partial penetration in the mixed state and total penetration in the normal state [18].*

Figure 1.7 illustrates the manifestation of magnetic flux density B within a superconductor for the three different states - Meissner, mixed and normal states. Figures 1.8(a) and (b) show the magnetization behavior with applied external magnetic induction. The variation of critical fields B_{c1} and B_{c2}, as a function of temperature is shown in Fig. 1.9.

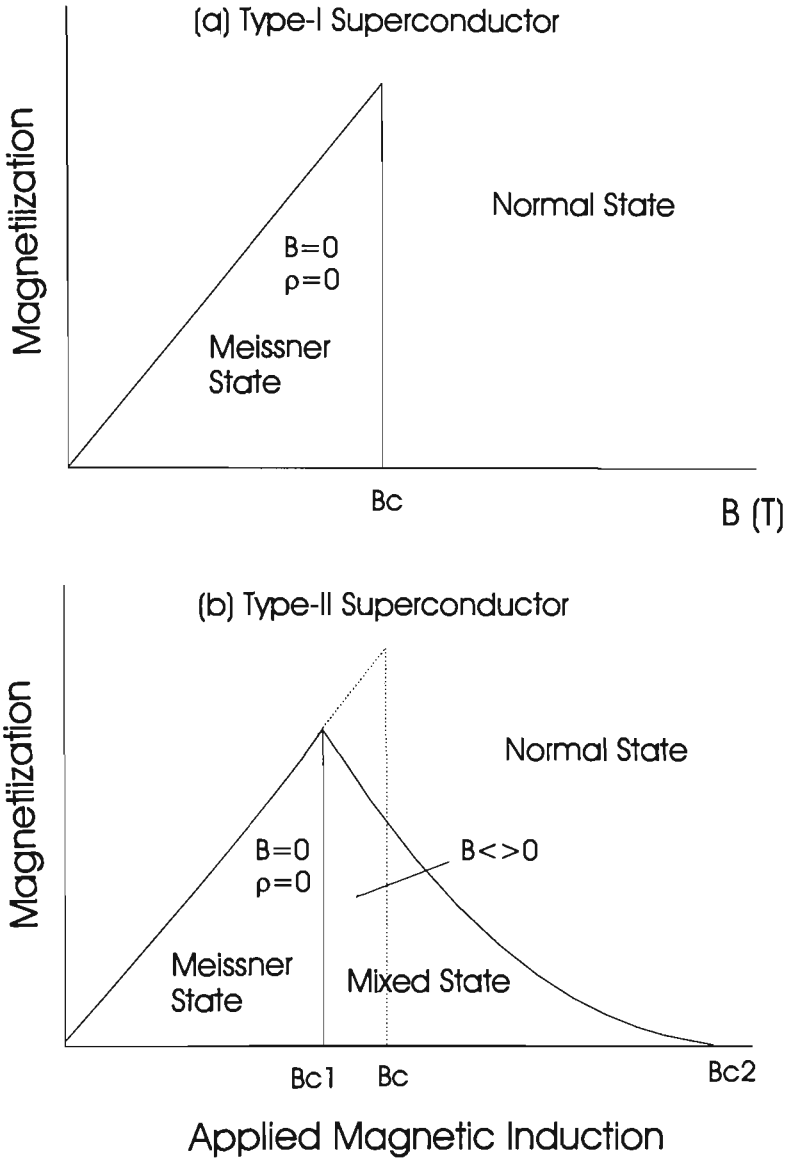

Figure 1.8 *Variation of magnetization as a function of applied magnetic induction for (a) type-I and (b) type-II superconductor.*

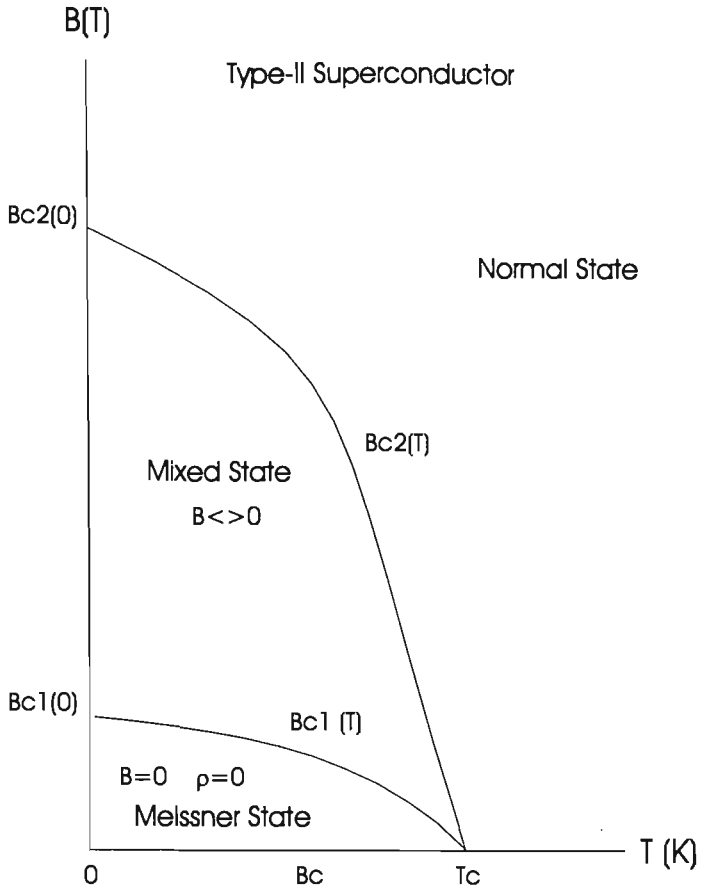

Figure 1.9 *Variation of critical fields B_{c1} and B_{c2}, as a function of temperature [18].*

Typical critical field values for various types of superconductors are given in Table 1.1(c). The product of Eqn. 1.18 and 1.19 gives rise to the following relation which gives some insight into the magnitude of critical fields of type-II superconductors:

$$B_{c2}B_{c2} = B_c^2 \ln\kappa \,. \tag{1.21}$$

As the value of the critical field does not vary very much in an isotropic type-II superconductors between 0.1 and 1 T, Eqn (1.21) implies that the higher B_{c2} is, the lower B_{c1} becomes. In high-T_c superconductors where B_{c2} is very high (of the order of 100 T) due to the short ξ, B_{c1} is very small of the order of 10 mT (see also Table 1.1(c)). The following expressions best describe the limiting values of critical fields for the HTSC oxides, derived from the anisotropic version of the GL equations:

$$B_{c1}^{c} = \frac{\Phi_0}{4\pi\left(\lambda^{ab}\right)^2}\ln\frac{\lambda^{ab}}{\xi^{ab}} \quad \text{for } B//c, \tag{1.22}$$

and

$$B_{c1}^{ab} = \frac{\Phi_0}{4\pi\lambda^{ab}\lambda^{c}}\ln\left(\frac{\lambda^{ab}\lambda^{c}}{\xi^{ab}\xi^{c}}\right) \quad \text{for } B\perp c, \tag{1.23}$$

for the lower critical field, and

$$B_{c2}^{c} = \frac{\Phi_0}{2\pi\left(\xi^{ab}\right)^2} \quad \text{for } B//c, \tag{1.24}$$

and

$$B_{c2}^{ab} = \frac{\Phi_0}{2\pi\xi^{ab}\xi^{c}} \quad \text{for } B\perp c, \tag{1.25}$$

for the upper critical field.

Although the phenomenological model proposed by Lawrence and Doniach [45] (two superconducting layers coupled by a Josephson junction) can be used to further describe the above properties of the layered oxides, the microscopic theory of BCS and GL still remain very useful as it accounts for many properties of these highly anisotropic HTSC oxides such as those of Bi- and Tl- based compounds.

1.2.3 Flux Pinning and Irreversibility

Superconductors find applications in areas such as power engineering and electronics primarily on the account of their ability to sustain extremely high current densities. Above a certain critical current density, J_c, however the material becomes normal or resistive. When current is flowing, flux motion requires a voltage to sustain that current, thus defeating the purpose of superconductivity. Flux line motion also originates from thermally activated fluctuations, and is therefore a means of dissipating energy within a superconductor. Flux pinning can then be understood as an interaction between defects or

inhomogeneities in type-II superconductors and the flux lines, and mostly connected with the variation of the order parameter (or wavefunction: $\psi(\mathbf{r}) = |\psi|\exp i\varphi(\mathbf{r})$, a complex scalar) in the homogeneity [23]. Pinning sites for flux vortices by almost all defects, such as dislocations (extended departure from regularity in crystals), point defects (defects which involve one atom or molecule), voids, grain boundaries, twin boundaries and precipitates, is based on this mechanism [46].

1.2.3.1 Flux flow

When a type-II superconductor is in a mixed state with a transport current density **J** flowing through the superconductor, the Lorentz-force on a unit length of a flux line, per area of superconductor is given by $\mathbf{f_L} = \mathbf{J}\times\Phi_0$ with the corresponding macroscopic Lorentz-force density is given as $\mathbf{F_L} = \mathbf{J}\times\mathbf{B}$, where **B** is the applied magnetic flux density. Flux line movement begins to set in when F_L exceeds F_p, the macroscopic pinning force density. This pinning force density is directly related to the critical current density J_c, by the expression $F_p = J_cB$, when the transport current and applied field are perpendicular to each other. The motion of flux lines is in the direction of the driving Lorentz-force with velocity **v** which induces an electric field **E** given by: $\mathbf{E} = \mathbf{B}\times\mathbf{v}$.

Flux flow is the motion of flux line lattice (FLL) induced when $J > J_c$. Thus the movement of the FLL is only retarded by viscous damping as there is now no pinning of the flux lines. The viscosity η, is an unknown parameter which experimentally has been observed to be independent of current and does not vary very much with B [47]. In terms of the normal state resistivity ρ_n, magnetic flux quantum Φ_0, and upper critical field B_{c2}, is given by [47]

$$\eta = \frac{\Phi_0 B_{c2}}{\rho_n}. \tag{1.26}$$

Once there is a flux flow and a resistance in the material (at the onset, as $J > J_c$), thermal heating may produce a positive-feedback mechanism to further enhance the flow. It has been proposed that this energy dissipation originates from the moving of a vortex core [48]. This

core area, with a radius of about ξ, is in the normal state and the energy dissipation in this area is caused by an ordinary resistivity process.

1.2.3.2 Flux creep and TAFF

In the case where $F_L < F_p$, when $J < J_c$, with sufficient temperature T, thermal fluctuations permit the flux lines to move and the phenomenon is often referred to as *flux creep*. Its prediction was made in 1962 by Anderson [49], investigated for conventional superconductors in 1969 by Beasley *et al* [50] and recently revived for the study of high-T_c superconductors in 1988 by Dew-Hughes [51]. Thermally assisted flux flow (TAFF) appears only in HTSC oxides for $J \ll J_c$, with the same type of mechanism as flux creep. The various regimes of flux motion are shown in Fig. 1.10 below.

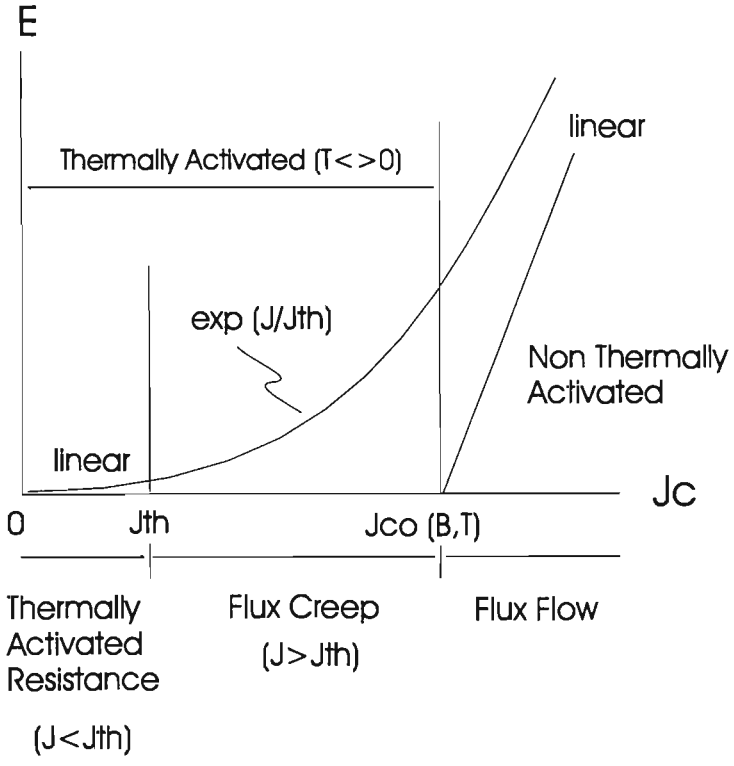

Figure 1.10 *E versus J plot at finite temperature, showing the effect of thermally activated flux motion. This giant flux creep (used to describe the behavior of HTSCs) causes energy dissipation (equivalent to resistance) at $J \ll J_c$ [35].*

In either flux creep or flux flow, a flux line or flux bundle is imagined to hop over the pinning energy barrier under the influence of a Lorentz-force. A series of wells evolves into a staircase with progressively less opposition to flux motion. Figure 1.11 illustrates this effect.

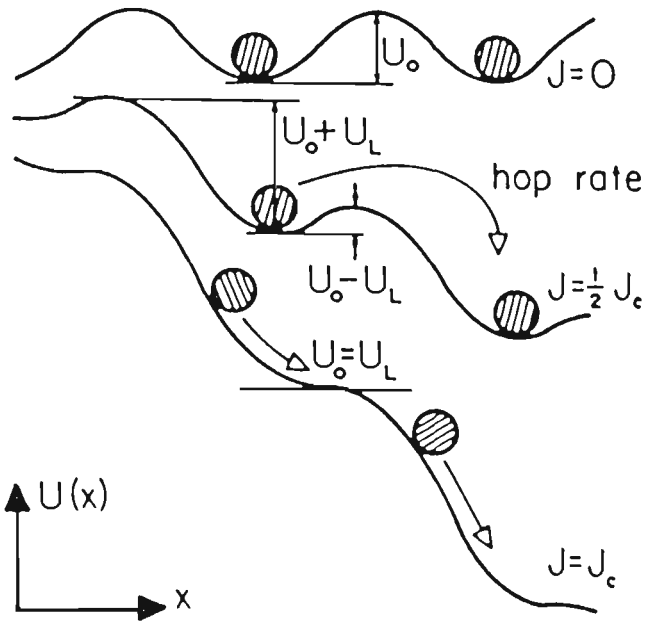

Figure 1.11 *The presence of current in a magnetic field generates a Lorentz force which tilts the staircase, allowing flux lines to hop out of their pinning wells more easily [35].*

On this model, the dissipated energy (or resistance) is given by an Arrhenius-type equation [52]:

$$\rho(T) \sim \rho_0 \exp(-U_0/k_B T), \tag{1.27}$$

where U_0 is the activation energy (with $U_0 \rightarrow 0$ as $T \rightarrow T_c$). For HTSCs, it has been experimentally observed that the pinning strength U_0 falls off as $(1\text{-}T/T_c)^{3/2}/H$ [53, 54]. TAFF is observable in particular, only when the potential barrier is low and gives rise to a resistivity as given in Eqn. 1.27.

In general, practical applications require that flux-flow be avoided and flux creep minimized. The maximum current density that a superconductor can sustain at the given temperature and magnetic field without energy loss is the current density at which the Lorentz force F_L equals the pinning force F_p. It is therefore evident that flux pinning plays a very important role in determining the current carrying capacity of these type-II superconductors as it dictates the suitability of a material for large-scale applications.

1.2.3.3 Hysteresis and irreversibility line

When magnetic energy is converted into heat during repeated cycles of applied ac-field, the dissipative or irreversible loss is called *hysteresis*. This occurs when the magnetization $\boldsymbol{M}$ is not a single-valued function of the applied field $\boldsymbol{H}$ - as with ferromagnetic materials and type II superconductors. Hysteresis arises from flux pinning in superconductors; those which exhibit irreversibility due to structural imperfections or chemical impurities which prevent the free motion of the flux line lattice. The dissipation of energy occurs by two different mechanisms: conventional electrical resistance, or changing magnetic flux. In the superconducting state, the first is absent, but Maxwell's equation requires that curl $\boldsymbol{E} = -\partial \boldsymbol{B}/\partial t$, which implies that a voltage is needed to sustain a current.

Just as a magnet iron is often referred to as *hard* when it has a significant hysteresis loop, a superconductor is also called hard when its hysteresis loop is significant. The hysteresis loop in the $\boldsymbol{M}$-$\boldsymbol{H}$ plane determines the energy loss per cycle for low-frequency applications. In general, this loss limits the potential use of type-II superconductors in ac-applications. For dc-applications, $\partial \boldsymbol{B}/\partial t$ is zero, flux is pinned by virtue of the hysteretic property, and there is no loss [55].

In a superconductor, the field at which the $\boldsymbol{M}$ vs. $\boldsymbol{H}$ curve is no longer double-valued is known as the *irreversible field*, H_{irr}. In conventional (LTSC) superconductors, such as NbTi and Nb_3Sn, H_{irr} is extremely close [56] to H_{c2}, and there is no important distinction between them. By contrast, in a HTSC, flux line motion near H_{c2} is easier due to greater

thermal activation. As a result, the following occurs: when H is reduced after reaching H_{c2}, the trajectory of M retraces its path as flux lines are free to move. Along this path, the superconductor becomes *soft*. Then comes a point when flux pinning becomes stronger, causing $\boldsymbol{B}$ to decline slower than $\boldsymbol{H}$, and $\boldsymbol{M}$ to deviate from the increasing-H curve. Along this path, the superconductor changes to hard. This value of H_{irr} in HTSCs is appreciably different from H_{c2}, although still quite far above H_{c1}.

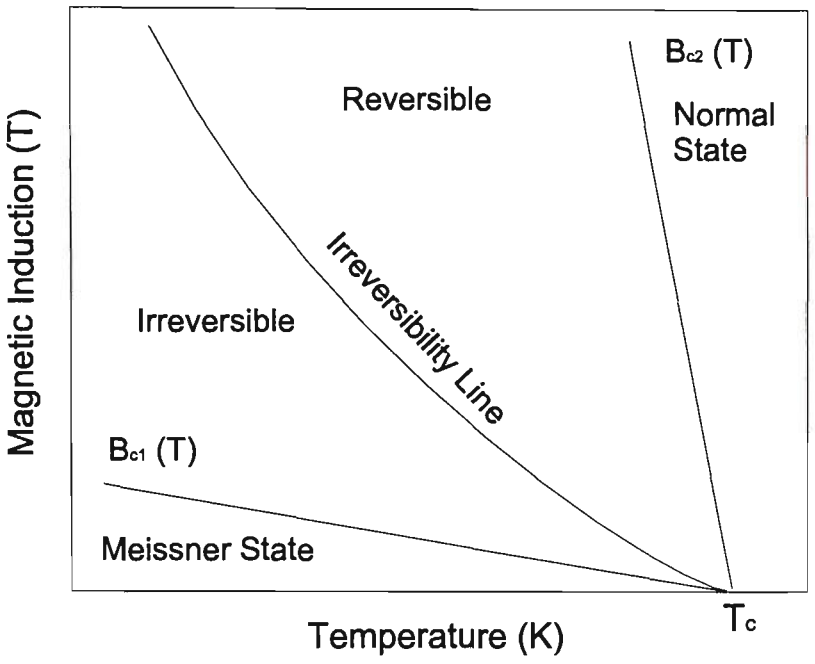

Figure 1.12 *Magnetic induction B(T) vs. temperature T(K) state diagram for high-T_c superconductors.*

The flux pinning properties of superconductors can be investigated by measuring the irreversibility line (IL). The IL, defined as the disappearance of flux pinning at a certain temperature and magnetic field, is a line existing between the B_{c1}-T and B_{c2}-T curves in the magnetic field versus temperature state diagram (or B-T plane), as shown in Fig 1.12. In this diagram, below and to the left of the IL the magnetic flux is pinned by flux pinning centers, and the material exhibits irreversible magnetic behavior and can sustain a rather high current density with little or no energy loss. Above and to the right of the IL, however, the pinning ability is lost, and the material exhibits reversible magnetic behavior, which can not carry current without dissipating energy.

The mixed state area (shown in Fig. 1.12) is divided into two areas (reversible and irreversible) by the IL. For Yttrium-based materials, and conventional superconductors, the IL can be described [57] by $1 - T_{irr}(B)/T_c \propto B^{2/3}$. For Bismuth-based bulk and tape, and Thallium-based bulk materials, the linear relationship $1 - T_{irr}(B)/T_c \propto B^{1/3}$ holds instead [58], where $T_{irr}(B)$ is the field dependence of the irreversibility temperature. The different dependence of $(1-T_{irr}/T_c)$ on B for Bi-based and Y-based materials has been attributed to the difference in the dimensionality of the superconducting properties of these two types of materials [58]. Both Bi-based and Y-based superconductors have layered structures, which lead to strong anisotropy of their properties. The anisotropy parameter, g, is given as $(m_c/m_a)^{1/2}$, where m_c and m_a are the effective superconducting masses for pair motion along the c direction and the a-b plane, respectively. g is reported to be in the range 25-50 for Bi-based materials [59, 60], while it is estimated to be 5 for $YBa_2Cu_3O_{7-x}$ [61]. This difference causes Bi-based materials to be considered two-dimensional, whereas $YBa_2Cu_3O_{7-x}$ is considered three-dimensional.

Thus, for useful high field applications it is necessary to push the IL to a high-temperature/high-magnetic field region, by such means as introducing efficient pinning centers into the superconducting materials and/or thermo-mechanically controlling the processing of composite wires and tapes to achieve an optimal microstructure [62] - HTSC materials such as Bi(Pb)-2223 are highly processing dependent, as large current carrying capacity (viz. the scientific superconductor critical current density, J_c, or engineering conductor critical current density, J_e) corresponds directly to how densely, well connected and aligned the grains are which depends very much on the history of sample preparation of these composite tapes [63].

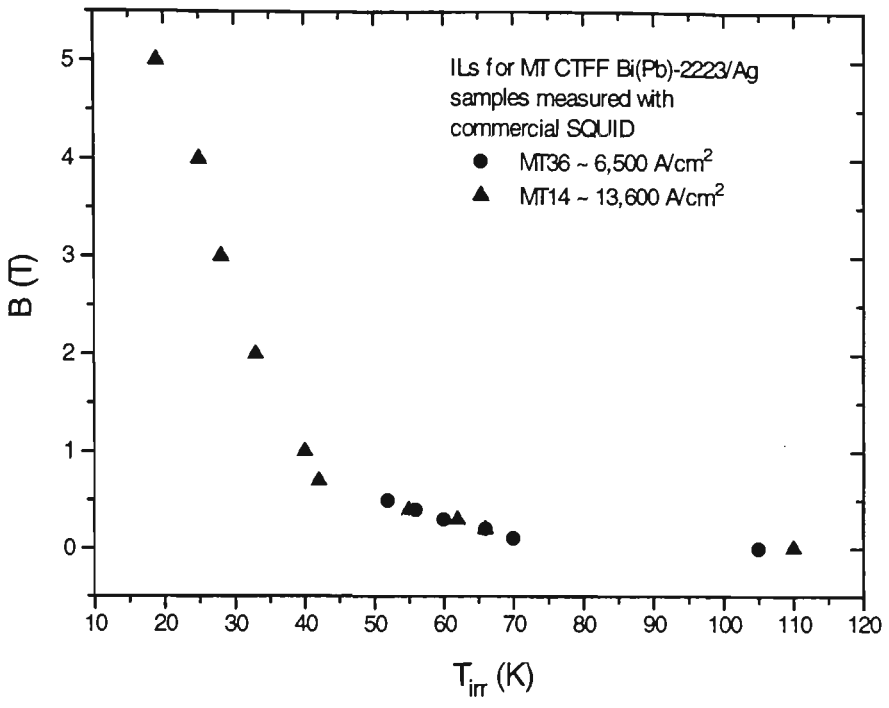

Figure 1.13 *Experimental data showing the irreversibility line (IL) for two multifilamentary tapes (MT) of Bi(Pb)-2223/Ag prepared by the method of continuous-tube-forming/filling (CTFF). The given J_c values are from transport measurements.*

For any given choice of temperature, there is a particular ***M*** vs. ***H*** diagram, and with it a value of H_{irr}. These values can be assembled into an IL as a function of T. Figure 1.13 shows some typical data for some MF tapes of Bi(Pb)-2223 plotted on a B-T plane. Notice that at or below ~ 40 K, the magnetic behavior of these composite superconductors favors high (dc) field applications. The IL shown in Fig. 1.13 was determined using magnetization measurements. In this method, the field-cooled (FC) and zero-field-cooled (ZFC) magnetizations were measured with a *superconducting quantum interference device* (SQUID) magnetometer and the irreversibility temperature was taken as the point which separates a high-temperature magnetically reversible region from a lower-temperature region exhibiting magnetic hysteresis. More on measurementation in chapter 2.

1.3 Materials, Power Applications and Stability Issues of Bi(Pb)-2223

Extensive studies on HTSC materials have shown that (Bi, $Pb)_2Sr_2Ca_2Cu_3O_{10+x}$ (or Bi(Pb)-2223) will not be able to match the performance of $YBa_2Cu_3O_{7-y}$ (or Y-123) at 77 K in terms of flux pinning, in particular on a thin film basis and under substantial magnetic fields [64-66]. The ease with which Bi(Pb)-2223 can be fabricated into composite tapes however, as well as applications of electrical transmission and those of electric power in nature which involve transporting currents in modest fields of no more than ~ 0.6 T at 77 K have resulted in a continual development in the production of its long length [67-69]. A common key feature of these composite tape conductors with highest J_c has been a high degree of crystallographic alignment of the superconducting oxides after thermo-mechanical processing [70]. Furthermore, recent studies have shown that thermo-mechanical processing in addition, determines the extent of cryo-stability [71] as well as mechanical strength [72] of these composite tape conductors, notably in coil, and magnet applications [73]. It is therefore imperative to understand the crystallography and microstructure of Bi(Pb)-2223 in its tape form before embarking on how to enhance its performance or bringing about its fullest potential by means of materials processing. This section concludes with a survey on stability issues concerning composite tape conductors produced from Bi(Pb)-2223 for use in electric power applications.

1.3.1 Bismuth-based High-T_c Superconductors

Although the first sign of superconductivity in the Bi-Sr-Cu-O system was first observed by Michel *et al* [74] in 1987, attributed to $Bi_2Sr_2Ca_2Cu_3O_{7+x}$, it was later revealed that the superconducting phase was $Bi_2Sr_2CuO_{6+x}$ (termed the 2201 phase) with a T_c of ~ 22 K [75, 76]. Bismuth cuprates of $Bi_2Sr_2CaCu_2O_{8+x}$ (2212 or low T_c phase) and $Bi_2Sr_2Ca_2Cu_3O_{10+x}$, (2223 or high T_c phase) with T_c of ~ 80 K and ~ 110 K respectively were then observed soon after [33, 34, 78]. Sunshine *et al* [81] and subsequently Y. Yamada *et al* [82] later showed the importance of Pb addition with its roll as a stabilizer in the partial substitution of Bi at elevated temperatures in the formation of 2223 phase.

1.3.1.1 Crystallography

The structure of $Bi_2Sr_2Ca_2Cu_3O_{10+x}$ is highly anisotropic. The anisotropy is due to the layered crystal morphology, which, according to current understanding, is essential for superconductivity with high transition temperatures. The layers of this material are composed of Cu-O planes, separated from each other by planes of various other oxides and rare earths - the resultant sequence of $Bi_2Sr_2Ca_2Cu_3O_{10+x}$ (2223) with n = 3 CuO_2 layers is [83] ... CuO_2 SrO $(BiO)_2$ SrO CuO_2 Ca CuO_2 Ca CuO_2 SrO $(BiO)_2$ SrO CuO_2 ... It is believed that the superconductivity and charge transport are mostly confined to the Cu-O planes [84].

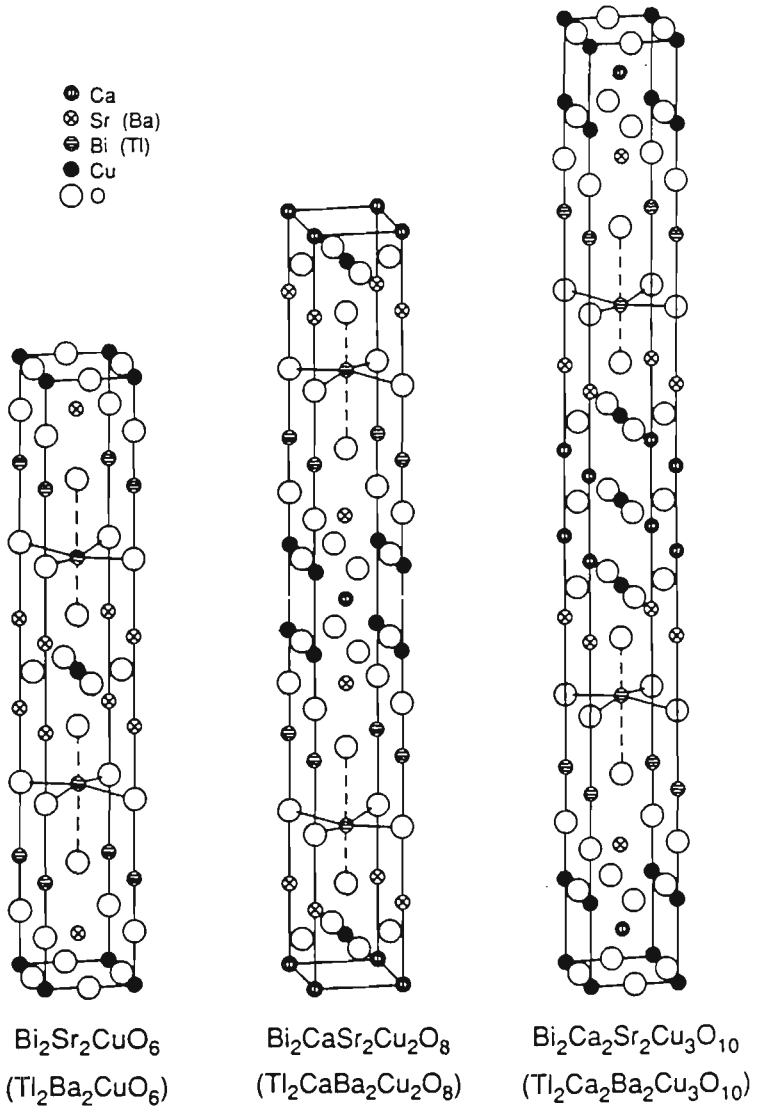

Figure 1.14 *Structural unit cells for the bismuth-based (and thallium-based) superconductors [85].*

The Bi-based compounds belong to a family of layered structures known as polytypoids, which in general have a pseudo-tetragonal structure [27], consisting of Cu-O pervoskite [86] lamellae alternating between NaCl-like double layers of Bi_2O_2, Fig. 1.14 depicts a simplified crystal structure. The bonding between the Bi_2O_2 layers is weakly cleaved [87], yielding similar mechanical properties with that of graphite and mica [30]. As a result, this presents difficulties in grain growth owing to the weak bonding along the *c* axis, but has an advantage for grain alignment in the *a-b* plane direction. Interestingly, the T_c value of various Bi-Sr-Ca-Cu-O phases increases with *n* number of CuO_2 layers in their crystal structure. For instance, the $n = 1$ (2201) polytypoid has a transitional temperature in the range of 7-22 K, the $n = 2$ (2212) a T_c of about 85 K and the $n = 3$ (2223), with a T_c of 110 K [88].

1.3.1.2 Microstructure

Since it exists as a ceramic, Bi(Pb)-2223 contains grains, grain boundaries, twins (twist boundaries, where successive layers have the *a*- and *b*-axes interchanged), voids and other imperfections - or defects. Despite the fact that impurities collect at grain boundaries, the weak-link behavior due to this effect has never been a problem with LTSCs as it is with HTSCs primarily due to the different coherence lengths, ξ. In HTSCs, ξ is typically 2-40 Å, which is comparable to the grain boundary thickness. Barrier penetration is therefore much more difficult and hence attenuation in high-T_c oxides is finite. This corresponds to a finite resistivity at the boundary. Apart from this shortcoming of the high-T_c oxides, these same grain boundaries have been found to play an important part in flux pinning and mechanical properties of BSCCO wires and tapes [89-92].

A very common defect occurrence is the presence of intergrowth defects in which different numbers of CuO_2 layers can be incorporated into pervoskite layers of different thicknesses [93-95]. Ramesh *et al* [96] found that regions adjacent to grain boundaries observed to be intergrowth defects correspond to a lower T_c in comparison with regions within the grains themselves. The 2201 phase was found to be adjacent to a grain boundary, followed by the 2212 and 2223 phases. The presence of the 2201 intergrowth adjacent to the grain boundary could well be a crucial factor in determining the T_c and J_c of composite tapes due to the loss

of connectivity of 2223 grains. With Pb-doping however (the substitution of Pb for Bi at elevated temperatures), better inter-grain connectivity can be attained attributing to the increase of compositional homogeneity [97, 98]. Figure 1.15 displays the superconducting core morphology of Bi(Pb)-2223/Ag monocore tape both parallel and transverse to the *a-b* (or tape) plane.

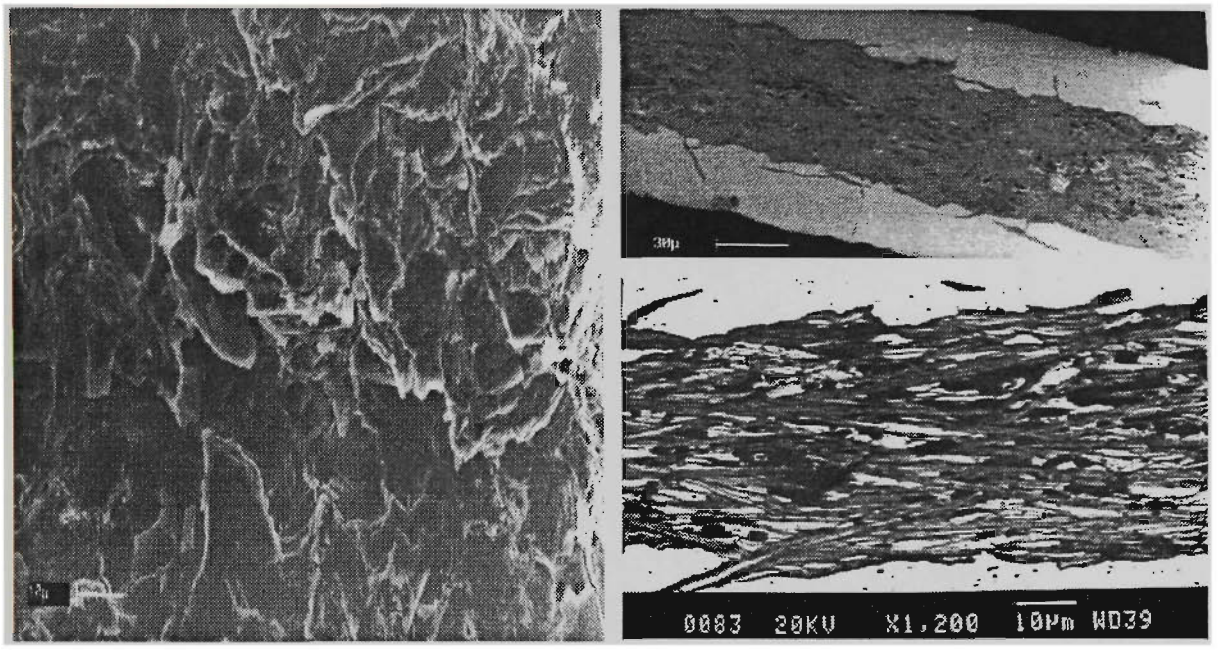

Figure 1.15 *SEM secondary electron images of a Bi(Pb)-2223/Ag monocore tape showing grain morphology parallel (left) and transverse (top right) to the a-b (or tape) plane. The grains of 2212 phase shows up as white, while that of 2223 appears greyish (using EDS) in another monocore tape's longitudinal cross-section SEM back-scattered-electron image (bottom right).*

Grain alignment is also equally important because of the inherent anisotropic nature of the HTSC crystals in general [99] and Bi-based compounds in particular [88], with J_c larger in the *a-b* plane and smaller in the *c*-direction. In Bi(Pb)-2223, a small misalignment between crystalline axis and applied magnetic field can dramatically change the J_c value [100]. Unlike YBCO which exhibits a *wide shoulder region* in a J_c vs. B plot [101], BSCCO samples are much more anisotropic which stresses the importance of grain alignment from the standpoint

of enabling practical design of high-field superconducting magnets at high operating temperatures. The anisotropy is shown in Fig. 1.16, depicting a plot of transport critical current I_c as a function of the angle between magnetic field and the *a-b* plane for Bi(Pb)-2223/Ag multifilamentary tape at liquid nitrogen (LN) temperature.

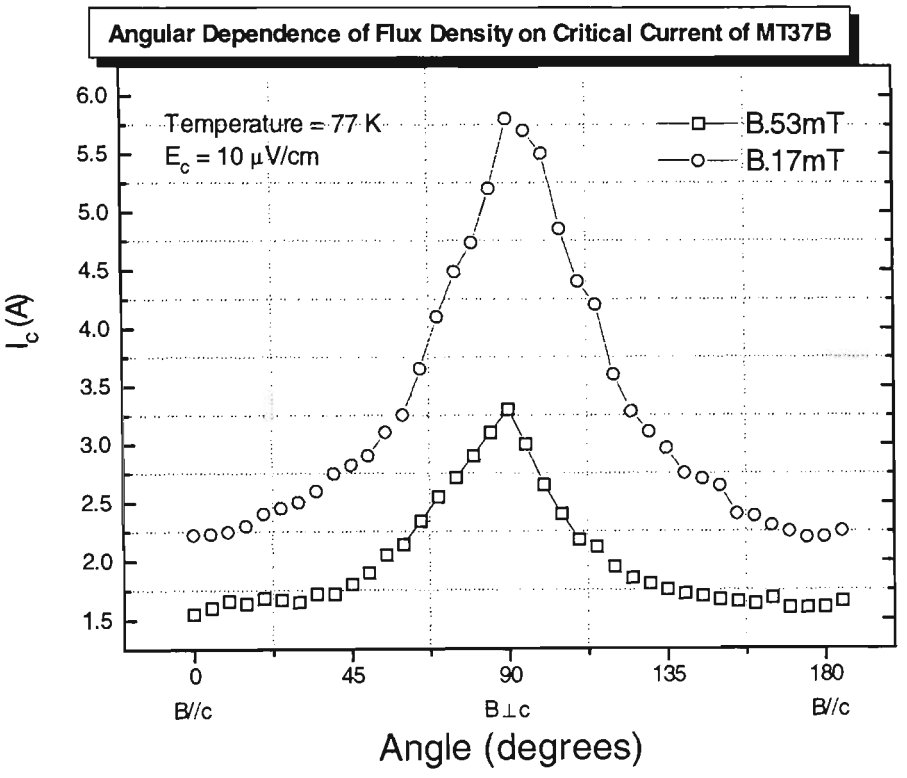

Figure 1.16 *Transport critical current I_c as a function of the angle between magnetic field and the a-b plane for Bi(Pb)-2223/Ag MF tape at LN temperature.*

With relation to the study of boundaries and alignment of grains, various models developed so far have yet to describe conclusively the flow of current through Bi(Pb)-2223 composite tapes. Among these, the "brick wall" [91, 102, 103] and the "railway switches" [104, 105] are commonly discussed models in numerous literature.

1.3.2 Electric Power Applications

Most electric power applications of superconductors have began with the use LTSC materials such as with NbTi wires and Nb_3Sn tapes [20, 22, 106]. It is only recently, since their discovery that HTSC materials have been manufactured into kilometer lengths of wire and tape (Bi-based) with high critical current capability at higher operating temperature in low magnetic fields, suitable for some large scale commercial applications [107-109].

Potential commercial products for power applications and for propulsion/levitation purposes include; current leads, Class II coils and magnets (compact in size, densely constructed), transmission lines, fault current limiters, electric motors and generators, superconducting magnetic energy storage (Class I - physically large), magnetic levitating (Maglev) trains, magneto-hydro-dynamic (MHD) generators [35], just to name a few. The industrial requirements of HTSC performance vary depending on the type of application. Table 1.2 lists some minimum values needed for a few of the aforementioned applications [110].

TABLE 1.2 *Industry-defined performance requirements for high-T_c superconducting wire {and tape}*[*].*

Application	**J_c** **(A/cm^2)**	**Field** **(T)**	**$Temp_{op}$** **(K)**	**I_c** **(A)**
Fault Current Limiter	$0.5\text{-}1.0\times10^3$	1-6	20-77	$10^3\text{-}10^4$
Large Motor (>745.7 kW)	$2.0\text{-}3.0\times10^4$	4-5	20-77	500
Generator (300 MVA)	$2.0\text{-}3.0\times10^{4\dagger}$	4-5	20-50	500-1,000
Transformer	1×10^4	0.1-0.5	65-77	---
Transmission Cable	$1.0\text{-}2.5\times10^4$	< 0.2	65-77	25-30[#]
Small Motor (93.2 kW)	1.5×10^4	1	27	75-80

Application	Length (m)	Strain Tol. (%)	Bend Radius (m)	Cost ($/kA-m)
Fault Current Limiter	100	0.2	0.1	10-100
Large Motor (>745.7 kW)	1,000	0.2-0.3	0.05	<10
Generator (300 MVA)	500-1,000	0.2	0.1	10
Transformer	1,000	0.2	1	10
Transmission Cable	100	0.4	2[@]	10-100
Small Motor (93.2 kW)	300	0.2	0.01	10-100

[*] *Values are from industrial sources. As a rule of thumb, superconductors give their best performance when at temperature below about 60 % of their critical temperature.* [†] *Minimum for high-T_c wire alone.*

[#] *Current for individual wire cables, with multiple wires, require current of 5 kA.*

[@] *Cable radius.*

Despite the broad application spectrum, the remainder of this section will be devoted to the applications and the design and operational issues of HTSC coils and magnets made with Bi(Pb)-2223 ceramic superconductor. The analysis on the thermal stability of HTSC coils and magnets are given in the next section. Further review on magnet quenching and protection will also be discussed there.

As relevant to the majority of research carried out at CSEM, IMTM, UW, the operating temperature of interest is that of LN_2, the HTSC material used is, once again Bi(Pb)-2223 and the subjective application under investigation is that of Class II coils and magnets.

1.3.2.1 Bi(Pb)-2223 magnet applications

Although the high field performance of long length Bi(Pb)-2223 composite tapes at 77 K has yet to satisfied industrial standards for several power applications, recent advances in the development of more flexible, strain tolerant, high I_c, J_c and J_e of these ceramic-composite tape conductors have already demonstrated the suitability for some commercial applications [111-113]. As a result, a large number of prototype Bi(Pb)-2223 coils (as solenoidal or pancake-shaped) and magnets (constructed from single or double pancake-shaped, or race-track-shaped [114, 115] coils - e.g. Fig. 1.17) have been developed and

tested, as a stand-alone unit [116-120, 114, 115] (at operating temperature at 77 K, or from 4.2 K to 77 K), or with an iron core [121] (at 77 K), or as insert coils part of a hybrid magnet with the outer coil often made from LTSC materials such as NbTi (at 4.2 K), capable of withstanding large background fields up to ~ 20 T [122, 123].

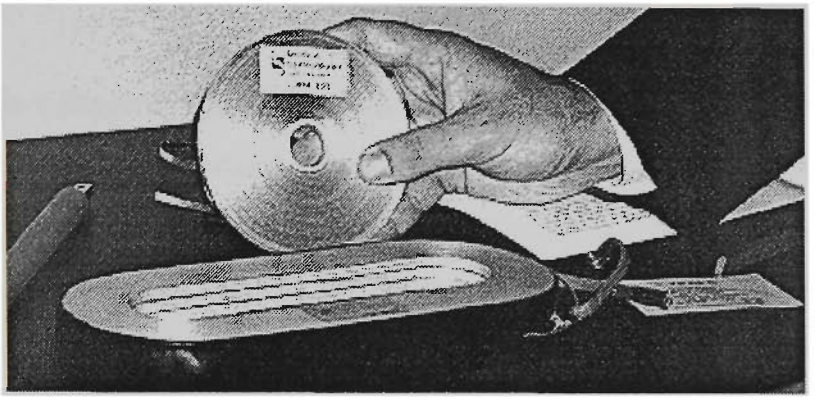

Figure 1.17 *Commercially produced HTSC Bi(Pb)-2223 double pancake-shaped and race-track coils (American Superconductor Corp. Appl. Supercond. Conf., 25-30 Aug., 1996, Pittsburgh, PA, US).*

1.3.2.2 Joints between Bi(Pb)-2223/Ag tapes

Many types of HTSC applications have need of high quality superconducting joints. Superconducting joints are required to provide the long lengths of conductor and the temporal stability necessary in HTSC magnets. The construction of a superconducting magnet inevitable requires joints between successive lengths of wire, and indeed, there have been studies carried out by various research groups on the development and characterization of HTSC joints, both with Bi(Pb)-2223/Ag tapes [124-126] and Bi-2212 composites [127]. Results are promising, with I_{cj}/I_c (where I_{cj} denotes the critical current across the joined section of two short tapes) reaching from 60 % to nearly 100 % depending on the joining angle. This is all very nice for test samples of short tape, but for practical applications however, applying this technique to two HTSC double-pancake-shaped coils has proven most difficult indeed. Instead, ordinary Sn-Pb and pure indium (by virtual of its low melting point) solder were used in the construction of magnets from single and double-pancake coils of Bi(Pb)-2223 [120], from the fact that the constructed

coils have low indices n [119, 120], where the index number, n, is defined [55] by the following VI characteristics applicable at and near I_c.

$$V = V_c \left(\frac{I}{I_c} \right)^n \tag{1.28}$$

V_c is the resistive voltage at which I_c is defined. Equation (1.28) implies that the conductor is resistive even when it is operated below I_c. It must be mentioned that for coils with high n, such as those used in NMR or in any application which requires persistent mode of operation, the joints must be lossless for the current to be persistent,else magnetic energy will be dissipated across the joint resistance.

1.3.2.3 Design and operational issues

For issues concerning the designing aspects, whether for experimental purposes or for a system component, the magnet must satisfy the requirements for spatial distribution and temporal variation of the specified magnetic field $\vec{H}(x, y, z, t)$. Normally, specifications include the following three parameters: 1) H_0, the field at the magnet origin ($(x, y, z) = (0, 0, 0)$); 2) V_0, the extended volume or work-space within which $\vec{H}(x, y, z, t)$ is specified; and 3) $H(t)$, the field time variation. Lastly, with relation to cost, weight and size, the volume of the windings should be at a minimum, yet at the same time meeting all required specifications.

With regard to the operational aspects, the coil or magnet system must be structurally strong to be able to withstand very large electromagnetic forces [128] (such as circumferential or axial magnetic stresses, under high field operation), thermally stable to maintain the conductor at its operating temperature and well protected from permanent damage in the event of a magnet quench [129]. Of these three considerations, the temperature stability is most unpredictable and least controllable as the energy stored in the magnet (magnetic and mechanical) can easily be converted into heat upsetting the thermal equilibrium of the system.

The thermal behavior or temperature stability therefore may be quantified by examining the three basic constituents of the magnet winding and the corresponding power equation operating on a unit volume of superconductor. These are 1) conductor, 2) coolant and 3) structural material. The conductor temperature T, is governed by the following power density equation [130]:

$$C_m \frac{\partial T}{\partial t} = \nabla \cdot \left(k_m \nabla T\right) + \rho_m(T) j_m^2(t) + g(t) - \frac{P_m}{A_m} q_l \tag{1.29}$$

Equation (1.29) shows that the change in stored energy (left-hand side) is balanced by the sum of the conduction heat flow, the joule heating, the heat generation (magnetic and mechanical) and the cooling of the conductor (right-hand side terms), where C_m is the heat capacity of the conductor element, k_m, $\rho_m(T)$ and j_m, the thermal conductivity, temperature dependent electrical resistivity and current density of the normal matrix respectively, with P_m denotes the conductor perimeter, A_m is the matrix's cross-sectional area and q_l represents the heat transfer flux.

1.3.3 Stability - Theories and Criteria

The topic of superconductor stability is concerned with determining permissible energy inputs as well as methods of modifying the configuration and components of a superconducting system to either limit the amount of energy inputs, or to make the system more tolerant of such inputs. Different approaches to stability modify different components of a composite superconductor. Adiabatic stability for instance, limits local energy inputs by controlling the dimensions of the superconductor; dynamic stability slows down flux motion; and cryostability improves heat transfer to expedite the thermal recovery of accidentally formed normal regions. The theories and concept for stability may be said to have evolved around specific solutions of Eqn. (1.29). Table 1.3 best sums up the different types of concept concerning stability, with '0' signifying that the parameter is negligible or not being considered in the equation, and '✓' means it is included.

TABLE 1.3 *Stability concepts derived from Eqn. (1.29).*

$C_m \frac{\partial T}{\partial t}$	$\nabla \cdot (k_m \nabla T)$	$\rho_m(T) j_m^2(t)$	$g(t)$	$\frac{P_m}{A_m} q_l$	Application
✓	0	0	✓	0	Flux jump
0	0	✓	0	✓	Cryostability
✓	✓	✓	0	✓	Dynamic stability
0	✓	✓	0	✓	"Equal area"
0	✓	✓	0	0	MPZ[#]
✓	0	✓	0	0	Protection
✓	✓	✓	0	0	Adiabatic NZP[&]

[#] *Minimum propagation zone.* [&] *Normal zone propagation.*

Some of the theories and criteria expressed subsequently can be found in various texts with more in depth treatment such as those specializing in how to avoid instabilities and in superconducting magnet systems. Among these are excellent texts written by H. Brechna [128], M.N. Wilson [129], E.W. Collings [20, 22], and Y. Iwasa [131]. Nevertheless, expressions are repeated where necessary (applicable to tape conductors), with some modification for the treatment of multi-filamentary Bi(Pb)-2223 edge- and face-cooled tapes - precedented by the work of Ogasawara [132, 133] on Y-123 mono- and multi-filamentary tapes at 20 K and 77 K.

1.3.3.1 Bean's critical state model

The *critical state* model, proposed by C.P. Bean [134] in 1962 (known as the Bean critical state model) evolved from the Goodman's "lamina" model (an alternative model to the "vortex" version proposed by Abrikosov [17]), forms the basis of calculations on stability and hysteresis loss. The model is used to derive a criterion for *flux jumping*, a kind of electromagnetic/thermal instability afflicting all high field superconductors. The critical state model introduces the hypothesis that whenever a current I_0 flows in a superconducting wire, the current density at the outside (surface) will immediately jump up to the critical current density value J_c. To transport more current, the shallow layer

thickens, again carrying J_c, but over a larger cross-sectional area. In this way, the total current flowing is always with critical current density J_c, but only the outer portion of the superconductor carries a current other than zero. The Bean critical state model has indeed been verified experimentally at various depths within the superconductor [135].

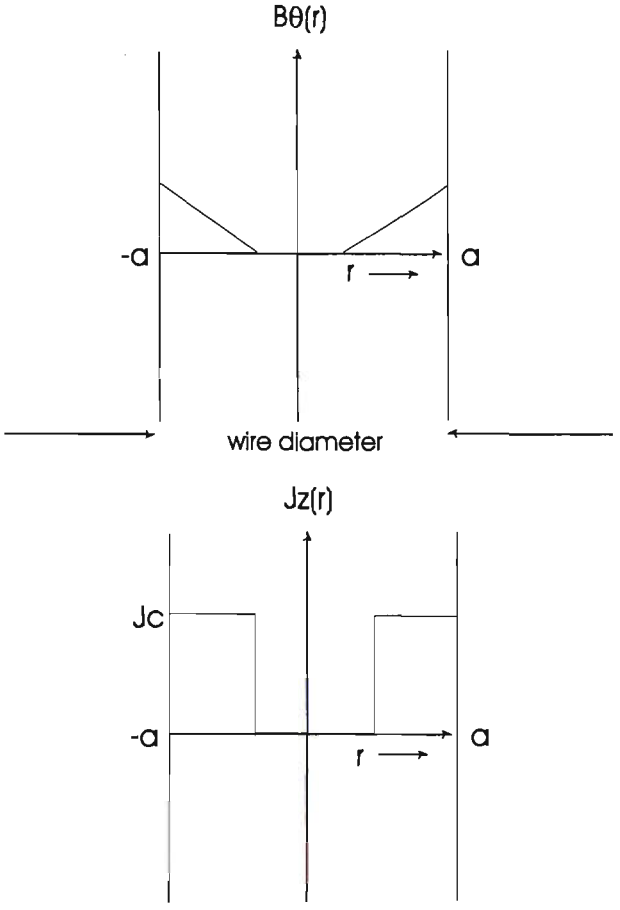

Figure 1.18 *Magnetic flux and current density distribution according to the Bean critical state model.*

1.3.3.2 Flux jumping - stability for edge-cooled tape conductors

As mentioned earlier, flux-jumping is the result of flux motion within the superconducting material which causes thermal runaway instability and in turn generates more magnetic flux motion. It is associated with the re-distribution of magnetic fields. This instability occurs most frequently at or near 4 K as the specific heat of the conductor (matrix and superconductor) is very small comparing to that of say liquid helium (LHe) [136]. Unlike

mechanical disturbances the effect of flux jumping is now well understood, and is no longer a serious problem for magnet operation. Precautions are made at the designing stage to prevent this effect from occurring during operation. For tape conductors, it's possible to calculate the critical size (d_c) above which flux jumping will occur [131] based on the Bean critical state model, with the assumption of a linear temperature dependence for $J_c(T)$:

$$J_c(T) = J_{co}\left(\frac{T_c - T}{T_c - T_{op}}\right) \tag{1.30}$$

Two criteria may be applied - adiabatic (worse case scenario with no heat transfer), giving

$$d_{ad} = 2\sqrt{\frac{3C_s\left(T_c - T_{op}\right)}{\lambda\mu_0 J_{co}^2}}, \tag{1.31}$$

and dynamic, with

$$d_{dyn} = 2\sqrt{\frac{3C_s\left(T_c - T_{op}\right)}{\lambda\mu_0 J_{co}^2} + \frac{(1-\lambda)6d_{dyn}\left(T_c - T_{op}\right)h_q}{\lambda\pi^2\rho_m J_{co}^2}}. \tag{1.32}$$

where h_q is the constant heat flux coefficient, C_s, the specific heat of capacity of the superconductor, ρ_m, the electrical resistivity of the matrix, T_c taken as 107 K (~ temperature at the midpoint of transition), J_{co}, the critical current density of the superconductor at operating temperature T_{op}, and d_{ad} and d_{dyn}, are the respective adiabatic and dynamic critical widths of the tape conductor. The composite nature of the tape conductor, λ_s, (originally used for mono-filamentary tape conductors) has been replaced by λ, (denoting the filling factor which is defined here as the ratio of superconductor to total conductor) for multi-filamentary tapes (refer to Fig. 1.19).

Cross section of monocore Bi(Pb)-2223/Ag tape.

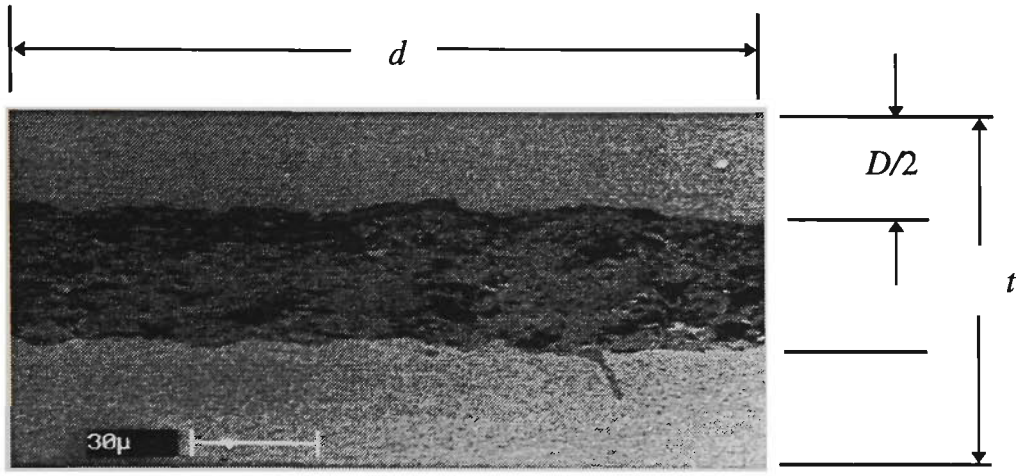

Cross section of multi-filamentary Bi(Pb)-2223/Ag tape.

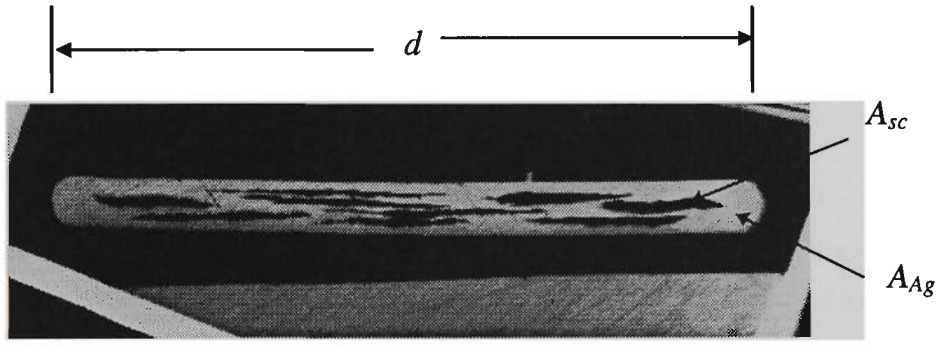

$$\lambda = \frac{A_{sc}}{\left(A_{sc} + A_{Ag}\right)} \qquad R_s = \frac{A_{Ag}}{A_{sc}}$$

Figure 1.19 *SEM images of cross-sections of single and multi-filamentary Bi(Pb)-2223/Ag tape conductors.*

From Eqn. 1.32, it can be seen that the criterion for dynamic stability is more general and covers the case of adiabatic condition when edge-cooling is absent. It is valid for HTS magnets operated in a bath of cryogen or for force-cooled magnets. For the case where the HTS magnets operated in vacuum ($h_q = 0$), the criteria is not applicable.

1.3.3.3 Cryostability

The idea behind cryostability is to restore superconductivity in an already flux-jump stabled composite conductor once an electrical or thermo-mechanical disturbance has occurred. In other words, cryostability allows the magnet to return to standard operation even from a condition where the entire coil has gone normal (a quench). The key to cryostability is heat transfer ($\dot{Q}$) to the surrounding cryogenic bath. Figure 1.20 shows $\dot{Q}$ as a function of temperature for both LHe and LN [136]. The 'dipping' part of the LHe curve (dashed lines) indicates unstability upon warming at temperatures near 4 K, whereby an instantaneous jump is made from the *nucleate boiling* regime (first region of increase in $\dot{Q}$) into the *film boiling* regime (second region of increase in $\dot{Q}$). The instability is due to a veneer of helium gas surrounding the warm object, which has a slow cooling rate in a medium whose effective $\dot{Q}$ is below ~ 0.25 W/cm^2. For LN on the other hand, a temperature rise can be as high as 20 K above the bath, nucleate boiling will still continues and there is no discontinuous jump to film boiling, which only takes place at temperatures above ~ 100 K or so [137].

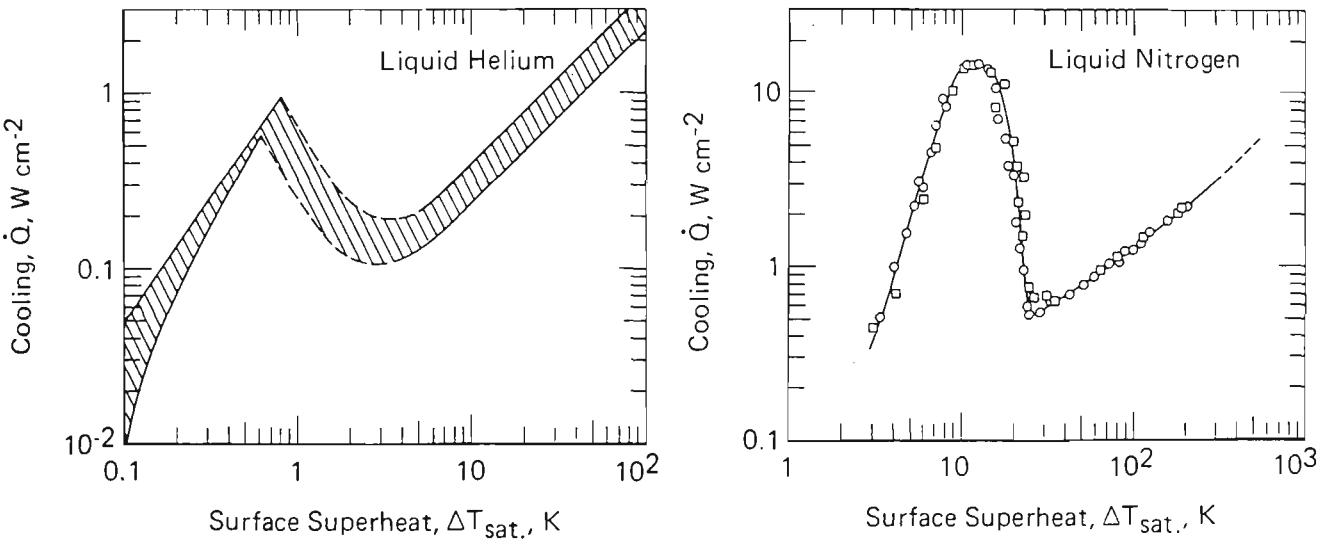

Figure 1.20 *Heat transfer as a function of temperature for LHe (left) and LN (right).*

Thus for HTSC magnets, nucleate boiling is the condition which they should be operating in. Based on this notion, Stekly's cryostability [138, 139] has been formulated to place an upper limit the size of the conductor to ensure sufficient cooling. Conditions for cryostability therefore involves determining conductor parameters such as R_s (the ratio of matrix to superconductor - refer to Fig. 1.19, which relates to λ), the area of matrix, A_m, or conductor diameter which is itself a function of R_s [22, 131]. As a result, the following criterion has been established as a condition for cryostability (or Stekly's cryostability criterion):

$$\alpha_{sk} \geq 1 \text{ (stable-sufficient cooling)} \tag{1.33a}$$

$$\alpha_{sk} < 1 \text{ (unstable-insufficient cooling)} \tag{1.33b}$$

where α_{sk} is a dimensionless number (known as Stekly's stability parameter), derived from equating the heat generation (Joule dissipation) density to the cooling density provided from the cryogen bath [131], and is given as

$$\alpha_{sk} = \frac{f_p P_{cd} A_m h_q \left(T_c - T_{op}\right)}{\rho_m I_{co}^2}, \tag{1.34}$$

with P_{cd} and f_p as the total conductor perimeter and fraction of P_{cd} exposed to the cryogen bath respectively. Since $\alpha_{sk} \propto A_m$, it can be understood from Eqn. 1.34 that there is a trade off between the amount of matrix material and the overall critical conductor current density to attain greater stability.

1.3.3.4 Quench propagation - 1-D analysis for tape conductors

The thermal recovery of a magnet system from a quench depends on heat transfer between each element of conductor and its surroundings, which includes other parts of the winding and the cooling reservoir. For a given current carrying superconducting tape with a hot spot at a temperature above T_c, there will be a balance between ohmic heating and thermal conduction along the tape. If the hot spot is very short, heat conduction will exceed heat

generation, the spot will contract and the tape will recover superconductivity; but if the hot spot exceeds a certain length, it will grow.

The term *minimum propagating zone* (MPZ) coined by Wipf [140] denotes the boundary between the expansion and contraction of the hot spot. The theory of MPZ enables the determination of the length (l_{MPZ}), the velocities (v_l and v_t) and the triggering energy (E_{MPZ}) of a normal zone. Models of the normal zone are usually of ellipsoidal [131, 141], sometimes cylindrical [141, 142] in shape and can require a 3-dimensional analysis [143] for superconducting wires. For composite tape conductors however, a 1-dimensional analysis can be adopted [131] and is the chosen treatment here for its simplicity. The schematic representation is shown in Fig. 1.21.

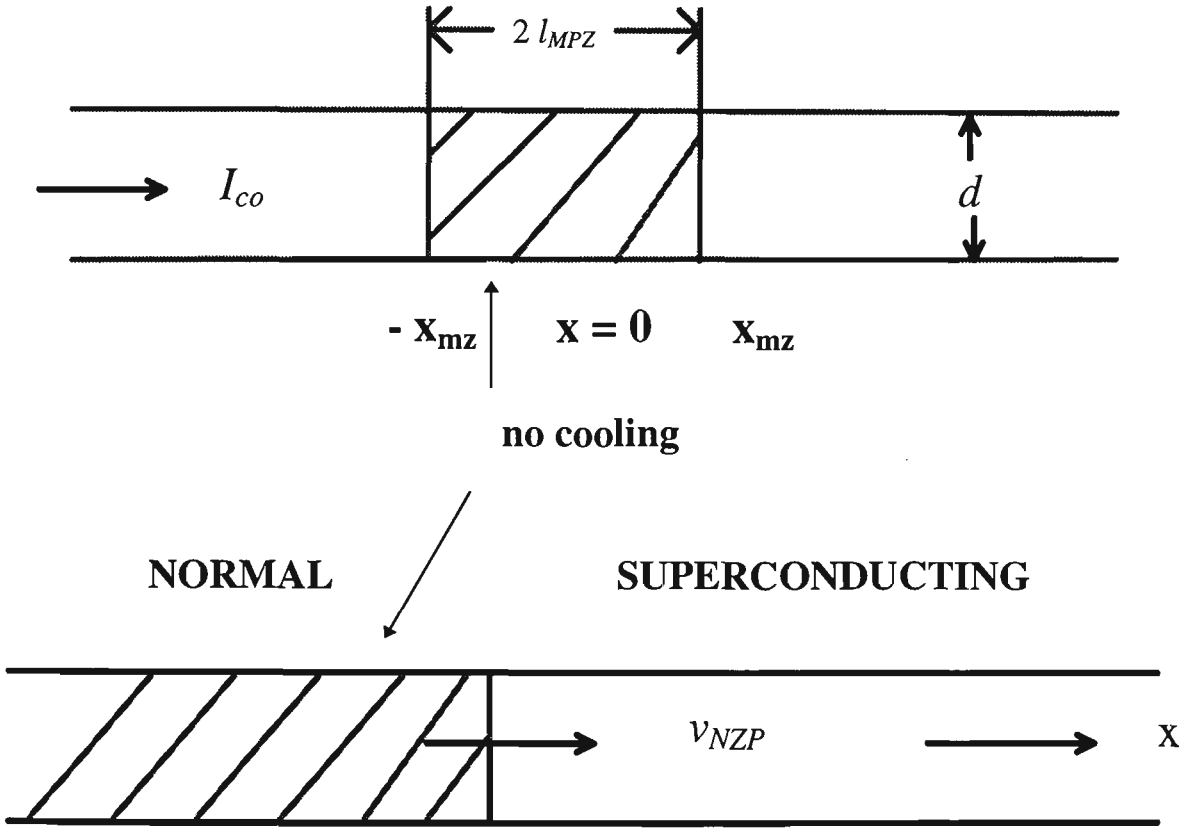

Figure 1.21 *One dimensional MPZ length and velocity representation in a composite superconducting tape.*

The 1-d treatment assumes that the MPZ region ($|x| \leq x_{mx}$) is insulated from cooling and that one of the tape's broad surfaces is exposed to cooling for $|x| \geq x_{mx}$, as shown in Fig. 1.21. The coolant temperature equals the operating temperature and surface cooling flux acting on *one* side of the broad tape's surface is given by $h_q(T\text{-}T_{op})$, with the assumption that the heat transfer coefficient, h_q, is constant. By considering the steady-state power density equations (from Eqn. 1.29) for regions $|x| \geq x_{mx}$, l_{MPZ} can be derived [131, 144] to be:

$$l_{MPZ} = R_s^2 \frac{(T_c - T_b)}{\rho_m [J_{co}]_s^2} \sqrt{\frac{h_q k_m}{D_{MT}}}, \tag{1.35}$$

where $D_{MT} \cong tA_m/A_{tot}$, ($t$ is the conductor thickness and A_{tot}, the total cross-section area of conductor), k_m, the matrix's thermal conductivity, T_b, the temperature of the cryogenic bath, and $[J_{co}]_s \cong J_{co}$, the critical current density in the superconductor at T_{op}.

The growth of the normal zone at a velocity in the longitudinal direction (along the conductor axis) v_l, (or v_{NZP} in Fig. 1.21) can be used as a safety measure to shut down a magnet at the onset of a quench. From a 1-d analysis of Eqn. 1.29, the normal zone propagation (NZP) longitudinal and turn-to-turn (between layers of composite superconducting tape in a tape-wound pancake coil) velocities (under adiabatic conditions) can be expressed as [131, 71]:

$$V_l = \frac{J_m}{C_{cd}} \sqrt{\frac{\rho_m k_m}{(T_t' - T_{op})}}, \tag{1.36}$$

and

$$V_t = \frac{J_m}{\tilde{C}_{cd}} \sqrt{\frac{\rho_m k_i \delta_{cd}}{2\delta_i (T_t' - T_{op})}} \tag{1.37}$$

respectively, where J_m, the matrix's critical current density, $T_t' = (T_{cs} + T_c)/2$, with T_{cs} the current sharing temperature $T_{cs} \cong T_c(I)$, and C_{cd} and $\tilde{C}_{cd}$ are the volumetric average of superconductor's and matrix's heat capacities at 77 K and over the temperature range of interest respectively. δ_i and k_i are the insulator's thickness and thermal conductivity and δ_{cd} (= t) is the thickness of the superconducting tape.

It is also of interest to calculate the minimum energy necessary to trigger the growth of a normal zone (E_{MPZ}), which in a way measures the sensitivity of the structure to thermal disturbances. The following expression [131, 71, 142] is used to quantify such energy concentration:

$$E_{MPZ} = A_{tot} l_{MPZ} C_{cd} \left(T_c - T_b\right). \tag{1.38}$$

In practice, quench-induced disturbances can be larger than the MPZ. Thus it is desirable to have their rate of expansion be as large as possible to prevent hot-spot formation. It is possible to control this rate by optimizing parameters such as R_s and λ.

Chapter 2

Processing and Characterization of Bi(Pb)-2223 Composite Wires and Tapes for Magnet Applications

2.1 Tape Processing and Magnet Development

The objectives of the extensive research carried out at CSEM, IMTM, UW were to conduct experiments leading up to and including the development of superconducting coils and magnets made from long lengths of Bi(Pb)-2223/Ag (or Ag-alloyed) composite tapes. Like other conductor applications, the objective here was to fabricate these tape conductors with the highest possible J_c, and, J_e (and also, although not so critical, their I_c as well) by means of material processing, using only of course what's available at the time. Needless to say that there are various ways to improve the J_c of the Bi(Pb)-2223 tape. Most of them would fall into one of the three main categories. They are: 1) manipulating the crystallographic structure of the precursor or of the reacted oxide to better its flux pinning property, 2) developing silver-alloyed sheathing material to further enhance not only the microstructure of the superconducting ceramic but the strength as well as current conduction property of the matrix, and 3) optimizing the conductor performance through the use of thermo-mechanical processing control methods. The results presented in this chapter thus details some of the research work performed at the Center pertaining to the latter two categories.

2.1.1 Powder Preparation

The precursor powders used in ceramic processing are stable compounds, sometimes hydrated, and are of defined purity. Powder processing involves the control of particle size and of mixing powder reagents, whether of the precursor powders or of the partially reacted powders - to enable the formation of new stable phases during the process of

thermal agglomeration (or *sintering*). Despite the numerous different ways of superconducting powder synthesis [145-151] these methods can essentially be classified into two types: 1) *solid state reaction*, and 2) *solution route*.

The solid-state reaction (two-powder-process, dry-mixing) technique involves mechanical mixing of appropriate amounts of starting materials followed by calcining, grinding and sintering to form the superconducting phase. Due to the slow reaction rates in this method, long sintering times and close temperature control are required to assure substantial formation of the major high-T_c (2223) phase. In particular, when metal carbonates such as $CaCO_3$ and $SrCO_3$ are used as starting materials, large particles of Sr-Ca-Cu-O, Ca-Cu-O and CuO phases are commonly found in the resultant powders [152].

The solution route for powder preparation includes thermal co-decomposition, co-precipitation, freeze-drying, sol-gel processing and spray-pyrolysis in which the metal nitrates and oxides are dissolved into a solution (*e.g.*, nitric acid), then dried and calcined. The solution route method provides a close control of the chemical and physical properties of the precursor powder with the main advantages being enhanced in homogeneity, uniform particle size and better maintainability of the stoichiometry [153]. However, special attention should be paid to the precise control of processing parameters, such as the *pH* values in co-precipitation and sol-gel methods, to avoid severe impurity segregation [154].

As common to both routes, the process of *calcination* is necessary to thermally decompose the mixed powder, with the amount of heating applied below the powder's melting point. The pre-calcined powders are not normally pressed, which would allow the escaping of gases produced as a by-product. The reaction is only partially completed (and is typically endothermic) owing to the small contact areas at the boundaries of grains. After the calcination process, it is necessary to grind, crush and/or mill (attrition- or ball-milled) the porous solid, after which pelletization (or pressing) of the finely grounded powder takes place by axial pressure applied with a hydraulic press to the powder using a set of cylindrical metallic die. Sintering of the pellet(s) then follows (by the use of a furnace), with the temperature set near the powder's melting point [155, 156] (~ between 835^0C and

850^{0}C) during which large crystallites are formed. The pellets are normally placed on chips or powder of the same material (superconductor) to avoid contamination from the underlying brick/ceramic plate during firing. Repeated grinding, mixing/crushing and sintering are needed to complete the chemical reaction, thus forming the single superconducting high-T_c (2223) phase. The pressing and sintering processes are usually repeated with an intermediate grinding step (with a porcelain mortar and pestle or into a nylon jar with zirconia balls as the grinding media and hexane as the carrier). Figure 2.1 perhaps best summarizes the processing steps involved in the preparation of Bi(Pb)-2223 precursor powders.

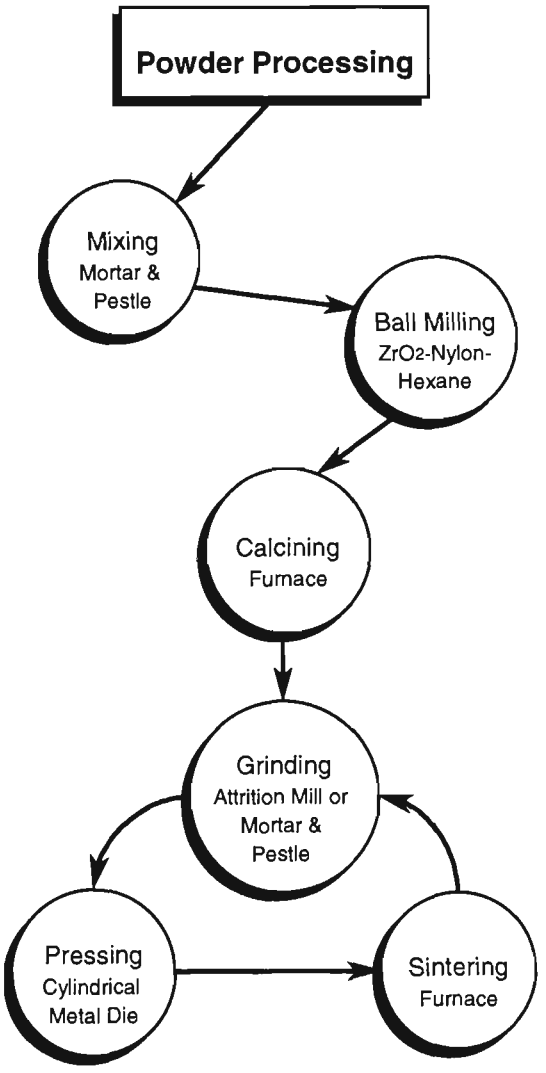

Figure 2.1 *Schematic representation of powder processing of Bi(Pb)-2223.*

The precursor powders of Bi(Pb)-2223 used for the processing of wires and tapes were produced from both methods of solution route and solid-state reaction and are designated as S, T, D, U, and B. The molar ratio and method of synthesis for the precursor powders are given in Table 2.1, with the corresponding processing description of each given in Table 2.2.

TABLE 2.1 *Molar (cation) ratios and method of preparation for the five precursor powders of Bi(Pb)-2223 used.*

Powder ID	Method	Bi:Pb:Sr:Ca:Cu
S	Thermal co-decomposition (solution route)	1.84:0.35:1.91:2.05:3.05
T	Two-powder route (solid-state reaction)	1.84:0.35:1.91:2.05:3.05
D	Dry-mixing (solid-state reaction)	1.84:0.35:1.91:2.05:3.05
U	Dry-mixing (solid-state reaction)	1.84:0.35:1.91:2.05:3.06
B	Spray-pyrolysis (solution route)	1.80:0.33:1.87:2.00:3.00

TABLE 2.2 *Methods and processing details for the five precursor powders of Bi(Pb)-2223 used.*

Powder ID	Processing description[#]
S	The nitrates of Bi, Pb, Sr, Ca, and Cu as the starting materials are mixed and stirred in aqueous solution of nitric acid until only the residue is left from evaporation. The powder is then grinded and calcined at ~ 700^0C for 24h. Calcination processes are normally carried out with the powders unpressed to minimize contact areas

	at the grain interfaces so reactions do not go to completion. Sintering is then performed at ~ 835^{0}C for 24h with the powder grinded and pressed (for homogeneity and greater contact surface between grains) before hand. To achieve fine particle size the sintered powder is further grinded (attrition or ball milled) and passed through a mesh for selected particle size.
T	This involves the mixing of oxides, peroxides and carbonates of Bi, Pb, Sr, Ca, and Cu as the starting materials. A 'one reduction in Ca stoichiometric' content of the final composition is first formed from calcination at ~ 750^{0}C for 15h then sintered at ~ 840^{0}C for 24h. The calcium copper oxide is formed separately with the same calcining condition but sintered at ~ 900^{0}C for 48h. It is then mixed with the 'one reduction in Ca stoichiometric' compound to give the final desired composition.
D	The process of dry mixing is quite similar to that for two-powder route. It involves the mixing of oxides, peroxides and carbonates of Bi, Pb, Sr, Ca, and Cu as the starting materials. Calcination is then carried out at first ~750^{0}C for 15h, then sintered at ~ 845^{0}C for 30h. Mixing, grinding and pressing were carried prior to each heat treatment.
U	Commercially made precursor powder from ISS Inc. (U.S.), containing 2212 as the major initial phase - refer to section 2.2 for powder characteristics.
B	Commercially available precursor powder from EM Industries, Inc., Merk Ltd. (U.K.), containing 2212 as the major initial phase - refer to section 2.2 for powder characteristics.

 # The heating and cooling rates for most precursor powders were 2°C/min. and 4°C/min. Sintering of the precursor powders were conducted at ambient atmosphere.

2.1.2 Fabricating Bi(Pb)-2223 Composite Tape Conductors

Silver, the chosen sheathing material because it fulfills (as does gold) several chemical requirements: 1) it doesn't react with the BSCCO during sintering, 2) no occurrence of oxidation during sintering, and 3) it allows the passage of oxygen through its sheath - an important property for any cladding material to be used for BSCCO since the oxygen content of these superconductors varies with temperature [157]. In addition, cladding the ceramic superconductor is required for reasons of mechanical strength and flexibility as well as providing a normal-conducting current path should the superconductor revert to the normal state. The disadvantages of using Ag however, are: 1) its relatively high cost, 2) its low strength, and 3) its thermal expansion of coefficient does not match that of BSCCO - a 1 m long Ag-bar shrinks ~ 3.6 mm when cooled down to 80 K [131]. Nevertheless, due to high manufacturing cost in purchasing Ag-alloys at the time, silver of ~ 99.99 % purity was used for the majority of the work performed at the Center.

Supplied from *Johnson Matthey Ltd.*, Australia, the Ag matrix arrived in the form of 1 m length hollow cylindrical tubes of various inner/outer diameters. This necessitated the processing of different combinations of the number of filaments in the processing of MF tapes. Besides providing a sheath in which compaction occurred, the Ag tube supplied the ductility necessary for drawing and rolling. Prior to processing, the tubes were 'burnished' - cleaned with silver paste by the use of an electric hand -drill and a stainless steel rod, then rinsed with acetone or ethanol, and finally fired to ~ 400-500^{0}C for 2-3 hr to burn away any residue. The tubes were then sealed one end by either: 1) cold forming on a lathe, 2) extrusion by swaging thus producing a tapered end - tagging, or 3) simply place a roll of pure silver tape at one end.

For the standard procedure of *oxide-powder-in-tube* (OPIT or simply PIT) [158-160] or the novel method of *oxide-wire-in-tube* (OWIT or simply WIT) [161-163, 157], the finely hydrated precursor powder was poured into the cleaned, one-end sealed tube by hand (with the use of a hammer and rod in the case of PIT) or with the aid of a vibrator [164], after which the other end of the tube was sealed. The frequency of vibration varied from high to

low (60-10 Hz) as more powder settled in. The initial packing density produced by using a hammer and rod ranged between 55-70 % of the theoretical value, while it was only between 25-35 % with the vibrator. The mass density of Bi(Pb)-2223 used was ~ 4,350 kg/m^3, comparing with ~ 6,490 kg/m^3 for Bi-2223 (containing no lead), or sometimes reported as ~ 6,100 kg/m^3 [165]. Using the vibrator (shown in Fig. 2.2) however, higher reproducibility and consistency were achieved. As an alternate method, rods of pre-compacted powder could be used to control the initial packing density. Next, the sealed powdered tube was then drawn or groove-rolled into wire form.

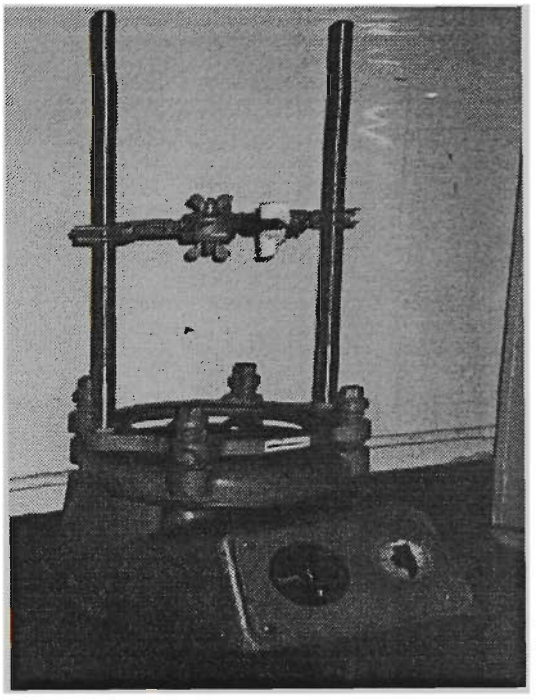

Figure 2.2 *Vibrator machine used for transferring powder in the PIT and WIT processes.*

2.1.2.1 Wire processing

With the processing of Bi(Pb)-2223 composite superconducting tapes, there are generally two standard procedures used. They are the method of *powder-in-tube* (PIT - the most commonly used method by wire/tape manufacturers such as Intermagnetics General Corporation (IGC), American Superconductor Corporation (ASC), Sumitomo Electric Industry (SEI), Vacuumschmelze, and Metal Manufactures Ltd. (MM) [166]) and the

continuous-tube-forming/filling (CTFF) process - which is quite different from the *Jelly roll* technique [167] where a layer of HTSC material is deposited on the silver substrate. Analogous to the PIT technique, a slight deviation in processing where a rod or wire is inserted in the center of the tube (hence wire-in-tube, or WIT) can be implemented to increase the J_c (but not I_c) of the superconducting tape quite substantially, by substituting some of the superconducting ceramic for the matrix material, based on the notion that supercurrent flow primarily at the matrix-core interface [161-163]. The schematic representation of the methodology for each of the three procedures used in the processing of Bi(Pb)-2223 wires and tapes are shown in Figs. 2.3-2.5.

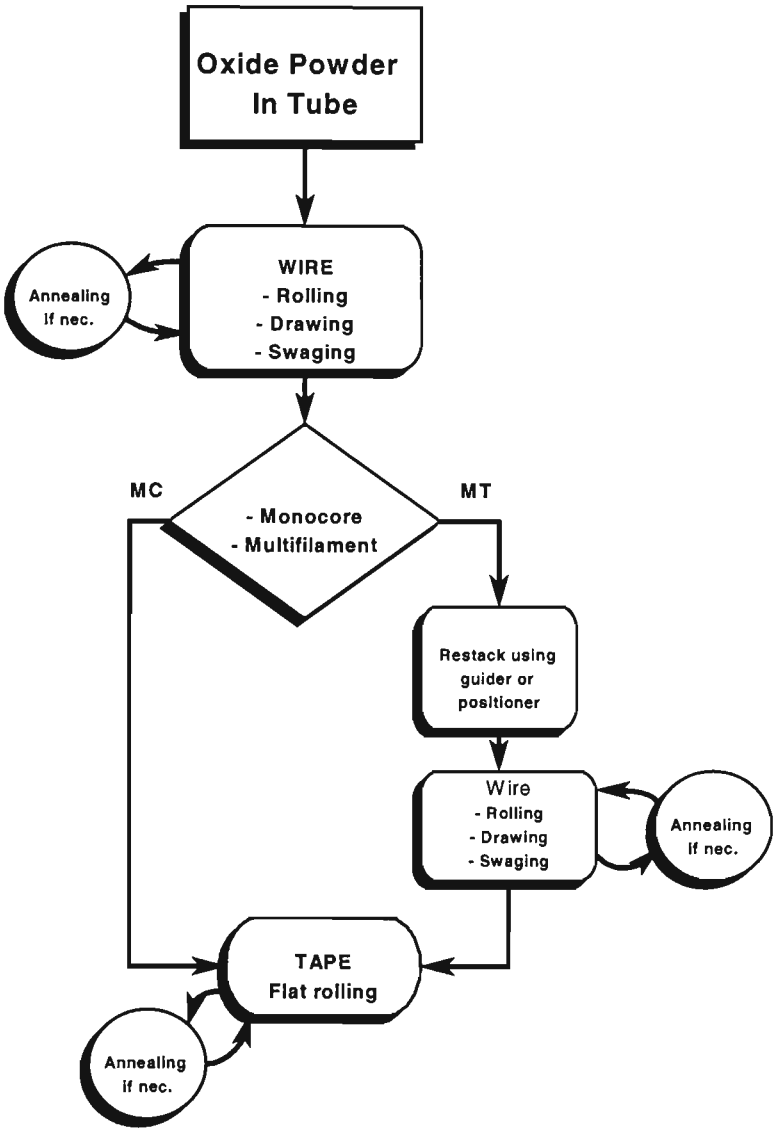

Figure 2.3 *Schematic of the powder-in-tube (PIT) method.*

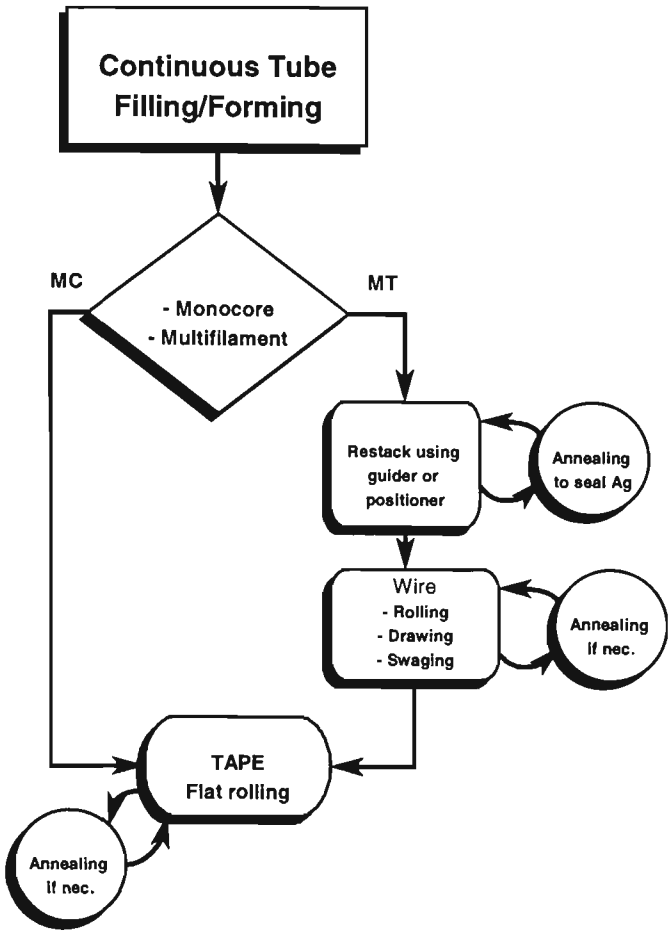

Figure 2.4 *Schematic of the continuous-tube-forming/filling (CTFF) process.*

From Figs. 2.3-2.5, the procedure of CTFF requires least processing time and effort as the drawing to thin wire stage has been by-passed. In brief, the process of CTFF can be explained as follows [168]; the powder is normally poured continuously through a calibrated orifice onto a moving strip of 99.99 % pure silver. The silver strip weighs about 4.5 kg (~ 10 pounds), 0.254 mm thick and 10.414 mm wide. The burden of the powder on the strip is controlled using a blade. The powder-bearing strip then enters a tube mill; in several stages the strip is folded and overlapped by passing through several sets of rolls and dies. The yield is ~ 335.3 m (1100 ft) of cylindrical finished 'cigarette' wire with diameter of ~ 1.5 mm.

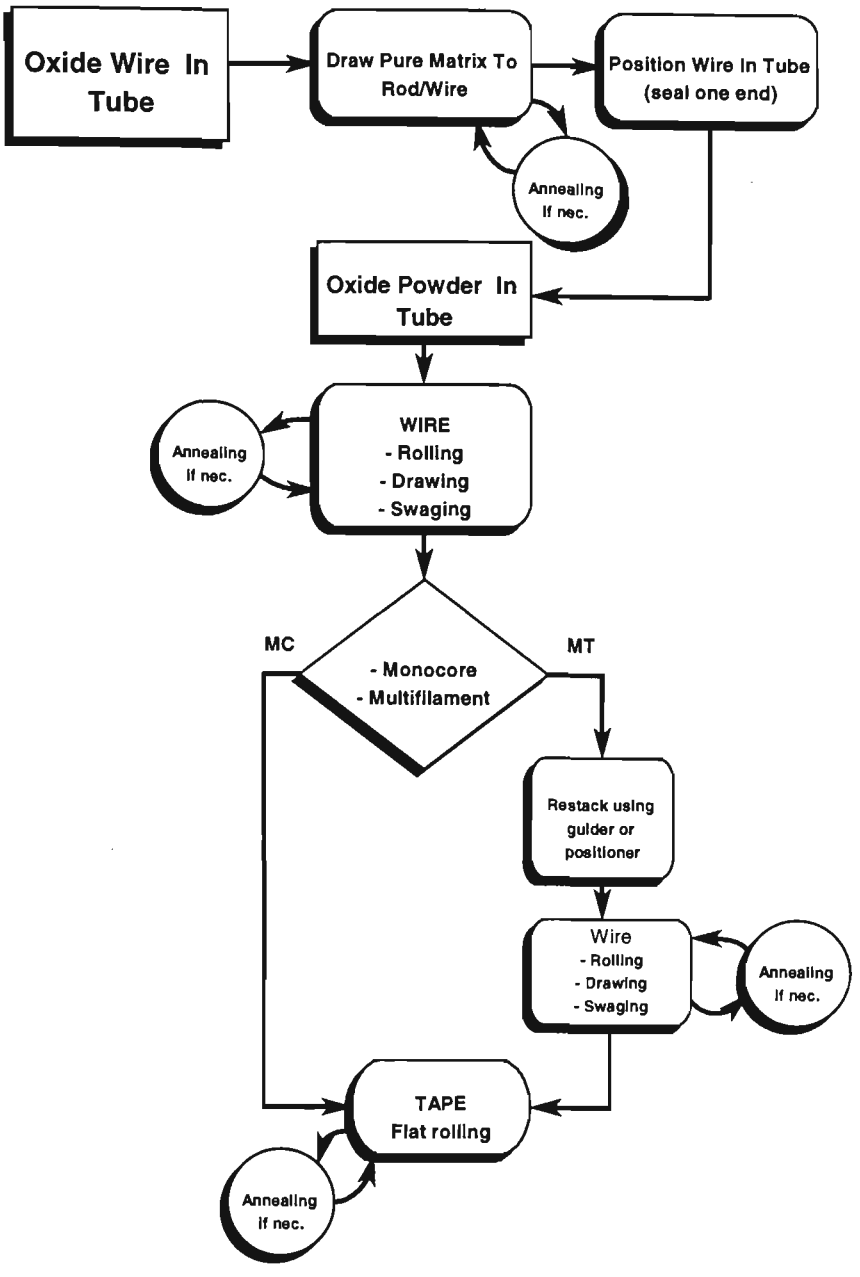

Figure 2.5 *Schematic of the wire-in-tube (WIT) procedure.*

In comparison with PIT, CTFF does give better uniformity at the matrix-core interface [169]. However, there is a processing problem with the CTFF wires - they tend to 'open up' during sintering, causing the powder to leak out. For multi-filamentary tapes (MT) this 'powder-leaking-problem' was circumvented with a pre-annealing step incorporated prior to drawing or groove-rolling stage at elevated temperatures between 750-780^{0}C for ~ 15 h. Figure 2.6 shows the cigarette wires 'closing' after annealing.

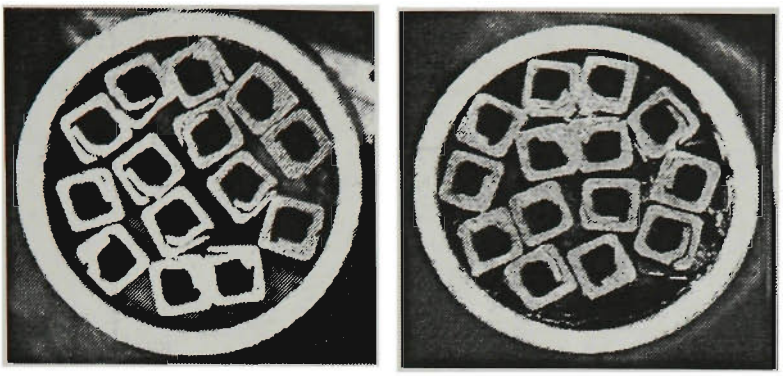

(a) *(b)*

Figure 2.6 *Cross-sections of 14 CTFF wires prior to wire forming: (a) before and (b) after annealing at ~ 760^{0}C for 15 hr in a tubular furnace.*

For wire forming, two options were available: 1) groove-rolling (with the cross-section of each groove being octagonal in shape - having alternating very short and long sides), and 2) drawing. It must be mentioned that the second option was not available (and operational) until early 1996, thus most of the wire processing was performed using groove-rolling.

The groove statistics are listed in Table 2.3, plotted in Fig. 2.7b, left. The mathematical treatment on area and area reduction calculations are detailed in Appendix A. Since each successive reduction in area was large, between ~ 22-42 % (except moving from groove 11 to 12), adjustments were made on the dual-rolling machine (Fig. 2.7a, left) such that each reduction was within the range between 10-15 % for all wires - as any greater reduction often results in work-hardening of the silver clad, which would require more frequent annealing at ~ 500^{0}C between 20-30 min. depending on the thickness of the Bi(Pb)-2223 composite wire.

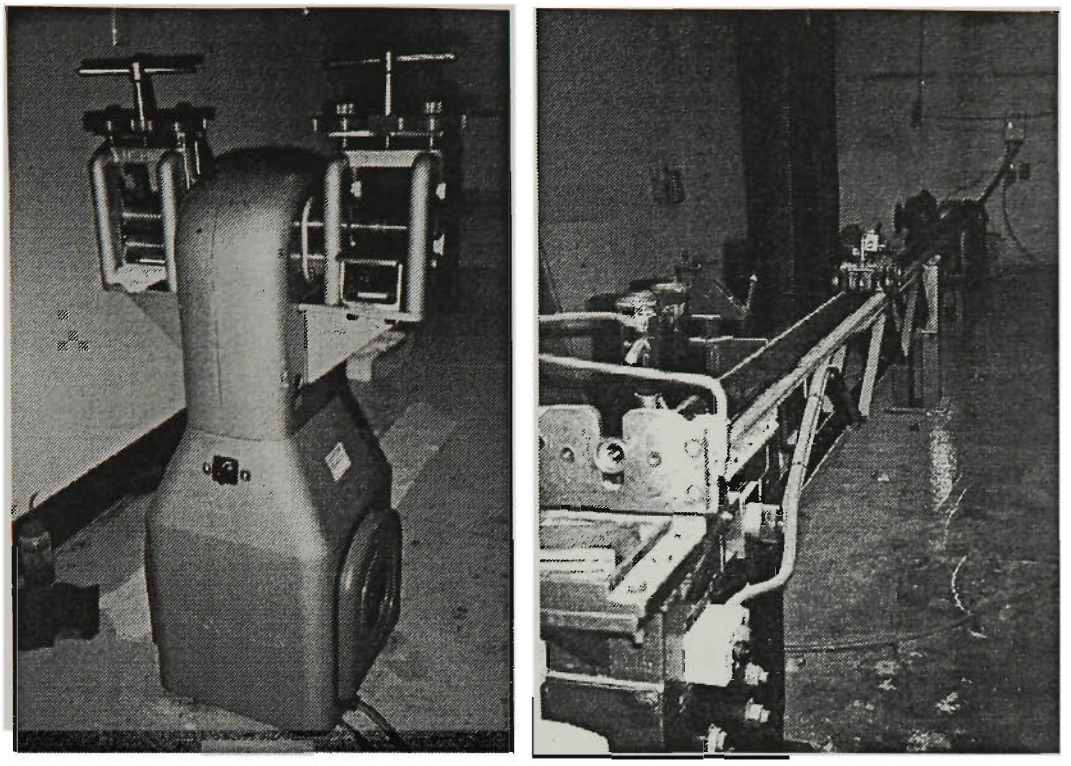

Figure 2.7a *Left is the dual-rolling machine (Model M.100/55 - 010 Mejora, F.11i CAVALLIN, Italian import) with groove-rolling on its left and flat-rolling on its right. Right is the draw-bench, also used in the processing of composite Bi(Pb)-2223 wires.*

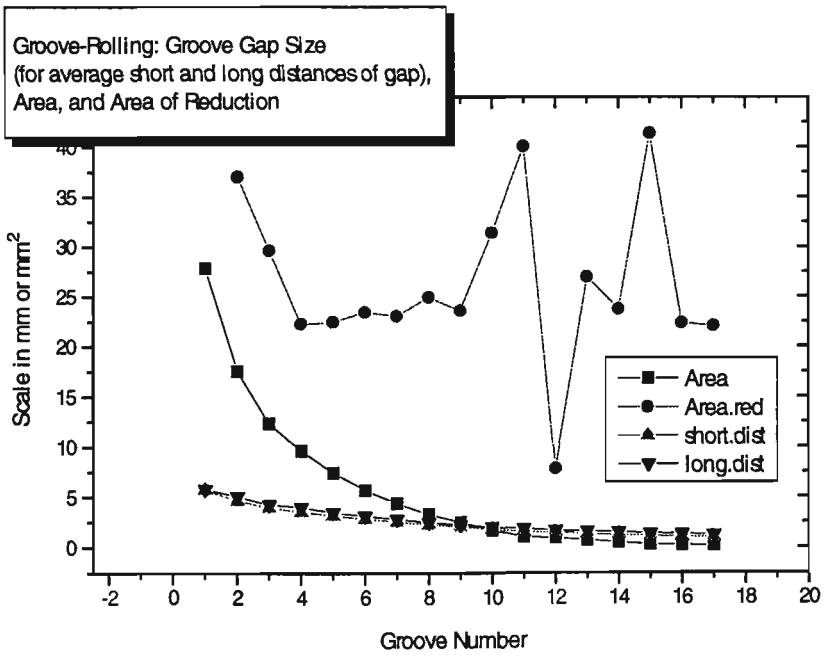

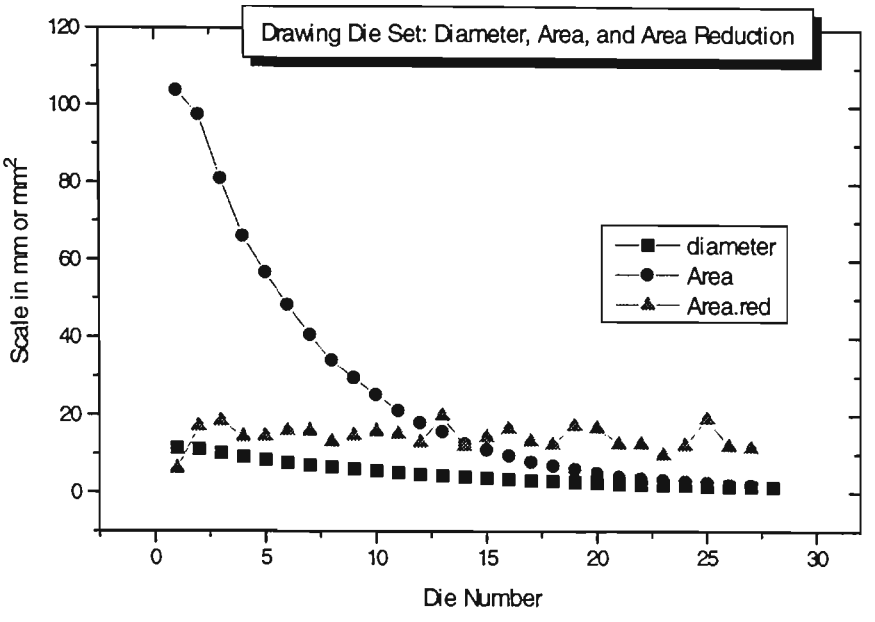

Figure 2.7b *Details for groove-rolling (top) and drawing (bottom) of wire, as given in Tables 2.3 and 2.4.*

For drawing, the wires were drawn with set die diameters on a straight draw bench (Fig. 2.7a, right) with a variable speedometer box (on the far back wall in the photograph), adjusted to give a slow controllable pace within several cm/s. The draw-pass schedule for Bi(Pb)-2223 composites is given in Table 2.4 with the reduction in cross-sectional area of the wire per pass lying between ~ 6-20 %. The corresponding data is also plotted in Fig. 2.7b, right. With drawing, intermediate annealing was performed after die numbers 13, 18, and 22 at ~ 500^{0}C for 20-30 min. depending on wire thickness. In both groove-rolling and drawing, more frequent intermediate annealing was necessary when thinner silver tubes (4.5/5.5 and 9/10 mm inner/outer diameters) were used.

TABLE 2.3 *Approximate groove statistics on the dual-rolling machine.*

Groove no.	long-opposite-side distance (mm)	Short-opposite-side distance (mm)	Approximate area of groove (mm^2)	Approximate area reduction between grooves (%)
1	5.71	5.78	27.83	---
2	4.62	5.06	17.53	37.01
3	3.95	4.24	12.34	29.60
4	3.55	4.00	9.60	22.22
5	3.18	3.48	7.45	22.43
6	2.84	3.13	5.70	23.42
7	2.55	2.83	4.39	23.05
8	2.27	2.47	3.29	24.93
9	2.06	2.24	2.52	23.60
10	1.80	2.04	1.73	31.43
11	1.57	1.87	1.03	40.05
12	1.48	1.68	0.95	7.83
13	1.33	1.59	0.70	26.95
14	1.24	1.52	0.53	23.75
15	1.13	1.39	0.31	41.36
16	1.04	1.31	0.24	22.34
17	0.98	1.25	0.19	22.06

The fabrication of multi-filamentary (MF) wires (Fig. 2.8) followed the same procedure as those of mono-filament. Prior to drawing however, the filaments were stacked using a 'filament-positioner' (simply a short section of the same silver tube), with one end of the tube tapered by either groove-rolling or by swaging. The swaging machine from *MFG Co.*, Proivdence R.I., U.S., is shown in Fig. 2.11, left, appearing on the right side of the double-pair-flat-rolling machine.

TABLE 2.4 *Draw-pass schedule used in the drawing of Bi(Pb)-2223 wires.*

Die no.	Diameter (mm)	Area (mm^2)	Area (%) reduction	Die no.	Diameter (mm)	Area (mm^2)	Area (%) reduction
1	11.50	103.87	---	15	3.76	11.10	12.08
2	11.15	97.64	5.99	16	3.48	9.51	14.34
3	10.16	81.07	16.97	17	3.18	7.94	16.50
4	9.18	66.19	18.36	18	2.96	6.88	13.36
5	8.50	56.75	14.27	19	2.77	6.03	12.43
6	7.86	48.52	14.49	20	2.52	5.00	17.24
7	7.20	40.72	16.09	21	2.30	4.15	16.70
8	6.60	34.21	15.97	22	2.15	3.63	12.62
9	6.15	29.71	13.17	23	2.01	3.17	12.60
10	5.68	25.34	14.70	24	1.91	2.87	9.70
11	5.21	21.32	15.86	25	1.79	2.52	12.17
12	4.80	18.10	15.12	26	1.61	2.04	19.10
13	4.48	15.76	12.89	27	1.51	1.79	12.04
14	4.01	12.63	19.88	28	1.42	1.58	11.57

Figure 2.8 *Filaments and tubes before and after stacking.*

With dc-applications in mind, the consideration of 'filament-design' is primarily governed by the metal-working such as stress and strain tolerance properties rather than electrical concerns as in the case of ac-applications. As the majority of the processed tapes were tested under dc condition, the assembly of filaments in MF wire was investigated for processing and stability studying purposes.

The *systematic removal scheme* (SRS) [22] can be used to demonstrate the assembly geometry which maximizes the number of hexagonal nuts able to be placed into a circumscribed circle with given diameter.

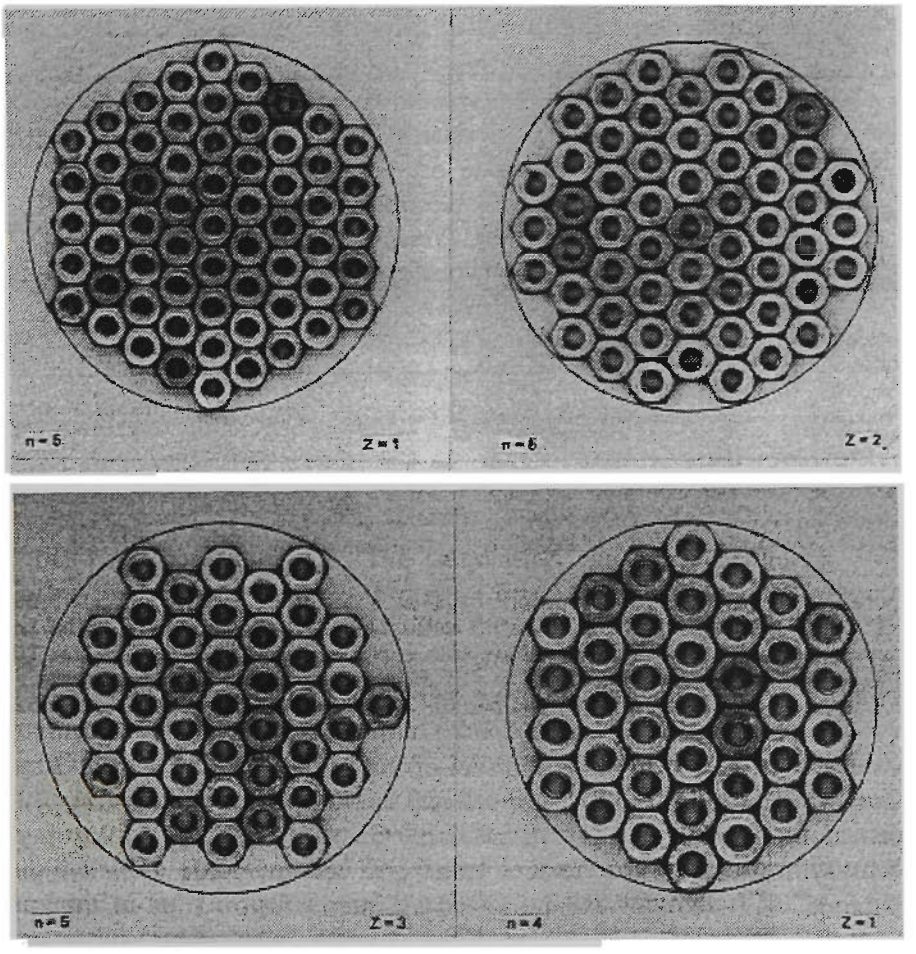

Figure 2.9 *'Nut-model' geometric configuration representing the stacking arrangement of filaments in a tube.*

As shown in Fig. 2.9, the SRS simply suggests that by using a systematic approach in removing groups of six hexagonal nuts at a time, the assembly of nut configuration returns to its original formation with one layer less after the third removal step. The nut-model shown starts with $n = 5$ layers (top left), and ends up with $n = 4$ layers (bottom right) after the third group removal, with Z a coded symbol used in the scheme.

The aim then was to maximize the number of filaments of various sizes to be inserted into a cylindrical tube of a given diameter. The total number of filaments can be derived to be $1+3m(m+1)$, where $m = n-1$, with n denoting the number of layers with the central filament being regarded as the first layer. This simple expression theoretically gives the highest filamentary density for any multifilamentary wire, refer to Appendix B for derivation. Several tube diameters were tried with various filamentary sizes. The resultant optical images of wire cross-sections using groove-rolling are shown in Fig. 2.10 for various combinations of tube sizes and filaments. The precursor powders used were dry-mixed powder U for OPIT wires and that of a similar type in synthesis for CTFF wires. Table 2.5 contains the corresponding dimensions and processing details.

It was subsequently found that the initial fill factor, λ (ratio of core to conductor area), was quite difficult to control primarily due to vacant spaces around the filaments being unfilled as well as the non-conforming octagonal shape of the filaments themselves. In commercial practice however, the vacant spaces remaining between the filaments and the cylindrical tube can sometimes be occupied by specially shaped filler pieces.

As listed in Table 2.5, increasing filamentary number is usually accompanied with a decrease in fill factor (or increase in Ag matrix), partly due to the limited tube sizes available. Investigations on the fill factor and critical bend strain dependence on critical current density and filamentary number are given in the next chapter.

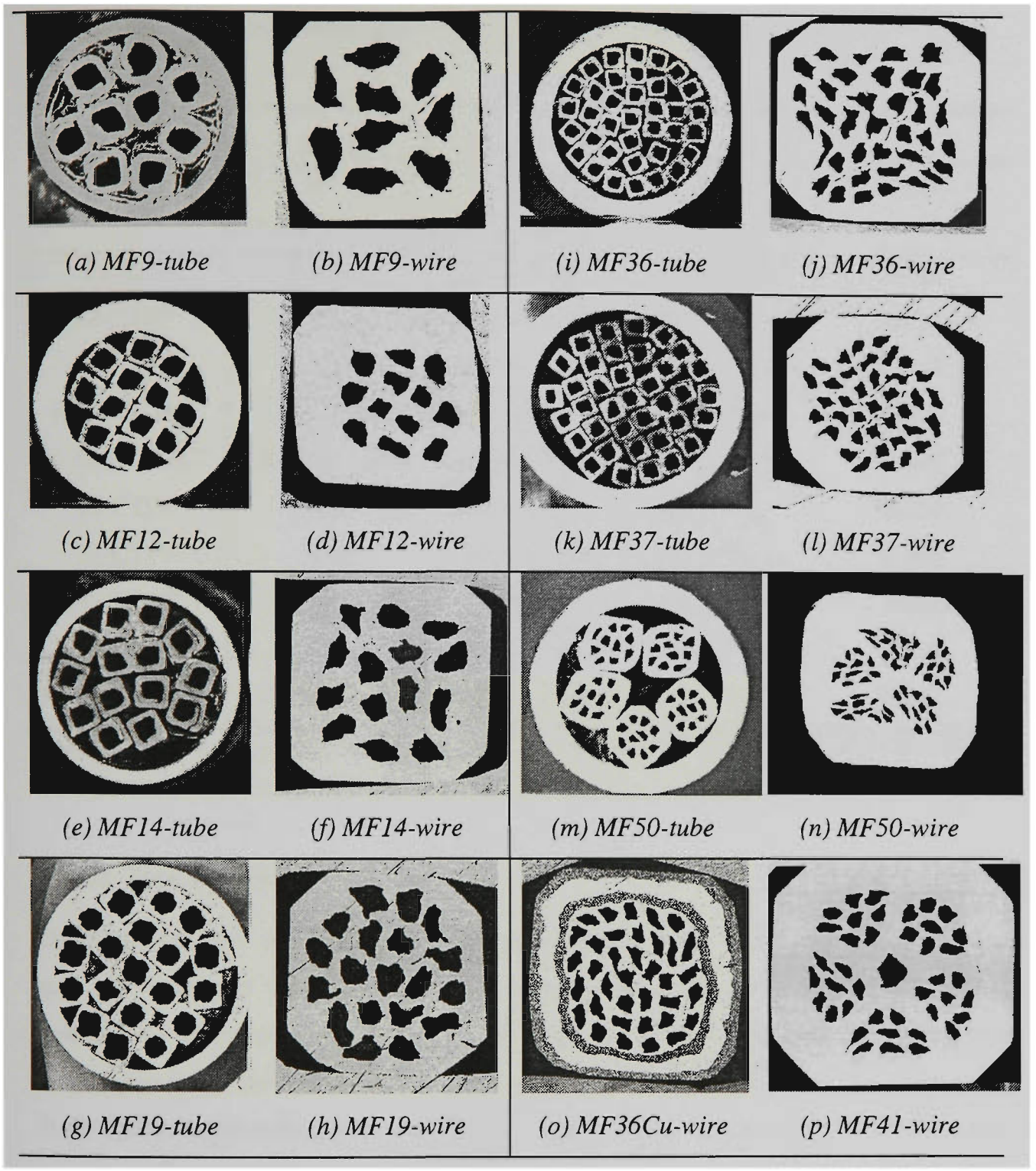

Figure 2.10 *Optical images of cross sections of Bi(Pb)-2223 MF CTFF (9, 12, 14, 36, 36Cu, 37, 50, and 41 filaments) and OPIT (19, and 31) composites, before (filaments stacked in tube) and after (wire forming) groove-rolling.*

TABLE 2.5 *Corresponding dimensions of cross-sections shown in Fig. 2.10.*

MF	Tube		Wire	
	1^{st}, 2^{nd} Stacking (o.d./i.d. - mm)	Filament size (groove-rolled)[#]	Wire size (groove-rolled)	Fill factor, λ
9-CTFF	6.5/5.5	after 13^{th} grv.	after13^{th} grv.	0.233
12-CTFF	6.5/4.5	after 13^{th} grv.	after13^{th} grv.	0.218
14-CTFF	6.5/5.5	after 17^{th} grv.	after13^{th} grv.	0.197
19-OPIT-vib[*].	6.5/4.5, 6.5/5.5	after 17^{th} grv.	after13^{th} grv.	0.297
31-OPIT-ham[@].	6.5/4.5, 10/8	after14^{th} grv.	after13^{th} grv.	0.257
36-CTFF	10/8	after 17^{th} grv.	after12^{th} grv.	0.210
37-CTFF	10/8	after 17^{th} grv.	after12^{th} grv.	0.184
50-CTFF[&]	10/8, 10/8	$12^{th}/7^{th}$ groove	after 5^{th} grv.	0.106
36Cu[%]-CTFF	10/8	after 17^{th} grv.	after12^{th} grv.	0.154
41-CTFF[&]	6.5/5.5, 10/8	$12^{th}/10^{th}$ groove	after 9^{th} grv.	0.142

[#]*The actual sizes in mm are given in Table 2.3.* [*] *Vibrator used for PIT.* [@] *Hammer and rod used for PIT.*
[&] *Double-stacked.* % *Pure Ag cladding for filaments, Stirling Ag (Ag:Cu ≈ 93:7) for outer sheath.*

2.1.2.2 Tape processing

Having produced wires of diameters/thickness of normally between 1 and 3 mm, the next step was to convert them into 'green' or unreacted tapes by cold-rolling. Three rolling machines were used for tape processing. These were: 1) the dual-roller (Fig. 2.7, left), 2) the double-pair-flat-roller from *Crofts, Engineers Ltd.*, Bradford, England (Fig. 2.11, left), and 3) the hydraulic flat-rolling machine (Fig. 2.11, right). These rolling machines also provided a mechanical means of intermediate deformation for long length composite reacted ('red') tapes after each sintering stage.

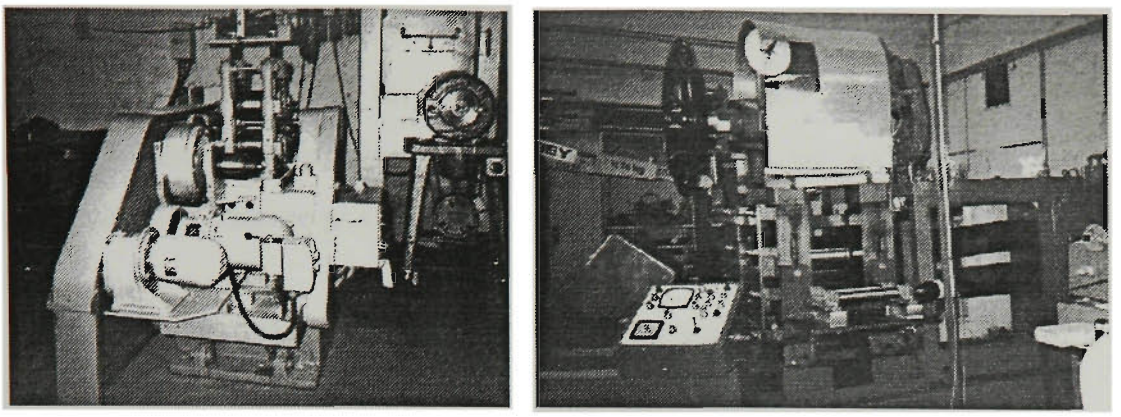

Figure 2.11 *The double-pair-flat-roller (left) and the hydraulic flat-rolling machine (right).*

Unlike the other two rolling machines, the hydraulic rolling machine has a variable speed controller. The slowest speed was used to produce tapes, ~ 1-3 cm/s. The majority of tape processing was performed using the dual roller (Fig. 2.7, left), whose characteristics are given as follows:

Roller diameter:	55 mm
Roller width:	100 mm
Roller speed:	1.6-1.8 rad/s
Maximum clearance:	14 mm
Production rate:	3 m/min
Motor:	2 HP
Overall sizes:	38 × 67 × 120 cmh
Weight:	175 kg

The roll spacings were reduced by about 15-20 % for each successive pass. The final tape dimensions range between 0.08-0.45 mm thick and 2-4 mm wide depending on the composite (moncore or multifilamentary). Again, intermediate annealing (at ~ 500^{0}C for ~ 20-30 min.) was necessary when either thin wall-tubes were used (to avoid edge cracking) or work-hardening was felt, or that the tape became hot and stiff (systematically after every 4 passes). Both short and long lengths of composites were produced. Long composite tapes

were wound onto alumina ceramic tubes of various diameters (furnace- and application-dependent), shown in Fig. 2.12, for sintering and annealing purposes. Short composite tapes of 20-40 cm in lengths were also fired in tubular and muffle furnaces, normally placed on rectangular alumina ceramic plates for heat treatment.

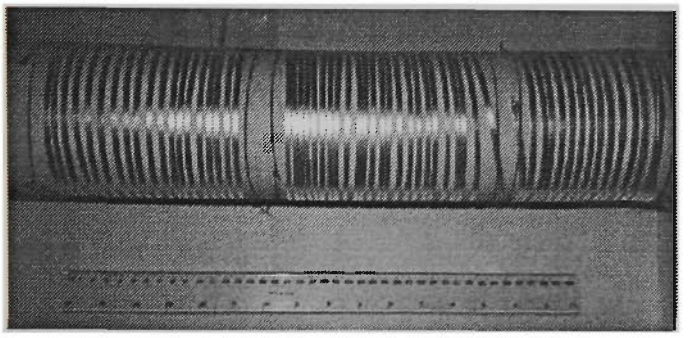

(a)

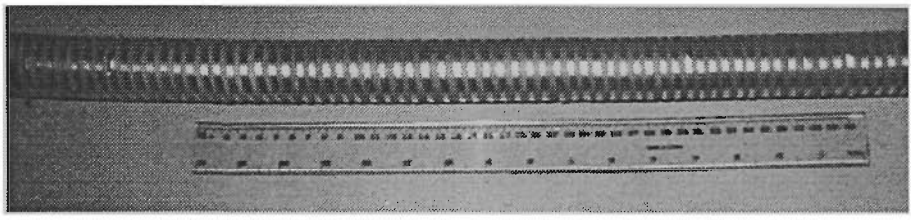

(b)

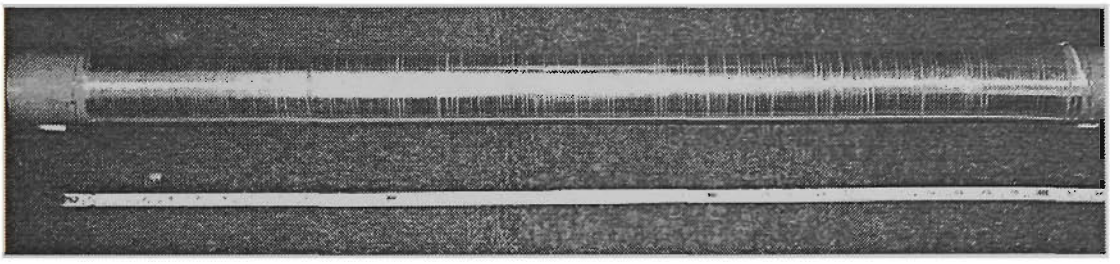

(c)

Figure 2.12 *Long lengths of reacted multifilamentary tapes: (a) 3×7-10 m segments of 31-filamentary PIT (powder U) tapes after first sintered, (b) 7 m 31-filamentary PIT (powder U) fully reacted tape used for winding a solenoidal coil, and (c) ~ 58 m 37-filamentary PIT (powder B) tape ready for the final sintering step.*

It has been reported [170], with continuous deformation processes such as rolling, drawing or extrusion, more uniform deformation should result with moderately large per-pass

reductions (such that mechanical mismatch in strength between core and matrix is minimized), small die angles, or large roller diameters [171-173] (giving greater contact surface area between rollers and tape) with small rolling speed (perhaps to simulate that of uniaxial pressing). In addition, considerations must be given to the strength of the ceramic core and that of the sheathing material as reported by Willis *et al* [174], where two distinct types of strain exist during deformation as a result of mismatching stress state between core and matrix. 'Sausaging' or symmetric (necking) mode is a result of a strong core and weak sheath while the anti-symmetric (undulating) mode is generated with a weak core and strong sheath.

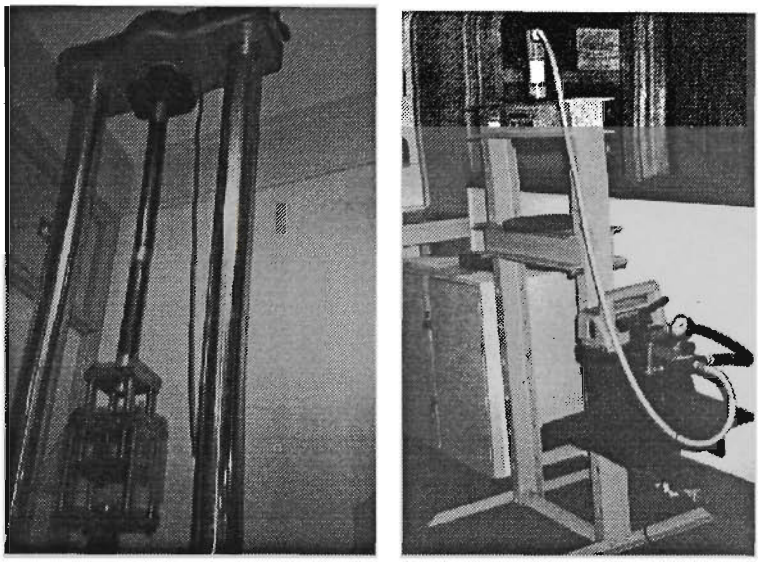

Figure 2.13 *The 'Mand 15 Ton' (left) and Enerpac hydraulic-driven (right) pressing machines.*

Uniaxial-pressing was also used as the intermediate mechanical deformation step for batch processing of short tapes, serving the same purpose as rolling by improving the density and grain alignment in the superconducting core of the tape. The pressing and sintering processes were repeated several times until a maximum critical current density was achieved.

Two pressing machines were used, shown in Fig. 2.13. The '*Mand* 15 Ton constant strain rate' pressing machine (*Mand Precision Eng. Co. Ltd.* Worcestershire, England) can apply a vertical force of up to ~ 120 kN (left of Fig. 2.13), while the capacity of the *Enerpac*

hydraulic-driven machine, from *Butler*, Wisconsin, U.S. (right of Fig. 2.13) is ~ 100 kN force (10 Tons). Typical uniaxial pressure applied to superconducting tapes was in the range of ~ 0.4-1 GPa depending on the area of the ceramic core. The rate of uniaxial pressing was kept to a minimum where speed control was available (with the *Mand* machine only).

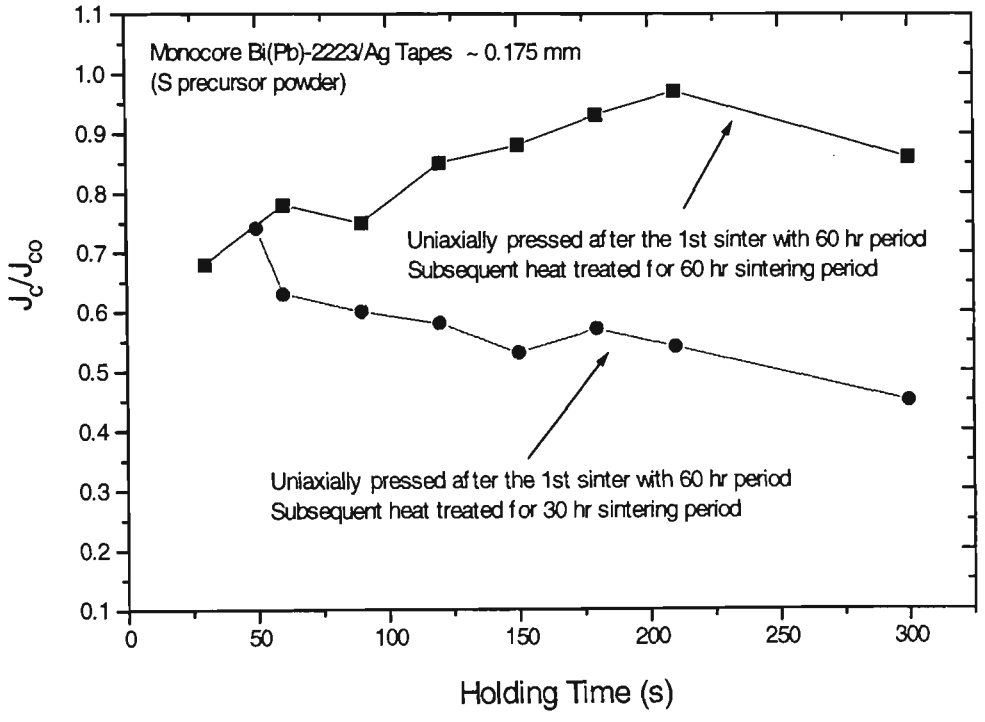

Figure 2.14 *Normalized J_c versus holding time during uniaxial pressing of monocore Bi(Pb)-2223 tapes (powder S), both ~ 0.175 mm thick.*

Once the pressing machine reaches the required force, it was found that keeping the pressure applied for at least ~ 30 sec. helped improve the J_c of the tapes. For sufficient sintering time necessary to fuse the cracks inflicted on the superconducting core during intermediate pressing, extended holding time up to several minutes can improve grain alignment and core density, although the upper limit seemed to be ~ 3-4 min. (Fig. 2.14), depending on the thickness of the tape.

2.1.2.3 Heat treatment

Both large and small electric tubular ('home-made' and purchased from *Ceramic Engineering, Furnace Manufacturers*, Sydney, Australia), as well as muffle furnaces were used in the heat treatment process. These are shown in Fig. 2.15 (with the controller brand-name indicated below) and 2.16.

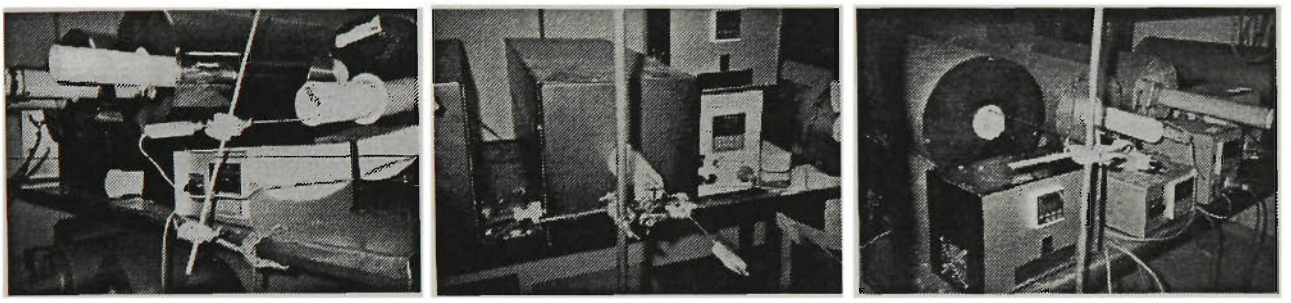

(a) *Shinko, and Shimaden (Japanese import)* | *(b) Jetflow (Australian made)* | *(c) Jetflow (Australian made)*

Figure 2.15 *Small tubular furnaces used for sintering of short composite tapes.*

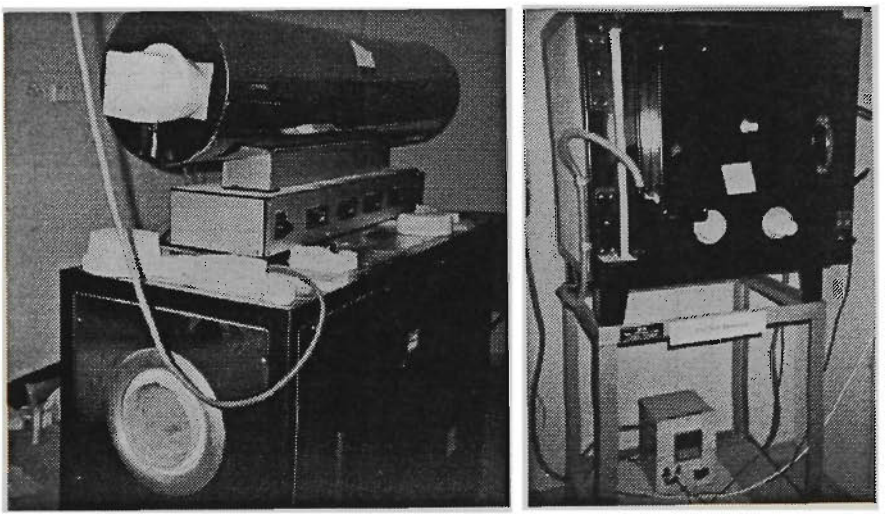

Figure 2.16 *Large tubular (left) and muffle furnaces (right) used for annealing and sintering of long length composite wires and tapes.*

The temperature profiles for the Top and Bottom tubular furnaces (Fig. 2.16, left) are given in Fig. 2.17. The 'hot-zone' (region of constant temperature, here taken as $\pm 1^0$C) of

the large Bottom furnace was measured to be ~ 1.10 m. For the Top furnace, the hot-zone was increased by the use of two concentric ceramic tubes, with the one containing the tape lying on the inside.

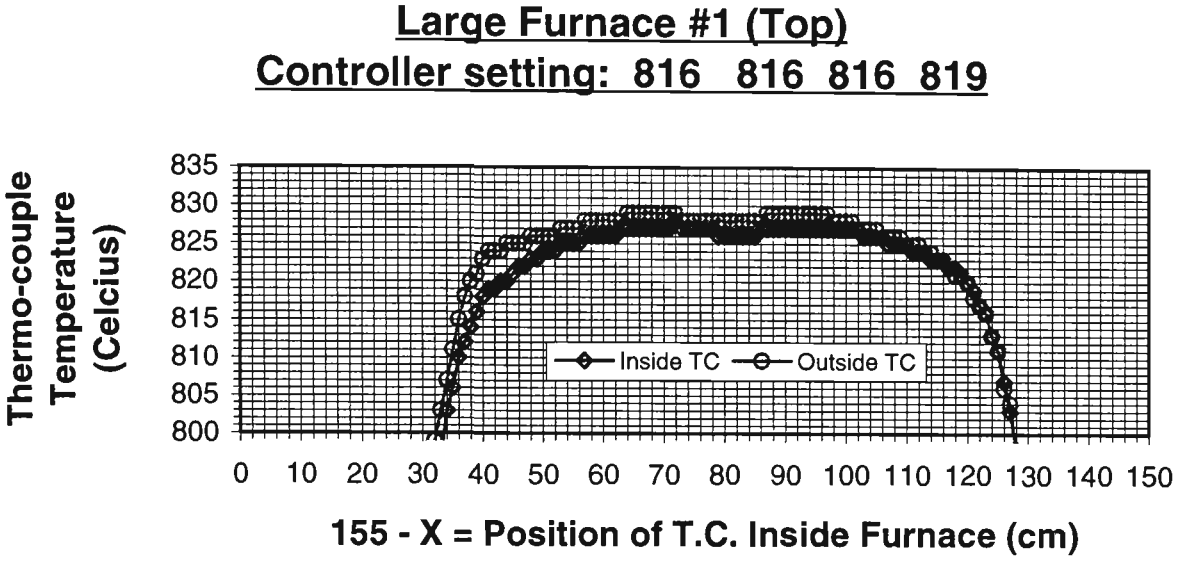

(a)

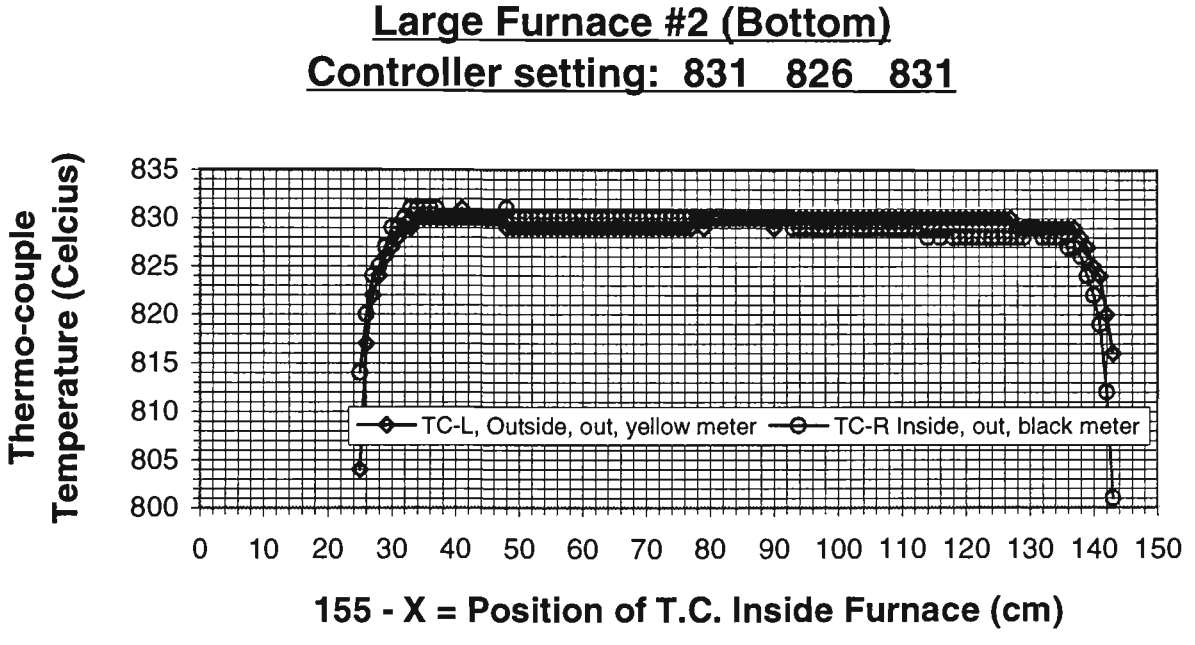

(b)

Figure 2.17 *Temperature profiles for the large Top (a) and Bottom (b) electric tubular furnaces used for the annealing and sintering of long length composite wires and tapes.*

A small heating and cooling rate (1.5 down to 0.25 ^{0}/min, Fig. 2.18) was used to minimize 'bubble formation' (or 'blisters') between the Ag sheath and the superconducting ceramic core, which normally occurred after the first sintering stage, most apparent with long length composite tapes. All tape sintering was conducted at ambient air atmosphere.

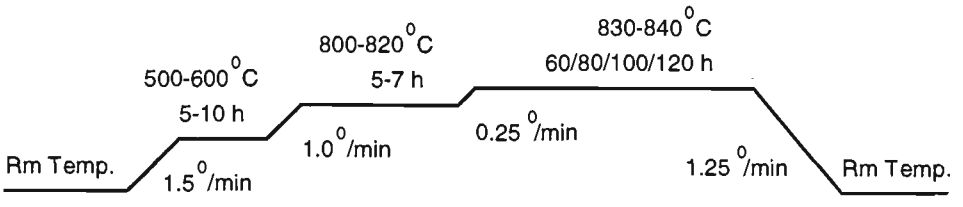

Figure 2.18 *Heat treatment pattern used in the processing of composite short tapes: monocore of powder S, T, D and multifilamentary of CTFF precursor powder.*

The heat treatment pattern shown in Fig. 2.18 was later modified to incorporate a 'drop in temperature' (of variable degrees, depending on the precursor powder type). The first two dwelling periods of heat treatment (Fig. 218) were eliminated, with the reduction in temperature during sintering including approximately 15 h into the last dwelling period. This step-wise reduction in temperature was found to expedite the high-T_c phase formation of 2223, making possible a two-sinter process. More on this topic in the next chapter.

2.1.2.4 Blisters, sausaging and edge-cracking

'Blisters' or 'bubbles' are the deforming or bulging of the sheathing materials due to high internal gas pressure build up during heat treatment at elevated temperatures [175] (Fig. 2.19). The source of the released gas has been attributed to condensed species such as $Ca(OH)_2$ or $Sr(OH)_2$ producing water, CO_2 and O_2 [157]. Water can enter the conductor as absorbed species on the surface of the powder, and the CO_2 can probably enter either as a carbonate from incomplete reaction or reaction between powder and the CO_2 in the atmosphere. For Bi(Pb)-2223 composite tapes, the problem of blisters was minimized with the annealing of the PIT tube containing dehydrated powder at temperatures between 650

(for powders S, T, D, U and B) and 800^{0}C (for precursor powder of CTFF wires and tapes) for approximately 10 hr. Alternatively, water and CO_2 could be eliminated by heating the powder in flowing O_2 or inert gas at ~ 800^{0}C, or in vacuum at 500-600^{0}C, for times ranging from 8 to 48 hr [157].

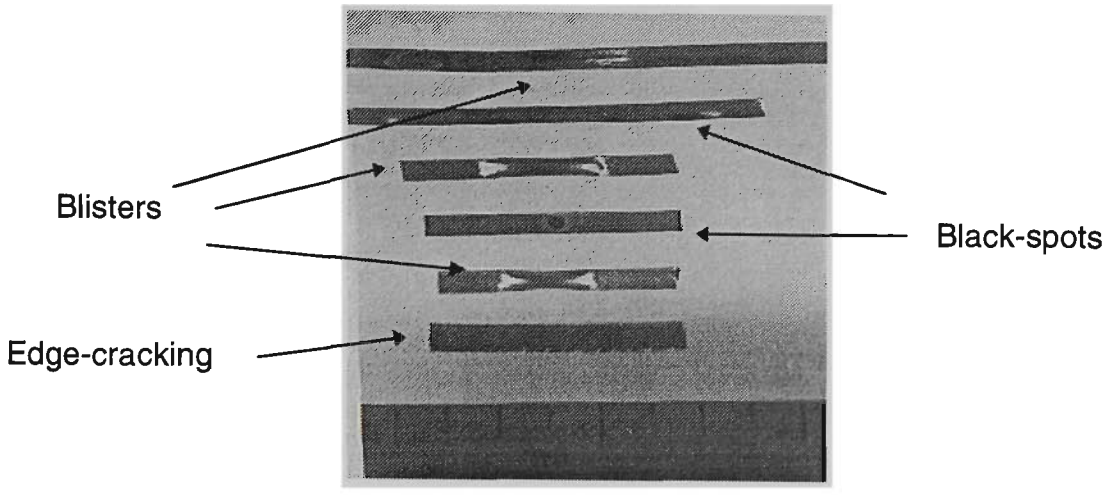

Figure 2.19 *Blisters, black-spots, and edge-cracking of sintered Bi(Pb)-2223 composite tapes.*

'Sausaging' (or 'necking') and edge-cracking are the result of mechanically induced defects which occur during deformation. The problem of edge-cracking (as shown in Fig. 2.19 and 2.20 - cracking of filaments within the MF tape) is normally the result of using {too} thin-wall tubes. This problem persists when insufficient annealing is made during cold-rolling, in conjunction with large reduction per-pass which work-hardens the matrix, and often can lead to surface cracking. Continuing heat treatment can result in 'black-spots' forming due to powder leaking (refer to Fig. 2.19).

To eliminate the problem of sausaging, it is necessary to understand the cause behind it. Sausaging is believed to be the end product of a bifurcation from a state of homogeneous strain to a state of non-uniform strain of composite materials undergoing mechanical deformation [176, 174]. The transport property of PIT Bi(Pb)-2223 composite tapes has been hampered by the presence of sausaging, which creeps in at an early stage of thermo-mechanical processing.

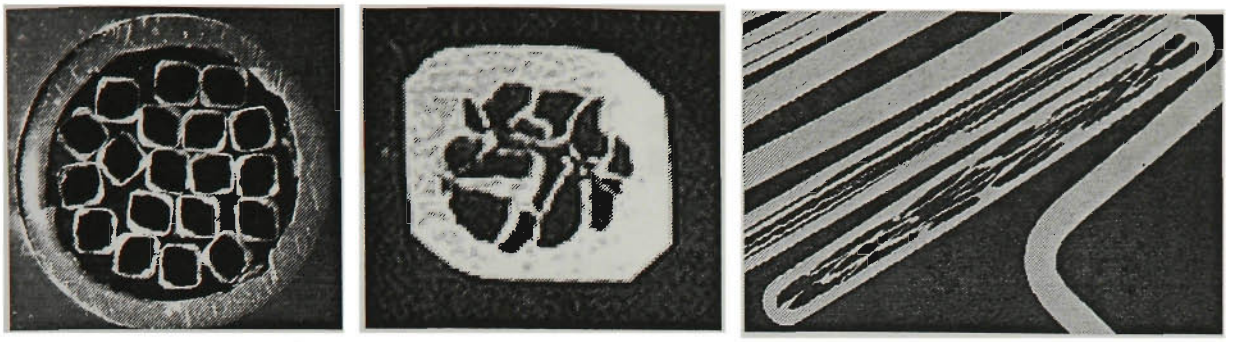

(a) MF19-tube *(b) MF19-wire* *(c) MT19-green*

Figure 2.20 *Non-uniform distribution of filaments as shown in (b) and (c), with some inter-filamentary cracking in tape form due to the use of thin Ag-cladding on the filaments (ϕ_{tube} = 6.5/5.5 mm), leading to mechanical non-homogeneity.*

As shown in Fig. 2.21(a)-(d), sausaging was found to occur in monocore tapes with oxide cores of approximately ≤ 40 μm in thickness, consistent with that reported by Hellstrom [157]. To combat this problem, alloys of silver such as Ag-7 at.% Cu (≈ $64H_V0.025$, red tape), depicted in Fig. 2.21, (e)-(f), and Ag-0.02 at.% Mg (≈ $44H_v0.025$, red tape) were used to reduce the mechanical mismatch between the relatively hard HTS core (≈ $125H_v0.025$) and the compliant Ag (≈ $38H_v0.025$) cladding during rolling. Indeed, a variety of Ag alloys, such as Ag-Al [177, 178], Ag-Mg [178-181], Ag-Cu [182, 168, 181], Ag-Ni [183], Ag-Mn [183], Ag-Au [184, 181], Ag-Au-Mg [181], Ag-Ni-Mg [183, 185], and Ag-Pd-Mg [181] have been examined as possible sheath materials to improve the mechanical strength.

Since the J_c values of Ag alloy sheathed tapes are normally lower than that of pure Ag sheathed tapes, studies have also been carried out by Maeda *et al* [186] on the effect of doping on the superconducting properties and microstructures of Bi(Pb)-2223 Ag alloy sheathed tapes with elements such as Ti, Zr and Hf to Ag-Cu sheath to further improve the J_c as well as the mechanical strength.

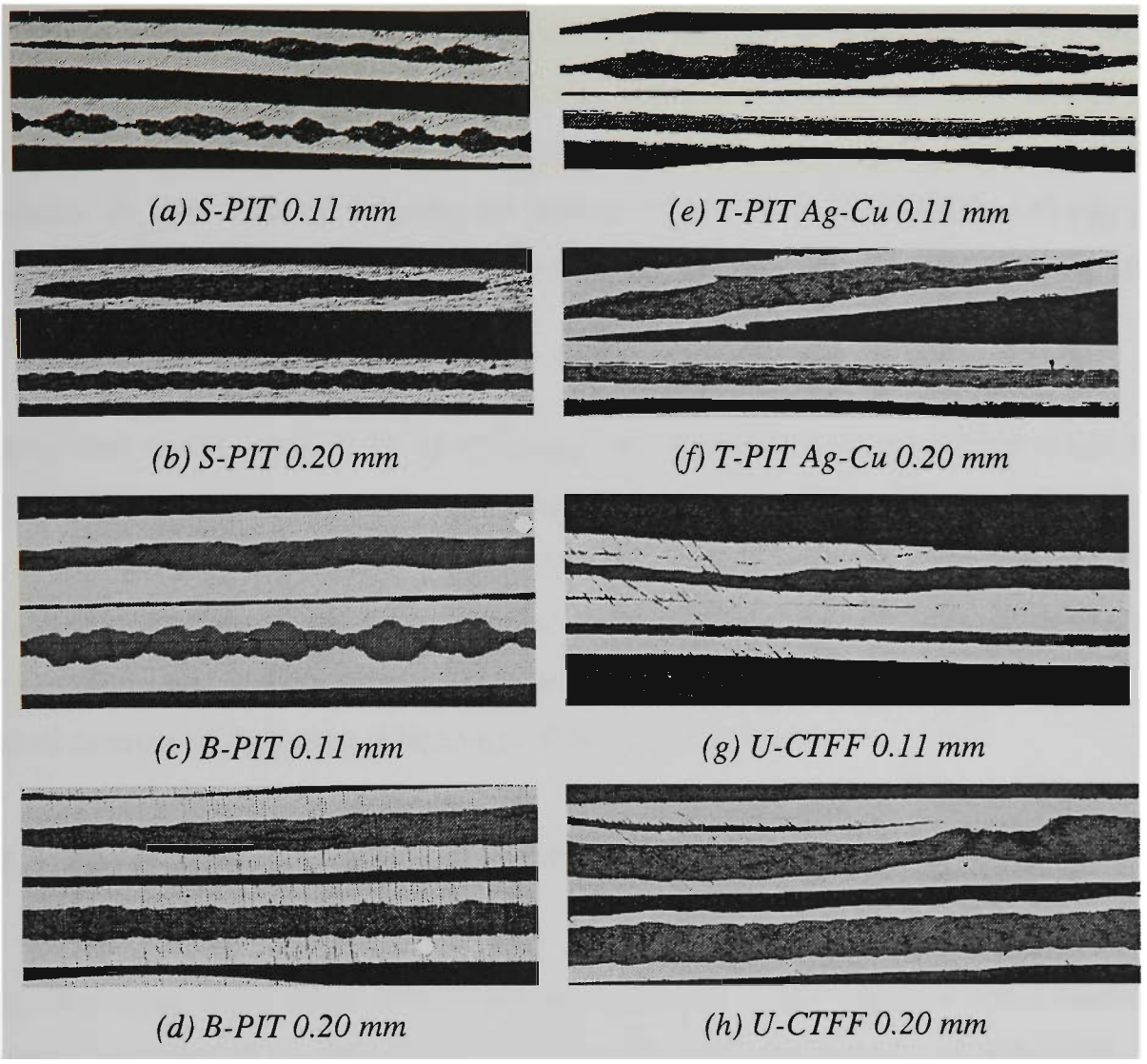

Figure 2.21 *Optical micrographs of transverse and longitudinal cross-sections of unreacted Bi(Pb)-2223 monocore tapes (prepared from powders S, T, B, and U) showing the onset of sausaging, occurs in tapes with cores approximately ≤ 40 μm thick, (a)-(d). Ag alloys such as Stirling silver was used to reduce the mismatch in mechanical strength between oxide and sheath, (e)-(f). The process of CTFF by-passes the bulk of mechanical drawing to fine wires giving in general more uniform and homogeneous structures of HTSC Bi(Pb)-2223 composite tapes, (g)-(h).*

On this same note, an equally important consideration is the determination of electrical resistivity and magnetoresistivity of the sheath material of HTS conductors to predict the stability and quench behaviour. Indeed, studies have been made by Dur *et al* [187] on

Mg doping (Ag-1.2 at%Mg) in Ag, showing an increase in reisistivity and a weak magnetic field dependence in these tape samples, possibly due to the inhomogeneity of Mg remnant in the silver lattice as well as the presence of MgO in the Ag-Mg sheath after heat treatment. In fact, even by reducing the content of Mg down to Ag-0.02 at.% Mg (as processed for a monocore and a 21-filament sample), the problem of oxidation of Mg after sintering still remained.

Getting back to the current topic of sausaging, an alternative remedy to this problem can also be found in the realm of mechanical processing (or controlled-deformation). A successful method in reducing the effect of bottle-necking is that of CTFF (refer to Fig. 2.21(g)-(h)), whereby much of the mechanical drawing of wires is by-passed, producing more uniform and homogeneous composite wires - with careful control in attaining the desired strength of Ag during prior to wire filling and forming.

2.1.3 Development of Bi(Pb)-2223 Coils and Magnets

In relation to the processing of long length Bi(Pb)-2223 composite tapes, the multifilamentary (MF) layout was chosen in recognition of the improved strain tolerance property over that of the monocore version [168]. Thus the majority of solenoidal and pancake-shaped coils produced have been wound with MF tapes of Bi(Pb)-2223. This section details the work conducted at CSEM on the production of coils and magnets following the React-Wind (R&W), and the Wind-React (W&R) procedures. The development of stacked single- (SP) and double-pancake (DP) coils is also discussed. Experimental details and characterizing of coils and magnets are given in section 2.2 and in chapter 4.

2.1.3.1 Coil fabrication

Depending on whether the method is W&R or R&W, the adopted approach in coil making is shown as a flow-chart in Fig. 2.22. For the W&R procedure, large furnaces (tubular and muffle) were used for the final sintering stage, with the coils normally placed alumina plate holders (pancakes) or supported by friable bricks (solenoids).

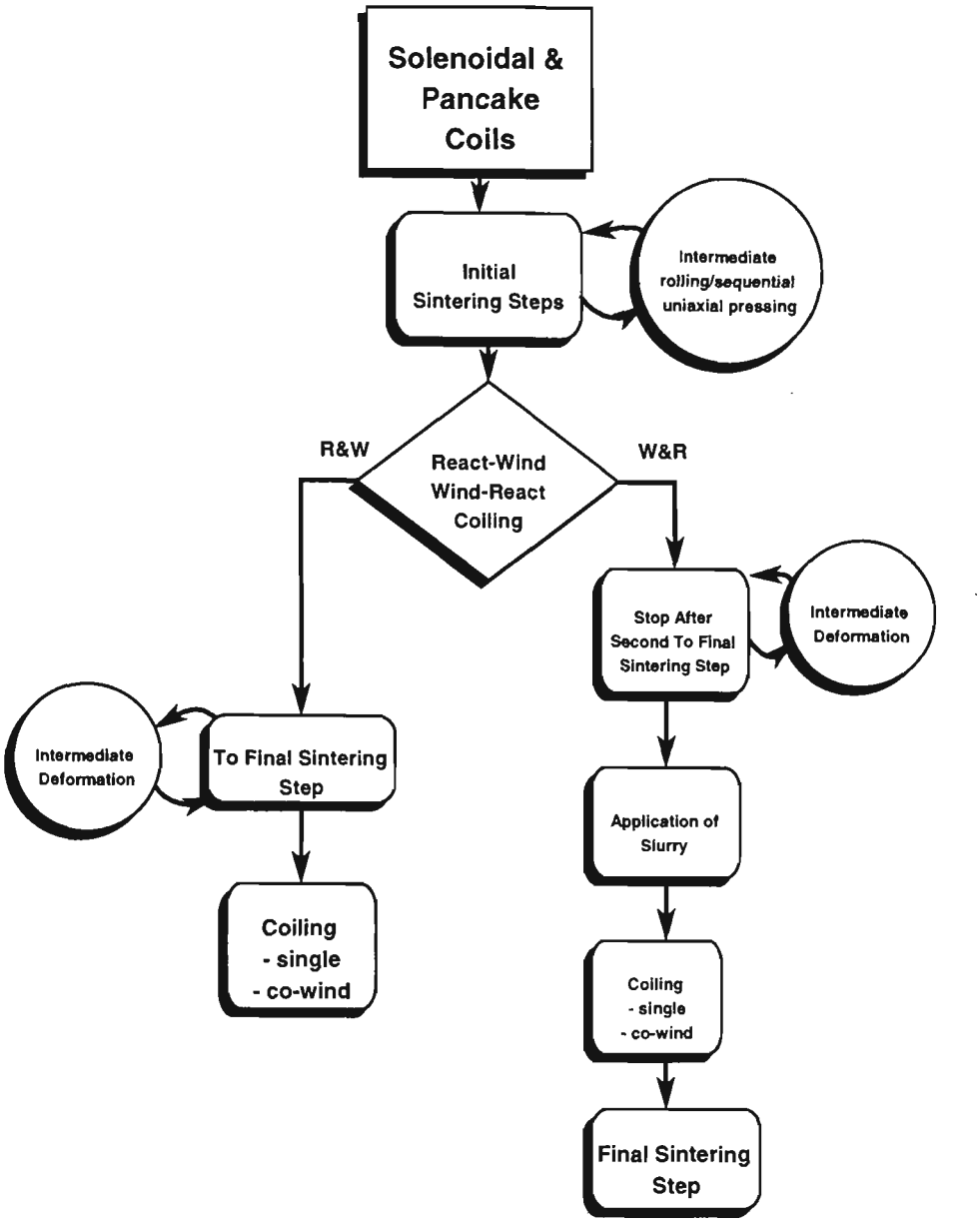

Figure 2.22 *Step-wise procedure for solenoidal and pancake-shaped coil production.*

Thick-wall alumina based hollow ceramic tubes (with small diameters) were used as formers in the production of solenoidal coils following the W&R procedure. These ceramic formers were selected because of their ability to withstand extreme temperature variation - during sintering (up to ~ 845^{0}C), and during LN and/or LHe testing. For the R&W method, materials such as high strength plastic, polypropylene, and copper (or

brass) were chosen to make formers. These insulated (prior to winding) metallic based formers offer high strength as well as the thermal ability to contract and expand (as do the composite tape) in conditions of changing temperature. The mean linear thermal expansion over a temperature range [131] for some selected materials are listed in Table 2.6.

TABLE 2.6 *Mean linear thermal expansion of some selected materials, [L(T) - L(293 K)]/L(293 K) in 10^{-3}.*

Material	*T [K]*			
	20	80	140	200
Aluminium[&]	-4.15	-3.91	-3.12	-2.01
Brass[#]	-3.69	-3.37	-2.60	-1.63
Copper	-3.24	-3.00	-2.34	-1.50
Silver	-4.09	-3.60	-2.70	-1.48
Epoxy	-11.5	-10.2	-8.99	-5.50
Teflon (TFE)	-21.1	-19.3	-16.6	-12.4
Solder[@]	---	-4.98	-3.65	-2.29

[#] 70Cu-30Zn, [@] 50Sn-50Pb.

[&] An Al bar 1-m long at 293 K shrinks by 4.15 mm when cooled to 20 K.

Unlike coils made from wires (the most suitable configuration for winding), coils produced from BPSCCO tapes are difficult to have their windings graded. Ideally, the conductor used for coil winding should be reduced gradually in size (cross-sectional area) in the outward radial direction according to its I_c vs. B characteristic curve. That is, since the magnetic field drops off radially away from the center of the coil, thinner wires or tapes can be utilized to carry the same critical current. This minimizes the use of material, and is cost effective [188].

Pancake coils both single and double were produced from winding partially (for W&R) or fully (for R&W) reacted composite tapes onto cylindrical tubes of a given diameter (such

as PVC conduits) which were often lubricated with vacuum grease or vaseline for later separation. The nylon-based double-grip hose clips (from *Adair Industrial Supplies, Australia*) were sometimes used as clamps on finished pancakes (as shown in Fig. 2.23), but normally not required when following the W&R procedure.

Figure 2.23 *Some of the solenoidal and pancake coils produced from Bi(Pb)-2223 composite tapes using the W&R and R&W procedures.*

The coils shown in Fig. 2.23 are numbered from left to right, top to bottom, with the details concerning powder type, processing procedure, filamentary configuration, dimensions, I_c, J_c, B_0 (central field), sintering treatment, and insulating materials used tabulated in Appendix C. Further details are given in Section 2.2.

Associated with the production of coils and magnets is the choice of insulating materials. The thermal properties of some are listed in Table 2.7. Those used in the R&W procedure include the teflon tape (polytetrafluoroethylene - PTFE) of ~ 0.03 mm in thickness (local hardware store), alumina paper (from *Morganite Insulating Products Pty. Ltd.*, NSW, Australia), and mylar tape (polyethylene) ~ 0.2 mm thick (courtesy of *Cadillac Plastic Australia*, NSW). It was found that teflon and mylar tapes were more suitable (better strength and easier to handle) for the R&W procedure. In case of the W&R procedure, alumina powder based slurries were used. These include the imported alumina based Aron

Ceramic D from *Toagosei Co. Ltd.*, Japan (with the average weighted mean (a.w.m.) of particle size distribution of ~ 37.7 μm - refer to Appendix D), and the 'home-made' version slurry created from fine (a.w.m. of ~ 0.1 and 1 μm size) alumina powders mixed in solution of sodium silicate ('water glass'). To reduce the viscosity and large particle size distribution of the slurry, fine powder of Al_2O_3 in aqueous solution was often added to the existing mixture to give a thinner coating layer (av. ~ 0.1 mm) when applied onto the surface of the tape prior to winding.

TABLE 2.7 *Thermal properties of some insulators.*

Material	Teflon Tape[*,^]	Mylar Tape[*,^]	Epoxy Resin[^]	Alumina Slurry[+]
Conductivity (W/cm-K)	~ 2.91×10^{-3}	~ 7.16×10^{-7}	~ 9.67×10^{-7}	~ 7.9×10^{-3}
Expansion Coeff. ($10^{-6}/^{0}C$)	~ 11.9	~ 0.3	~ 10.1	~ 8

[*] *A.R. Haines, Cadillac Plastics, NSW, Australia.* [^] *Modern Plastic Encyclopedia 1982-1983.*

[+] *Toagosei Co. Ltd., Japan.*

To minimize coil degradation through the frictional heat of a component motion, epoxy resin and acrylic resin were tested as potting materials. These were *Araldite* epoxy resin (LC191) mixed with hardener (HY956), using a ratio of ~ 4:1, resin to hardener (from *Ciba-Geigy Australia Ltd.*), and *Acryfix*, a fast curing acrylic resin from *Struers*, Copenhagen, Denmark, with pre-determined mixture of 2 parts liquid to 1 part solid (by volume). The notable cracking of these setting resins (in particular the *Araldite* epoxy) has indicated their unsuitability for cryogenic applications, as well as not being able to withstand the stress-induced motion from the test-coil structure when cooled down to 77 K. The thermal insulation from these potting materials was also a major concern since it could cause damage to the entire coil should a quench occur. Instead, the use of 'tight' construction techniques was adopted in conjunction with the use of an alumina based impregnant to eliminate conductor motion. Despite, this attempt, 'training' of some of the new constructed magnet systems were often encountered. Perhaps other impregnants such

as paraffin wax [189, 190], alcohol [191], and Wood's metal [192] would be a better choice - any material that has good thermal property, and hardens or solidifies as the magnet is cooled down to its operating temperature would make a good impregnant.

2.1.3.2 Magnet construction

The question of which type of joint is best suited for use in connecting superconducting composite tapes has been faced by every experimentalist who has embarked on the development of superconducting applications such as coils and magnets. A review on the various types of HTSC Bi(Pb)-2223 joints is given in section 1.3. In general, the fabrication of joints can be classified into 4 different splice types - butt, lap, scarf, and mortise [22], as defined in Fig. 2.24.

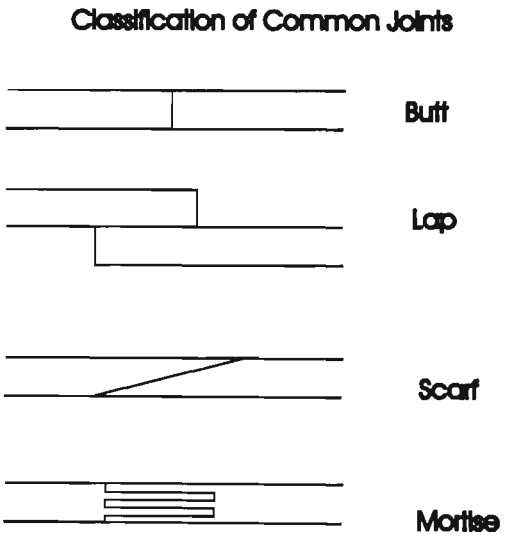

Figure 2.24 *Classification of common joints in increasing order of complexity. The scarf may be derived from the lap by subsequent external scarfing to a constant thickness across the joint.*

The adopted joint type for the construction of Bi(Pb)-2223 SP and DP coils and magnets has been the lap-splice, joined by the same superconducting tape used to wind the coils using solder of ordinary Sn-Pb (whose electrical resistivity varies with composition and is magnetic field dependent [193]), and pure indium (electrical resistivity ~ $8.37\times10^{-6}\Omega$/cm, at room temperature, in zero field [30]). It must be mentioned that since the solder used to

splice two broad surfaces of the conductors is often an alloy of tin and lead, the conductivity does not improve with decreasing temperature as do the conductivities of pure metals.

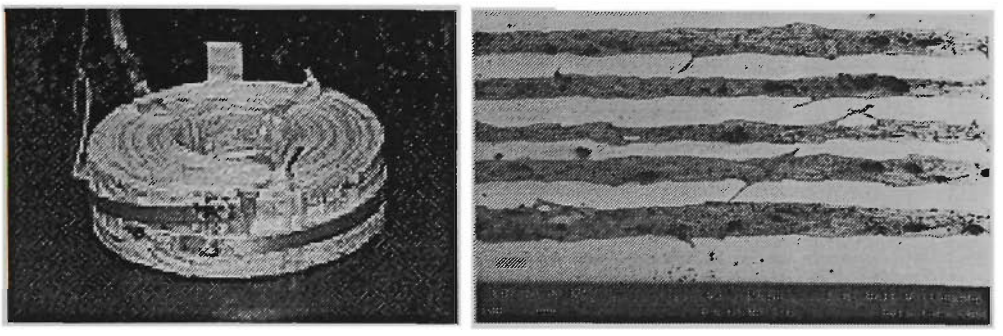

Figure 2.25 *The added use of a superconducting strap in the construction of two double-pancake coils, co-wound from two layers of 37 filamentary tape (SEM-QBSD image of cross-sectional areas on the right), produced from the method of PIT, powder type B, following the W&R procedure.*

Extra 'straps' were also incorporated as alternate current paths for diverting current between successive coils. These straps helped stabilize the magnet system mechanically and at the same time increased (slightly) the ampere-turns of the magnet. Figure 2.25 shows an example of a magnet system constructed from two DP coils with the use of a superconducting strap. The testing of this magnet system is given in chapter 4.

2.2 Characterization - Measurements, Standards and Criteria

Crucial to the development of Bi(Pb)-2223 composite tapes for magnet production is the understanding of their microstructural morphology and phase assemblage. To acquire this knowledge, it is necessary to conduct certain measurements and microstructural observations on these composite tapes. This section thus concentrates on the experimental details with some of the results obtained in characterizing the processed tapes together with the principles behind various equipments used.

2.2.1 Particle Size Analysis

The particle size analysis (PSA) was performed using the Malvern MasterSizer, from *Malvern Instruments Ltd.*, Worcestershire, U.K. This instrument uses the technique of laser light diffraction (more correctly called Low Angle Laser Light Scattering - LALLS) to measure the particle size distribution of a particulate material as dispersed in a liquid media [194]. Distilled water was used to disperse the material under analysis. The solution is pumped through a flow cell in such a manner as to present a thin (mono) layer of particles to a laser beam. The resultant distribution reported is a representation of the volume of material that is within the stated size class (up to 100 size classes in the range of 0.1 - 80 μm) expressed as a percentage. The data reported represents the diameter of a spherical particle which has the equivalent volume as that detected. The Malvern MasterSizer is shown in Fig. 2.26.

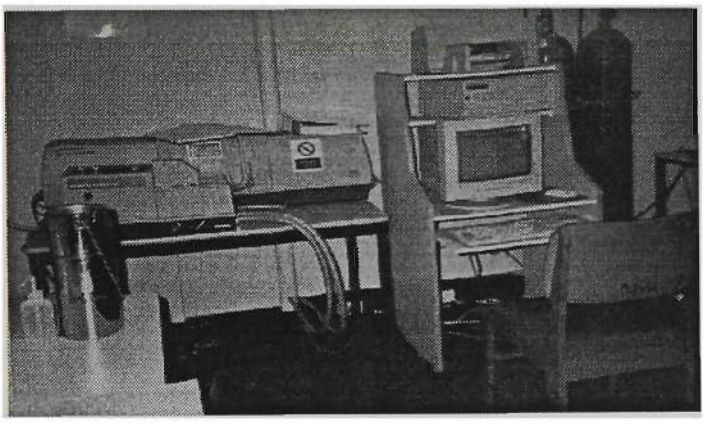

Figure 2.26 *The Malvern MasterSizer used in the determination of particle size characteristics for precursor powders and alumina based slurries.*

The statistics of the distribution of the analyzed powder particles are calculated from the raw result using the derived diameters $D[m,n]$ - an internationally agreed method of defining the mean and other moments of particle size [195]. The derived diameters are defined as:

$$D[m,n] = \left[\frac{\sum V_i d_i^{m-3}}{\sum V_i d_i^{n-3}} \right]^{\frac{1}{m-n}}, \qquad (2.1)$$

where V_i is the relative volume in class i with mean class diameter of d_i. m and n are integer values which describe the type of derived diameter, e.g. D[4,3], D[3,2], and D[1,0] are the volume weighted, surface weighted, and arithmetic mean diameters respectively. The cumulative volume under size percentiles for 10 %, 50 %, and 90 % of the total volume of all particles in the distribution are expressed respectively as $d[v,0.1]$, $d[v,0.5]$ (or median of the volume distribution), and $d[v,0.9]$. To give a quantitative description of the distribution, the *Span* (which describes the width of the distribution) and *Uniformity* (a measure of absolute deviations from the median) are defined as

$$Span = \frac{d(v,0.9) - (v,0.1)}{d(v,0.5)} \qquad (2.2)$$

and

$$Uniformity = \frac{\sum V_i \left| d(v,0.5) - d_i \right|}{d(v,0.5) \sum V_i}. \qquad (2.3)$$

The details of the PSA for five powder types, an Al_2O_3 based slurry, and a standard of fine alumina particles are tabulated in Table 2.8. Here it can be seen that the solid state reaction of dry-mixing (precursor powders of type D, and U) gives a slightly more uniform particle size in comparison with those prepared from a solution route (powders of type S, and B). Apart from the slow reaction rate, large agglomeration of particles often remain unsegregated when metal carbonates such as $CaCO_3$ and $SrCO_3$ are used as starting materials (as with powders of type T) in the solid state reaction technique. All Bi(Pb)-2223 powders shown to have comparable particle sizes with reasonable distribution spans, except for precursor powder of type B - perhaps as a result of bulk materials processing. In contrast to the oxide powders of Bi(Pb)-2223, the particle size characteristics obtained for an alumina based slurry showed large variation in particle size ranging from ~ 0.4 to over 100 μm (Table 2.8). The uniformity value for this slurry is nearly 2, with a volume

weighted mean of ~ 38 μm. The actual plots of distribution for each powder and slurry are included in Appendix D, together with that obtained for a standard using fine Al_2O_3 powder of 1 μm particle size.

TABLE 2.8 *Particle size characteristics of Bi(Pb)-2223 precursor powders, a selected alumina based slurry, and a standard of fine Al_2O_3 powder.*

Powder ID	S	T	D	U	B	Slurry	Standard*
D[4,3] (μm)	20.82	29.00	11.02	5.09	8.76	37.68	0.89
D[3,2] (μm)	8.40	12.20	8.00	3.54	4.23	1.32	0.45
$d[v,0.1]$ (μm)	3.72	5.97	4.59	1.87	2.14	0.38	0.22
$d[v,0.5]$ (μm)	16.13	21.80	9.59	4.63	5.84	17.52	0.58
$d[v,0.9]$ (μm)	45.33	60.60	19.61	8.96	20.75	104.18	1.98
Span	2.58	2.51	1.57	1.53	3.18	5.93	3.00
Uniformity	0.82	0.80	0.48	0.47	0.91	1.99	0.95

* *Fine Al_2O_3 powder of 1 μm in particle size.*

In general, to achieve a high degree of grain alignment in Bi(Pb)-2223 tapes, the oxide core of these tapes should be thin (~ 40-50 μm or less), which requires the initial powder to have a small particle size. As mentioned in section 2.1, tapes with ceramic cores ≤ 40 μm thick often exhibit sausaging. This phenomenon exists primarily due to the variation in mechanical attributes of the composite material being processed. Thus to reduce this variation, the powder should ideally contain a single phase so that each grain has the same mechanical properties and the powder deforms more uniformly. To give an indication of the J_c values obtained with various powders used, Fig. 2.27 shows roughly the highest J_c achieved, obtained with single- (SF) and multi-filamentary tapes (MT) using several processing techniques for the corresponding powders of Bi(Pb)-2223.

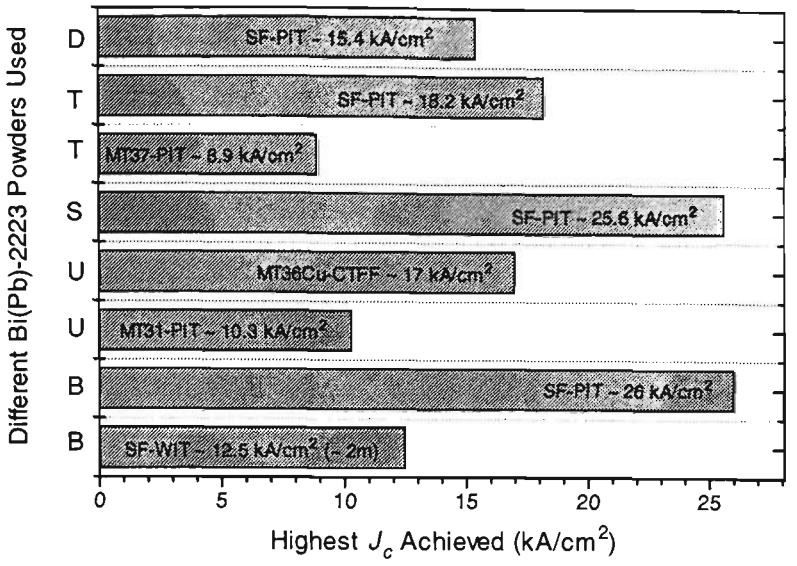

Figure 2.27 *Highest J_c values achieved, obtained with single- (SF) and multi-filamentary tapes (MT) using various processing techniques for the corresponding powders of Bi(Pb)-2223. (The S powder used at the time had a volume weighted mean diameter of ~ 5 μm).*

2.2.2 Microstructural Studies With SEM/EDS and OI

The scanning electron microscope (SEM) is one of the most versatile instruments available for the examination and analysis of the microstructural characteristics of solid objects. The primary reason for the SEM's usefulness is the high resolution which can be obtained when bulk objects are examined. The SEM system used for microstructural studies of specimens of Bi(Pb)-2223 was the *Leica Cambridge Stereoscan S440*, equipped with x-ray analytical capabilities. The topographic (typically in secondary electron or SE mode), crystallographic or atomic variation (best with backscattered electron or BSE mode) and compositional information can thus be obtained simultaneously from the same area of a given specimen. The basic components of the SEM are the lens system, electron gun, electron collector, visual and recording cathode ray tubes (CRTs) and the electronics associated with them. The setup of the *Leica S440* SEM with energy-dispersive spectrometer (EDS) is shown in Fig. 2.28. A detailed description on the operation of the SEM/EDS system can be found in *Scanning Electron Microscopy and X-ray*

Microanalysis, by Goldstein, *et al* [196]. For optical imaging (OI), the MD-20 optical image analyzer from the *Flinders University of South Australia* was used, also shown in Fig. 2.28.

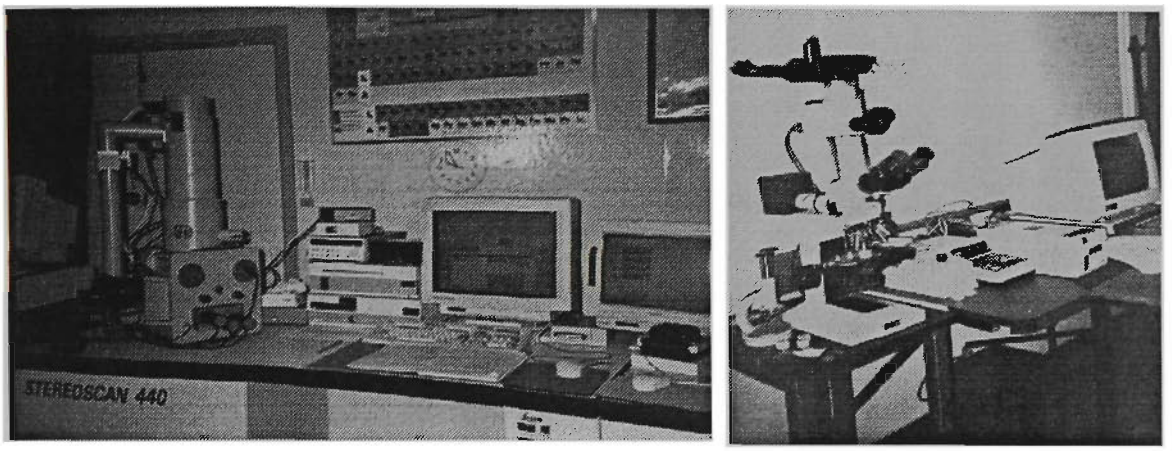

Figure 2.28 *The SEM setup (left) equipped with EDS Link System Detector. For optical imaging, the MD-20 optical image analyzer was used (right).*

The preparation of SEM specimens involved mounting ~ 5-10 mm long pieces of tape in epoxy resin mounts. The bottom surface (with the tape's cross section exposed) of the mount was then polished using the various grades of SiC grinding papers. The specimens were then polished on a 6-μm and a 1-μm diamond embedded pads (from *Struers*) for up to 20 minutes each, with a further final 0.06 μm finishing touch on a *Buehler* micro-cloth with colloidal silica used as a lubricant. The polished specimen was then glued onto an Al stub (holder). Prior to SEM examination, the polished specimens would normally be sputtered with gold or alternatively, amorphous carbon coated by vapour deposition if EDS analysis was to be performed, since the characteristic peaks of C are positioned well away (of lower energy) from those of the elements contained in Bi(Pb)-2223.

Powder S

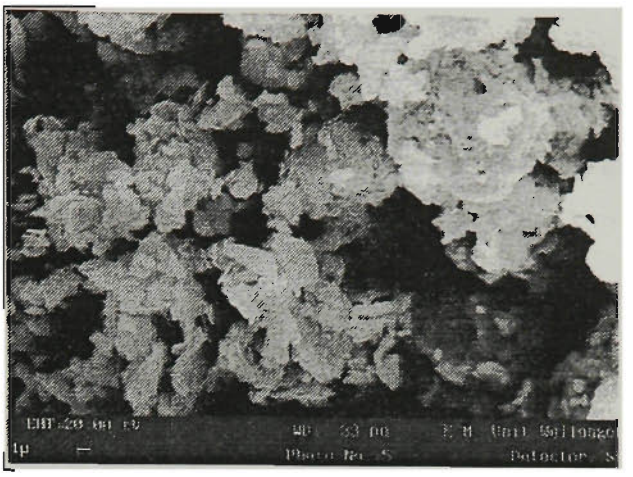

Powder T

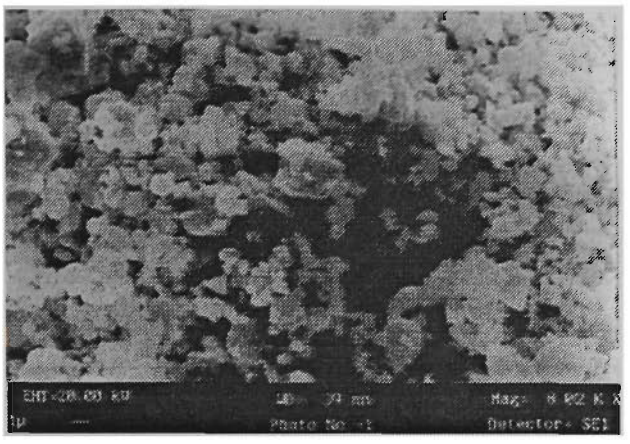

Powder D

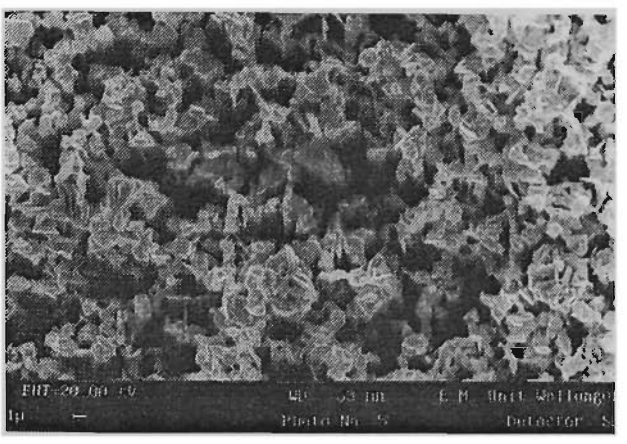

Powder B

Figure 2.29 *Secondary electron SEM micrographs of the unreacted precursor powders S, T, D, and B of Bi(Pb)-2223 used for the fabrication of the composite tapes.*

For initial powders of Bi(Pb)-2223, SEM specimen preparation involved sprinkling of some of the powder onto a thin layer of silver paste applied on the surface of the aluminium stub. The granulometric study performed using SEM has demonstrated that $CaCuO_2$ particles exhibited a size distribution with a majority of the particles below ~ 1 μm, but also showing the presence of larger aggregates, ranging from ~ 5 to 15 μm, depending on the powder type. The secondary electron (SE) images of the precursor powders of S, T, D, and B are shown in Fig. 2.29, agreeing well in particle size characteristics with the results obtained from PSA, as discussed previously. The appropriate morphology of the unreacted Bi(Pb)-2223 precursor powders observed in these SEM images show large aggregates of 2212 platelet

type grains, surrounded by smaller $CaCuO_2$ particles. The presence of smaller secondary phase particles such as $CaCuO_2$ and CuO not only enhanced the reaction kinetics for 2223 phase formation, but also improved their uniformity due to an increase in the contact surface between 2212 grains and secondary phases.

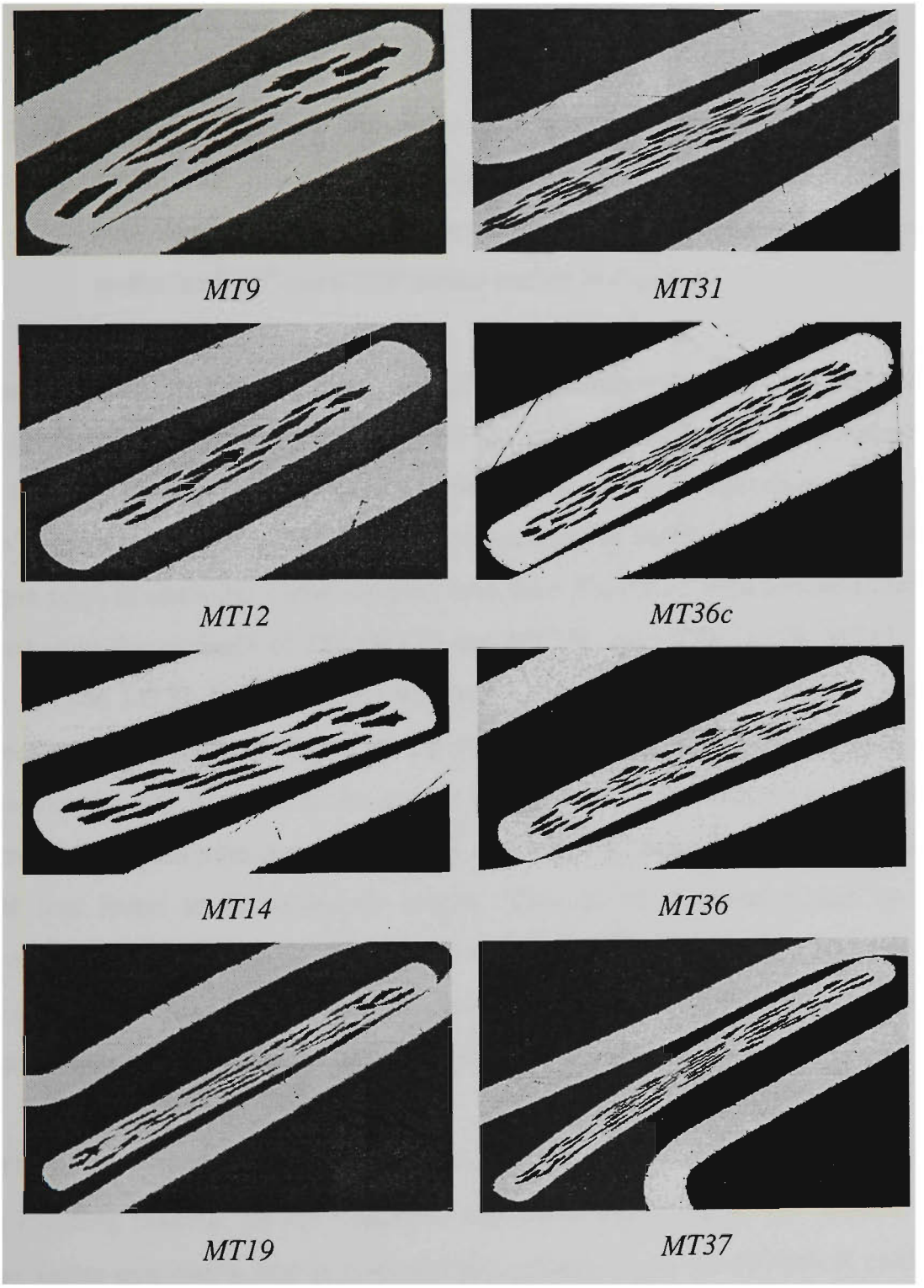

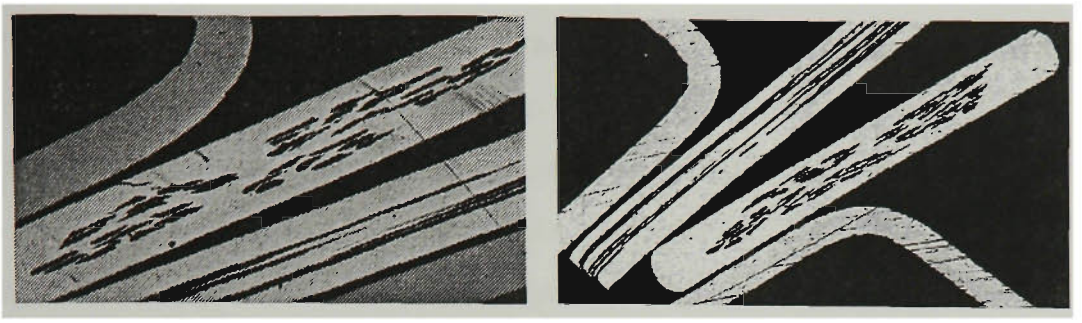

MT40 *MT50*

Figure 2.30 *Optical images of transverse and longitudinal cross-sections of Bi(Pb)-2223 composite green tapes prior to sintering. These samples have been flat-rolled from groove-rolled wires prepared using the methods of PIT and CTFF shown earlier in Fig. 2.10.*

The use of optical imaging includes calculating the transverse cross-sectional area of a composite tape for the determination of its fill factor, J_c, J_e, and for observational purposes on the spatial distribution and uniformity of the filaments. Figure 2.30 shows some optical images of the transverse and longitudinal cross-sections of Bi(Pb)-2223 unreacted (green) MF tapes prior to sintering. These samples have been flat-rolled from groove-rolled wires prepared from the methods of PIT (MT19 and MT31) and CTFF (MT9, MT12, MT14, MT36, MT36c, MT37, MT40, and MT50) shown earlier in Fig. 2.10. As can be seen from the cross-section of MT9 of Fig. 2.30, the filaments can sometimes be displaced during wire processing which results in an uneven distribution of the filaments throughout the composite tape. With pure Ag as a cladding material, the distribution of the filaments in general was found to be uniformly spaced. This spatial distribution can be further improved by the use of various alloys Ag. To arrange the position of the filaments closer to the edge and evenly across the tape for uniform cooling of the filaments, several tubes of various sizes would be needed for the preparation of wires.

For MT36c, the outer layer (or strand) matrix was that of Ag-Cu alloy, with pure Ag used as the cladding material for the filaments. The initial ideas behind this attempt were to achieve better uniformity, and to provide extra reinforcement in mechanical strength for the conductor, plus at the same time eliminate the possibility Cu reacting with the oxide

core at elevated temperature. As a result, the J_c was found to increase by two fold (cf. between MT36 and MT36c) as well as an improvement in strength (through Vickers microhardness tests) was achieved. These gains were not without their price of course. Added problems includes firstly, the formation of 'lobes' during tape processing whereby the filaments towards the center of the tape received the greatest amount of vertical strain causing those near the edges to bulge outwards (as can be seen with MT36c in Fig. 2.30). This was attributable to the added mismatch of mechanical property between Ag-Cu and Ag, and secondly, the oxidation of Cu at elevated temperature (identified with EDS on SEM image of MT36c, as shown in Fig. 2.31) which has been shown (in particular, for the oxidation of Mg) to increase the matrix's electrical resistivity [187], which in effect would have an adverse influence on the stability of the tape in terms of the matrix's thermal conductivity.

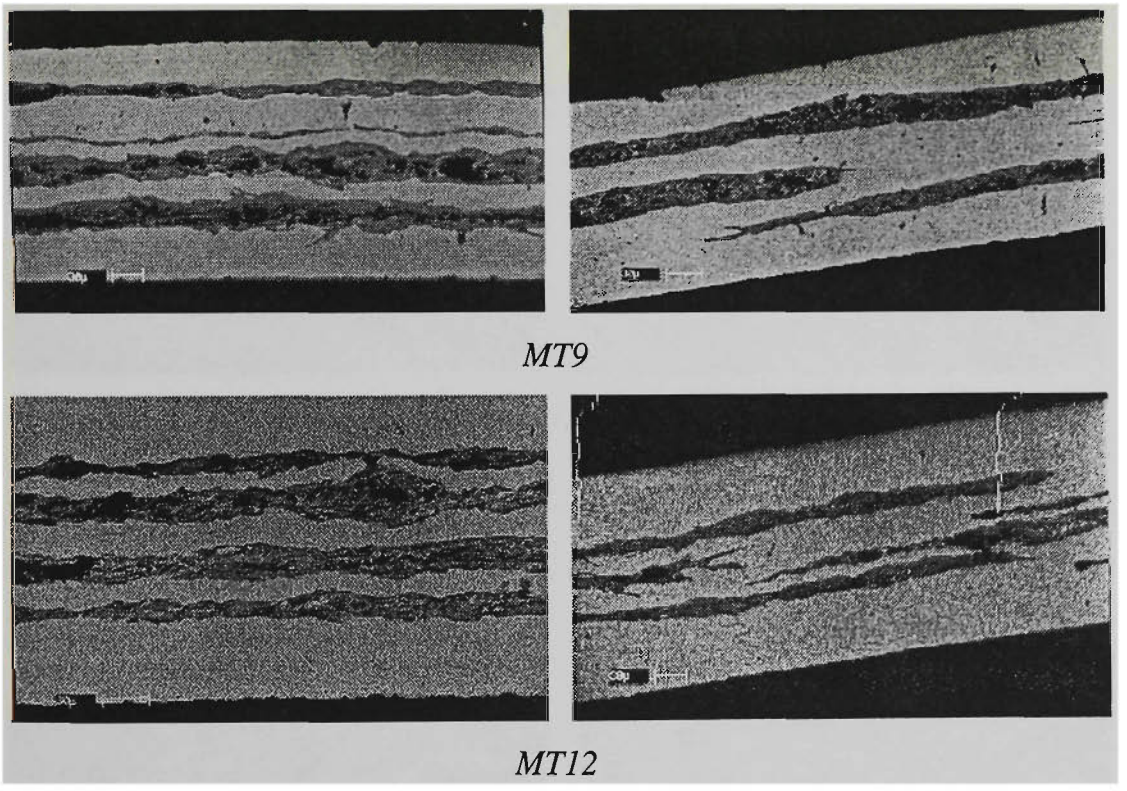

MT9

MT12

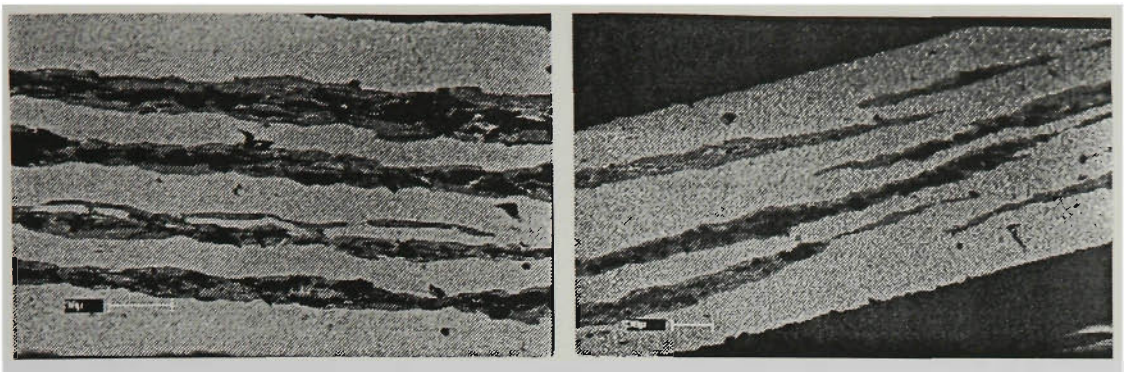

MT14

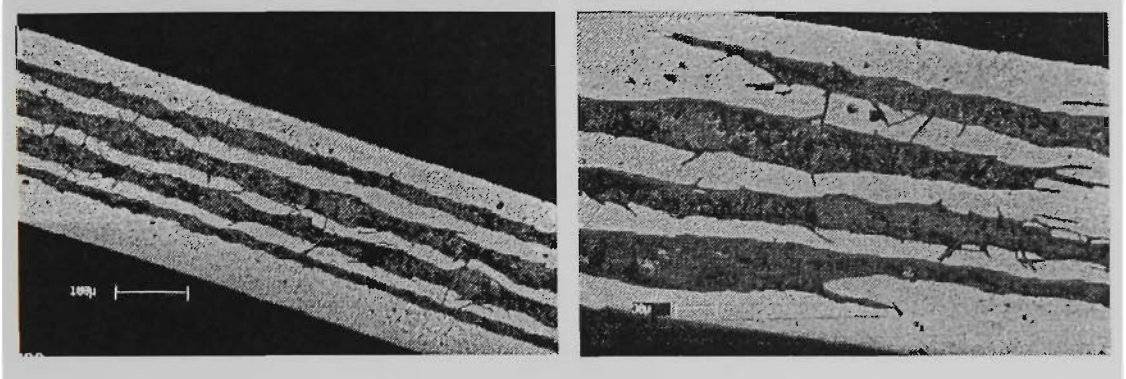

MT19

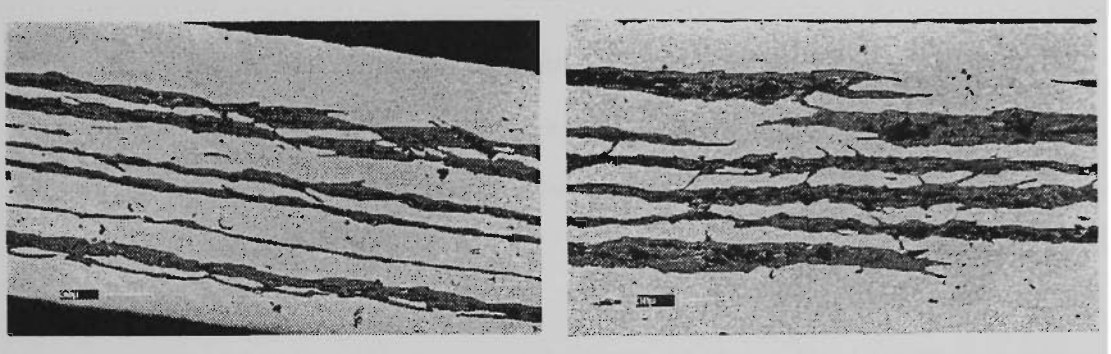

MT31

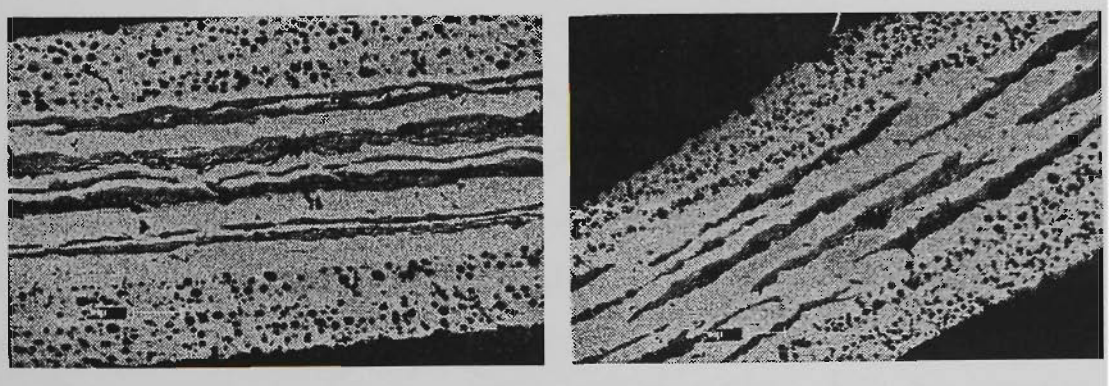

MT36c

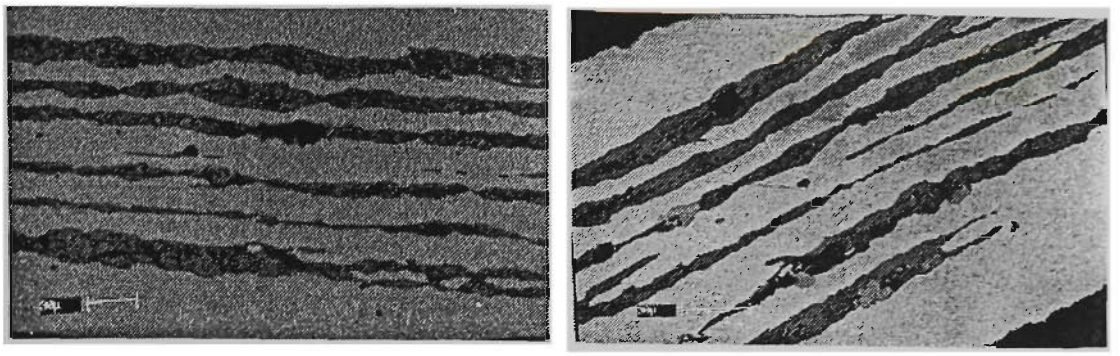

MT36

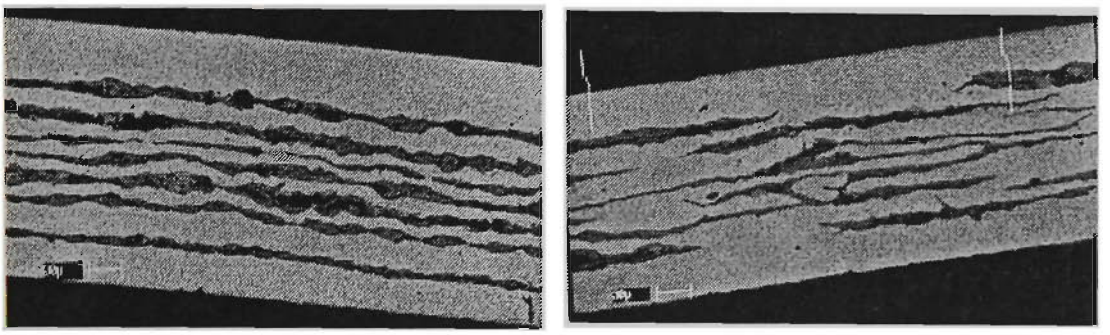

MT37

Figure 2.31 *Backscattered electron images of longitudinal (left column) and transverse (right column) cross-sections of Bi(Pb)-2223 composite red tapes obtained after the final sintering step, predecessors of those shown in Fig. 2.30.*

The backscattered electron images of the longitudinal (left column) and transverse (right column) cross-sections of Bi(Pb)-2223 composite PIT and CTFF red tapes obtained after the final sintering step shown in Fig. 2.31 are the predecessors of the wires shown in Fig. 2.10 and green tapes shown in Fig. 2.30. Apart from the problem of sausaging, prominent in filaments of thickness less than ~ 30 μm, the undesirable presence of the current-shunting needle-like intergrowth between filaments was often encountered. This inter-filamentary phenomenon is sometimes referred to as 'bridging'. The manifestation of bridging is demonstrated in samples MT19 and MT31 of Fig. 2.31. Nevertheless, good grain connectivity and alignment has generally been observed with increase in core density and texture following the final heat treatment. Most of the plate-like grains were observed to be well aligned longitudinally (along the tape length or rolling direction) parallel to the wide surface of tape. The high mass density and high degree of grain alignment in the silver-

clad tapes are believed to be responsible for the enhancement of J_c and J_c-magnetic field characteristic of these tape conductors.

The identification of different phases present was made from direct SEM observations supplemented with qualitative EDS microanalyses. Apart from the superconducting platelets of low- and high-T_c phases of 2212 (light grey) and 2223 (dark grey), large black regions with mixtures of oxides, $Ca_{1-x}Sr_xCuO_3$ (up to ~ 25 μm) were observed as well as the very fine plates of Ca_2PbO_4 (~ 0.1-0.3 μm thick) which cannot be seen directly with the contrast and magnification used in the microimages shown in Fig. 2.31. It is possible that these non-superconducting Ca-Cu-O phases consolidated into larger grains through sintering of the smaller $CaCuO_2$ grains which originally were part of the agglomeration present in the precursor powder. These black regions can be understood to have a negative effect on the tape's electrical as well as mechanical property, attributed to the low plasticity of these secondary phases, which tend to accumulate in specific areas of the core. As a consequence, these are the culprits in the diminishing of grain alignment of the superconducting phases during mechanical deformation, and are also the cause of multiple ruptures often found in the relatively softer and ductile silver sheath. At the same time, these large Ca-Cu-O phases can significantly inflict large transversal cracks during the bending operation of tapes.

2.2.3 Phase Assemblage Analysis with XRD

An understanding in the phase assemblage and reaction kinetics is of obvious importance for controlling the microstructure and hence achieving high current densities for the composite tape conductors. For this reason, X-ray diffraction (XRD) patterns were obtained from prepared samples of powder and tape for phase identification. For tape specimens, typical samples of ~ 5 mm × 5 mm exposed surfaces of reacted oxide cut from tapes were used. A razor blade or scalpel was used to split the surface of a small section of tape open after trimming off the edges, then with tweezers to peel off the sheath, and finally with a glass slide to gently flatten the fractured surface. A rectangular cavity at the

centre of a flat perspex sample holder was used for positioning the fractured tape sample as well as for containing the powder specimens for the duration the scan.

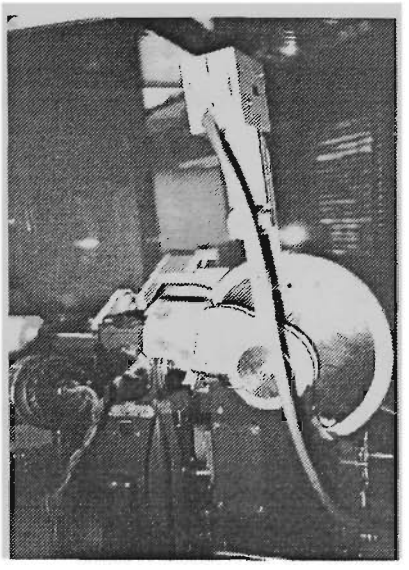

Figure 2.32 *X-ray diffraction measurements using the PW1730 Philips vertical diffractometer, with Cu-Kα radiation.*

All XRD patterns were taken at room temperature using the PW1730 Philips vertical diffractometer (Fig. 2.32) with counter monochromatized Cu-$K\alpha$ radiation (from a Cu tube), of wavelength ~ 1.5406 Å, through a Ni filter in the reflecting geometry. The voltage and current settings were set at 40 kV and 20 mA, respectively. All samples were examined over the angle range of $2\theta = 3°$ to 70°, which covers the major characteristic reflections for all superconducting phases in the Bi-Pb-Sr-Ca-Cu-O system. The scanning speed and incremental step-size used were $2\theta = 1°$/min. and 0.02°, respectively.

The identification of the phase assemblage in XRD patterns was made based on the pre-defined [197] high- and low-T_c peaks listed as relative intensities in Table 2.9, with corresponding 2θ, observed d-spacings, and lattice spacing reflection indices, (hkl). These high- and low-T_c peaks are plotted in Fig. 2.33. The secondary phases, referred here to 2201 (which can either be superconducting or non-superconducting), CuO, Ca_2PbO_4, and Ca_2CuO_3 are plotted in Fig.2.34.

TABLE 2.9 *Powder X-ray diffraction data for Bi-Pb-Sr-Ca-Cu-O superconductor.*

2θ (^{0})	d_{obs} (Å)	$(hkl)^*$	$(hkl)^\wedge$	I/I_0	2θ (^{0})	d_{obs} (Å)	$(hkl)^*$	$(hkl)^\wedge$	I/I_0
4.86	18.167	(002)		28	44.66	2.027	(0018)		66
5.78	15.278		(002)	26	44.86	2.018		(2010)	41
17.62	5.029		(006)	17	45.14	2.006		(1113)	32
23.16	3.837		(008)	73	47.32	1.919		(220)	39
24.00	3.707	(113)		38	47.62	1.908	(222)		54
24.83	3.573		(113)	30	48.08	1.891	(2014)		37
26.06	3.401	(115)		29	48.56	1.873		(0212)	30
27.70	3.240		(115)	82	50.58	1.803		(1115)	57
29.68	3.074	(0012)	(0010)	100	56.36	1.631	(0218)	(1117)	39
31.01	2.878		(117)	94	56.74	1.621		2210)	34
31.86	2.808	(119)		45	57.46	1.602		(137)	30
33.18	2.701	(200)	(200)	87	57.74	1.595	(1121)		29
33.80	2.652		(202)	45	57.96	1.589	(139)		37
34.28	2.616	(0014)		26	58.38	1.580	(319)		30
34.58	2.593	(204)		26	59.48	1.553	(2214)	(2016)	37
35.06	2.560		(0012)	79	60.24	1.535		(139)	42
35.44	2.532	(1111)	(204)	54	60.64	1.526		(2212)	40

* *2223,* $^\wedge$ *2212.*

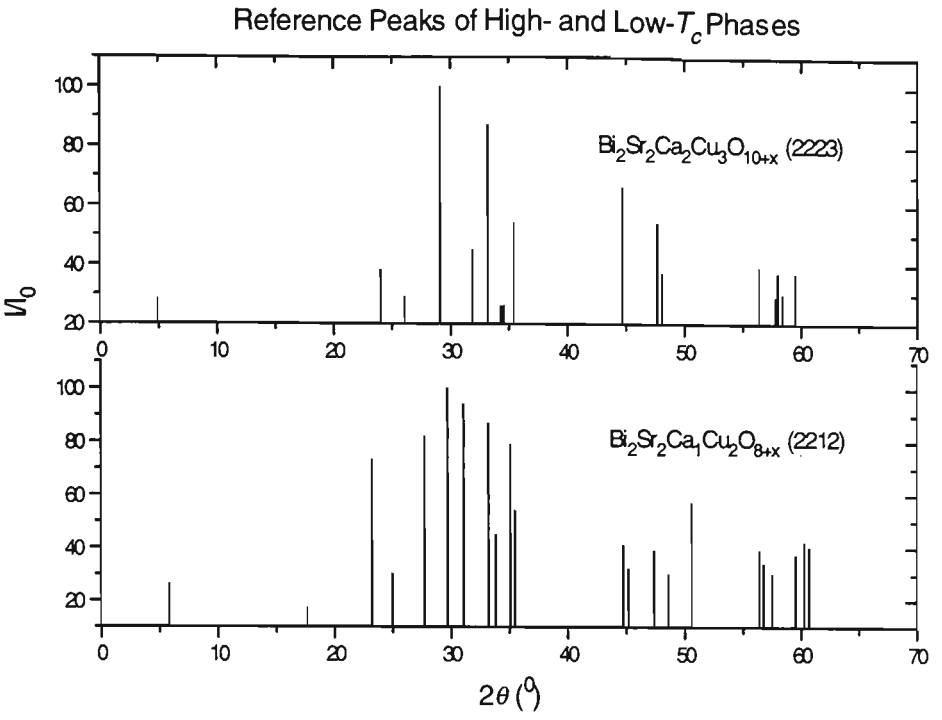

Figure 2.33 *XRD reference peaks of the high- (2223) and low-T_c (2212) phases.*

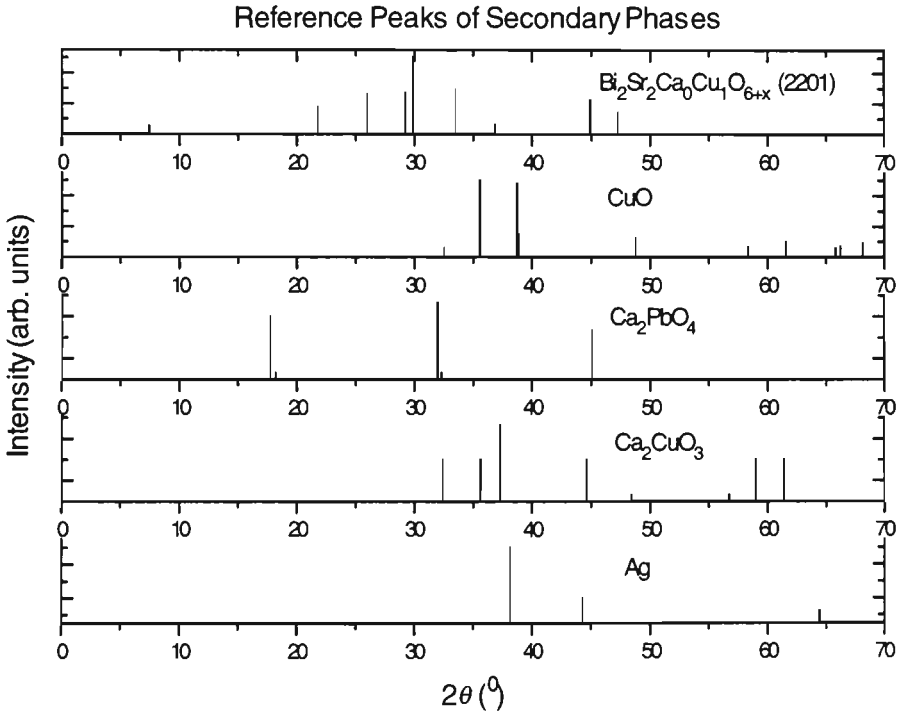

Figure 2.34 *XRD reference peaks of the secondary phases of to 2201, CuO, Ca_2PbO_4, and Ca_2CuO_3, and also those of pure Ag is shown.*

The enhancement of 2223 grains has generally been reported [198-200] to take place with the aid of a partial melting liquid phase in the presence of the secondary phases of 2201, Ca_2PbO_4, CuO, and Ca_2CuO_3 and that precipitation from this melting phase occurs. The 2223 phase is formed through 2201 and 2212 phase transition according to the following chemical reactions [201]:

$$Bi_2Sr_2CuO_5 + \frac{1}{2}Ca_2CuO_3 + \frac{1}{2}CuO \longrightarrow Bi_2Sr_2CaCu_2O_7 \tag{2.4}$$

$$Bi_2Sr_2CaCu_2O_7 + \frac{1}{2}Ca_2CuO_3 + \frac{1}{2}CuO \longrightarrow Bi_2Sr_2Ca_2Cu_3O_7 \tag{2.5}$$

for the unleaded Bi-Sr-Ca-Cu-O system, and

$$Bi_2Sr_2CuO_5 + \frac{1}{2}Ca_2PbO_4 + CuO \longrightarrow (Bi,Pb)_2Sr_2CaCu_2O_{8+x} \tag{2.6}$$

$$(Bi,Pb)_2Sr_2CaCu_2O_{8+x} + \frac{1}{2}Ca_2PbO_4 + CuO \longrightarrow (Bi,Pb)_2Sr_2Ca_2Cu_3O_{10+x} \tag{2.7}$$

for the leaded Bi-Sr-Ca-Cu-O system. Hatano *et al* has also shown that the precipitation of the impurity (i.e. secondary and minor) phases at the grain boundaries of 2223 is inevitable during the cooling process, which is a disadvantage for producing a material with superior superconducting properties. He suggested the use of non-equilibrium synthesis processes to improve the J_c in the Bi-Pb-Sr-Ca-Cu-O system.

Thus to facilitate liquid phase formation in the subsequent sintering processes it was necessary for the precursor powder to have 2212 as the major phase [202, 203]. Fig. 2.35 shows the XRD patterns of partially reacted precursor powders designated S, T and D with 2212 as the major phase and Ca_2PbO_4, Sr-Ca-Cu-O, and 2223 as the minor phases. All precursor powders had the same stoichiometric composition prior to OPIT. The synthesis description has been given in section 2.1.1.

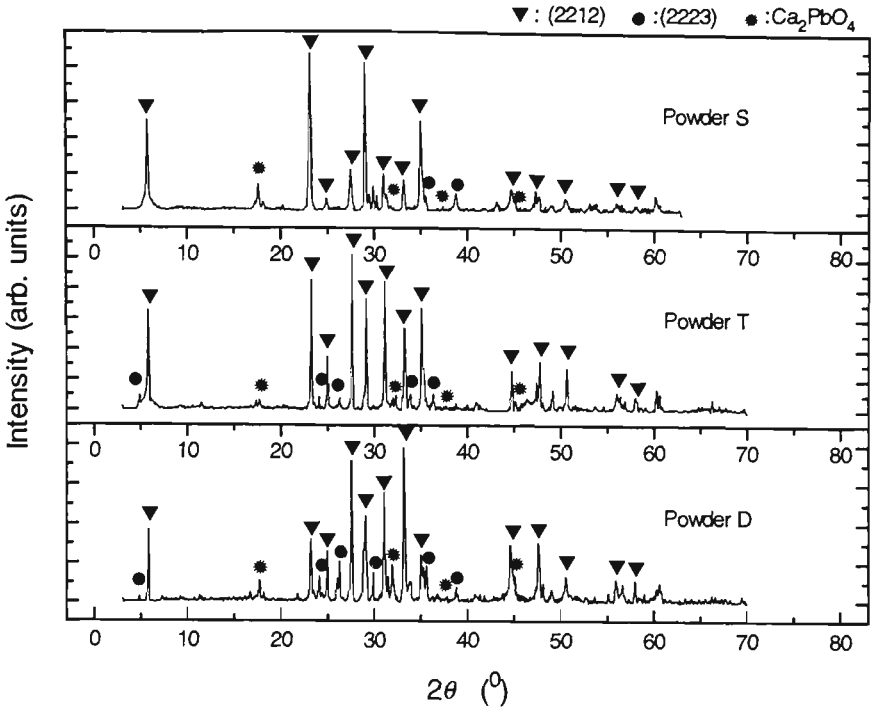

Figure 2.35 *XRD patterns for the partially reacted powders S, T, and D showing the major phase (2212) and minor phases (2223 and Ca_2PbO_4).*

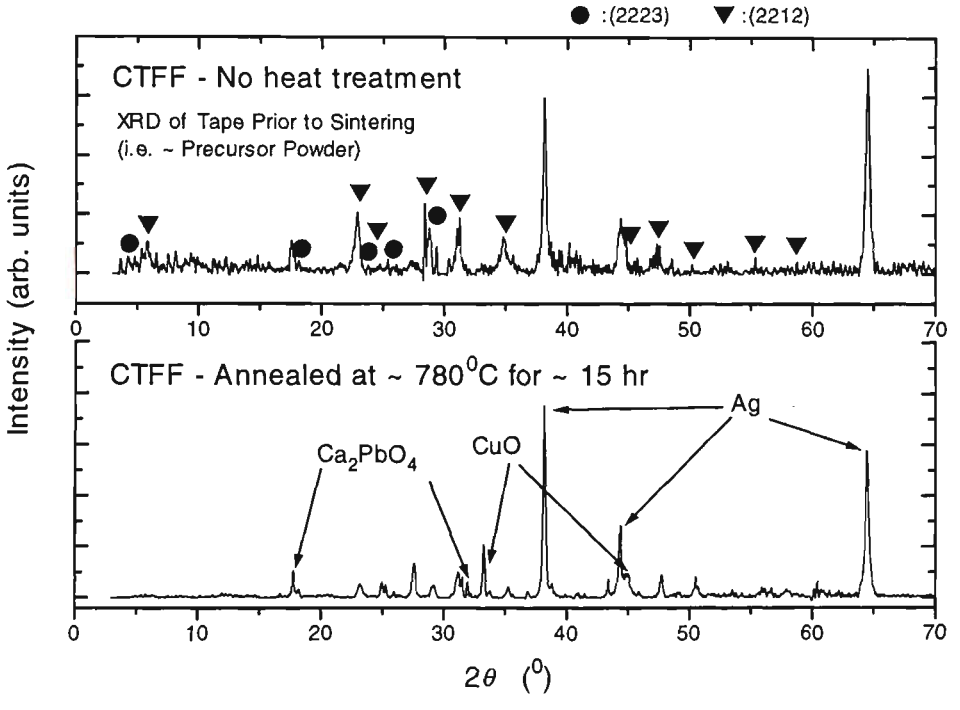

Figure 2.36 *XRD patterns of untreated and partially annealed CTFF tapes showing 2212 as the major phase with minor traces of Ca_2PbO_4, CuO and 2223.*

Similarly, XRD patterns for an untreated and partially annealed (at ~ 780^0C for ~ 15 h) CTFF tapes, given in Fig. 2.36 also reveal a major phase of 2212 with minor traces of Ca_2PbO_4, CuO and 2223. The XRD pattern of the untreated CTFF tape is equivalent to that obtained for the precursor powder itself since no heat treatment was carried out during tape processing. For the annealed CTFF tape, a slight reduction in the 2212 and secondary phases are apparent from Fig. 2.36.

In order to decide how much intermediate deformation should be applied and the extent of the following sintering period on a partially reacted composite tape, XRD data were often obtained to determine the compositional phase change. It must be pointed out that all the XRD data presented are only a representative of the superconducting region close to the BPSCCO-matrix interface. The stated percentages calculated from XRD intensity peaks are approximations only. These values are normally interpreted with the assistance of other analytical tools such as SEM and DTA/TG, etc., since the effective penetration depth for the Cu radiation (~ 8.04 keV) into the ceramic core is only ~ 3-4 μm [204, 205].

Figures 2.37 and 2.38 show successive XRD patterns belonging to short tape samples obtained from long lengths of 31-filamentary tape prepared with precursor powder U. The XRD information was obtained for each short sample after each sintering period with different duration to study the compositional change of phase. From inspection of the XRD patterns, the high-T_c phase of 2223 can be seen to generally increase with repeated cycles of intermediate deformation (cold-rolling) and sintering, and at the same time a reduction in secondary phases (estimated to be less than ~ 4 %). A notable fluctuation in the 2212 phase can also be observed at 2θ ~ 23.20^0 (or (008) reflection) in Fig. 2.38, possibly due to the displacement and exposure of the 2212 grains as a result of intermediate mechanical deformation. This is consistent with the fact that the (0010) and (0014) peak intensities increase with the amount of cold rolling reduction as reported by Yoo *et al* [206].

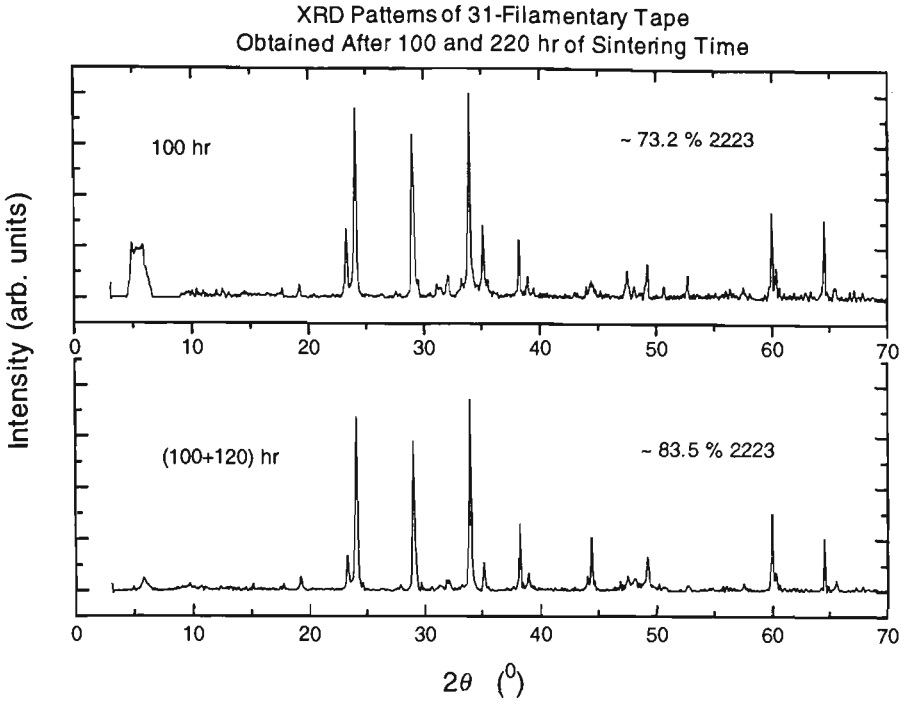

Figure 2.37 *XRD patterns obtained after 100 and 220 hr of sintering time for a 31-filamentary tape prepared using powder U.*

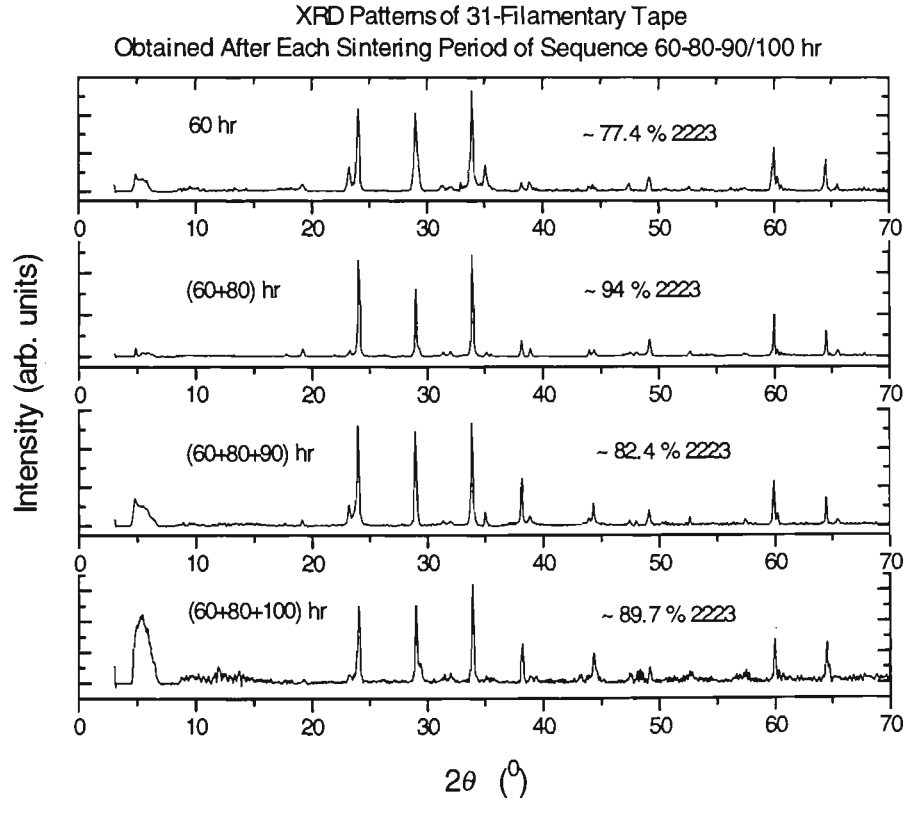

Figure 2.38 *XRD patterns obtained after 60, 140, 230/240 hr of sintering time for a 31-filamentary tape prepared using powder U.*

The fraction of 2223 calculated so far (and subsequently) has been estimated from the expression: $I_{r1}/(I_{r1} + I_{r2})$, where I_{r1}, and I_{r2} representing the relative intensities of the (0010) (at $2\theta \sim 23.92^0$) , and (1110) (or (008), at 2θ of $\sim 23.20^0$) reflections for the 2223 and 2212 phases respectively. Figures 2.37 and 2.38 have demonstrated that it is possible to achieve a significantly pure single-phase of 2223 (~ 94 %) within approximately 140 hr of sintering time following a two-sinter process each with a sintering period of ~ 60-80 hr in duration for tapes prepared using powder U. The sintering temperature used was ~ 832 ± 1 ^{0}C. The results were later found to be the same for the other precursor powders, with the use of a slightly modified sintering schedule for the second sintering period.

Texturing evaluation of composite tape samples was determined based on a simple method introduced by Lotgering [207, 181, 208] by making use of the results obtained from XRD analysis. Since the ratio of the intensities of the (00*l*) and (*hkl*) reflections increases with the improving *c*-axis orientation, the extent of texturing of the superconducting ceramics can therefore be quantified. The Lotgering factor *F*, indicating the degree of grain orientation, is defined as:

$$F = \frac{(P - P_0)}{(1 - P_0)} \tag{2.8}$$

where

$$P = \frac{\sum_{l} I_{(00l)}}{\sum_{hkl} I_{(hkl)}}, \tag{2.9}$$

I refers to the X-ray peak intensities. *P* is the sum of integrated intensities for all (00*l*) reflections divided by the sum of all intensities of (*hkl*) in the textured sample. P_0 is an equivalent parameter for the randomly oriented powder sample. For a perfect alignment and complete texture, such as for a single crystal, *F* would be unity.

TABLE 2.10 *XRD data for the randomly oriented Bi(Pb)-2223 powder B.* $\Sigma(00l) = 305$, $\Sigma(hkl) = 630$, $P_0 = 0.484$.

(*hkl*)	2θ (^{0})	d_{obs} (Å)	I/I_0 (%)	(*hkl*)	2θ (^{0})	d_{obs} (Å)	I/I_0 (%)
(002)	4.96	16.002	57	(10$\underline{1}$0)	29.02	3.074	46
(004)	9.476	9.401	6	(119)	32.18	2.779	20
(103)	18.14	4.886	6	(200)	33.18	2.698	100
(008)	19.10	4.643	5	(00$\underline{1}$4)	33.88	2.644	37
(00$\underline{1}$0)	24.04	3.699	60	(11$\underline{1}$1)	35.56	2.523	22
(113)	24.38	3.648	21	(20$\underline{1}$2)	44.64	2.028	37
(115)	26.24	3.393	62	(220)	47.30	1.920	38
(00$\underline{1}$2)	27.52	3.238	98	(11$\underline{1}$7)	48.20	1.880	5

TABLE 2.11 *XRD data for the sintered SF Bi(Pb)-2223 tape of powder B.* $\Sigma(00l) = 277$, $\Sigma(hkl) = 315$, $P = 0.879$, $F = 0.766$.

(*hkl*)	2θ (^{0})	d_{obs} (Å)	I/I_0 (%)	(*hkl*)	2θ (^{0})	d_{obs} (Å)	I/I_0 (%)
(002)	4.90	16.046	12	(00$\underline{1}$4)	33.88	2.644	97
(103)	17.66	5.018	14	(11$\underline{1}$1)	35.56	2.523	12
(008)	19.10	4.643	2	(00$\underline{1}$6)	38.78	2.320	10
(00$\underline{1}$0)	24.04	3.699	81	(20$\underline{1}$2)	44.04	2.054	6
(115)	26.24	3.393	6	(11$\underline{1}$7)	48.21	1.689	15
(00$\underline{1}$2)	28.82	3.095	43	(00$\underline{2}$0)	49.04	1.857	13
(119)	31.90	2.803	4				

Tables 2.10 and 2.11 lists respectively the XRD data obtained for the randomly oriented Bi(Pb)-2223 powder B and the subsequent SF tape (initial thickness ~ 0.1 mm), with a J_c of ~ 21.5 kA/cm^2 at 77 K, 0 T, processed using a two-sinter procedure with uni-axial pressing as the intermediate deformation. By using eqns (2.8) and (2.9), P_0, P and hence F were calculated to be 0.484, 0.879, and 0.766 respectively.

The effect of rate of uni-axial loading was also examined in order to understand how it affects the development of the 2223 phase. SF tapes of initial thickness of ~ 0.175 mm, prepared using powder D, were uni-axially pressed at two different loading rates (viz. fast -> 150-155 rpm, and slow -> 50-60 rpm of motor speed) on the '*Mand* 15 Ton' pressing machine (shown in Fig. 2.13, section 2.1.2.2) in between sintering periods each of 60 hr duration. The applied vertical force was ~ 90 kN for each intermediate loading operation and the same for both rates. This force corresponded to a uni-axial pressure of ~ 1 GPa. Table 2.12 lists the J_c measured (in LN, and self field) after each sintering period for the two different rates.

TABLE 2.12 *Critical current densities of SF tapes processed with different intermediate uni-axial pressing rates.*

90 kN Uni-axial Force	J_c (kA/cm^2) after 60 hr	J_c (kA/cm^2) after 60×2 hr	J_c (kA/cm^2) after 60×3 hr
Fast pressing rate	3.28	7.13	11.05
Slow pressing rate	2.43	9.05	15.02

The XRD patterns obtained after 60×3 hr of sintering time for the two rates are shown in Fig. 2.39. From these patterns two contrasting features can be seen. They are: 1) the prevailing traces of secondary phases, and 2) a significant amount of 2212 phase still remain (notable at the (008) intensity peak) after 180 hr of sintering time in the sample intermediately pressed with a fast rate. In short, the results from both J_c measurements and XRD analysis have conclusively shown that the uni-axial force should be loaded slowly to avoid excess fracturing of the elastically stiff 2223 grains as a result of textural hardening.

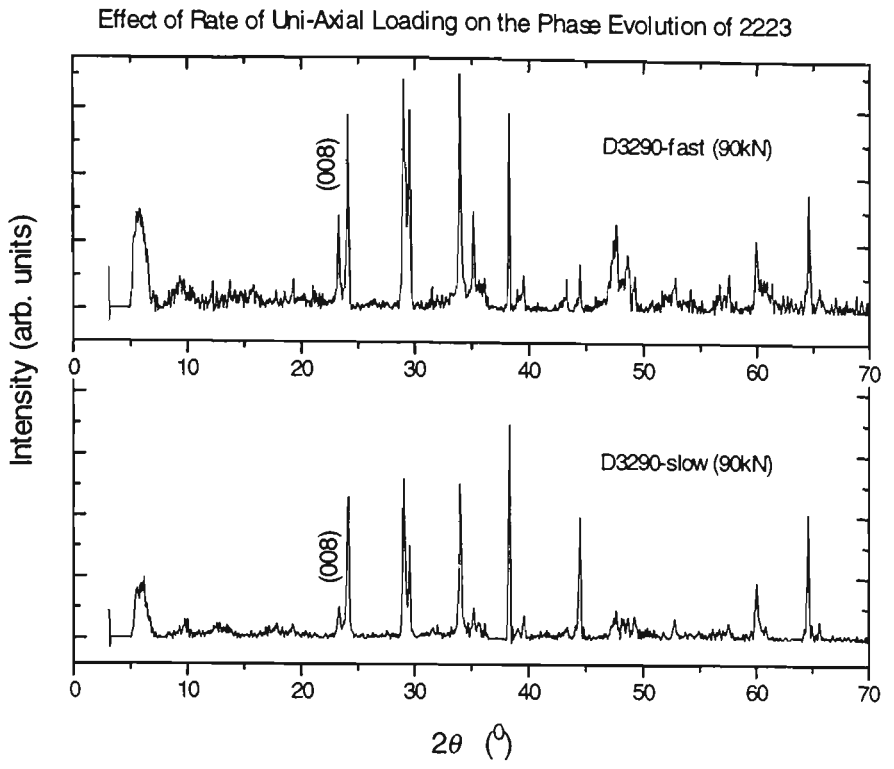

Figure 2.39 *The effect of rate of uni-axial loading on the development of the 2223 phase in SF tapes prepared from powder D.*

2.2.4 Reaction Kinetics with DTA/TG

To obtain information concerning the events which occur during the sintering of Bi(Pb)-2223 composite tapes, differential thermal analysis (DTA) and thermo-gravimetric (TG) measurements were conducted on green tapes samples as well as precursor powders in ambient air atmosphere. The DTA/TG measurements were performed in a SETARAM thermal analyser (imported from France) using Al_2O_3 as reference, with a heating rate of 10 ^{0}C/min, reaching ~ 1100^{0}C from room temperature. The setup of the equipment is shown in Fig. 2.40.

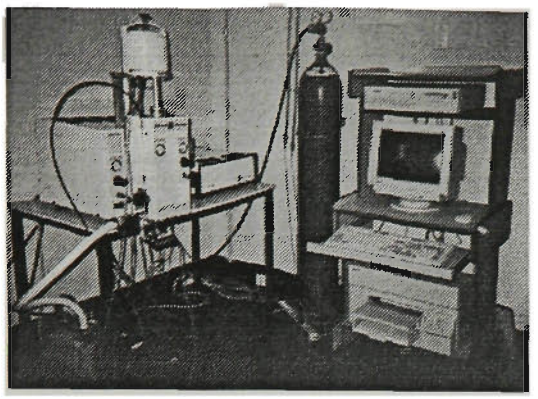

Figure 2.40 *The SETARAM thermal analyzer setup.*

The initial parameters used for each measurement, the onset temperature of melting (T_m) and sintering temperature (T_s) obtained from the DTA curves (Fig. 2.41 and 2.42) are listed in Table 2.13. The onset temperature was determined from the intersection of the negative slope tangent and the line joining two chosen points on the DTA curve.

TABLE 2.13 *DTA/TG parameters used with onset and hence chosen sintering temperatures obtained for powders and composites of Bi(Pb)-2223.*

Sample ID*	S	T	D	U	B	S_tape	CTFF
Sample mass (mg)	44	60	50	50	58	36	52
Expt. Duration (min)	96	96	96	96	96	96	96
Atmosphere	air	air	air	air	air	air	air
Crucible type	Al_2O_3	Al_2O_3	Al_2O_3	Al_2O_3	Al_2O_3	Al_2O_3	Al_2O_3
Max. temp. (^{0}C)	1000	1000	1000	1000	1100	1100	1100
Heating rate (^{0}C/min)	10	10	10	10	10	10	10
Melting onset (^{0}C)	877	860	862	842	848	837	833
Sintering temp.# (^{0}C)	834	838	832	832	841	--	--

* *S, T, D, U, and B designate the precursor powder type. CTFF represents the untreated CTFF wire.*

\# $\pm 1^0$C.

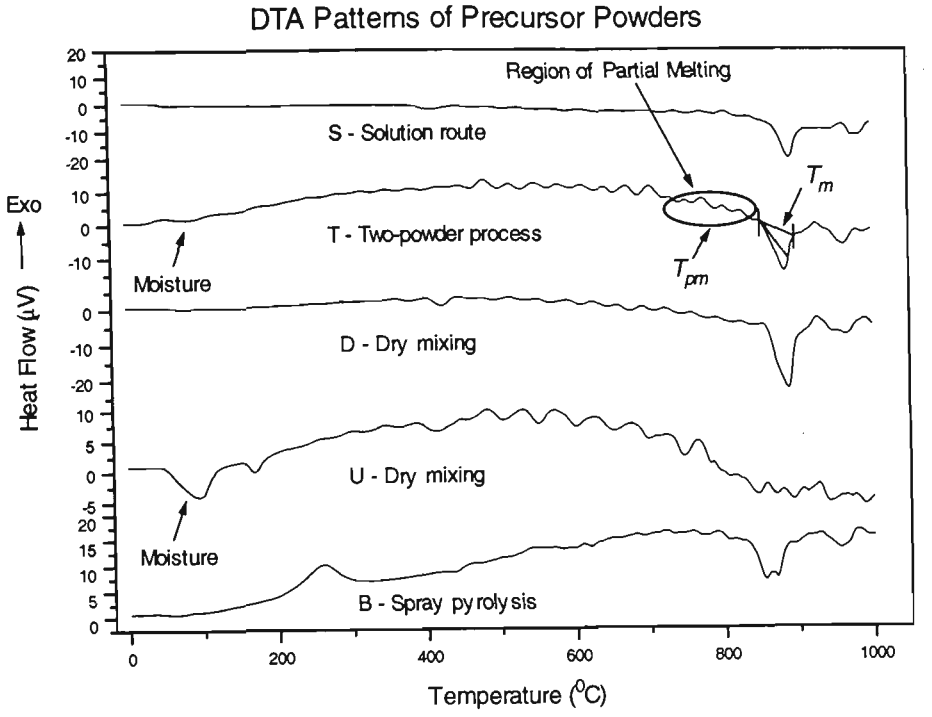

Figure 2.41 *DTA curves of the five different precursor powders of Bi(Pb)-2223.*

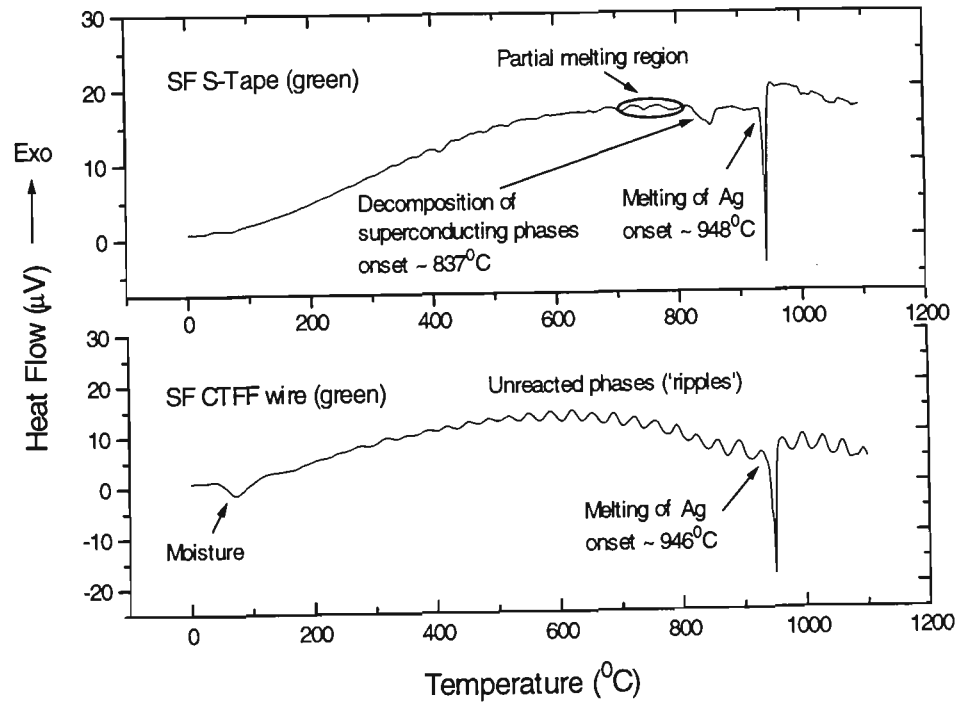

Figure 2.42 *DTA curves of a green SF tape produced from powder S (top), and that of a CTFF wire (bottom).*

Various authors have reported that the reaction corresponding to the DTA peak just before melting occurs seems to be a necessary condition for growth of the 2223 phase [198-200]. The region sustaining a liquid phase is often referred to as the region of *partial melting*, which can cover a temperature range of up to ~ 30^0C before the onset of melting, as reported by Yamada *et al* [209]. The favorable sintering temperature (T_s) for 2223 phase formation for precursor powders has also been shown to be bounded between the endothermic partial melting peak (T_{pm}) and the maximum peak at which melting occurs (T_m), obtainable from DTA curves [200, 198, 210].

Figures 2.41 and 2.42 show respectively the DTA curves obtained for the five different precursor powders and two composites of Bi(Pb)-2223. The latter figure contains additional endotherms indicating the melting of silver at an onset temperature of approximately between 946-8^0C. The accompanying TG curves which show the corresponding weight loss due to any liquid phase formation are included in Appendix E.

Firstly, it appears that the solid-state reaction method of synthesis (for powders of T, D, and U) seems to generate more unreacted phases which can be seen as small 'ripples'. These ripples appear on both the powder and tape DTA spectra and are identifiable via XRD analysis discussed earlier. Secondly, the presence of moisture (which is the prime suspect behind the cause of 'bubbling') in the solid-state reacted precursor powders seems to be more prominent. Thirdly, T_s for each precursor powder type has been chosen such that: ~ $T_{pm} < T_s < T_m$, since the presence of a liquid phase enhances the diffusion rate and facilitates the formation of the 2223 phase. It has also been found that any deviation in sintering temperature from this region has resulted in a decrease in J_c. Electrical transport measurements were performed on one-sinter heat treated SF tapes of initial thickness of ~ 0.28 mm prepared from various precursor powders to narrow down T_s. Plots of critical current versus sintering temperature are shown in Fig. 2.43.

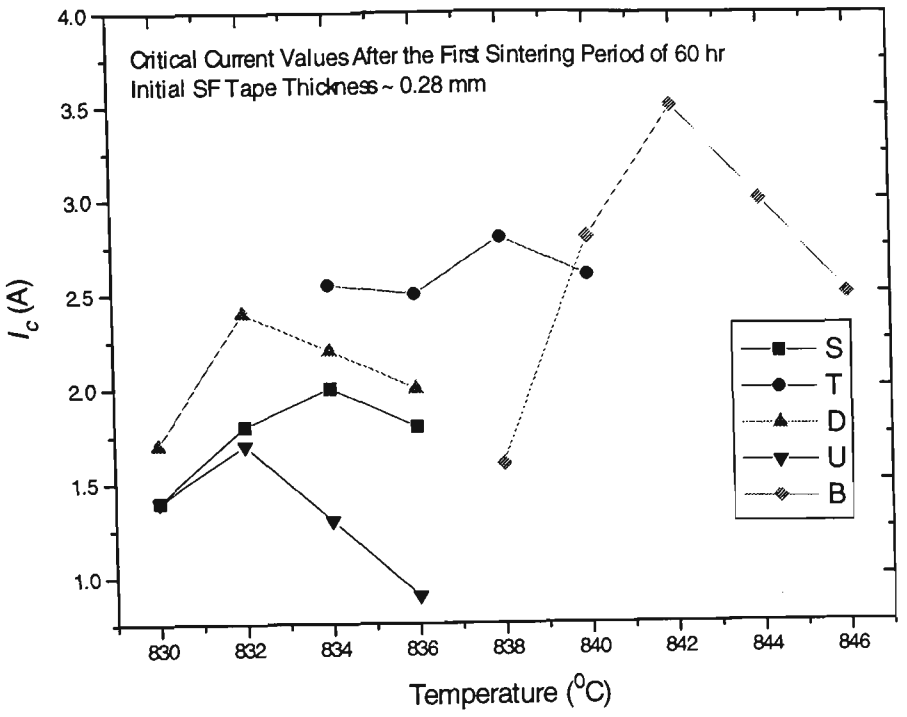

Figure 2.43 *Critical current versus temperature plots, after the first sintering period (60 h) for SF tapes produced from different precursor powders.*

Finally, the growth process of the ~ 107 K 2223 phase during sintering can be attributed to the reaction between the secondary phases of 2212, Ca_2PbO_4, and CuO. The large endotherm present on all DTA curves is presumed to be the melting of 2212, or a decomposing reaction of the superconducting phases [198]. It is known that the onset temperature near the partial melting region tends to decrease as calcium is substituted for strontium [211, 212]. Slight variation in onset temperatures between these powders (877, 860 and 862^{0}C for S, T and D, respectively) near partial melting can be attributed to small variation in calcium and strontium concentration.

2.2.5 Magnetic Measurements

Magnetic measurements refer to those which measure the induced current rather than current driven directly from a power supply (i.e. transport). The majority of the dc-magnetization data presented in this section were obtained from the superconducting quantum interference device (or SQUID) at AMES Laboratory, Iowa State University in the

US. Ac-susceptibility measurements, results to be presented in later chapters, were performed using a mutual inductance bridge method.

2.2.5.1 Magnetization measurements

A great many measurements of critical current densities obtained via magnetization measurements for HTS during the late 1980s were perhaps due to insufficient materials available or because of the difficulty of producing long length samples, or both. Consequently, the magnetic critical current density (J_{cm}) data were often extracted from magnetization data (such as hysteresis loops) through the Bean model [134]. Since the geometry of the superconducting tape samples is elliptical in cross-section, or closer to rectangular than circular, the magnetic J_{cm} (in A/cm^2) can be generalized [213, 214] and is given by the following equation:

$$J_{cm} = 20\frac{\Delta M}{w(1-\frac{w}{3l})} \approx 20\frac{\Delta M}{w} \tag{2.10}$$

for $l > w$, where ΔM is the width of the magnetization loop in emu/cm^3, l is the length and w the width of the superconductor in cm.

In an attempt to examine the origin and compare the history effect of three 37-filamentary tapes prepared from different precursor powders, B, T, and U, dc-magnetization curves were measured on rectangular pieces of cut tapes using a SQUID magnetometer. In brief, the operation of a SQUID is based on the principle of Josephson effect. A typical SQUID magnetization setup consists of a test sample, at constant temperature, placed in a uniform field. The test sample is then moved back and forth in the uniform field, which, during each cycle it passes through the measurement coils, one located at one end of the test sample, the other located at the other end. The induced current in each measurement coil is measured by the SQUID in terms of a field generated by the current, which, in turn, is a measure of the test sample's magnetization.

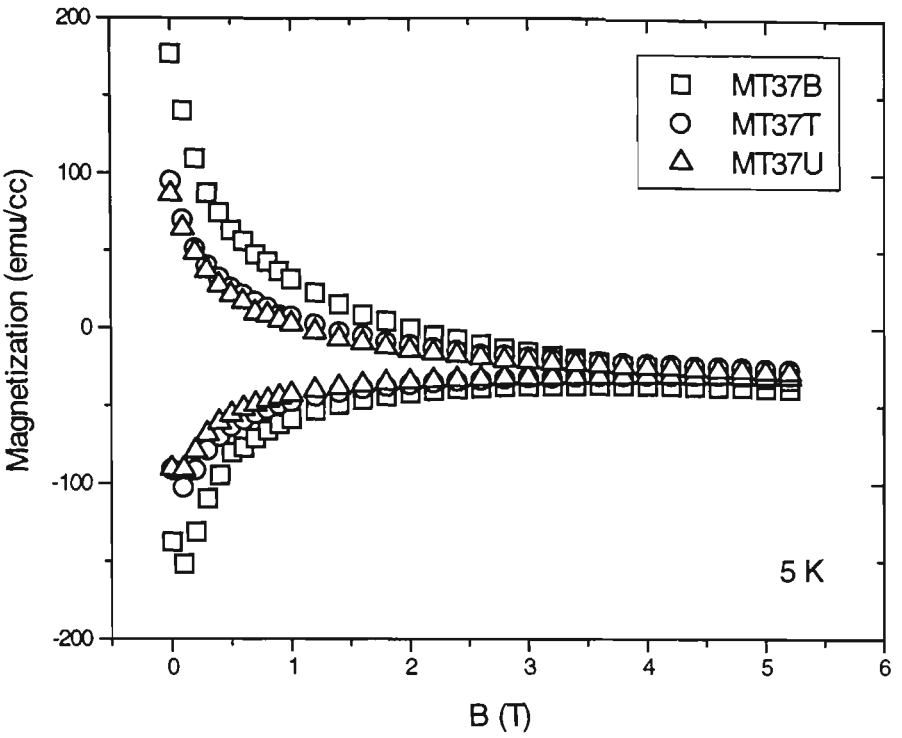

Figure 2.44 *Magnetization curves under H//c for three 37-filamentary Bi(Pb)-2223 tapes.*

Figure 2.44 shows the magnetization curves of magnetic moment versus applied magnetic flux density obtained at a constant temperature of 5 K with H//*c* for the three tape samples, identified respectively as MT37B, MT37T, and MT37U. The metallurgical details and electrical transport property for these tapes are listed in Table 2.14. These samples were extracted from long length composites which went through similar processing procedures except for the different sintering temperatures used. A two-sinter schedule with a temperature drop in the second sintering period (60/25-40 hr) was employed for their heat treatment.

The magnetic J_{cm} was then calculated based on the magnetization data of Fig. 2.44 using eqn (2.10). The resultant plots are shown in Fig. 2.45, which exhibit an exponential J_{cm} dependence which is typical for flux creep.

TABLE 2.14 *Metallurgical details and transport property of three 37-filamentary tapes of Bi(Pb)-2223.*

Sample ID	MT37B	MT37T	MT37U
No. of filaments	37	37	37
Powder type	B	T	U
Procedure	OPIT-grv.rolled	OPIT-grv.rolled	OPIT-grv.rolled
l_{cond}* (mm)	~ 0.8	~ 1.35	~ 1.30
w_{cond}* (mm)	~ 3.30	~ 3.30	~ 3.50
t_{cond}* (mm)	~ 0.3	~ 0.3	~ 0.3
Fill factor (λ)	0.114	0.168	0.159
w_{sc} (mm)^	4.5/5.2×3.3≈2.85	3/4.2×3.3≈2.36	4.5/5.2×3.3≈2.85
A_{cond} (cm^2)	9.9×10^{-3}	1.08×10^{-2}	1.05×10^{-2}
A_{sc} (cm^2)+	1.13×10^{-3}	1.81×10^{-3}	1.67×10^{-3}
Weight& (mg)	7.04	11.32	11.55
V_{sc} (cm^3)!	9.04×10^{-5}	2.44×10^{-4}	2.17×10^{-4}
I_c (A)#	~ 7.2	~ 6.7	~ 4.6
J_c (kA/cm^2)#	~ 5.99	~ 4.62	~ 3.85

Symbols: A, V, sc, and cond denote area, volume, superconductor, and conductor respectively.

* l_{cond} = *length,* w_{cond} = *width, and* t_{cond} = *thickness of the cut composite tape conductor.*

! $V = m/\rho$ *with* ρ = *4350 mg/cc for the leaded Bi-2223.*

^ *Fraction ratio of SC's effective width to the tape width, determined optically.*

\# *Transport measurements in LN, 0 T, cut from coils, fully heat treated.* + $A_{sc} = \lambda A_{cond}$.

& *Weight of the cut conductor sample.*

A comparison between the three samples show that MT37B possesses better flux pinning ability than the other two (since it has a larger irreversible field) giving higher J_{cm} in B//*c* at 5 K. This order is followed by MT37T, then MT37U. Although there were slight processing variations between the samples, such as different sintering temperature used and the extent of intermediate deformation imposed, which might be the determinant factor, the precursor characteristics attributable to the fineness and homogeneity of the

solution route method of synthesis of precursor powder B can not be ruled out. In general, with a suitable thermomechanical treatment, finely produced precursor powders of appropriate composition of Bi(Pb)-2223 underpins the rate of reaction kinetics, which in turn determines the core density, grain alignment and connectivity.

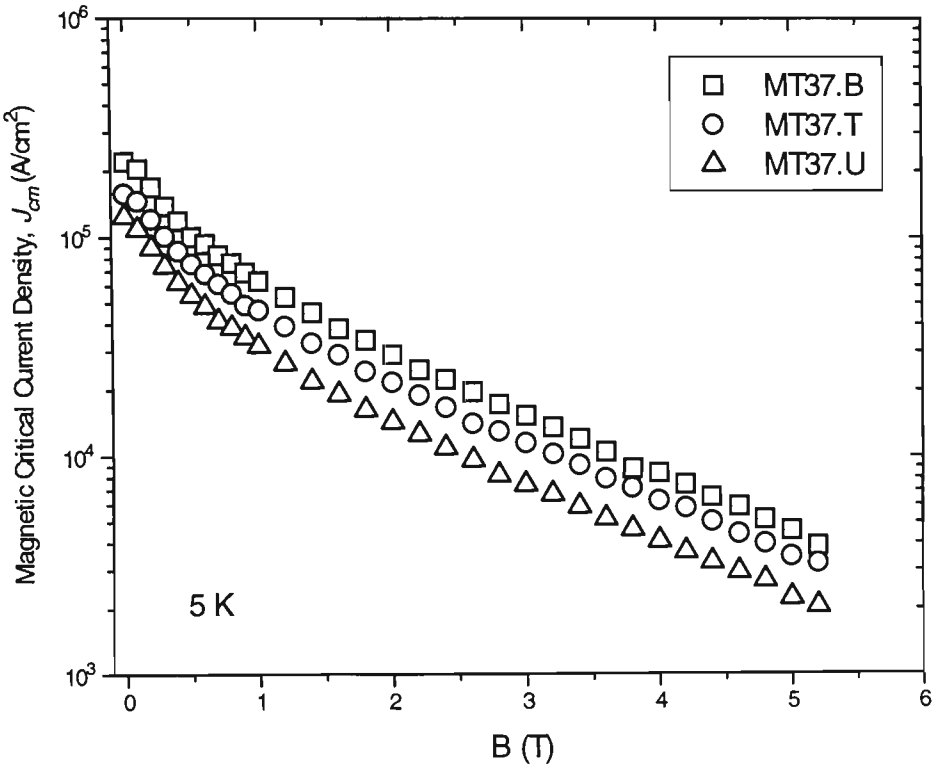

Figure 2.45 *Field dependence of magnetic J_{cm} under H//c for the three Bi(Pb)-2223 37-filamentary tapes.*

As detailed studies in HTSC have resulted in the observation that there exists a thermodynamic reversible region in (H, T) space, just below the normal-superconductor phase boundary ($T_c(H)$ line), various techniques have been developed to determine the so called irreversibility line, (T_r, H_r), below which hysteretic behavior sets in. The following three different procedures [41] show how the IL can be found in HTSC:

1. Field-cooled (FC) and zero field-cooled (ZFC) magnetization curves in a constant dc field H measured as a function of temperature. The temperature at which the curves merge gives a point, $T_r(H)$, on the irreversibility line.

2. Measure of hysteretic isothermal magnetization curves, i.e. M *vs.* H. The field, $H_r(T)$, at which hysteresis vanishes gives a point on the (T_r, H_r) line.

3. The complex ac magnetic susceptibility ($\chi = \chi'_H + i\chi''_H$) measured in constant dc field H as a function of temperature. A thermodynamic response requires that $\chi'_H(T)$ be positive just below T_c which is called the *Differential Paramagnetic Effect* (DPE) [215]. The temperature at which $\chi'_H(T)$ switches from positive to negative is identified as $T_r(H)$.

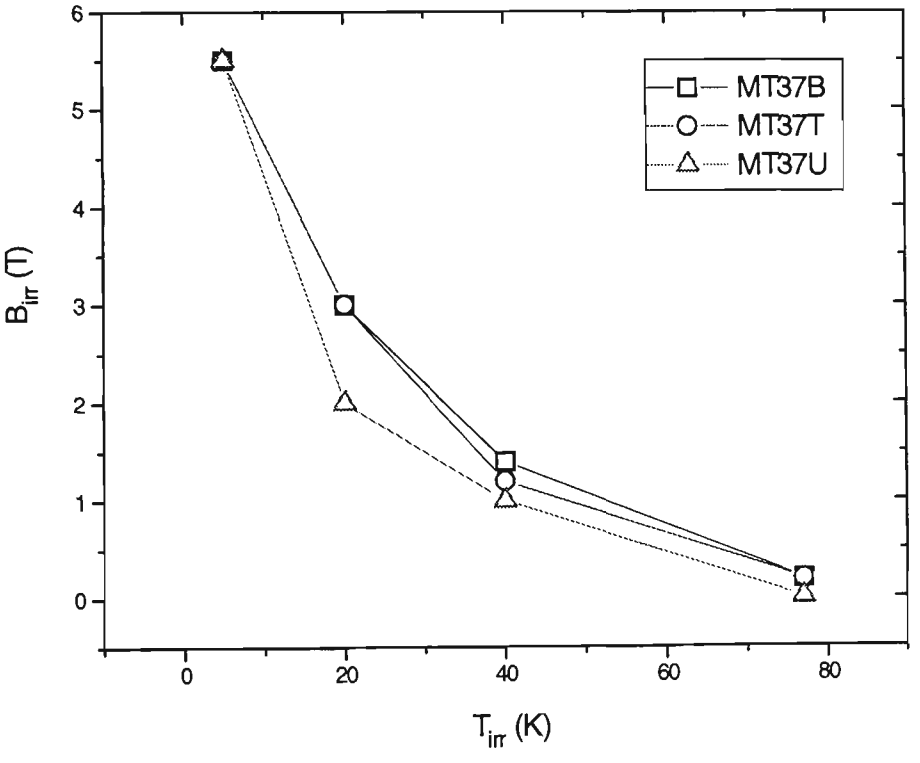

Figure 2.46 *Irreversibility lines determined based on magnetic hysteresis data for the three 37-filamentary Bi(Pb)-2223 tapes.*

Figure 2.46 shows the three ILs for MT37B, MT37T, and MT37U, extracted from individual measurements of m *vs.* H, under $H//c$ (included in Appendix F) over a temperature range from 5 to 77 K (m here denotes the magnetic moment and has units of emu). A slight shift of the IL for samples MT37B, and MT37T towards the higher temperature and field region is an indication of better flux pinning. At lower temperatures however, an enhancement of the flux pinning property for sample MT37U is noticeable, possibly due to the potentially good pinning sites of the 2212 and impurity phases - recalling that solid state reactions of powder synthesis tends to leave behind traces of 2212 and secondary phases in processed tapes, as discussed in previous sections.

Figure 2.47 shows the field dependence of irreversibility temperature, T_{irr}, obtained from field-cooled (FC) and zero field-cooled (ZFC) magnetization curves in a constant dc magnetic field ($H//c$), measured as a function of temperature (given in Appendix F) for a moncore (T-P) and a 31-filamentary (MT31-P) tape. Uni-axial pressing was used as the intermediate deformation between sintering periods for both samples. The applied vertical load was ~ 100 kN. A two-sinter schedule with a temperature drop in the second sintering period (60/25-40 hr) was also employed for T-P and MT31-P. Metallurgical details and electrical transport property of the samples are given in Table 2.15. As can be seen from Fig. 2.47, the pinning strength of the single-filamentary (SF) tape is larger (i.e. weaker field dependence) in comparison with that of the multi-filamentary (MF) one. The shifting of sample T-P's IL up to the high temperature region in the B-T_{irr} phase diagram (most apparent at temperatures approximately $\leq$ 50 K) can be associated with the microstructure and grain orientation, which are extrinsic to the materials. Since the same vertical loading force was used for both samples during tape processing, the larger value of fill factor (λ) of T-P over MT31-P suggests that much of the vertical pressure was absorbed in aligning the grains themselves rather than spreading the ductile matrix sideways (due to horizontal strain) as would likely to happen with MF tapes, and in particular in tapes with small λ.

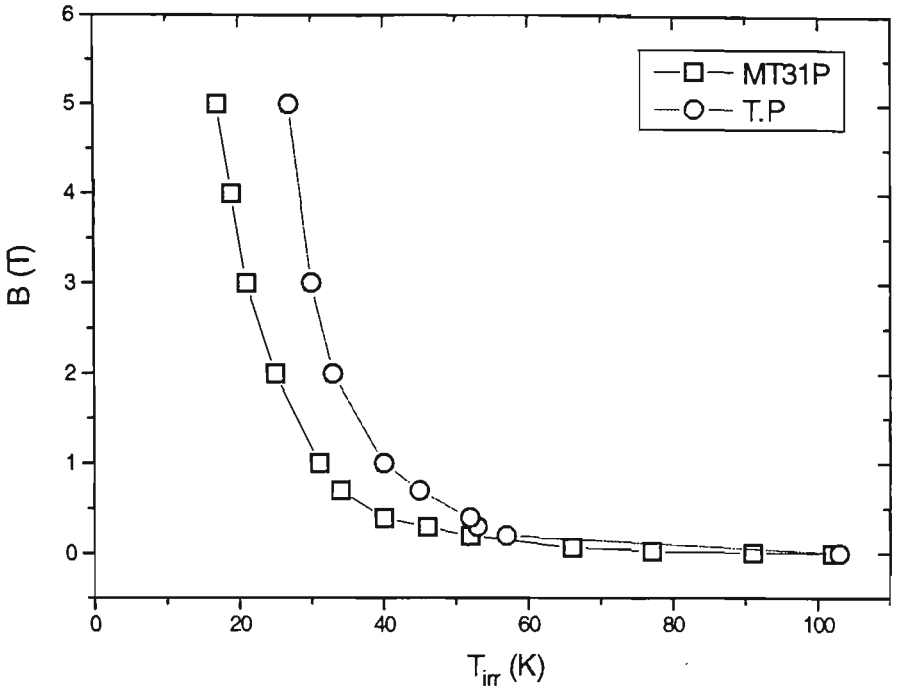

Figure 2.47 *Field dependence of irreversibility temperature, T_{irr}, obtained from FC and ZFC magnetization curves for uni-axially pressed SF (T-P), and MF (MT31-P) tapes of Bi(Pb)-2223.*

Although larger hysteresis loops are associated with greater energy loss as with ac operations, under dc conditions however, this means better flux pinning properties. Based on isothermal hysteretic measurements at 20, 40, 60, 70, and 80 K, a significant increase in flux pinning was found, again, for the SF format over the MF format. This time, cold-rolling was the intermediate mechanical deformation of choice. These two samples, cut from longer lengths of reacted tape, are identified as T-R (monocore) and MT31-R (MF). The metallurgical details and electrical transport property of these samples are also contained in Table 2.15.

TABLE 2.15 *Metallurgical details and transport property of uni-axially pressed, and rolled composite tapes of Bi(Pb)-2223.*

Sample ID	T-P	T-R	MT31-P	MT31-R
No. of filaments	1	1	31	31
Powder type	T	T	U	U
Procedure	OPIT-Pressed	OPIT-rolled	OPIT-Pressed	OPIT-rolled
l_{cond} (mm)	0.75	1.25	1.55	1.32
w_{cond} (mm)	3.25	3.25	3.45	3.60
t_{cond} (mm)	0.25	0.25	0.30	0.30
Fill factor (λ)	0.291	0.212	0.162	0.146
Weight[&] (mg)	3.30	6.01	13.8	12.24
J_c (kA/cm^2) [#]	5.4	6.3	5.0	6.0

[#] Transport measurements in LN, 0 T, fully heat treated. [&] Weight of the cut conductor sample.

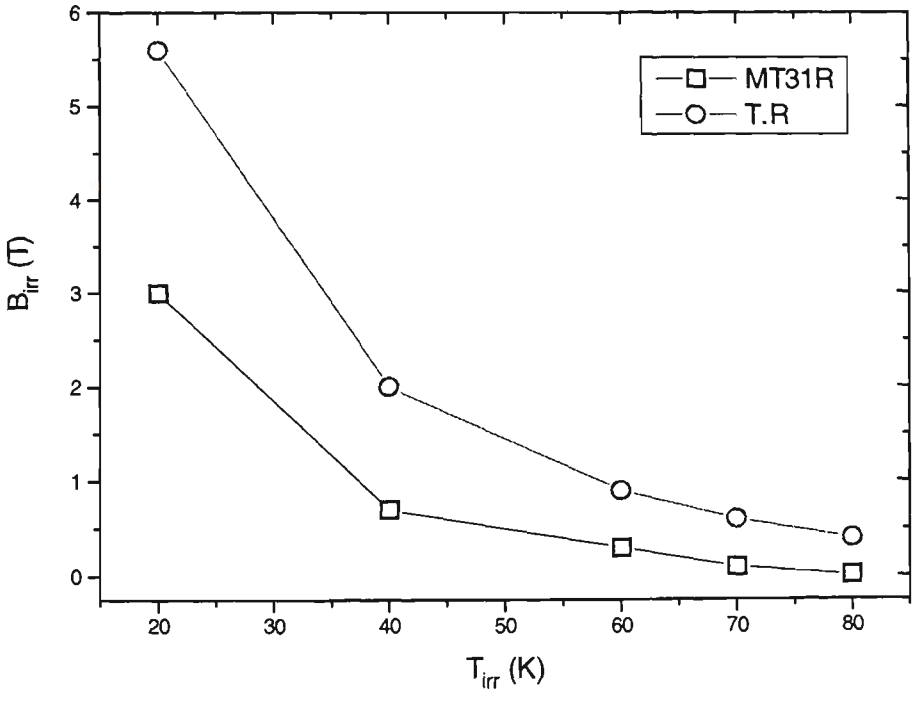

Figure 2.48 *Magnetic phase diagram for the monocore and multi-filamentary tapes produced by cold-rolling, showing that (T_r, H_r) is increased by having a SF format.*

As shown in Fig. 2.48, a notable shift of the IL towards both higher temperature and field region can be seen. Once again, since the IL provides information on the core pinning strength, the large shift of the IL for T-R is an indication of the enhancement of core pinning. It has been reported by Liu *et al* [216] that the grains in tape samples contain more defects than those for powders, and that as a consequent (after having eliminated most of the grain boundaries by scraping powder from tape), intra-grannular defects and interfacial pinning can be improved via harsh thermomechanical deformation during tape processing. Thus the reason for the improvement in core pinning of T-R over MT31-R once again has to come from the history of sample preparation which takes into account factors such as sintering temperature and period (which determines the compositional phase), and the amount of reduction on the tape thickness during intermediate mechanical deformation (which determines the final value of λ).

2.2.5.2 Ac-susceptibility

With the discovery of HTSC materials, ac magnetic susceptibility measurements have become widely used for characterization of samples as well as for fundamental study purposes. The ac-susceptibility measurement is based on the mutual inductance technique where a primary coil and two secondary (oppositely wound) coils form the basic circuitry. In the absence of the sample, which is normally centered in one of the secondary coils, the net flux across the secondary coils is zero (by having an additional compensation system to adjust the output of the secondary coils to a minimum). In the presence of a sample, the induced magnetization due to the ac primary field results in an off-balance signal of the secondary coils, which picks up by the detection system (a lock-in amplifier) and recorded using a computer based data acquisition program. The temperature is measured by placing a copper-constantan thermocouple near the sample.

Sintered HTSC tapes, and LTSC composite wires with closely spaced filaments exhibit two critical temperatures. One is intrinsic to the superconductor and the other is characteristic of the coupling between either grains [217, 218], or filaments [219, 220]. A

typical measurement for a sample of sintered high-T_c $(Bi,Pb)_2Sr_2Ca_2Cu_3O_{10-x}$ bulk is presented in Fig 2.49, with the intrinsic and coupling segments identified. The onset of intrinsic diamagnetism corresponds to the initial decrease in electrical resistivity upon cooling, but the onset of inter-grannular coupling coincides with the temperature for zero resistivity. The lower critical field may be determined by the field at which the imaginary part of susceptibility increases from zero.

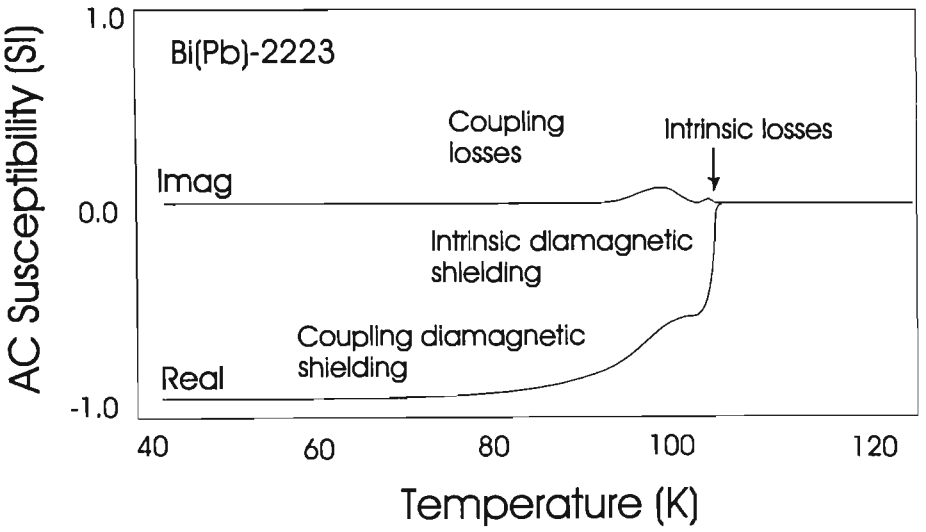

Figure 2.49 *Ac-susceptibility as a function of temperature for a sintered Bi(Pb)-2223 bulk, with the intrinsic and coupling components identified (After Goldfarb et al [220]).*

In dc-susceptibility the ZFC curve demonstrates flux shielding (flux exclusion) upon warming, and the FC curve demonstrates the Meissner effect (flux expulsion) upon cooling - refer to Appendix F for examples. Whether measured upon warming or cooling, ac-susceptibility (with no dc-bias field) always measures shielding. More discussion on ac-susceptibility is given in chapter 3.

2.2.6 Electrical Transport Measurements

Although magnetic measurements are useful for sample characterization and fundamental studies, large scale applications make it necessary to measure the actual current moving

down the wire or tape, known as *transport current*. For this purpose, three different methods were devised to measure the critical transport current, I_c, of Bi(Pb)-2223 composite tapes of various lengths. As shown in Fig 2.50, for short and long lengths of composite tape, the standard 4-probe dc technique was employed. In case of testing for current uniformity, a '50-probe' instrument was used to measure straight Bi-based tapes up to 50 cm in lengths. The criteria for I_c were 1μV/cm for short samples and $10^{-11}\Omega$-cm for long lengths, coils, and magnets.

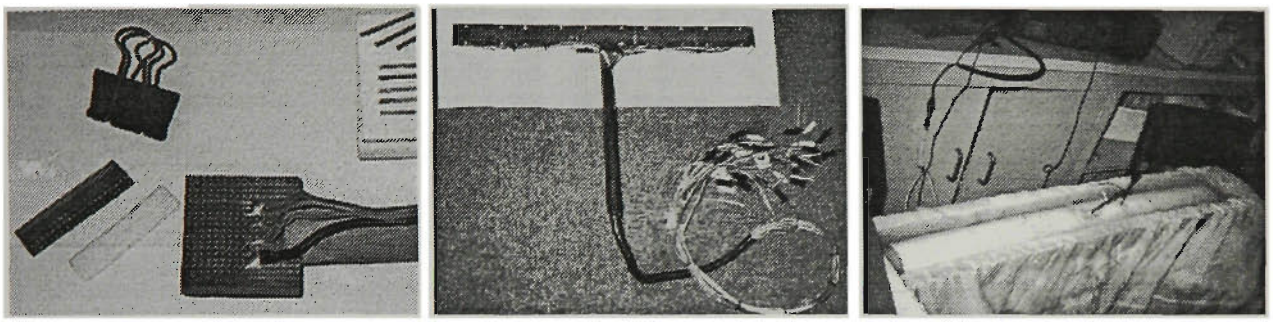

4-probe *50-probe* *4-probe*

Figure 2.50 *Instruments and methods used for the determination of transport I_c of short and long lengths of Bi(Pb)-2223 composite tapes.*

To determine the J_c and J_e of superconducting tapes, the core area of cross-sections must be known. To measure these, and values of λ, the MD-20 Image Analysis System from *The Flinders University of South Australia* was used, shown in Fig. 2.28. Table 2.16 contains the corresponding J_c and J_e of fully reacted MF tapes prepared using the method of CTFF. The metallurgical and microstructural details of these samples are given in sections 2.1.2.1 and 2.2.2 respectively. Although it has been found [154] that J_c generally increases with thinner core, $J_e = \lambda J_c$ means that a compromise in fill factor must be taken into consideration in order to improve the overall engineering critical current density, yet at the same time keeping J_c at a respectable level.

TABLE 2.16 *Transport property of some CTFF and OPIT Bi(Pb)-2223 composite tapes.*

Sample ID (Preparation method)	Thickness (mm)	J_c (kA/cm^2) (77 K, 0 T)	J_e (kA/cm^2) (77 K, 0 T)
MT9 (CTFF)	0.24	~ 10.81	~ 2.16
MT12 (CTFF)	0.20	~ 15.54	~ 1.99
MT14 (CTFF)	0.25	~ 15.80	~ 2.58
MT36 (CTFF)	0.25	~ 15.84	~ 3.14
MT36Cu (CTFF)	0.28	~ 18.53	~ 2.80
MT37 (CTFF)	0.24	~ 9.75	~ 0.73
MT40 (CTFF) - double stacked	0.24	~ 4.51	~ 0.50
MT50 (CTFF) - double stacked	0.37	~ 2.65	~ 0.29
MT19 (OPIT)	0.28	~ 10.75	~ 2.11
MT31 (OPIT)	0.24	~ 6.87	~ 1.28
T (OPIT)	0.18	~ 4.62	~ 1.25

Figure 2.51 shows the variation in I_c over 50 cm long strips of MF tapes. The I_c determination for each strip was based on the 1μV/cm criterion, obtained by tapping the voltage at specific points along its length (using the 50-probe instrument). The fluctuation was found to be ~ 7, 10, and 11.5 % for MT36Cu (processed with Ag-7 at.% Cu as the outer sheathing material), MT37B, and MT37T respectively. The smaller variation of I_c in MT36Cu over the other two strips is a testimony of improved mechanical strength in using alloys of silver as the cladding matrix. Long lengths including ~ 7 and ~ 55.3 m of MF tapes were also tested for uniformity. The I_c variation was determined to be within ~ 15 % over the entire lengths of these long composites, as shown in Fig. 2.52. The V-I curve shown in Fig. 2.53 gives an I_c of ~ 7.5 A, corresponding to a J_c ~ 7 kA/cm^2 over the 55.3 m length based on the following equations:

$$R = \frac{\rho l}{A_c}, \text{ and} \tag{2.11}$$

$$V = IR$$

$$= I_c \frac{\rho l}{A_c} \tag{2.12}$$

where I_c is the short tape critical current using 1μV/cm criterion, ρ=10^{-11} Ω-cm as the resistivity, l the length of the long tape, and A_c, as the cross-sectional area of the superconductor. The J_c over the entire length of the tape was found to be in reasonably good agreement with those obtained for short sections (~ 8.5-9 kA/cm^2). A two-sinter process with a temperature drop in the second sintering period was used for the heat treatment of the 55.3 m long composite tape. Further details on heat treatment schedule are given in chapter 3.

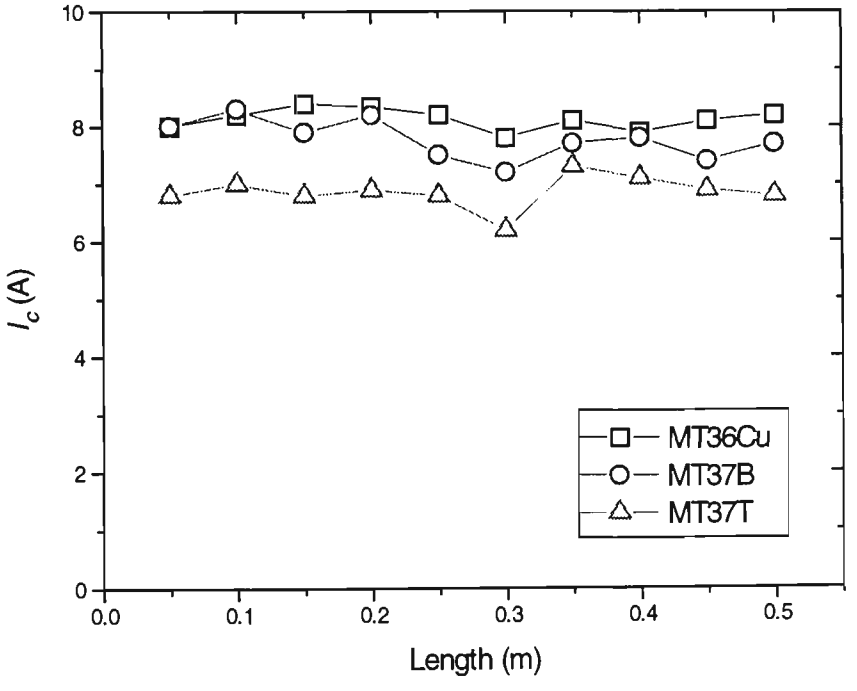

Figure 2.51 *Variation of I_c over 50 cm long strips of MF tapes of Bi(Pb)-2223.*

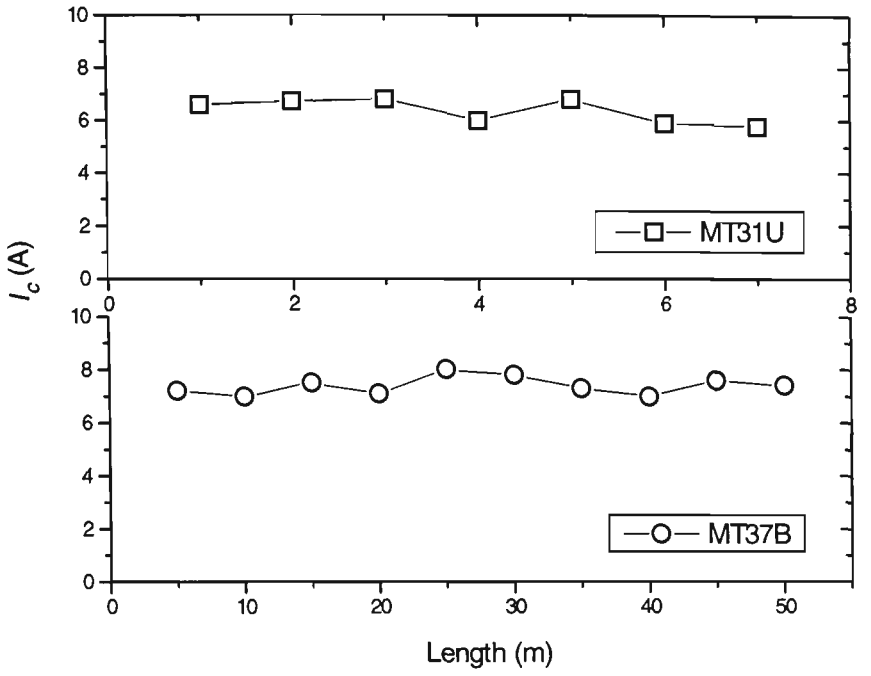

Figure 2.52 *Variation of I_c over long lengths MF tapes of Bi(Pb)-2223 up to 55.3 m.*

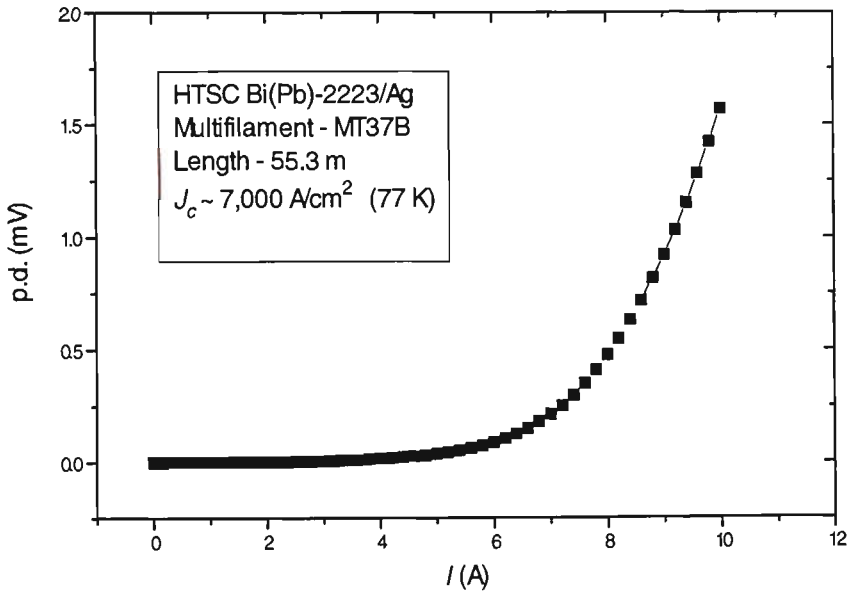

Figure 2.53 *V-I curve obtained over 55.3 m of 37-filamentary Bi(Pb)-2223 tape.*

The setup for testing of coils and magnets is shown in Fig. 2.54. Also shown in Fig. 2.54 is the 90 mm bore water-cooled 1T magnetometer, *Walker Scientific Inc.*, used for performing transport measurements of short composite tapes. The 4-point technique was used in both cases. For the latter, solder and thin copper wires were used to provide current and voltage contacts.

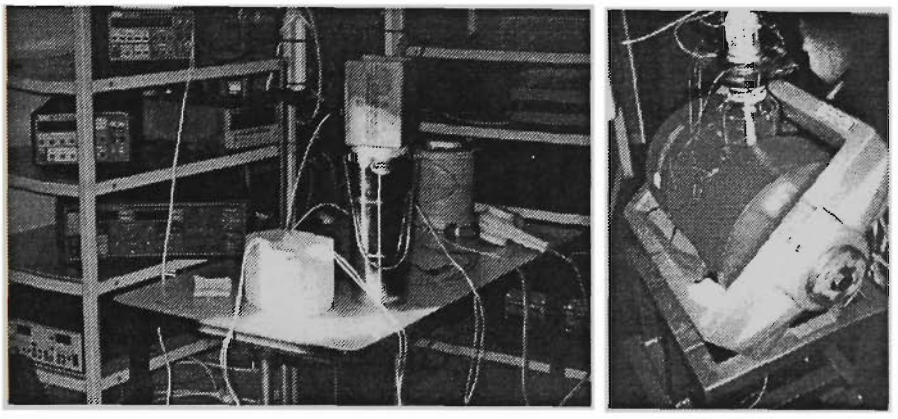

Electrical testing of coils and magnets. *Magnetometer.*

Figure 2.54 *Setup for electrical measurements of coils and magnets (left). A 90 mm bore water-cooled 1T magnetometer, Walker Scientific Inc., used for performing transport measurements of short composite tapes (right).*

The calculated self (central) field for each coil was made based on the following eqns. (2.13) and (2.14) depending on the coil type [131]. For a solenoid

$$B_{total} = \frac{\mu_0 NI}{L}, \tag{2.13}$$

based on the long solenoidal approximation, $\beta \rightarrow \infty$ and

$$B_i = \frac{\mu_0 N_i I_i}{2a_i}\left(\frac{\ln \alpha_i}{\alpha_i - 1}\right) \tag{2.14}$$

for a pancake-shaped coil, using the limit $\beta \rightarrow 0$. $\alpha \equiv b/a$, and $\beta \equiv l/a$, where $2a$, $2b$, N, I, and L are the inner and outer diameter, total number of turns, total current, and height (or

length) of the coil respectively. Appendix C contains the processing, dimensions, and measured properties of some of these coils (refer to Fig. 2.23).

The critical temperature, T_c, of Bi(2223) composite tapes was also measured using the standard four-probe dc technique. The circuit layout of the instrument is shown in Fig. 2.55.

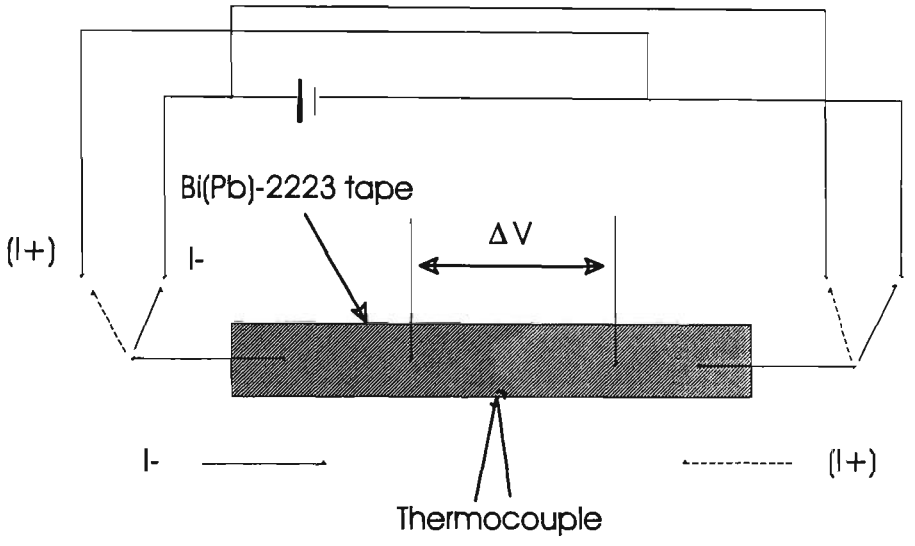

Figure 2.55 *Circuit layout of 4-probe dc method used in T_c measurements.*

To describe briefly the procedure involved, a short tape specimen of ~ 20 mm in length was mounted on a copper block of a specially designed sample holder with four leads attached using solder or indium for contacts. A copper-constantan thermocouple was located inside the copper block with its tip just beneath the measuring specimen to monitor the temperature. A thermoflask filled with a mixture of ice and distilled water was used to provide the reference temperature (273 K) for the thermocouple.

During the course of the measurement, the chamber together with the specimen was immersed in LN, held for a few minutes to cool thoroughly, then raised above the LN level to allow the specimen temperature to increase. The rate of temperature change was controlled to be between 1~2 K/min. A constant current of 0.05 A was supplied by a 100 W constant current/voltage source (*Model 228, Keithly Instrument Inc.*, Cleveland, OH, US) and voltages across the two inner leads were measured using a digital multimeter (*Model 196, Keithly Instrument Inc.*, Cleveland, OH, USA) with a precision of 10^{-7} V. A constant

current was provided in two directions to avoid the deviation of voltage resulting from composition heterogeneity and thermoelectrical potential shift. Temperature and voltage data were recorded using a computer based data acquisition program.

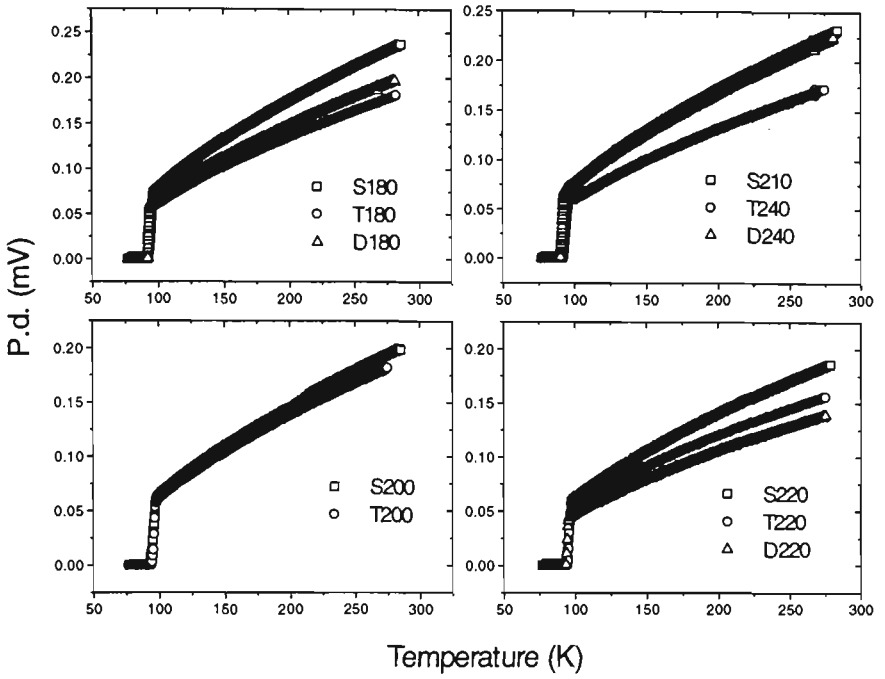

Figure 2.56 *Temperature dependence of electrical resistivity of heat treated SF Bi(Pb)-2223 tapes.*

Figure 2.56 shows some T_c measurements obtained for SF tapes prepared from powders S, T, and D, heat treated with different sintering periods. The alpha-numeric labeling in each legend of the plots indicate the powder type and total sintering time. The 180 and 240 h samples are multiples of 60 h sintering periods. The 200 h samples are multiples of 40 h sintering periods, while the 220 h is equivalent to (100+120) h of sintering time. The 210 h in particular equals (3×60+30) h. Due to the percolative nature of the dc-resistivity measurement, the onset T_c of these plots is no more than ~ 100 K. The more accurate and informative ac-susceptibility measurements obtained for some of these tapes however, showed an onset T_c of ~ 108 K (given in chapter 3) since the technique is primarily volumetric. Nevertheless, dc-resistivity measurements can be used qualitatively for comparison purposes between tapes by determining parameters such as pinning potential, $U(T, B)$ and activation energy, $U_0(B) \equiv U(T=0, B)$.

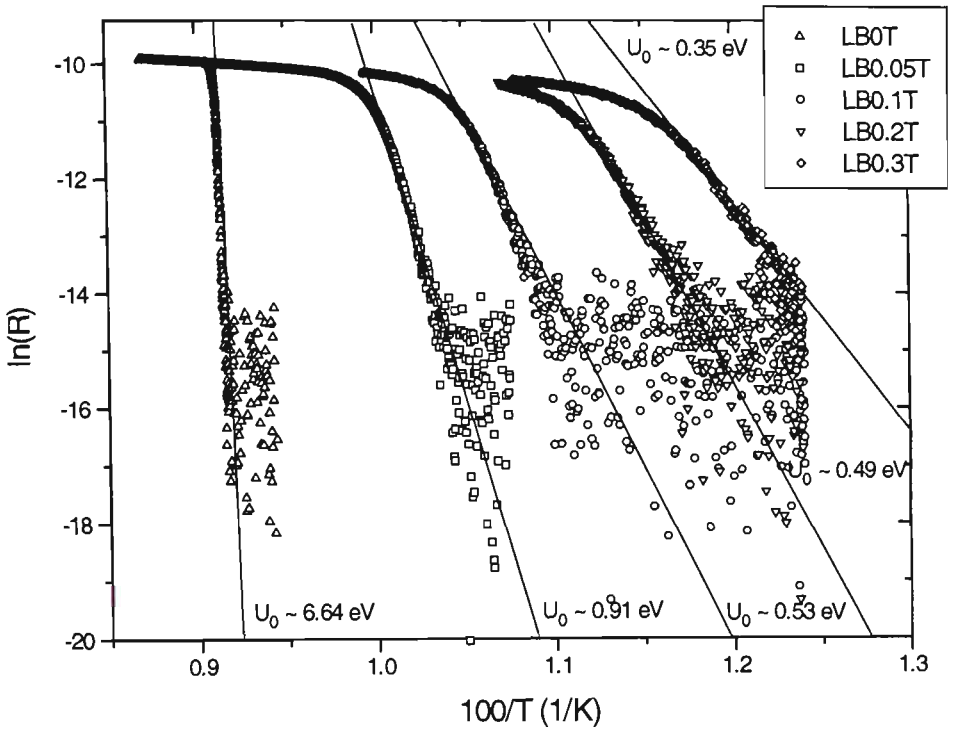

Figure 2.57 *Arrhenius plot of the tape resistances (lower curves) and the estimated core resistances (upper curves) for a 37-filamentary CTFF tape in magnetic fields H//c at B = 0, 0.05, 0.1, 0.2, 0.3 T (left to right).*

Kusevic *et al* [221] have recently shown that by assuming a macroscopically uniform resistivity of the core, it is possible to single out the core resistance R_c from the total tape resistance R and the estimated sheathing resistance R_A. Figure 2.57 shows the Arrhenius plot (after Fig. 1.3) of the tape resistances (lower curves) and the estimated core resistances (upper curves) for a 37-filamentary CTFF tape in magnetic fields $H//c$ at B = 0, 0.05, 0.1, 0.2, 0.3 T. The lines are fitted to $ln(R) = R_0\text{-}U_0/(k_BT)$. It can be seen that initially both R and R_c follow the same exponential variation of $exp(-U/k_BT)$ reminiscent of the thermally activated motion of the flux lines in type-II superconductors [50]. As expected, the exponential variation of R_c extends over larger range of T than that of R, since at higher temperature R_c becomes larger than R_A and hence R approaches R_A (parallel conduction). However, the initial slopes of $ln(R)$ and $ln(R_c)$ versus $1/T$ are the same for a given B and hence yield the same U. The variation in U_0 is also given in Fig. 2.57.

Chapter 3

Optimization of the Thermomechanical Processing of Bi(Pb)-2223 Composite Tapes

3.1 Initial Packing Density

Since the advent of the cuprate high-T_c superconductors in 1986, a great deal of research has been pouring into developing long length superconducting tapes that can operate at high current density in high magnetic fields at elevated temperature. To fabricate such a superconductor in such a way that it can be reproduced easily is a major concern for industrial and commercial purposes. Controlling the parameters such as in the thermo-mechanical deformation, annealing of wires, sintering and intermediate deformation of these tapes well is the key to high quality reproducible HTSC tapes, long or short.

This section discusses different ways of applying the powder-in-tube (PIT) technique, in particular how powder packing density (which is perhaps one of the 'earlier' parameters attributable to the final electrical transport and magnetic properties of HTSC tapes) affects the final phase formation and electrical transport property of monocore Bi(Pb)2223-based short tapes.

3.1.1 Experimental Details

All tapes were made from initial 99.99 % pure silver tubes of inner and outer diameters 4.5 and 6.5 mm respectively. Two different powders were used in the fabrication process. One made in our laboratory (identified as powder S), the other imported (identified as powder U). The powder processing procedure involved the solution route technique [222]. Microstructural particle size distribution analyses of the powders were performed by laser diffraction. Both precursor powders have similar average particle size of between 4 and

6μm. Prior to usage, the powders were dried thoroughly for several hours between 100 and 200^{0}C. The silver tubes were cleaned with silver polish and acetone successively using an electric hand-drill and a stainless steel rod (i.e. 'burnishing' the silver tubes). These burnished tubes were then passed through a tubular furnace set between 400-500^{0}C to evaporate any remaining residue. One end of each of the purged tubes were then sealed off using the technique of 'cold-forming' on a lathe.

The conventional PIT method was used but in different ways to examine the effect of uniformity and density of the initially packed powder on the electrical transport properties of the final treated monocore tapes. In the first instance, a hammer and a stainless steel rod were used. For the second alternative, the rod was used but without the hammer to force the powder into the silver tube thus achieving lower powder density. The third way was to employ a vibrator whereby a silver tube was firmly secured on a vibrating platform. Precursor powder was then slowly poured into the tube while the platform was vibrating. The frequency of vibration was varied from high to low (60-10 Hz) as more and more powder settled in.

After PIT, the opened ends of the tubes were sealed and the process of thermo-mechanical deformation began. The tubes were groove-rolled into thin wires with 10-20 % reduction per pass at room temperature with frequent intermediate annealing. Annealing was necessary between these passes to relieve stress and strain built up in the silver sheath, to evolve volatile gasses and to assist the distribution of powder during rolling. The wires were then flat rolled into thin 'green' (unreacted) tapes (between 0.1 and 0.2 mm, see Discussion for more details) ready for the high-temperature heat-treatment (sintering) process. The pattern shown in Fig. 2.18 (of section 2.1.2.2) was implemented in the sintering process of the monocore HTSC short tapes.

Two different batches of tapes were processed separately. Those made from powder S were pressed uniaxially at room temperature between sintering (i.e. high temperature heat-treatment) in the range of 0.4-1 GPa. Those fabricated with powder U were intermediately rolled at room temperature.

TABLE 3.1 *Details of heat-treated samples, including phase composition of precursor powders and of the treated tapes, initial powder packing density, and zero field transport critical current densities and percentage fill factors.*

Sample ID^ & l×w×t (mm^3)	PIT Method and % Powder Density	Heat Treatment (Reduction~15-25%)	$\frac{2212}{2223+2212}$ (%)	J_c (kA/cm^2)* & λ (%)
U32100r	hammer & rod	832-835 C 1×100 h	$\frac{16}{83+16} \approx 16\ \%$	~ 1.1 (~ 37)
30×3×0.23	~ 60-70 %			
U32200r	hammer & rod	832-835 C 2×100 h	$\frac{6}{63+6} \approx 9\ \%$	~ 3.5 (~ 35)
30×3×0.19	~ 60-70 %	Intermediate rolling		
U32100v	vibrator	832-835 C 1×100 h	$\frac{54}{73+54} \approx 42\ \%$	~ 1.2 (~ 28)
30×3×0.22	~ 20-30 %			
U32200v	vibrator	832-835 C 2×100 h	$\frac{11}{31+11} \approx 26\ \%$	~ 2.9 (~ 20)
30×3×0.20	~ 20-30 %	Intermediate rolling		
S34180r	hand & rod	832-835 C 3×60 h	$\frac{9}{19+9} \approx 32\ \%$	~ 7.1 (~ 23)
30×3×0.10	~ 30-40 %	Intermediate pressing		
S34240r	hand & rod	832-835 C 4×60 h	$\frac{6}{22+6} \approx 21\ \%$	~ 9.1 (~18)
30×3×0.09	~ 30-40 %	Intermediate pressing		
S34180hr	hammer & rod	832-835 C 3×60 h	$\frac{13}{87+13} \approx 13\ \%$	~ 8.2 (~ 39)
30×3×0.10	~ 60-70 %	Intermediate pressing		
S34240hr	hammer & rod	832-835 C 4×60 h	$\frac{5}{94+5} \approx 5\ \%$	~ 16.5 (~ 31)
30×3×0.09	~ 60-70 %	Intermediate pressing		

^ *v = vibrator, r = hand & rod, hr = hammer & rod.* * *B = 0T at 77K*

At the end of each period of sintering, the I_c of each tape was found (in self-field at 77 K, based on the 1 μV/cm criterion) using the standard 'Four-Terminal DC Method' (custom made instrument shown in Fig. 2.51 of section 2.2.6). The J_c was then determined by measuring the transverse cross-sectional area of the ceramic core of the cut tape embedded in resin. Another small section of the red tape was then cut for characterisation. X-ray diffraction (XRD) analysis with a diffractometer (Sietronics XRD Automation System)

using Cu$K\alpha$ radiation and scanning electron microscope (SEM Leica Cambridge Stereoscan S440) with a Link Systems energy dispersive spectrometer (EDS Link System Detector with Moran Scientific Software) were made for each small section of the fractured tape. The initial tape thickness' for samples with IDs begining with S were ~ 0.12 mm. Those with IDs begining with U, the initial thickness' were ~ 0.2 mm (refer to Table 3.1 for their final dimensions).

3.1.2 Results and Discussion

As a general rule of thumb, the better the initial powder quality the higher the performance of the final superconductor. Still, there are many variables to be optimized in the earlier stage of the fabrication of HTSC tapes; such as cation stoichiometry, volatile impurity phase content, percentage of predominant phases of 2223 and 2212 [223-225] and particle size distribution [226]. The percentage of low-T_c phase of 2212 from XRD analysis indicates that the denser the powder is initially packed the quicker the conversion process from low- to high-T_c phase as shown in Table 3.1. Perhaps even smaller particle size would expedite such processes [227].

Pressing or rolling of tapes do indeed necessitate the improvement of core density, and grain alignment [228] in between sintering stages. In general, uniaxially cold-pressed tapes have superior transport electrical and magnetic properties while flat-rolled tapes tend to be less so [229-231]. The J_c in self field at 77 K of pressed tapes (the S samples in Table 3.1) demonstrate this effect. Furthermore, to see how the initial packing density affect the final J_c, four samples (two of similar initial packing density, the others with less initial packing density, different from each other) were processed in a very similar fashion except two of them involved intermediate rolling while the other two were intermediately pressed uniaxially between sintering stages.

Both the U (rolled) and S (uniaxially pressed) samples show higher initial packing powder density resulting in higher J_c. It was noted that after 100 hours of sintering time, although the measured I_c of the sample made using hammer and rod (U32100r) was greater than the

one using a vibrator (U32100v), the J_c of the former tape was approximately 10 % less. This could be explained due to the fact that there was much more core (or surface or interfacial area between oxide and silver) for the supercurrent to flow through (since the oxide ratio of the former to the latter was measured to be approximately two to one). This fact is reflected in the fill-factor ratio. The fill factor is defined here as the ratio of the transverse cross-sectional area of the superconducting core to the total transverse cross-sectional area of the conductor. Furthermore, SEM micro-images of fractured surfaces parallel to the *ab*-plane of Fig. 3.1(a)-(b) reveal the grain morphology of U32100r as being much more closely spaced (hence higher mass density and better grain connectivity - this can be seen more clearly in Fig. 3.1(e)-(f) after a further 100 hours of heat treatment) as well as appearing larger in surface area (average grain lengths are ~ 30 μm and 20 μm for U32100r and U32100v respectively).

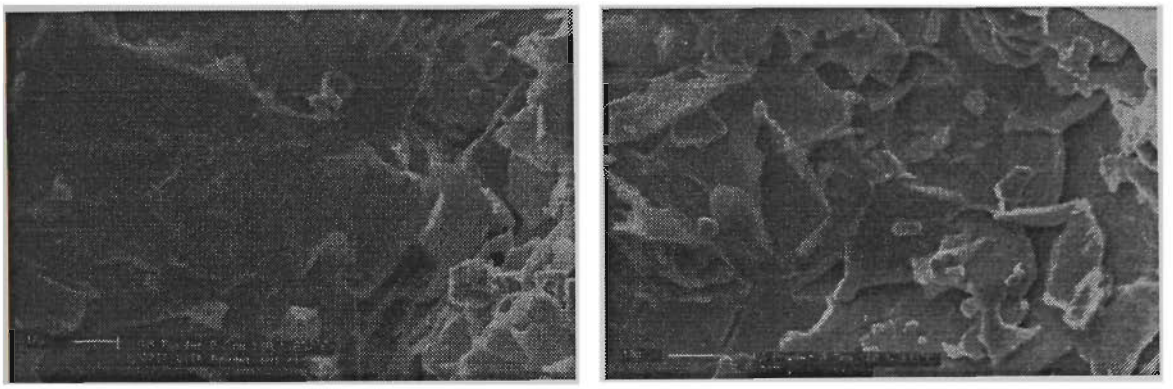

10μm —— 10μm ——

(a) *(b)*

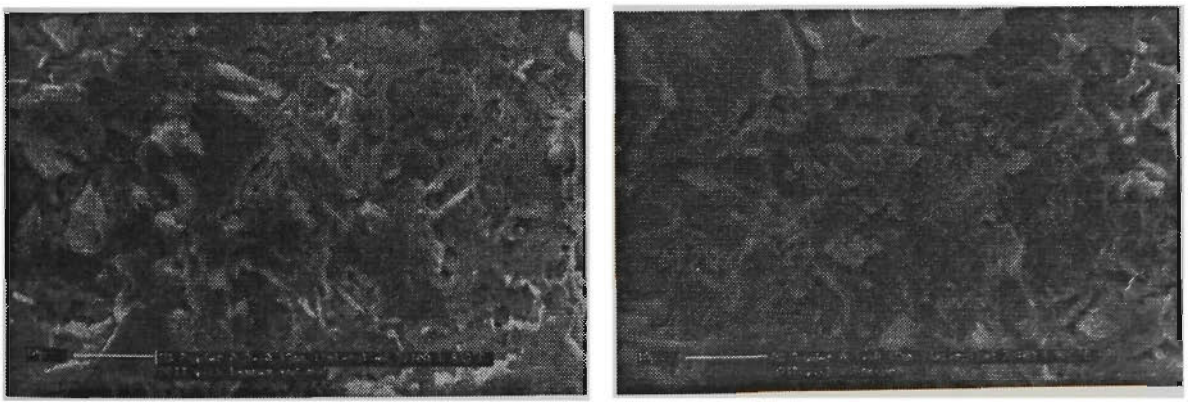

10μm —— 10μm ——

(c) *(d)*

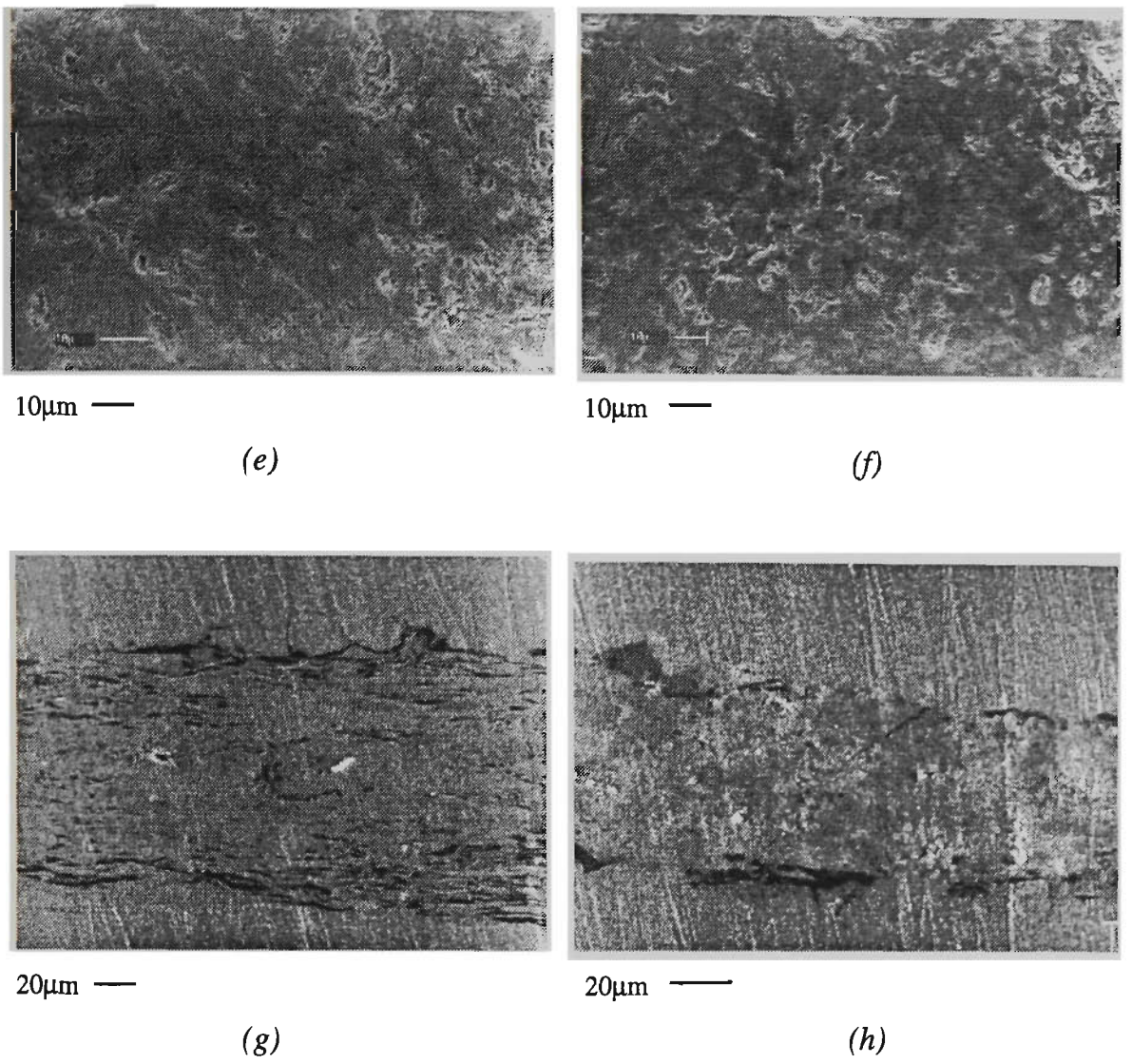

Figure 3.1 *SEM micro-images of fractured surfaces of samples (a) U32100r, (b) U32100v, (c) U32200r (d) U32200v, unfractured surfaces of samples (e) U32200r, (f) U32200v and unfractured cross-sections perpendicular to the ab-plane of samples (g) U32200r and (h) U32200v.*

Fig. 3.1(c)-(d) depict SEM images of fractured surfaces parallel to the *ab*-plane showing similar grain sizes between the vibrator and hammer-rod made tapes, after an extra 100 hours of sintering time. However, the SEM images of unfractured surfaces of these samples perpendicular to the ab-plane (in Fig. 3.1(g)-(h)) do indicate better grain alignment for U32200r thus this higher initial packing density sample is capable of carrying higher currents due to the greater absence of intergrannular weak-links [232]. In

addition, the phase composition from XRD analysis of the former, indicates a very large amount of low-T_c phase present. The sample with lower initial packing density contains an amount quadruple that of the one with higher initial packing density. This explains the notably improved J_c in the hammer-rod made tape. The numerical values were calculated from Fig. 3.2 and tabulated in Table 3.1.

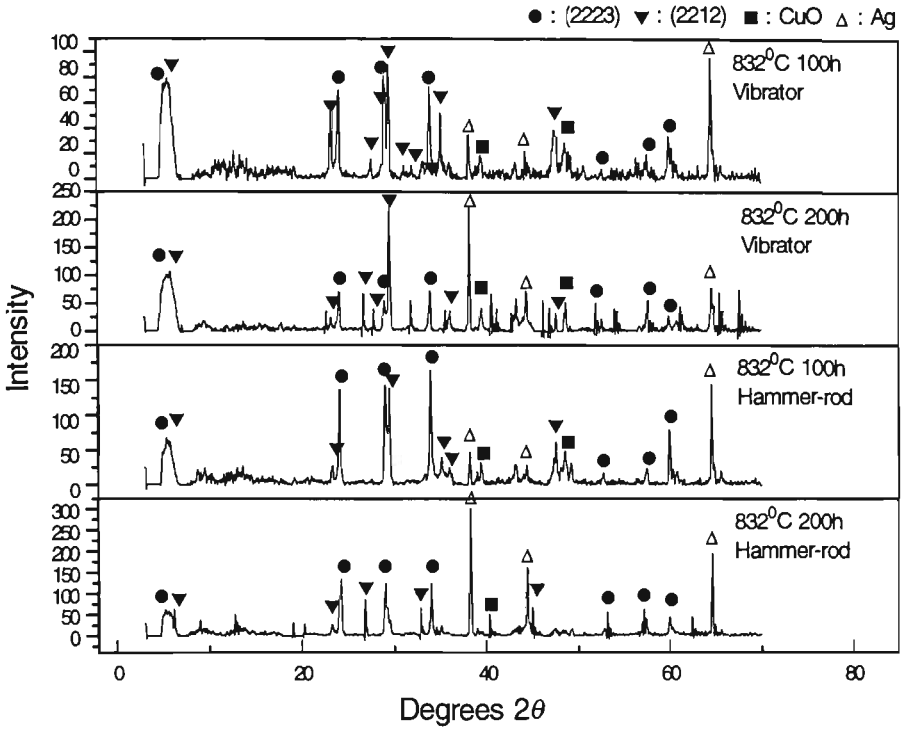

Figure 3.2 *XRD patterns of the U samples at different sintering stages (832^0C 100-200 h).*

Now, let's consider the S samples. Again, information from XRD analysis reveals the amount of 2212 which is converted to 2223, as shown in Fig. 3.3. After 180 h and subsequently 240 h of sintering time, the amount of 2212 phase present is approximately more than double in the initially lower packing density sample than in the initially higher packing density sample.

It is among the general consensus that there are two important factors that limit the J_c of these new high-T_c bismuth-cuprate-based superconductors; the presence of weak links at grain boundaries and perhaps within the grains as well; and the ability or strength of flux pinning [81, 233-237].

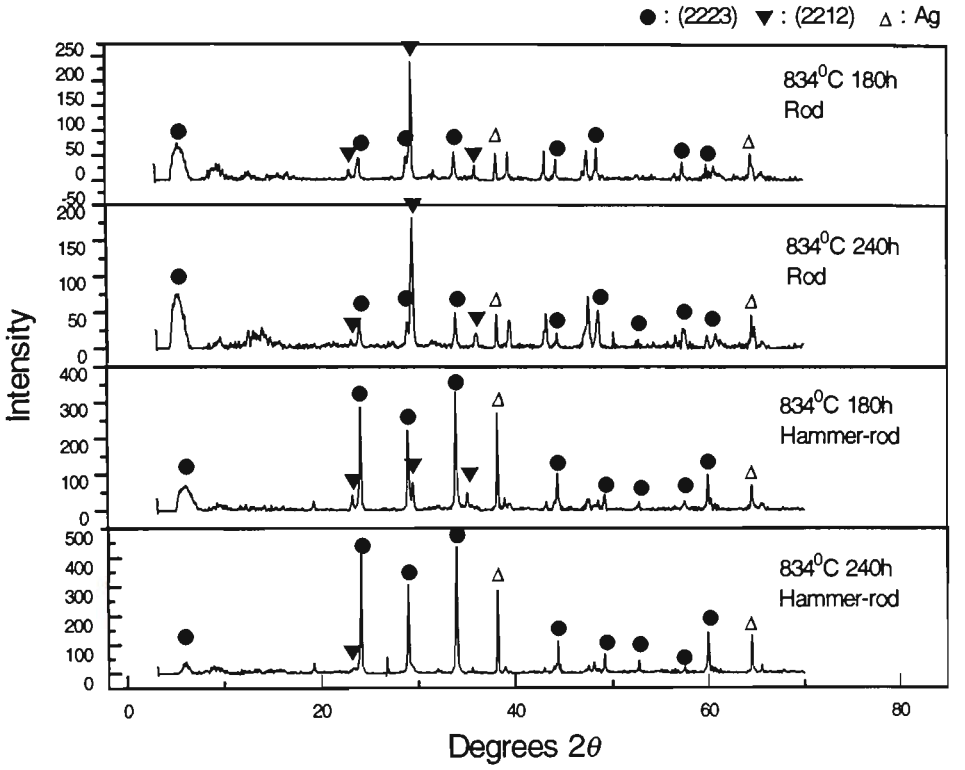

Figure 3.3 *XRD patterns of the S samples at different sintering stages (834^{0}C 180-240 h).*

SEM images of fractured surfaces of the S samples (Fig. 3.4(a)-(b)) after 180 h of sintering time show similar grain morphology between the two samples with different initial packing density. For a further 60 h of sintering, the SEM images (Fig. 3.4(c)-(f)) reveal generally larger grain morphology and higher degree of texture (less voids and fewer weak links) for the sample with higher initial packing density. This compactly formed core indeed assists in the formation of high-T_c phase as can be from Table 3.1 (calculated from Fig. 3.3). The difference between final J_c values of the higher and lower initial packing density tapes dictates why these features are desirable.

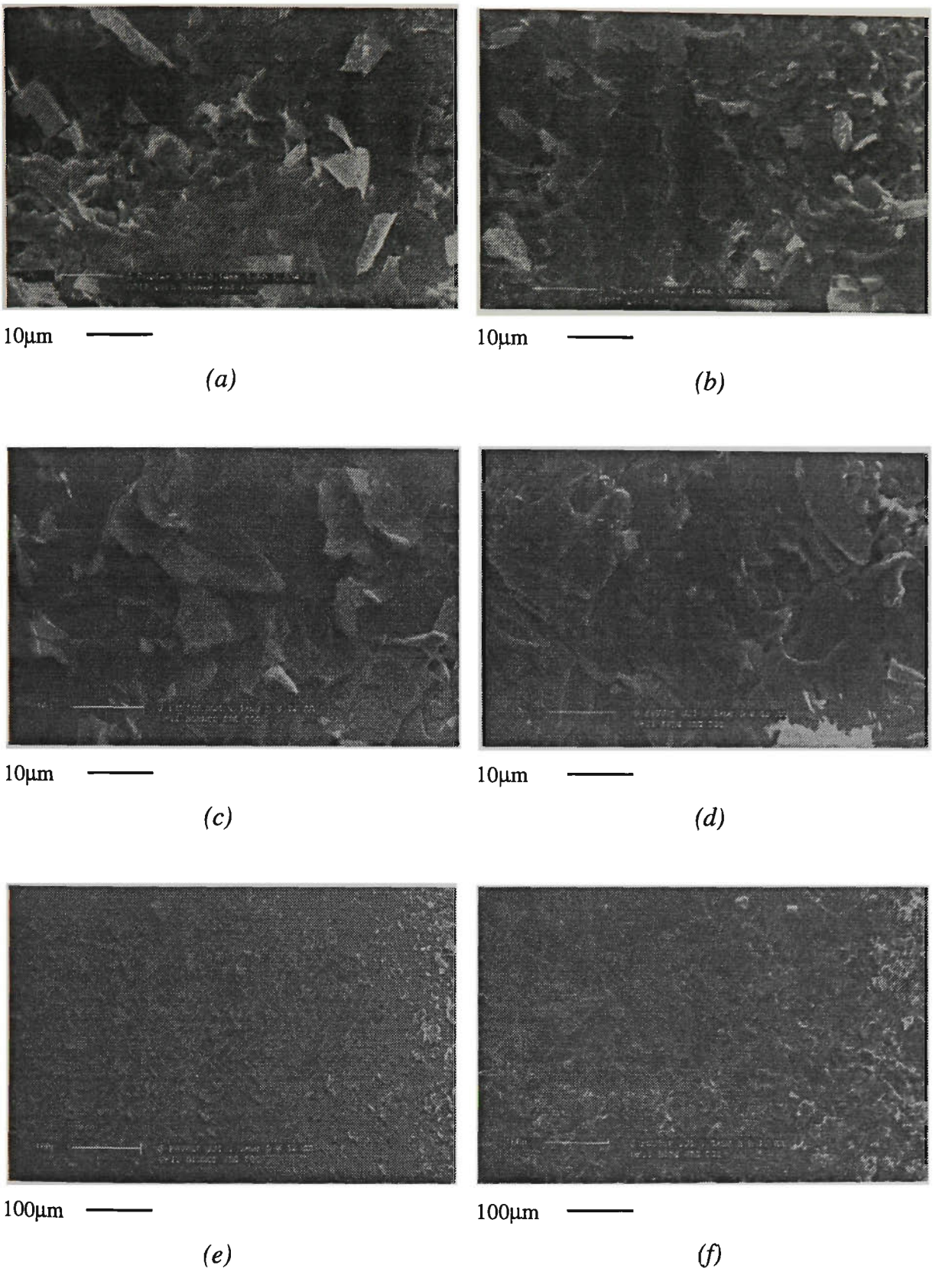

Figure 3.4 *SEM micro-images of samples (a) of S34180r , (b) of S34180hr, (c), (e) of S34240r, and (d) and (f) of S34240hr.*

Uniformity in the longitudinal orientation is crucial to sustain the high J_c value over the entire length of the tape. To compare uniformity between those made using 'hammer&rod', 'rod' and 'vibrator', SEM images and optical micro-graphs have been taken. Figures 3.5(a)-(b) are SEM images of fractured surfaces of (green) tapes showing how the undulation on the surface (or 'surface sausaging') is greatly reduced for the tape made with a vibrator. Figures 3.5(c)-(e) are optical micro-graphs of (red) tapes made with the same heat treatment and deformation process, showing the vibrator made tape have better uniformity along its longitudinal direction.

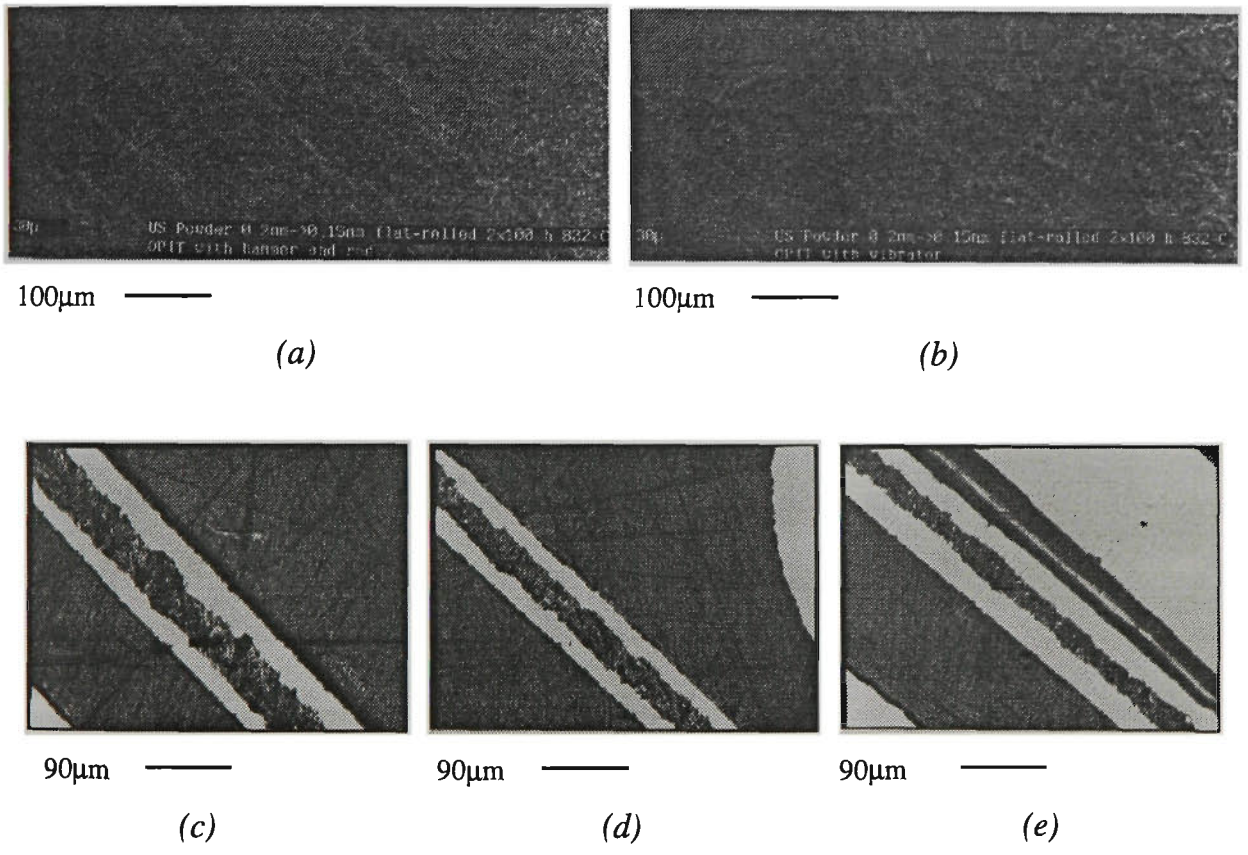

Figure 3.5 *SEM (a)-(b) and optical micro-slides (c)-(e) showing better uniformity in the longitudinal orientation, minimising the "surface sausaging effect" by using the vibrating method of PIT.*

For commercial applications the electrical as well as mechanical performance of high-temperature superconductors needs to be optimised. The electrical performance of HTSC

tapes are sometimes measured in terms of the engineering or conductor critical current density, J_e. This parameter is especially useful in long length multifilamentary tapes [238]. Thus by maximising the J_c and fill factor, J_e will be maximized. The mechanical performance aspect of the monocore short tapes can be seen from the normalised J_c values, (i.e., J_c/J_{co}, where J_{co} is the zero strain critical current density) versus surface bend strain, ε curves of Fig. 3.6. The surface bend strain, ε, is defined here as r_t/R where r_t is the half thickness of the conductor (core and silver) and R is the radius of the bend curvature.

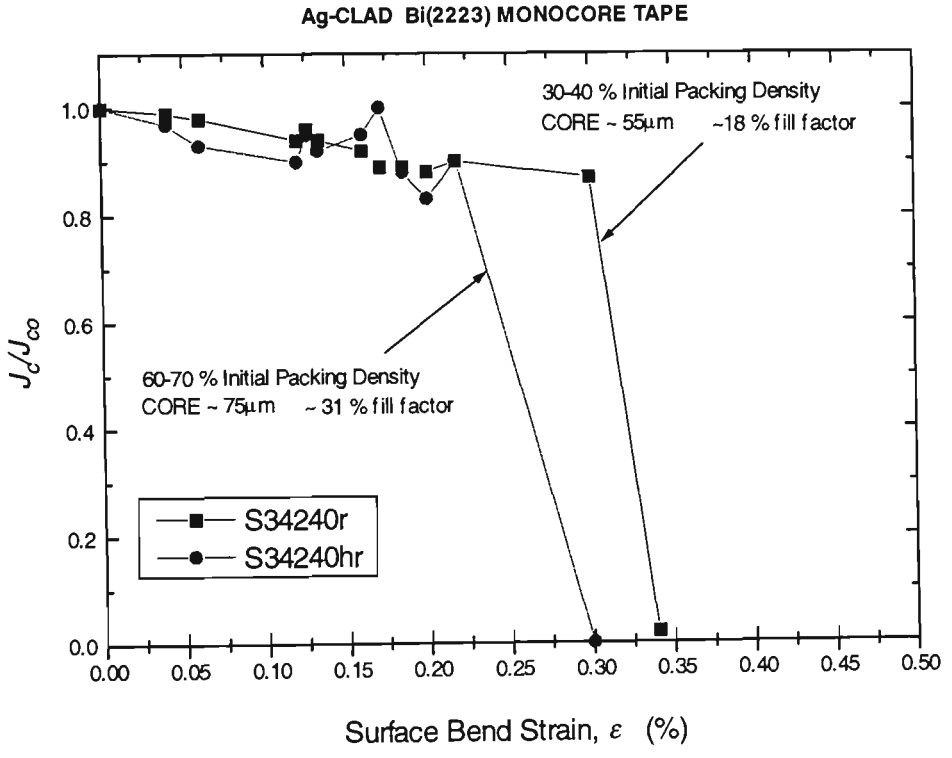

Figure 3.6 *Normalised critical current density versus surface bend strain curves of two different packing density monocore short tapes. Critical strains for superconducting core thickness' of 55 and 75 μm are approximately 0.34 and 0.23 % respectively.*

Figure 3.6 shows how the electrical transport performance of monocore short tapes degrades with increasing fill factor. This degradation is much more gradual with the initially less dense PIT tape. This perhaps attributable to the uniformity of the entire tape (as can be seen in Fig. 6(a)-(e)). Its critical surface bend strain is ~ 0.34 %. In comparison,

the initially higher density PIT one displays much more variation in mechanical performance with an abrupt degradation at a critical surface bend strain of about 0.23 %. It appears that there is a compromise between electrical and mechanical performance.

3.2 Sintering Periods

With HTSCs, successful fabrication of long length tapes for full-scale applications such as coils and magnets requires accurate control of deformation and heat treatment to achieve the optimal result as far as materials processing is concern. The transport and magnetic properties of the tapes are highly dependent on how well the tapes were made [90, 239-242]. Another important feature of HTSCs is the dissipation below T_c in magnetic fields caused by thermally activated flux depinning of vortices [243, 244]. Since practical applications normally involve high field generation, the prevention of flux-line movement at high field is the prime factor in the production of high current density devices.

Unlike Bi-2212 tapes, the fabrication of Bi(Pb)-2223 HTSC tapes normally involve more than one sintering process, with an intermediate mechanical deformation step either by means of rolling or pressing between each sintering period [245-251]. This increases the chance of damaging the tape by accidental breakage of the superconducting core due to repeated processes. For a particular precursor with a specific stoichiometry, it is desirable to determine the optimal thermo-mechanical treatment in order to maximize the J_c. One of several crucial parameters is the sintering period between which the sintered tape is pressed or rolled. It is therefore desirable to determine the best least number of sintering periods in order to minimize the frequency of handling on these tapes. To achieve this, three differently processed precursor powders all having the same stoichiometric composition were used to fabricate monocore short tapes.

This section is set out to show the effect of different sintering periods on the microstructure, phase development and electrical transport properties of high-T_c superconducting Bi(Pb)-2223 composite tapes.

3.2.1 Experimental Details

The monocore HTSC tapes were fabricated as follows. A silver tube of 99.99 % Ag purity, one meter long having inner and outer diameters of 4.5 and 6.5 mm respectively was burnished, heated at about 600^0C to eliminate organic contaminants, then cut into shorter sections of length 100 mm. One of the ends from each of these Ag sections were sealed by 'cold forming' on a lathe ready for oxide-powder-in-tube (OPIT).

Three different powders were used to see whether different powder processing routes have any effect on the final properties of the tapes. They are designated as powders S, T and D, all with the same composition (BPSCCO) with their stoichiometric ratio being Bi:Pb:Sr:Ca:Cu = 1.84:0.35:1.91:2.05:3.05 (refer to section 2.1). The powders were thoroughly dried in a muffle furnace (with an opening, to allow any gases to escape) between 100 and 200^0C for several hours, then packed into 100 mm silver tubes to be rolled into wires and tapes. The initial packing density using OPIT method was calculated to be approximately 65 % for all three powders.

The opened ends of the powder filled tubes were then partly sealed by cold forming so that no powder is lost during the mechanical deformation process yet allowing trapped gases such as H_2O and air to escape during deformation, after annealing between 500 and 600^0C. Wires were then made by 'square groove' rolling with 10 to 20 % reduction per pass. Long length tapes were processed by flat-rolling the wires, until a final thickness of ~ 0.12 mm was achieved. The final tape samples were obtained from cutting the long tapes into short sections of approximately 35 mm.

These short segments of tapes were then placed on top of an alumina ceramic plate of ~ 99 % purity. The plate and tapes were then embedded inside a moderately friable alumina semi-cylindrical brick. The whole unit was then inserted into a tubular furnace at a position well within the furnace's hot-zone (within $\pm$ 1^0C). Sintering of tapes was conducted at ambient air atmosphere. The sintering schedule used was determined from

the green (unreacted) tape's change in melting point based on TG, and DTA respectively. DTA was carried out using a 'Setaram' thermo-analyzer, with the heating rate being 2^0C/min reaching ~ 900^0C. All samples were processed with the same sintering condition based on the results obtained from DTA and TG curves (refer to section 2.2.4). Throughout the sintering process a type K thermo-couple of chromel (Cr-Ni) and alumel (Al-Ni) with stainless steel sheath was used to monitor the temperature.

The sintered tapes were pressed uniaxially within the range of 0.4 - 1 GPa in between sintering periods at room temperature. Tapes from each batch (for each powder) were treated together for every different sintering period to ensure consistency. Each tape's thickness was reduced by roughly 20-30, 15-20, 10-15 % after the first, second, third and successive sintering periods.

After each sintering period, a small section of the tape was cut for XRD, and SEM analyses. For XRD analysis, a ~ 5 mm × 5 mm exposed fractured surface of the section from the tape was used. A razor blade or scalpel was used to split the surface of a small section from the tape open and tweezers to peel the rest with a glass slide to flatten the fractured surface. Microstructural characterization was performed with a Leica Cambridge Stereoscan S440 scanning electron microscope analyser, using backscattered and secondary electron images of the surface. Magnetic field dependence of transport critical current density for S, T and D samples with the applied field parallel and normal to the *c*-axis was made at LN temperature of 77 K in static fields up to 1 Tesla. For dc-resistivity and ac-susceptibility measurements, more samples of S, T and D powders from a different batch were used. These samples went through the same heat treatment and mechanical deformation sequence as those used in transport measurements. With ac-susceptibility it was necessary to cut the treated tapes longitudinally into thin strips for measurements. These measurements were obtained using a mutual inductance bridge, conducted at a fixed ac of 350 mG and fixed frequency of 1 kHz.

3.2.2 Microstructure and Phase Development

Figure 3.7 shows the SEM images of the surfaces of three S samples. They are identified as S-6×40h, S-3×60+30h and S-100+120h according to the sintering period and time used. These surface images are representative of the result along the entire tapes' surfaces due to different sintering periods employed. One common feature observed for all three surfaces of the tapes was the wavy and plate-like grain formation. The plate-like grain structure in all three samples show an average plate dimensions in the range of 10 to 50 μm (and perhaps even larger still). With S-6×40h however, the plate like grains have been broken due to surface cracks. These visible microcracks (a few microns wide) due to insufficient sintering period time for complete healing to take place are mechanically induced and run parallel to the tapes length, which are reminiscent of pressed tapes [182].

Sample S-100+120h on the other hand exhibits a more flaky morphology showing its high porosity nature due to prolong sintering for each period. These large voids and cracks (due to extensive grain growth) can only have a negative effect on the enhancement of flux-pinning ability in Bi-2223 tapes (refer also to Fig. 3.15 for comparison). In addition, sample S-3×60+30h, with sintering period of 60 h, revealing a better surface microstructure in terms of cracks and porosity. Note that the extra 30 h of sintering time added on to the S-3×60+30h was to make the sintering time comparable to the other two samples (240, 210 and 220 hours) as well as to increase the high-T_c phase of 2223 contents.

The corresponding X-ray diffraction patterns for the three samples are depicted in Fig. 3.8. The relative percentages of 2223 to that of the total phase contents of 2223 and 2212 are approximately 76, 94, and 86 for S-6×40h, S-3×60+30h and S-100+120h respectively. As can be seen from these patterns, the dominance of the 2223 phase over the 2212 is strongest for sample S-3×60+30h.

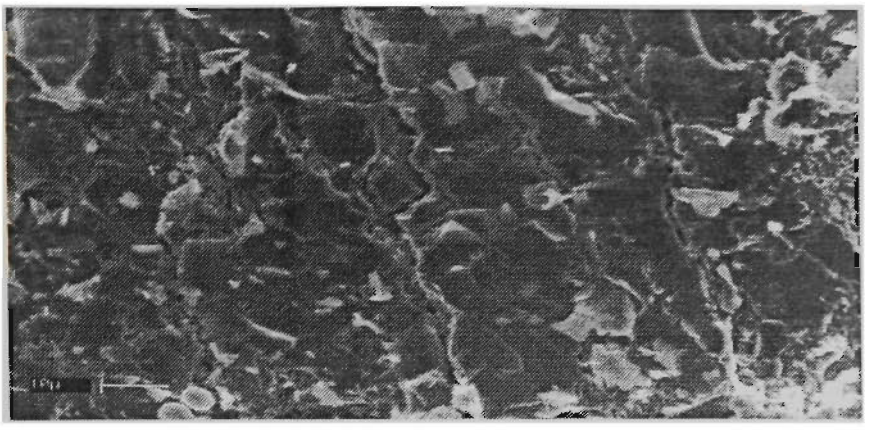

(a) S-6×40h

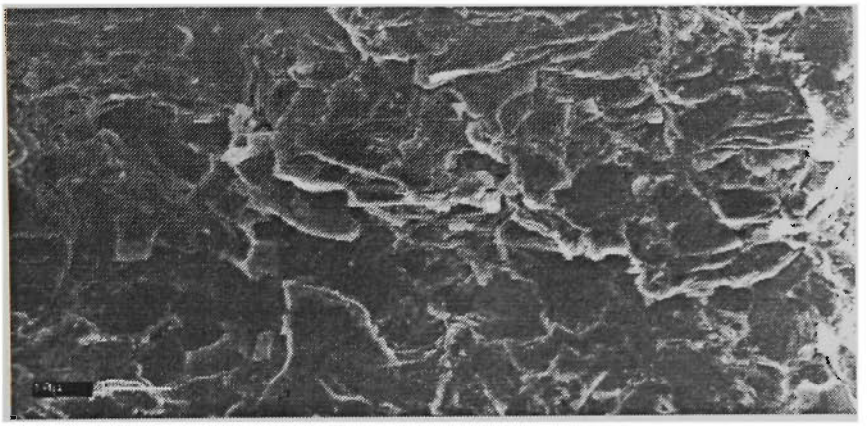

(b) S-3×60+30h

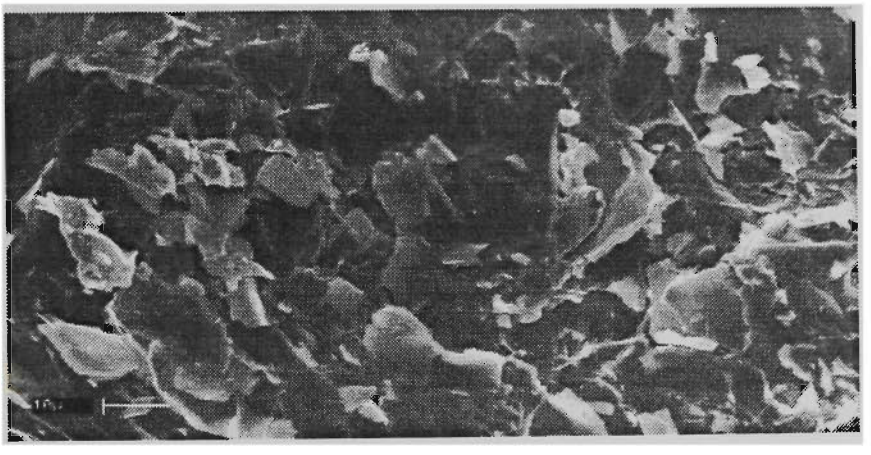

(c) S-100+120h

Figure 3.7 *SEM images of the longitudinal surfaces along the ab-plane of S samples after (a) 6×40 (b) 3×60+30 (c) 100+120 hours of sintering time. Short sintering period can lead to a fractured grain growth due to insufficient time for the mechanically induced cracks to heal, as in (a), while prolong heat treatment can result in greater porosity, as shown in (c).*

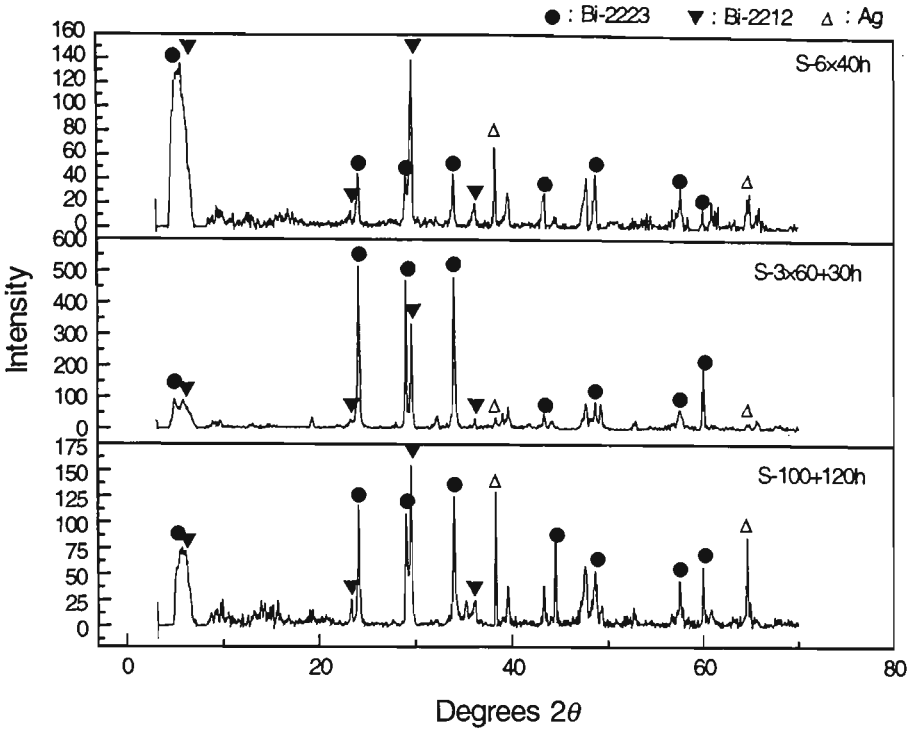

Figure 3.8 *X-ray diffraction patterns for three S-tapes with different sintering periods used. Although the total sintering time for each sample does not differ much, the different sintering periods employed exhibit significant contrast in the present of the relative amount 2223 phase. The relative percentages of 2223 to that of the total phase contents of 2223 and 2212 are approximately 76, 94 and 86 for sintering periods of 40, 60 and 100h in duration respectively.*

Careful examination on the microstructure of samples heat treated with sintering periods of 40 h from SEM images for T samples in Fig. 3.9 reveal microcracks (from a few to several microns wide) appearing as a common feature among these samples. The induced cracks are not the result of thermal cycle from the J_c measurement or from polishing. The planes of the cracks in these uniaxially pressed tapes run longitudinally due to greater width strain than length strain, most apparent with T-160, T-200 and T-240. These cracking patterns are consistent with the 'stress state' models proposed for rolling and pressing by Korzekwa *et al* [230]. The reason is that the tape is much longer than it is wide thus creating a greater frictional constraint in the direction of current flow which leads to

greater width strain. The 'stress state' models however neglect the frictional effect from the much softer silver sheath. When under extreme pressure, as is the case during intermediate uniaxial pressing between sintering periods, the silver sheath spreads itself over the microscopically uneven surface of the ceramic core.

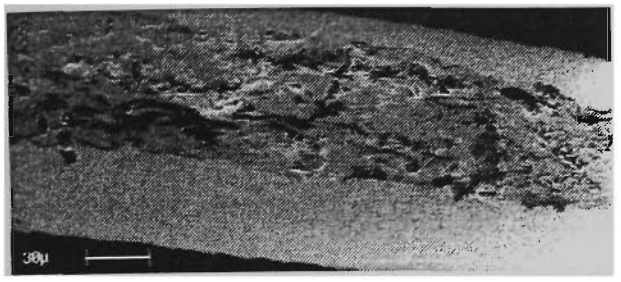

T-40

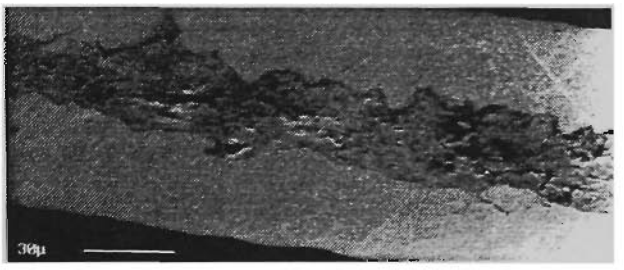

T-80

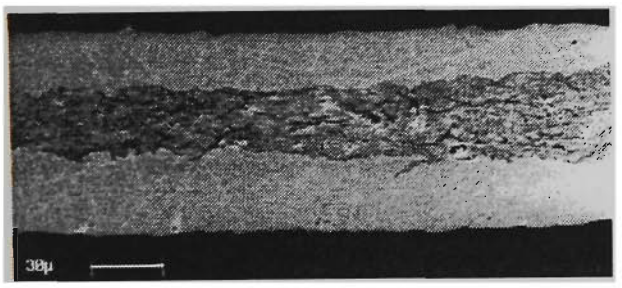

T-120

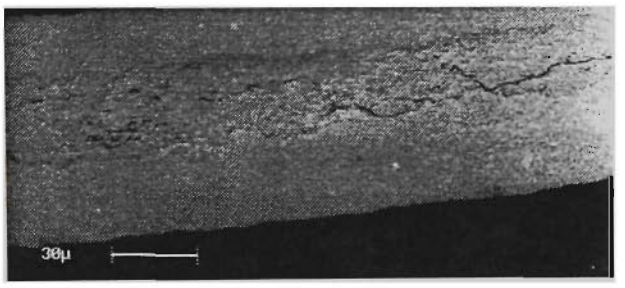

T-160

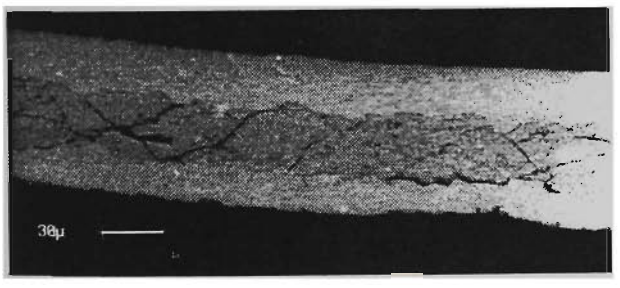

T-200

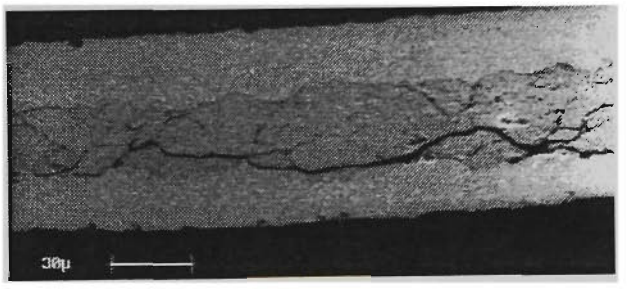

T-240

Figure 3.9 *SEM images of the transverse cross-sections for T samples with 40 h sintering period.*

The interfacial strength of core-matrix is enhanced during heat-treatment. As the number of deformation steps is increased the silver matrix thins out and can easily be broken if the pressure applied is too great or if there is pre-severe surface fracturing of the ceramic core which can dig into the silver sheath, since the ceramic core is much harder than the sheath.

The breakage on the surface of the tape will become more apparent during sintering and can be visible as little 'black-spots' (caused also by particles of dirt impregnated into the silver matrix during deformation) exposing the superconducting core. In addition, undesirable surface fracturing as well as insufficient sintering time can lead to unhealed cracks induced during pressing whose planes run parallel to the superconducting/silver interface. This is indicative of the strong bonding at the interfacial layer between Bi-2223 and silver.

For tapes with sintering periods of 100 h or greater, fewer cracks were found as there was sufficient time for healing to take place. Only SEM images of T samples are shown here, in Fig. 3.10. The grains of these samples were found on average to be larger than those with smaller sintering periods, as the grain growth is very much favoured by prolong sintering. One drawback with long sintering period is that as the degree of preferred orientation of 2223 grains increases during sintering the core density decreases dramatically as greater porosity is incurred due to the formation of pores.

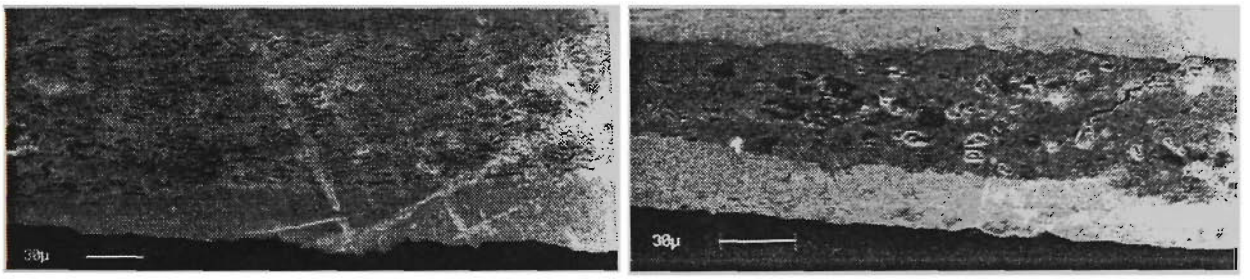

T-100 *T-220*

Figure 3.10 *SEM images of the transverse cross-sections for T samples with sintering periods ≥ 100 h.*

Samples with 60 h sintering periods on the other hand were found to exhibit in general a much denser ceramic core and a less disruptive microstructure. The SEM images of these samples are depicted in Fig. 3.11. These samples have consistently shown to have a much smoother core/silver interface in comparison to other samples with sintering periods of 40 and 100 h. The intrusion of Bi-2223 grains into the silver matrix normally creates a

misalignment of grains which ultimately degrades the J_c [253]. This disruption in microstructure has been suppressed greatly through the use of appropriate sintering period and frequency of pressing. The 60 h sintering period has indeed been shown to produce tapes with better overall electric and magnetic properties over those heat treated with 40 and 100h [254] and is in good agreement to the development of superior microstructure as revealed through SEM images. Once again, an extra 30 h of sintering time was added to those with sintering periods of 60 h duration after 180 h (for S and T samples only, with much reduced intermediate uniaxial pressing force) to increase the percentage of 2223. The SEM images obtained here (after 210 h of sintering time) further suggests that the amount of mechanical force applied to the surface of the tape during intermediate deformation and sintering period are inter-related [255, 256].

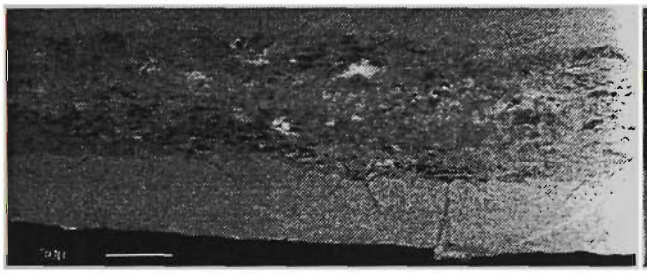

S-60

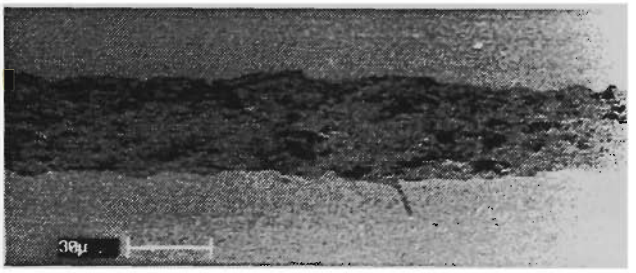

S-120

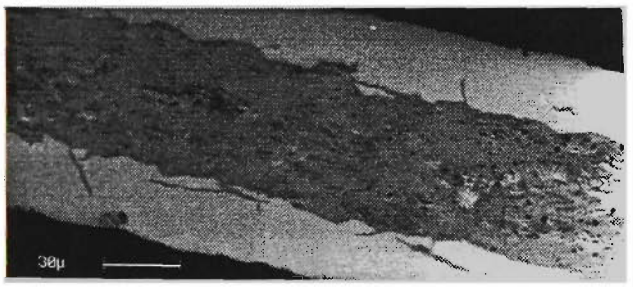

S-180

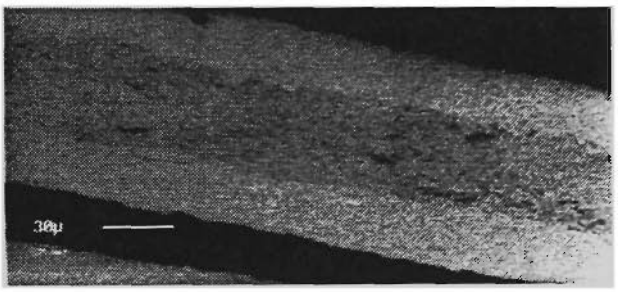

S-210

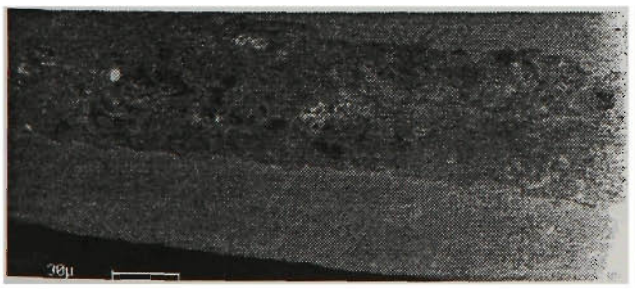

T-60

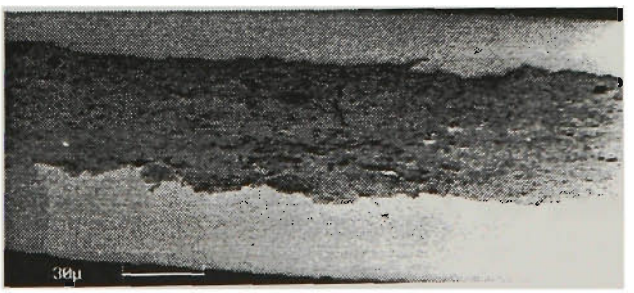

T-120

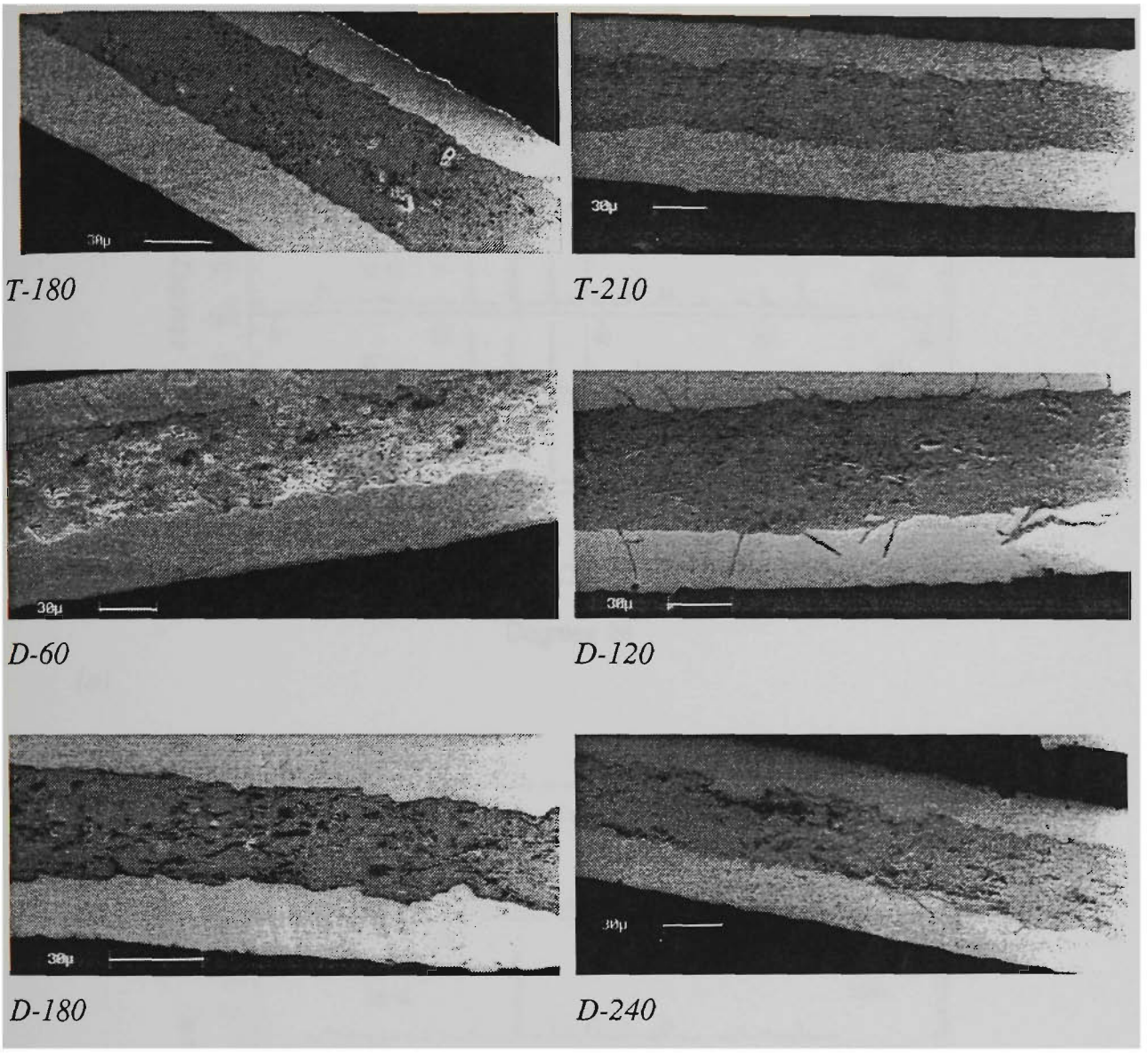

Figure 3.11 *SEM images of the transverse cross-sections for S, T and D samples with 60h sintering period (up to the first three sintering steps).*

Heat treatment of Bi-(Pb)-Sr-Ca-Cu-O whether in the form of powder or tape usually goes hand in hand with the characterization on the phase transformation of 2223 by means of XRD [257-261, 82, 88]. XRD analysis was performed on a short section of tape after every sintering period, as was done with SEM. The results are shown only for T samples in Fig. 3.12(a)-(c), demonstrating the behaviour between sintering period and phase development.

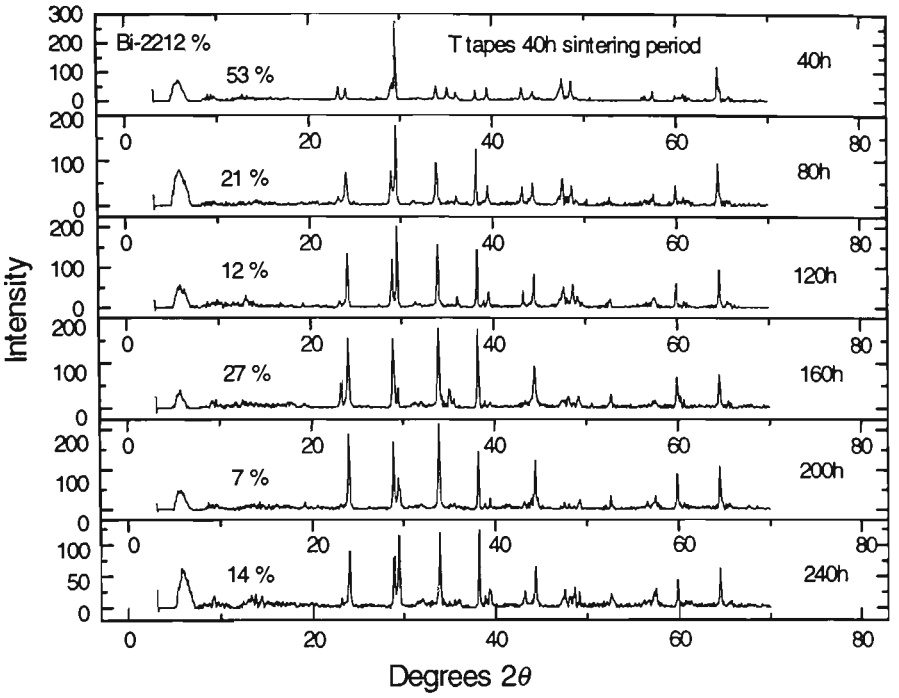
Bi-2212 %
T tapes 40h sintering period
53 %
40h
21 %
80h
12 %
120h
27 %
160h
7 %
200h
14 %
240h
Intensity
Degrees 2θ

(a)

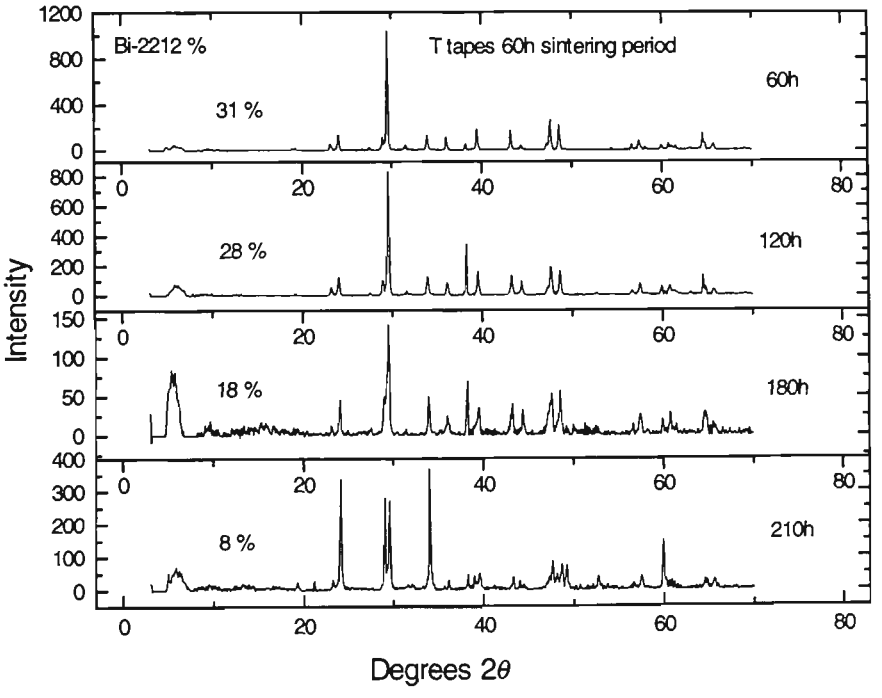
Bi-2212 %
T tapes 60h sintering period
31 %
60h
28 %
120h
18 %
180h
8 %
210h
Intensity
Degrees 2θ

(b)

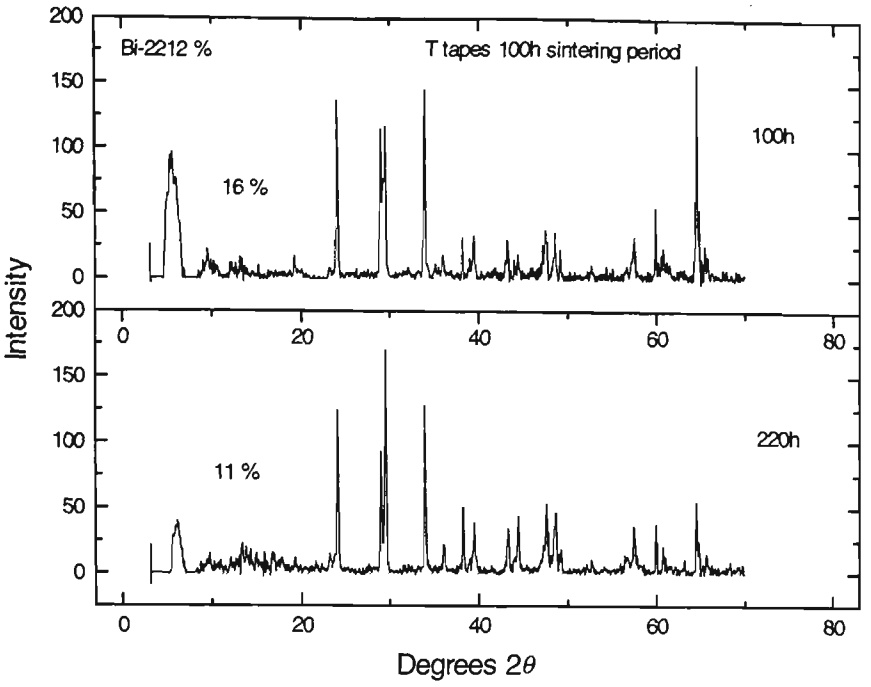

(c)

Figure 3.12 *XRD patterns of T samples after every (a) 40h (b) 60h (up to the first three sintering steps), and (c) ≥ 100h sintering period.*

For samples with 40 h sintering periods, a notable fluctuation between 2223 and 2212 phases was found after approximately 120 h (the third sintering step). This is possibly due to insufficient sintering time to necessitate the recovery of the 2223 grains which being partially 'destroyed' (or altered) after intermediate deformation prior to sintering. Recent work [256] has suggested that intermediate deformation (at room temperature) between sintering periods does indeed affect the relative amount of high- and low-T_c phases significantly. This observation can be seen clearly when there is an increase rather than decrease in 2212 phase after further sintering with the T tapes of Fig. 3.12(a). The transformation process of the liquid phase with 2212 to 2223 for samples with 60 h sintering period, however, is much smoother (one way) in that there is no increase in the low-T_c phase due to the disruptive microstructure inflicted upon during intermediate pressing. Figure 3.12(b) demonstrates this trend.

For samples with longer sintering duration, i.e. those with sintering periods of ≥ 100 h (e.g. Fig. 3.12(c) for T samples), the rate of change of 2212 appeared to be relatively slower than those with shorter periods of heat treatment, possibly due to exhaustive liquid phase and low core density. This is perhaps attributable to the core density and connectivity of grains (larger contacting surface between grains) of the shorter period sintered samples as being much greater than those with sintering periods of ≥ 100 h, hence necessitating the conversion process. This rate of conversion is also much higher for 40 h period sintered samples than those sintered with sintering period ≥ 100 h. The overall conversion rate from low- to high-T_c phase for all samples is plotted in Fig. 3.13 for each sintering sequence in order to get a more general picture.

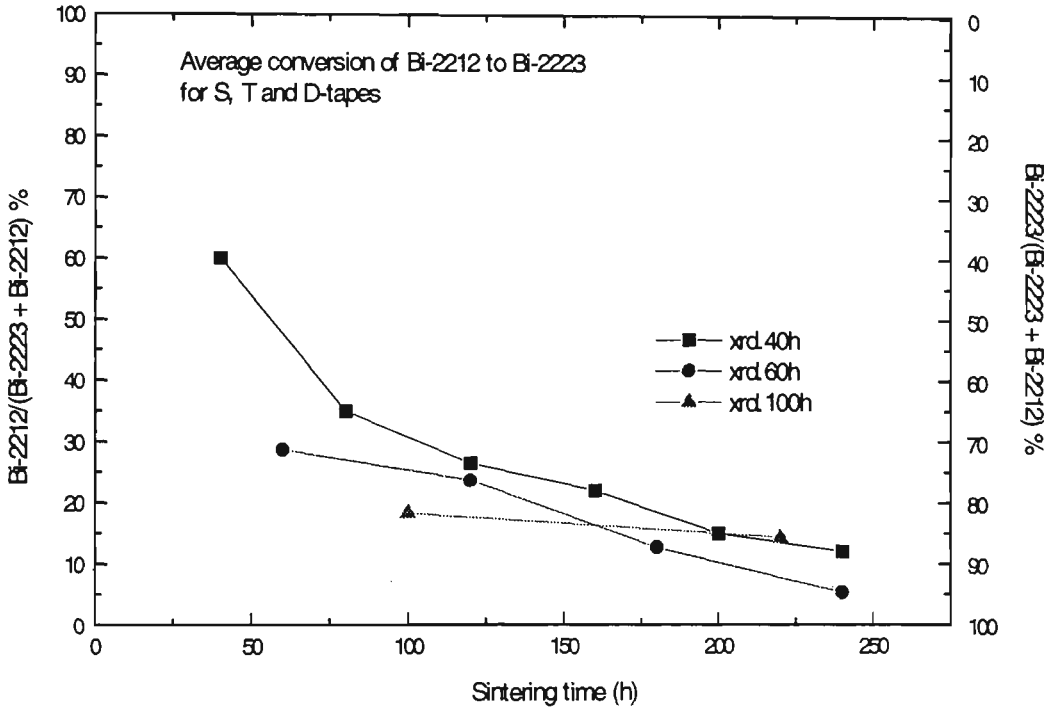

Figure 3.13 *Average conversion percentage of 2212 and 2223 for three sintering sequences. Each sequence is fitted with the average percentage of 2212 for samples S, T and D. For the 40 h sequence, the curve obtained from the fitted average of relative percentage of 2212 phase for S and T samples only.*

Each curve is the fitting average of relative percentage of 2212 and 2223 for a particular sintering period sequence of 40, 60 or 100 h. Each sintering sequence is fitted from the average relative percentage of 2212 for samples S, T and D. For the 40 h sequence, the curve was obtained from the fitted average of relative percentage of Bi-2212 phase for S and T samples only. The average conversion curves show, unsurprisingly, much similarity in the relative phase percentage regardless of sintering period, especially after 100 h of sintering time. For the short period sequence (xrd.40h curve), the conversion is much slower at first (less than ~ 100 h) while longer period sequences (xrd.60h and xrd.100h curves) show greater average conversion rate. This is understandable as more sintering time is allowed. After approximately 100 h of sintering time, all three curves show a similar average rate of phase conversion from 2212 to 2223, independent of powder processing, and perhaps independent of sintering period and particle size distribution. A closer examination of Fig.3.13 reveals curve xrd.100h has a slightly slower conversion rate (after ~ 100 h) possibly due to exhaustive liquid phase and low core density.

3.2.3 Electrical Transport Property

For each batch of S, T and D samples, the J_c (percentage 2212 and fill factor, λ) of each tape was calculated after every sintering for periods of 40, 60 and $\geq$ 100 h (Table 3.2). These values were then normalized to the maximum J_c value found for that particular batch. The three different periods of sintering sequences were then plotted for each batch against sintering time. This is shown in Fig. 3.14.

For all batches, the result is conclusive. The graphs of Fig. 3.14 indicate that the most desirable sintering period for S, T and D tapes is ~ 60 h for achieving the highest J_c. This is independent of powder processing route and particle size. Thus it can be stated more concisely that for any precursor powder with the stoichiometric Bi:Pb:Sr:Ca:Cu = 1.84:0.35:1.91:2.05:3.05, a sintering period of around 60 h should be most suitable in providing higher core density, and hence J_c for the processed tapes.

TABLE 3.2 *Critical current density (J_c), corresponding relative percentage of Bi-2212 phase, and percentage fill factor, at 77 K, 0 T for successive sintering periods in multiple steps of 40, 60 and 100 h for S, T, and D samples. Ω = 30 h for S, and T samples.*

Sintering time (h)	$\frac{2212}{2223+2212}$ (%)	J_c (A/cm^2) (**B** = 0T at 77K) and λ (%)
S-tapes		
1×40	73	523 (18.0 %)
2×40	44	4 383 (27.3 %)
3×40	33	8 091 (25.9 %)
4×40	33	8 052 (25.0 %)
5×40	13	5 753 (28.3 %)
6×40	24	3 180 (24.8 %)
		av. λ ~ 24.88 %
1×60	38	1 115 (31.1 %)
2×60	29	6 125 (24.5 %)
3×60	13	8 655 (31.3 %)
3×60+$\Omega^{@}$	5	9 370 (31.2 %)
		av. λ ~ 29.53 %
1×100	22	1 590 (38.8 %)
100+120	19	4 445 (32.6 %)
		av. λ ~ 35.70 %
T-tapes		
1×40	53	860 (28.0 %)
2×40	21	5 470 (20.8 %)
3×40	12	3 197 (27.7 %)
4×40	27	4 428 (31.4 %)
5×40	7	4 607 (24.4 %)

6×40	14	3 508 (32.5 %)
		av. λ ~ 27.47 %
1×60	31	1 213 (32.1 %)
2×60	28	7 394 (25.1 %)
3×60	18	11 120 (28.0 %)
3×60+Ω	8	13 522 (25.0 %)
		av. λ ~ 27.55 %
1×100	16	523 (32.9 %)
100+120	11	4 383 (29.2 %)
		av. λ ~ 31.05 %
D-tapes		
1×40		700
2×40		4 830
3×40		8 200
4×40		6 700
5×40		4 800
6×40		2 900
1×60	17	1 309 (27.7 %)
2×60	14	7 800 (31.6 %)
3×60	7	8 560 (25.7 %)
3×60+Ω	3	14 810 (29.7 %)
		av. λ ~ 28.68 %
1×100	17	1 833 (31.8 %)
100+120	13	11 230 (28.3 %)
		av. λ ~ 30.05 %

[@] *Ω = 30 h for S and T tapes.*

The calculated average percentage value of λ is also included in Table 3.2 where possible for each sintering period sequence. It appears that the percentage value of λ increases with

increasing period of sintering. This can be attributable to the porosity and presence of cracks for tapes with sintering periods ≥ 100 h.

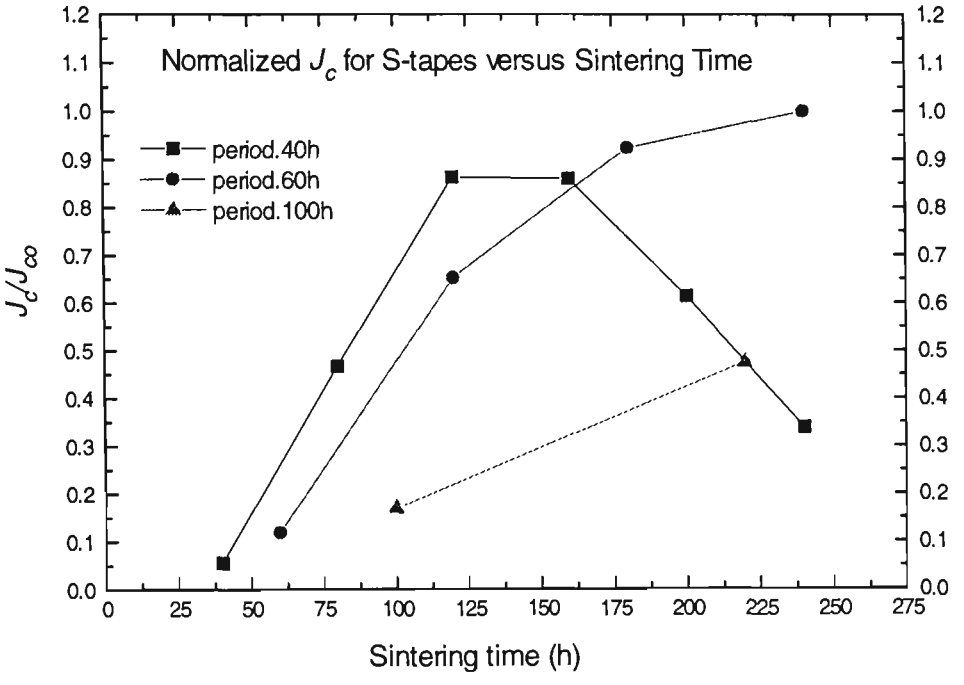

(a)

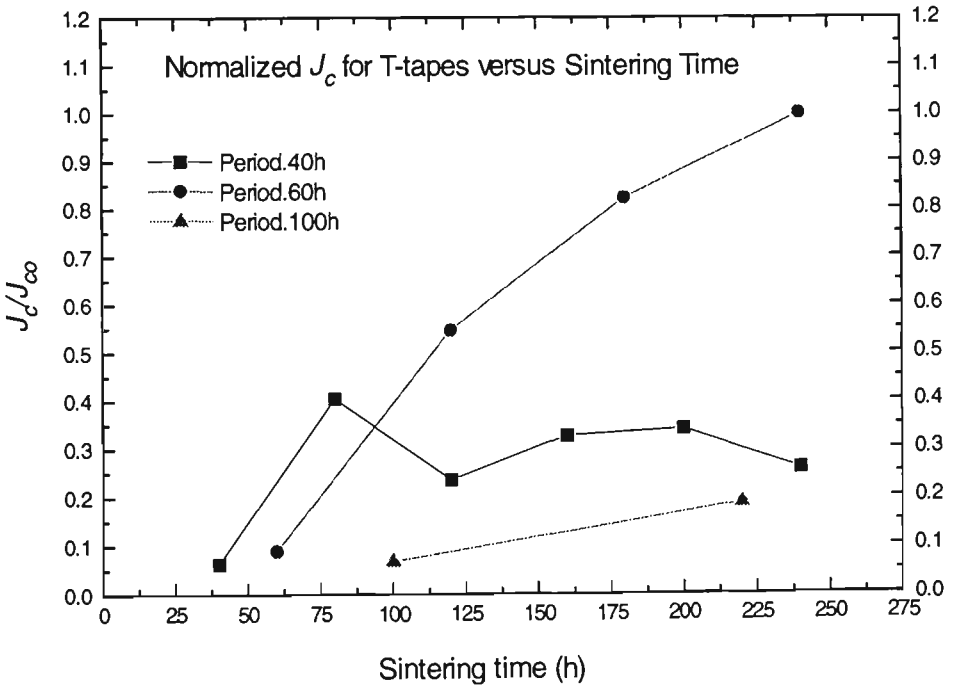

(b)

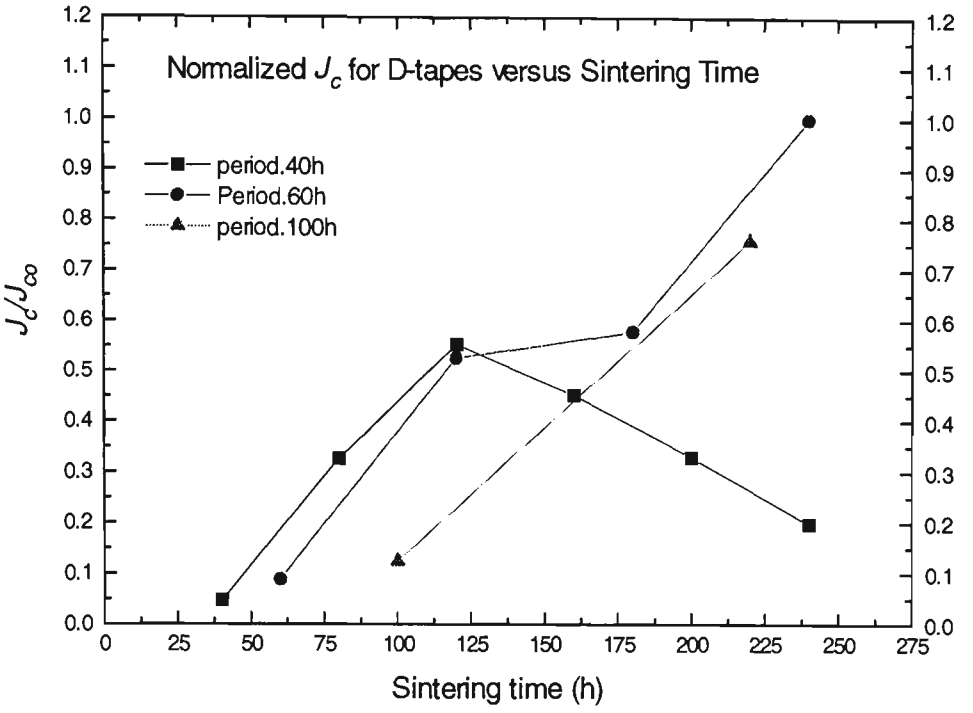

(c)

Figure 3.14 *Normalized J_c values for (a) S, (b)T, and (c) D samples against sintering time for different sintering periods.*

Indeed, it appears that there is an optimal sintering period for achieving higher J_c, which in more ways than one depends on powder composition and the amount of intermediate deformation between sintering periods. Table 3.3 shows comparatively the highest J_c in zero magnetic field at liquid nitrogen temperature (77K) for SF Bi(Pb)-2223/Ag S, T and D (as indicated in brackets next to the sintering period) treated with the corresponding sintering period. The measured value of λ for each tape is also included in Table 3.3. These J_c values are by no means maximized since only the sintering period has been optimized. With optimization performed on other processing parameters such as particle characteristics, mechanical deformation prior to sintering, intermediate deformation between sintering periods, stepwise reduction/increment in sintering temperature, filling factor, etc., it is expected that much higher J_c values can be achieved.

TABLE 3.3 *Highest J_c range achievable at 77K in self field with the fill factor interval for corresponding sintering period cycle. These J_c values were obtained after the second or third sintering step.*

Sintering period (h)	J_c (kA/cm^2) range at 77K	Fill factor range (%)
40 (S)	8-9	25-26
60 (S)	16-17	30-31
100 (S)	4-5	32-33
40 (T)	5-6	20-21
60 (T)	17-18	21-22
100 (T)	4-5	29-30
40 (D)	8-9	24-25
60 (D)	14-15	29-30
100 (D)	11-12	28-29

3.2.4 Pinning Force, Activation Energy, and Magnetic Property

Here, the flux-pinning force density via transport measurements and activation energy by resistivity measurements are compared between tapes made from three different precursor powders S, T and D. Figure 3.15 shows the magnetic field dependence of transport critical current density for all samples at 77 K, with the applied field perpendicular and parallel to the *c*-axis. The values of J_c for the 60 h sintering period samples always exhibit higher values in any current-field configuration and combination than those found for 40 and 100 h sintering periods, independent of powder processing methods. With S samples, the values of J_c drop much more slowly in the low-field regime for the 60 h sintering period tape. For comparison, these J_c values at 0.1 T sustained ~ 27.8 and 60.6 % of their zero field values with the applied field parallel and perpendicular to the *c*-axis respectively. This can thus be attributable to an improvement in the grain boundary, alignment [262, 232] and better interfacial microstructure. With increasing field, however, the degradation of J_c is slightly more pronounced. The J_c for all S samples appear to merge at high field region. For T and D samples, the values of J_c for the 60 h sintering period tape are also

generally greater. At 0.1 T the degradation of J_c with increasing field is roughly the same as those with 40 and 100 hour sintering periods. Thus samples made from T and D powders tend to sustain their original J_c better in high field regions. In any sense, it can be stated that Bi(Pb)-2223 tapes, with the given stoichiometric composition produced with sintering period of around 60 hour generally show superior transport property over those with 40 and 100 h sintering periods. Table 3.4 contains the percentage drop of J_c values for all samples in field of 0.1 T to zero field with the field applied both parallel and perpendicular to the samples' c-axis.

The right column of each graph of Fig. 3.15 shows the corresponding pinning force density, F_p defined as $\mathbf{F_p} = \mathbf{J_c}(B,T)\times\mathbf{B}$ versus the applied magnetic flux density, B at 77 K for each sample. As expected from transport measurements, $F_p(B)$ peaks highest for all samples treated with 60 h sintering period.

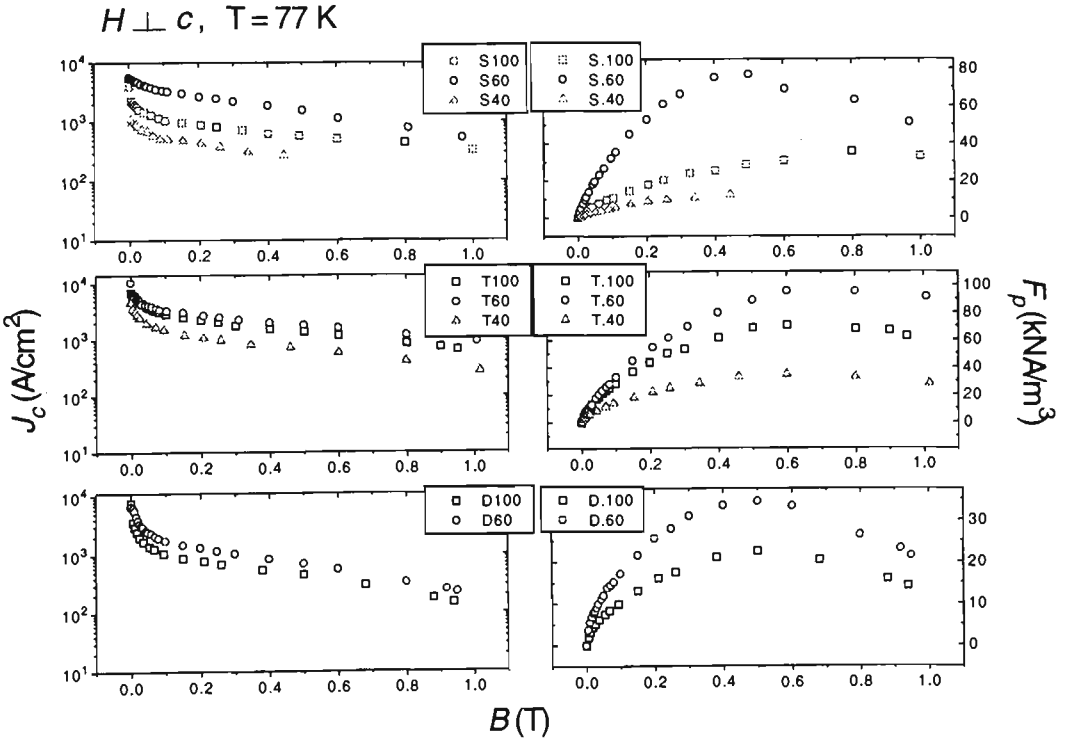

(a)

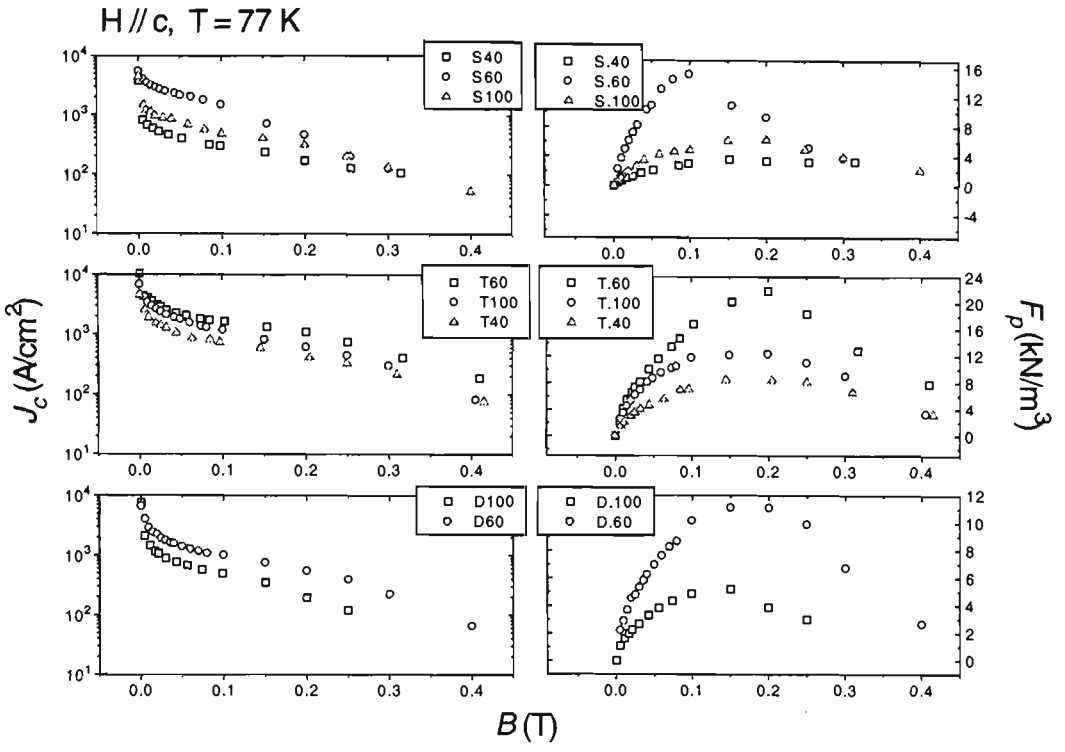

(b)

Figure 3.15 *Magnetic field dependence of transport J_c for S, T and D samples with the applied field (a) perpendicular, and (b) parallel to the c-axis. The J_c for the 60 h sintering period in each case exceeded those found for 40 and 100 h sintering periods. The right column of each graph shows the corresponding volume density of the flux-pinning force, F_p versus the applied magnetic flux density, B.*

Although the pinning force density does not say anything about the pinning mechanism of flux lines it does however, give an indication of how relatively strong the flux lines are being pinned as well as the shear strength of the flux-line lattice, for example the model proposed by Kramer to explain experimental results obtained for conventional type II superconductors [263]. The peak of $F_p(B)$ is found where the pinning strength of the flux lines equals the shear strength of the flux-line lattice. Flux motion occurs by depinning of pinned lines in the lower field range ($B < B_{peak}$ region, B_{peak} is the field where maximal pinning, F_{pmax} occurs) while in the higher field ($B > B_{peak}$) flux line movement is due to synchronous shear of flux line lattice around strongly pinned lines. Results obtained for S

samples have indicated that the 60 h sintering period sample exhibits greater pinning strength as the peak of F_p occurs at a lower reduced field region as shown in Fig. 3.15. This behaviour is less apparent with T and D samples as the maximum pinning force density peaks at about the same magnetic flux density for each sample in both orientation of applied field. Note that the apparent "discontinuity" in the $F_p(B)$ curve for S40 tape (B > 0.1 T) of Fig. 3.15(a) is not a consequence of the presented cracks but merely an incompletion of experimental measurements. Nevertheless, the difference in pinning strength between tapes with different sintering periods can still be observed with S samples.

TABLE 3.4 *Percentage drop of sample J_c values at 0.1 T field to J_c values at zero field parallel and normal to the c-axis.*

	S ($J_{c\,0.1T}$ /$J_{c\,0T}$)		T ($J_{c\,0.1T}$ /$J_{c\,0T}$)		D ($J_{c\,0.1T}$ /$J_{c\,0T}$)	
Sintering period (h)	**H** // *c*	**H** ⊥ *c*	**H** // *c*	**H** ⊥ *c*	**H** // *c*	**H** ⊥ *c*
40	8.0	13.2	15.9	32.2	--	--
60	27.8	60.6	15.9	31.1	15.4	26.0
100	10.9	23.5	17.2	41.2	6.6	14.0

The phenomenon of superiority of the 60 h sintering period samples in terms of their microstructure and transport properties over those heat treated for periods of 40 h and 100 h can further be revealed through the determination of the flux-pinning activation energy, U_0. It has recently been shown by Kusevic *et al* [221] that the determination of U_0 for Bi(Pb)-2223 tapes enables a clearer comparison in any improvement made since U_0 is representative of the tapes bulk characteristics. More accurate values of U_0 can be obtained from transport rather magnetic measurements due to the widening of the transition. The calculation of U_0 made here by using the 'Line Pinning Model' [264] where U_o was approximated from resistivity measurements [265, 266] via an Arrhenius-type method. With the assumption that the resistivity, ρ has the following dependence:

$$\rho(T) = \rho_o \exp(U_o / k_B T) \tag{3.1}$$

where k_B is the Boltzmann's constant.

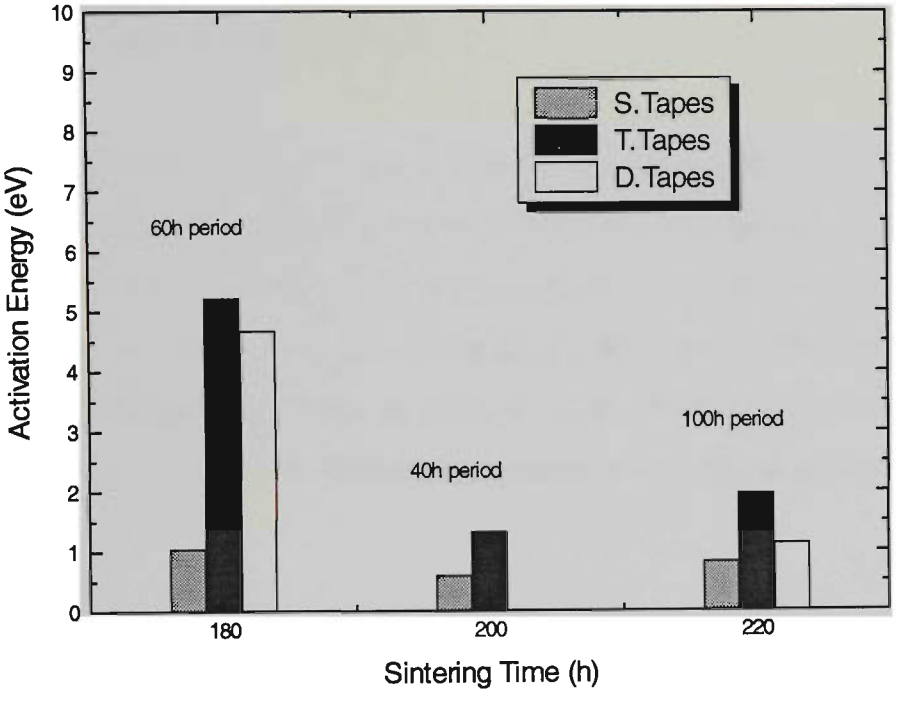

Figure 3.16 *Activation energy obtained via resistivity measurements from the Arrhenius-type method for different sintering periods. U_o for a sintering period of 60 h was consistently found to be greater than sintering periods of 40 and 100 h for three different precursor powders of S, T and D type.*

Thus by plotting ln(ρ) against $1/T$ from ρ *vs* T, the slope gives the activation energy U_0. Note that ρ is also field dependent. The results obtained here (perhaps qualitatively), represented in Fig. 3.16 show more convincingly that there is a sintering period for which the activation energy is greatest. In particular, samples with 60 h sintering period exhibit relatively larger U_0 over those with sintering period of 40 h and 100 h. It must be emphasized that since there are relatively few data points during the transition from the normal to the superconducting state, the values obtained here are within experimental

errors. Dou *et al* has shown that a slower decrease in J_c with increasing field normally indicate enhanced flux-pinning [267], however the transport measurements for S samples in particular in fields perpendicular to the tapes' surfaces show a more rapid decrease in J_c for the 60 h sintering period sample over the others with increasing field yet resistivity measurements (on a different batch) have indicated higher activation energies for those with 60 h sintering period. This is not inconsistent in the sense that the resistivity measurements were made at zero (or self) field.

Even so, the conclusion is quite clear in that samples with a sintering period around 60 h do exhibit overall, better performance over those with a sintering period of 40 h and 100 h in terms of transport properties. Intragrain flux pinning can be increased to a maximum with the appropriate sintering period, of approximately 60 h, plus sufficient total sintering time to expedite the phase conversion of 2212 to 2223. A decreasing trend in pinning activation energy of samples is attributable to greater voids and defects as revealed by SEM microimages.

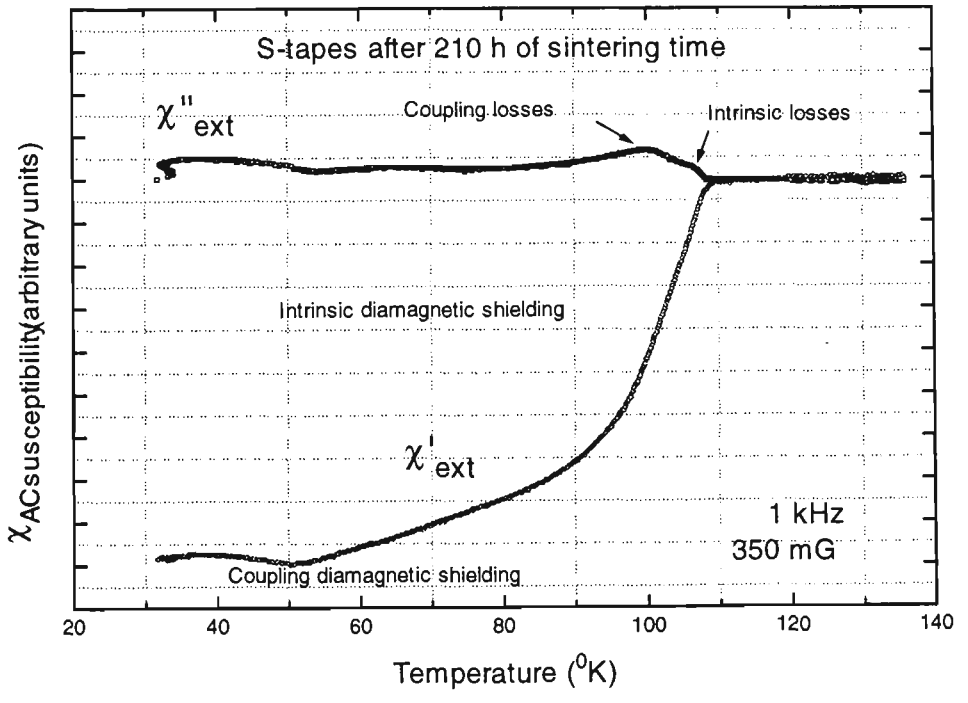

(a)

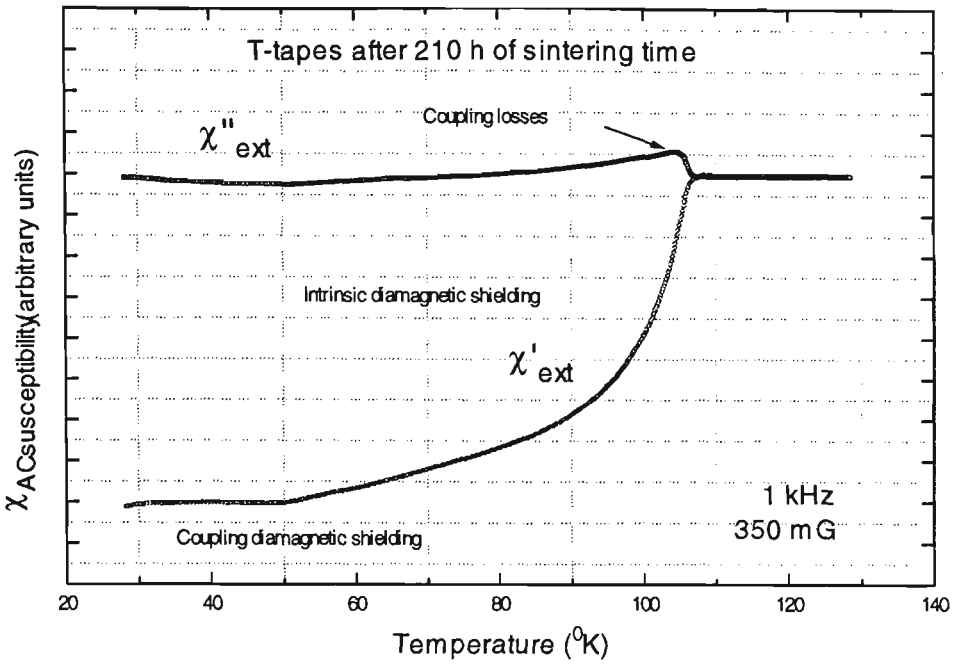

(b)

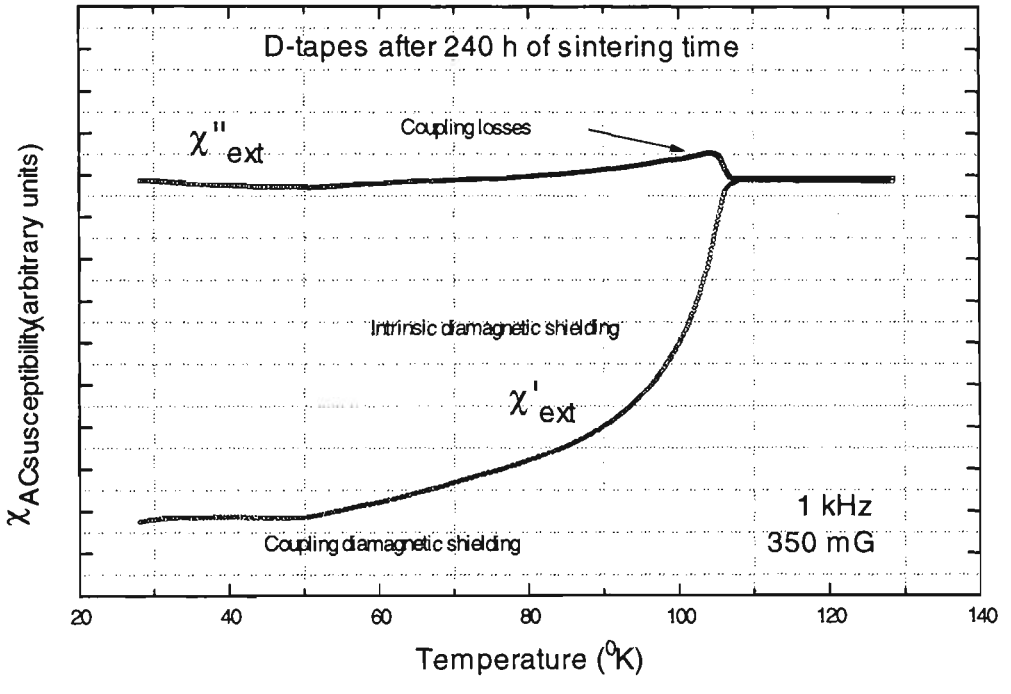

(c)

Figure 3.17 *Real and imaginary magnetic ac-susceptibilities, χ' and χ" as a function of increasing temperature in field of 350 mG at 1kHz, with the intrinsic and coupling segments identified.*

To further relate the samples' pinning behaviour to their microstructure, magnetic ac-susceptibility measurements were made for 60 h sintering period samples of S, T and D powders. Figure 3.17 shows the in-phase and quadrature components of susceptibility, χ''_{ext} and χ'_{ext} respectively for these three samples, where '*ext*' is used to indicate that the susceptibility measured here is characteristic of the *sample* (external susceptibility, e.g. tapes) and not the *material* (internal susceptibility, e.g. thin films) [268, 269]. For sample S, the onset temperature, defined here as the critical temperature T_c of the χ'-T curve, is ~ 108 K, and ~ 107 K for samples T and D, is due to intragrain shielding critical current. This intragrain shielding is most apparent with the S sample as the χ''-T curve shows the presence of an intrinsic-loss peak. The 'closeness' of this intrinsic-loss peak to the coupling loss might be reasoned that the measurement field is not large enough to separate the two components and/or that it may be attributed to the cracks presence in the superconducting ceramic core in the S sample considering the sintering sequence used for S and T samples (60×3+30 h) with a short final sintering period, even with much reduced uniaxial pressing force prior to this last heat treatment. For intergrain shielding of critical current, there is no obvious second drop in the χ'-T curve. However, the coupling-loss peak is quite pronounced with all samples. This particular peak represents the maximum hysteresis loss due to intergrain flux-line (or Josephson vortices) motion. In addition, it confirms that the transport measurements made were indeed that of decoupling currents in nature ($J_{c\text{-}decoupling}$), namely the transport current flows via multiple grains. From these coupling peaks, it appears that the hysteretic losses are slightly greater with the S sample, which explains the rapid J_c degradation with increasing field discussed earlier with the 60 h sintering period S sample. Furthermore, the χ''-T curve for the S sample shows a slightly broader coupling peak with a substantial shift to the lower temperature region. This means that the S sample has a weaker pinning force. With samples T and D however, the losses were less with narrower coupling peaks which indicates stronger pinning force. Hence the conclusion based on the results from ac-susceptibility measurements presented here might be that powders T and D are perhaps better candidates than S especially in high field applications.

3.3 Intermediate Deformation

For high field applications of high-T_c superconducting (HTSC) Bi-(Pb)-Sr-Ca-Cu-O tapes, high quality long lengths must be fabricated. Uniformity in the longitudinal direction as well as high superconducting core density and texture (or grain alignment) [270-272, 228, 230] are both desirable attributes of the processed long length tapes. For HTSC Bi(Pb)-2223 tapes, both SF and MF, it is generally agreed that a sequence of heat treatment and mechanical deformation steps are necessary to obtain high J_c [273-275, 232, 249, 251]. Since ultimately the performance of the HTSC tape depends on its microstructure, the roll of mechanical deformation from wire to tape and especially that carried out between sintering stages plays an important part in the quest of achieving the best possible microstructure. Although the highest J_c values reported thus far in a Bi(Pb)-2223 tape (by powder-in-tube) [276] were obtained by uniaxial pressing between sintering periods, longer lengths (order of kilometres) of superconductors can not efficiently be produced this way. Indeed, manufacturing production of long lengths of Bi(Pb)-2223 normally involves rolling as the intermediate deformation step between sintering periods for this sole reason.

As part of an extensive study on the processing of Bi(Pb)-2223 composite tapes leading to the production of long lengths for coil and magnet applications, various processing related parameters have been investigated in an attempt to enhance the performance of these tapes. Presented here is the effect of intermediate cold-rolling deformation on the transport property, microstructure, HTS conducting phase development, and fill factor on Bi(Pb)-2223 composite tapes prepared by methods of PIT and CTFF.

3.3.1 Experimental Details

The precursor powders used were D, T and U or US. More details can be found in section 2.2.1. Similarly, the processing details concerning CTFF composite and PIT MF tapes (MT31) are given in section 2.1. For SF PIT tapes, Ag tubes (of 99.99% purity) with inner/outer diameters 4.5/6.5 (thick wall) and 5.5/6.5mm (thin wall) were burnished, rinsed, cleaned, low temperature treated, sealed one end by cold forming and separately

filled with the precursors of D (thick wall tube), T (thick and thin wall tubes) and U (thick wall tube) using the standard PIT method. With precursor U however, a vibrator was used to assist in powder packing. Initial packing densities were roughly between 65 and 70% of the theoretical value (~ 4.35 g/cm^3 for Bi(Pb)-2223, and ~ 6.1 g/cm^3 for the unleaded Bi-2223) for D and T powdered tubes and approximately between 60 and 65% for the U powdered tube. Tape forming was performed by flat-rolling, after the wires had reached a diameter ~ 1.2mm. The reduction in thickness for the tapes committed between 5 and 15%. The final dimensions of the rolled tapes were ~ 0.125 mm thick, and ~ 2.0 mm wide for D and T (with thick-wall tube Ag tubes), and ~ 0.2 mm and 2.5 mm for U and T (using thin wall Ag tubes). Square and flat-rolling shared the same shaft one on each side of the rolling machine thus having identical rolling speed - refer to section 2.1 for more details.

Short sections of tapes with length about 40mm were cut and sintered at various sintering periods (discussed later). The temperature used for D and T samples was ~ 834 ± 1^{0}C and ~ 832 ± 1^{0}C for U samples. At the end of each sintering period, the I_c of each heat treated tape was measured (at liquid nitrogen temperature of 77K) using the standard '*four-terminal dc method*', with 1μV/cm criterion. The J_c was then determined by optically measuring the transverse cross-sectional area of the ceramic core of the cut tape embedded in resin, after being polished. A large number of samples from tapes with precursors D, T and U were prepared. Some went through the same sintering process and intermediate (cold) flat-rolling treatment. Each different run (a sequence of sinter-roll-sinter steps) contained between six and ten samples from the same batch (samples with the same precursor).

Transport measurements with a temperature range between 4.6 K and 86 K with applied flux density field up to 1 T were carried out specifically for two CTFF Bi(Pb)-2223/Ag MF tapes with J_c values of 15.8 kA/cm^2 (14 filaments) and 11.0 kA/cm^2 (37 filaments) at 77 K. The I_c was measured using the single pulse method. The saw-tooth pulses of 1-10ms with Imax ≤ 100A were used. The temperature was controlled with heated helium gas and was measured with a Au-Fe/Chromel thermocouple in contact with the sample.

X-ray diffraction (XRD) analysis with a diffractometer (Sietronics XRD Automation System) using Cu$K\alpha$ radiation, scanning electron microscope (SEM Leica Cambridge Stereoscan S440) observation, particle size analysis (PSA - Malvern Master Sizer) and differential thermal analysis/thermo-gravimetry (DTA/TG) were performed to check the existing phases, particle size distribution and partial melting temperature of the powders - section 2.2 for details. Bi-2212 was found to be the starting major phase for all precursors. The volume weighted mean diameters for particles of powders T, D and U were found (from bulk materials) to be 29.00, 11.02 and 5.09 μm respectively. The sintering sequence used for heat treatment was determined based on results obtained from DTA/TG analysis - refer to section 2.2.4 and Appendix E for more details.

3.3.2 Transport Property

The aim was to see whether there is a general trend or guideline to follow as to how much deformation is the best between sintering periods every time a Bi(Pb)-2223 tape is being prepared. Figure 3.18 shows the results of eight processed D tapes. The sintering period chosen here is 40 h. The tapes were sintered and each rolled with different reduction ratio, then a further sintering period of 40 h was applied to all samples. The graph indicates the best reduction ratio or percentage after a further 40 h sintering is between 25 and 30 % of the sample's thickness. Within this range of reduction ratio, the J_c is at its highest (normalized as shown in Fig. 3.18(a) where J_{c0} is the highest achievable value between sintering periods, ~ 1.2 kA/cm^2). For U and T samples (6 and 9 respectively) on the other hand a period of 100 h was selected as the first step of heat treatment after which different reduction ratio was applied to each sample which then sintered for an additional 80 h. The results are represented as bar graphs shown in Figs. 3.18(b), and (c). The highest J_c attainable was when the tapes were reduced with a ratio between 25 and 35 % for U samples (~1.8 kA/cm^2) and between about the 25 and 40 % mark for those of T (~5.5 kA/cm^2). The slight differences in reduction range between 40 h and 100 h could be explained in terms of the different sintering periods employed. Prolong sintering such as

100 h period (as discussed in the previous section (3.2), tends to exhibit large porosity and voids.

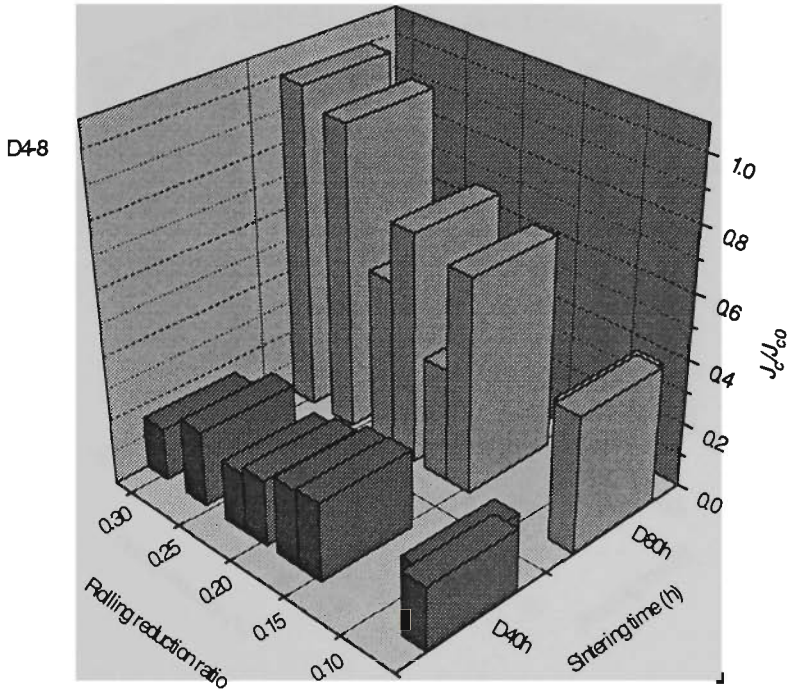

(a)

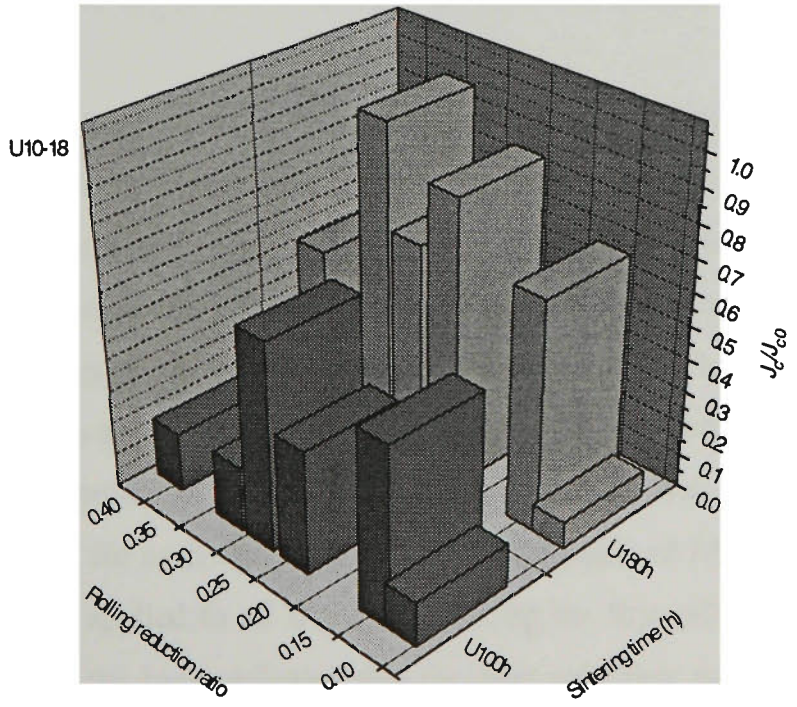

(b)

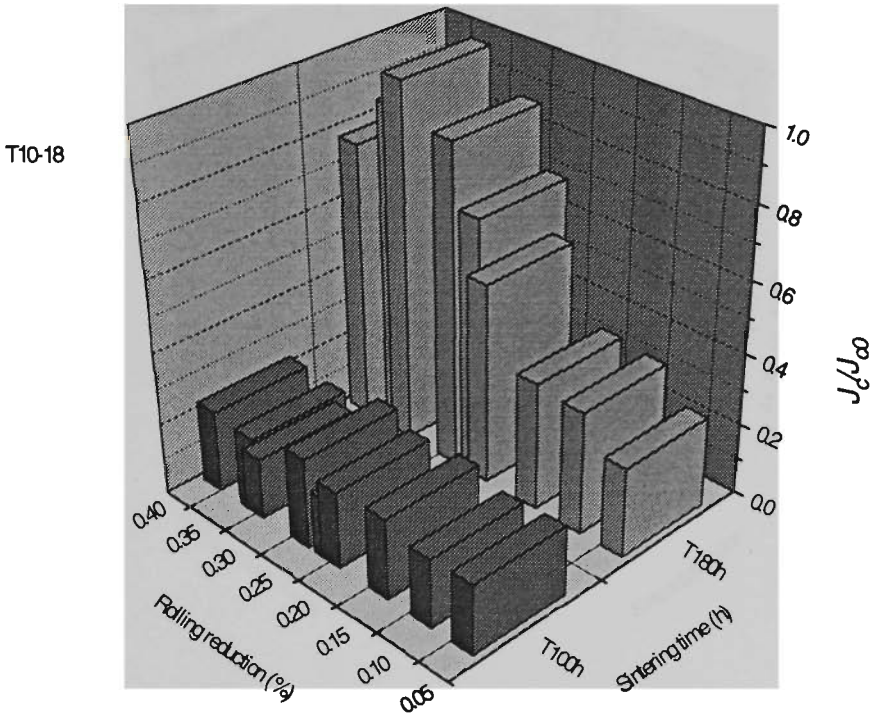

(c)

Figure 3.18 *Rolling reduction ratios between the first and second sintering periods versus sintering time, and normalized J_c for (a) D (b) U and (c) T tapes.*

Further down the sintering time scale where the first and second sintering steps have been made, it is the second intermediate rolling ratio that is now of interest. Figures 3.19(a), and (b) respectively, show the result of normalized J_c as before, for U and D samples obtained after the third sintering step for various degree of rolling reduction prior to this sintering period. Samples of U8-14-3 were initially sintered for 40 h, all were next rolled to give a 30 % reduction ratio, then sintered for another 40 h after which various degree of reduction ratios were applied to the batch. This batch of tapes was then heat treated for 60h and the J_c obtained for each sample. Similarly for samples of D8-14-2, except here a reduction of 20 % was applied to all D samples during the first rolling step. The results from Figs. 3.19(a), and (b) have indicated that the best reduction range is approximately between 15 and 20 %. The J_{c0} for U8-14-3 and D8-14-2 are ~ 10.0 and 4.5 kA/cm^2 respectively.

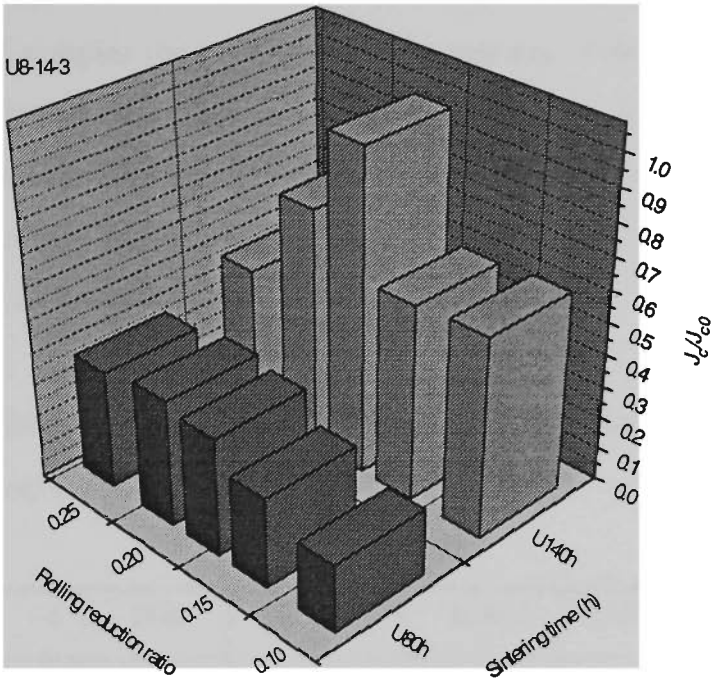

(a)

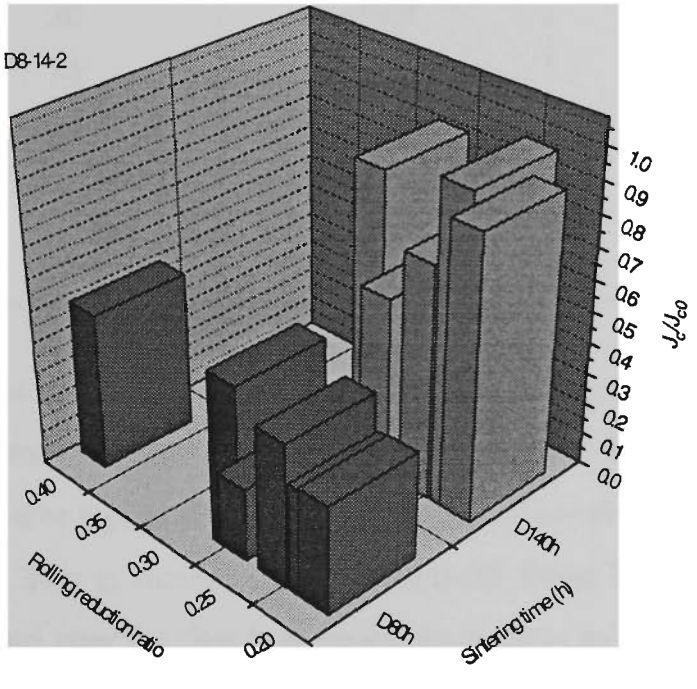

(b)

Figure 3.19 *Rolling reduction ratios between the second and third sintering periods versus sintering time and normalized J_c for (a) U and (b) D tapes.*

Knowing the range of reduction ratios for first and second rolling at room temperature from the aforementioned samples the next step was to proceed with samples cut from a longer length tape and determine an optimal 'reduction window' for every rolling step until the J_c began to drop. Eight samples were then cut from a long length SF Bi(Pb)-2223 tape made from precursor U. The sequence of reduction ratios between sintering periods for each sample is shown in Table 3.5.

TABLE 3.5 *Intermediate reduction ratios for U samples each with initial thickness of 0.2 mm.*

Sample ID	60h → % 80h	80h → % 2×80h	2×80h → % 3×80h
U-a	30	9.3	6.1
U-b	30	20.4	6.2
U-c	10	19.8	3.4
U-d	20	19.9	7.1
U-e	30	22.2	7.7
U-f	30	12.8	7.4
U-g	30	28.2	10.2
U-h	30	16.7	8.3

A three-co-ordinate point (*s, r, j*) (which corresponded to sintering period, rolling reduction and critical current density respectively) was obtained for each sample. The results were then converted to a gridded matrix with the points correlated from which a 2D contour map was plotted. This is shown in Figs. 3.20(a)-(c). From Fig. 3.20(a) it is clear that the best reduction ratio after the first heat treatment is close to 30 %. This reduction rate is in agreement with the work performed by Suzuki *et al* for 'differential speed rolling' [231]. After the second heat treatment, this ratio region is less than ~ 23 % for optimal results, as in Fig. 3.20(b). A further sintering step after the third heat treatment shows a decline in J_c values as the highest achievable J_c after the forth sintering period is no greater than 50 % of the value obtained after the third heat treatment. The reduction

regime here remains anywhere less than ~ 13 %. The drop in J_c after the third sintering treatment was also found by Osamura *et al* for uniaxially pressed Bi(Pb)-2223 tapes [273]. Thus a gradual decrease in rolling reduction is necessary with progressive sintering steps to achieve high J_c values. The frequency of sinter-roll-sinter cycles does indeed assist grain to grain connectivity and improve core density [90] while the decrease in reduction ratio from one cycle to the next avoids detrimental breaking of the platelet-like grains which are aligned by stacking the platelets like a structure of railway tracks, or bricks [102].

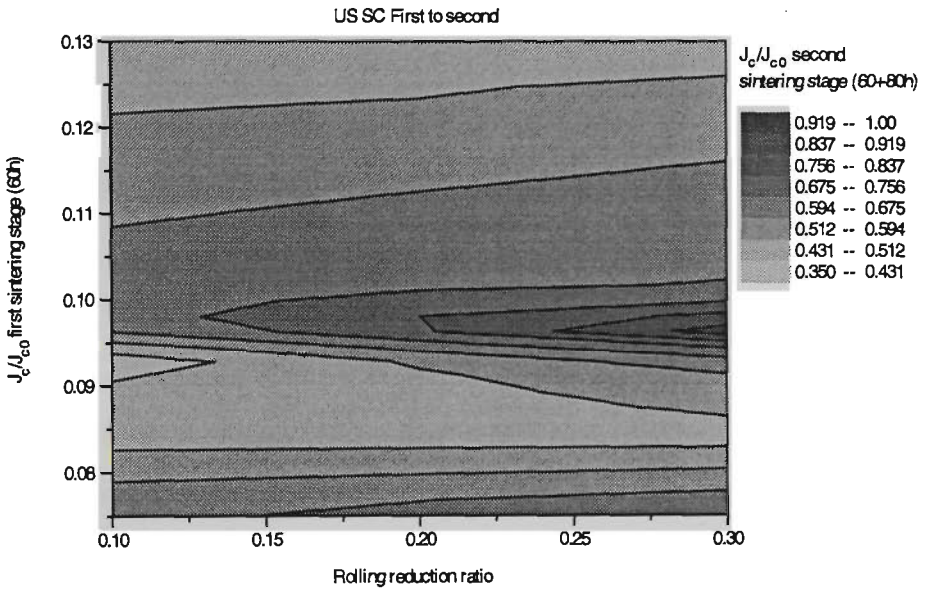

(a)

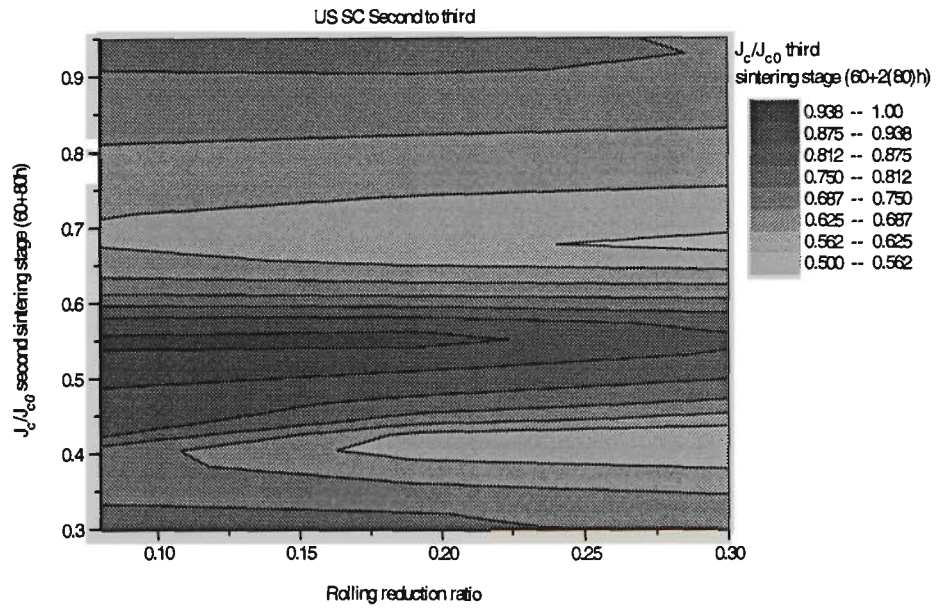

(b)

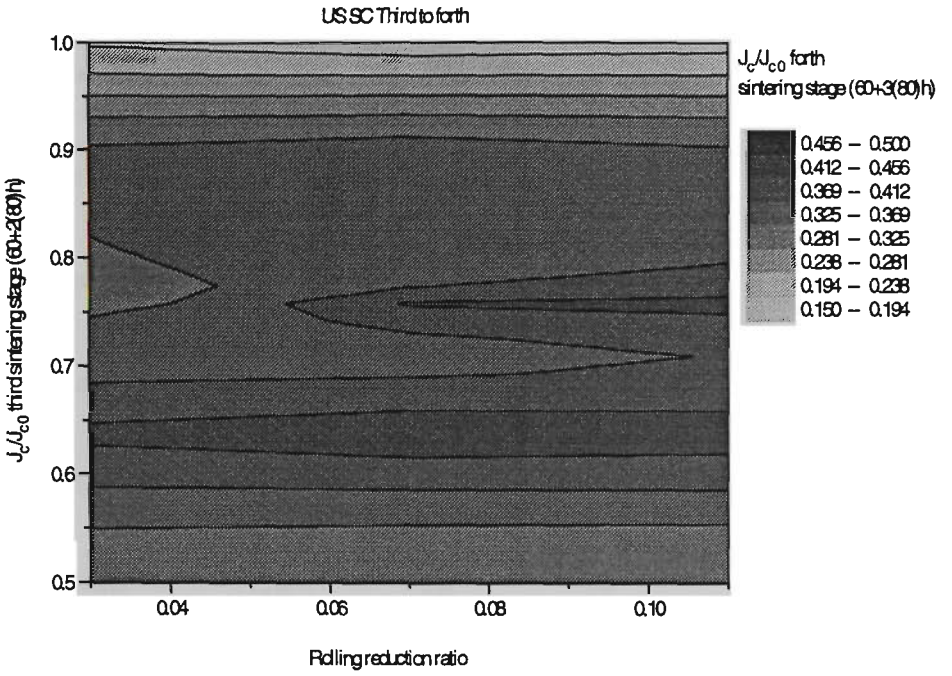

(c)

Figure 3.20 *Contour surfaces of rolling reduction ratios, sintering time and normalized J_c values for U tapes between (a) first-second (b) second-third and (c) third-forth sintering periods for SF U batch.*

Similar results to Fig. 3.20 were obtained also for batches of 31-filamentary PIT tapes. The results from Fig. 3.21 indicate that the highest J_c can be obtained after three sintering periods (Fig. 3.21(b)), although after the second sintering period (Fig. 3.21(a)), the data suggests that about 95 % of the highest J_c can be achieved. The three 2-D contour plots show not only when approximately the highest J_c can be reached, but also reveal the existence of a reduction zone or window within which the J_c for these tapes show substantial improvement.

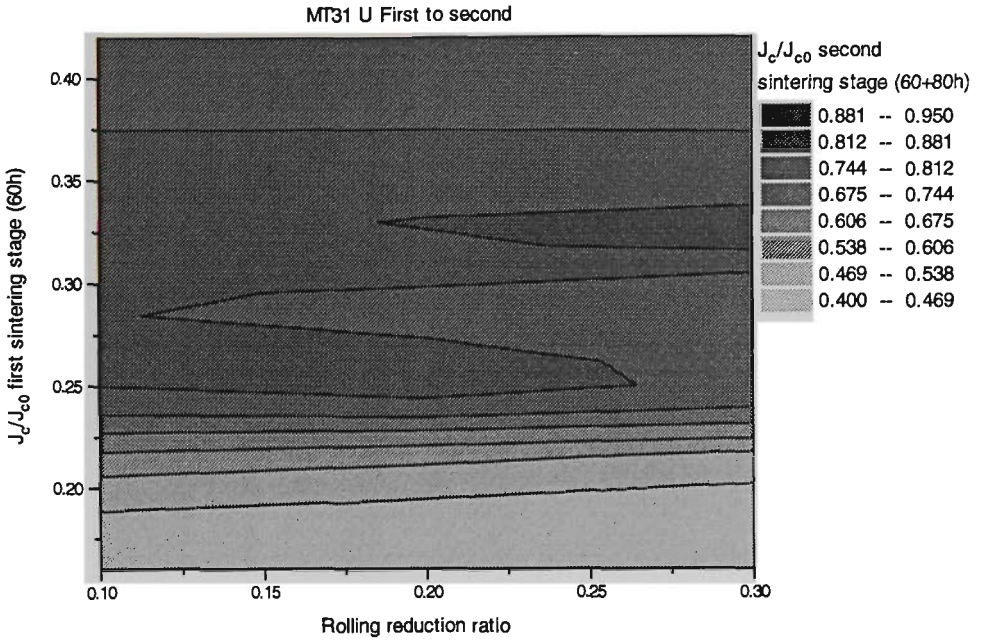
MT31 U First to second
J_c/J_{c0} second
sintering stage (60+80h)
0.881 -- 0.950
0.812 -- 0.881
0.744 -- 0.812
0.675 -- 0.744
0.606 -- 0.675
0.538 -- 0.606
0.469 -- 0.538
0.400 -- 0.469
J_c/J_{c0} first sintering stage (60h)
0.40
0.35
0.30
0.25
0.20
0.10
0.15
0.20
0.25
0.30
Rolling reduction ratio

(a)

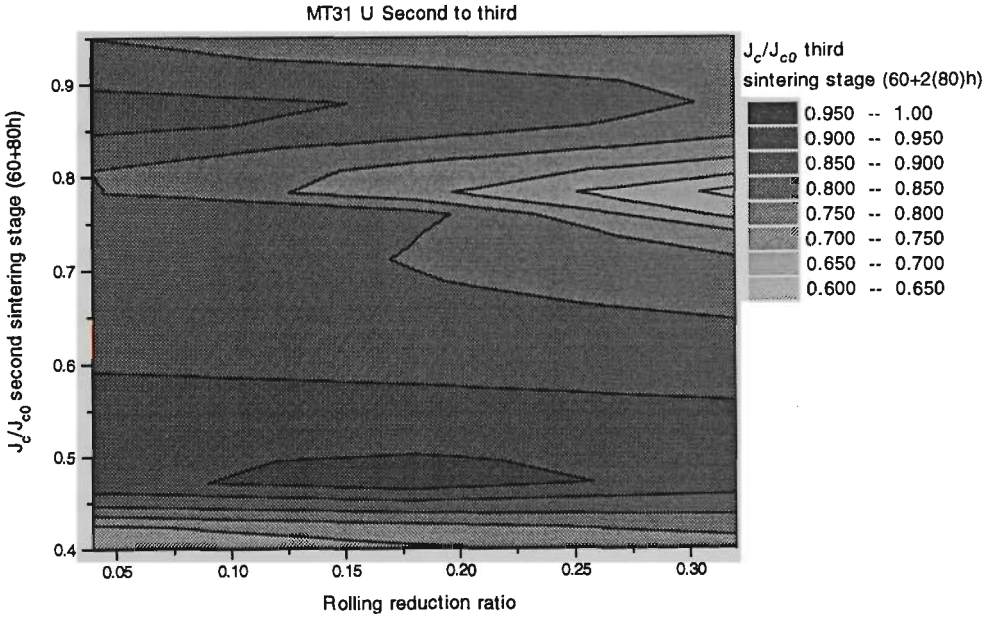
MT31 U Second to third
J_c/J_{c0} third
sintering stage (60+2(80)h)
0.950 -- 1.00
0.900 -- 0.950
0.850 -- 0.900
0.800 -- 0.850
0.750 -- 0.800
0.700 -- 0.750
0.650 -- 0.700
0.600 -- 0.650
J_c/J_{c0} second sintering stage (60+80h)
0.9
0.8
0.7
0.6
0.5
0.4
0.05
0.10
0.15
0.20
0.25
0.30
Rolling reduction ratio

(b)

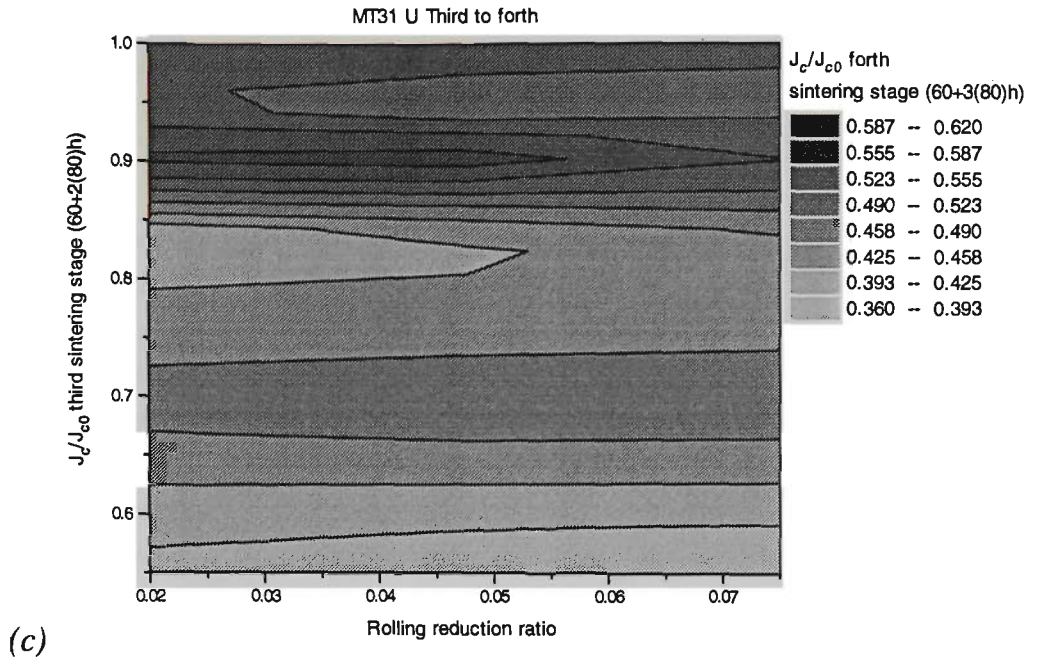

(c)

Figure 3.21 *Contour surfaces of rolling reduction ratios, sintering time and normalized J_c values for 31-filamentary batch between (a) first and second, (b) second and third, (c) third and fourth sintering periods for.*

For MF CTFF tapes, the plots of Fig. 3.22 show the amount of intermediate mechanical reduction induced (perpendicular to the tape's surface) between sintering stages (dependent on sintering time) varies over a range of values within which (dark areas) the J_c can be enhanced (obtained from batch processing of MT9 tapes). This 'optimal region' of reduction ratio reduces in size with progressive sintering of tapes. Figure 3.22 also reveals the highest J_c for this batch, which peaks after the second sintering period. The first region (of Fig. 3.22(a)) shows that the reduction ratio made after the first but before the second sintering stage spans over a large range of values, anywhere up to 30 % (perhaps even more) of reduction in tape thickness. The second region of reduction ratio (of Fig. 3.22(b)) however, narrows to values of less or equal to about 15 %. The last region (Fig. 3.22(c)) shrinks to anywhere less than ~ 5 %. The decrease in the amount of reduction ratio with sintering stages can be explained in terms of the phase assemblage with respect to the amount of 2223 present, where excessive mechanical pressure can create irreparable cracks (to the micaeous nature of the 2223 grains) prior to subsequent

sintering stages. These regions of reduction ratio has been found to vary with the filamentary characteristics as well as powder composition.

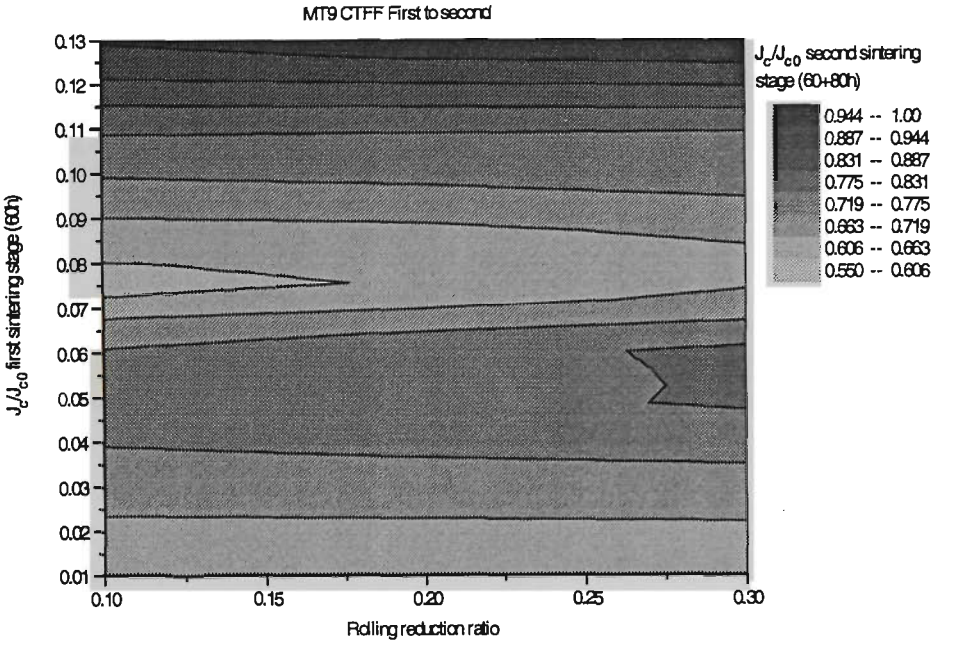

(a)

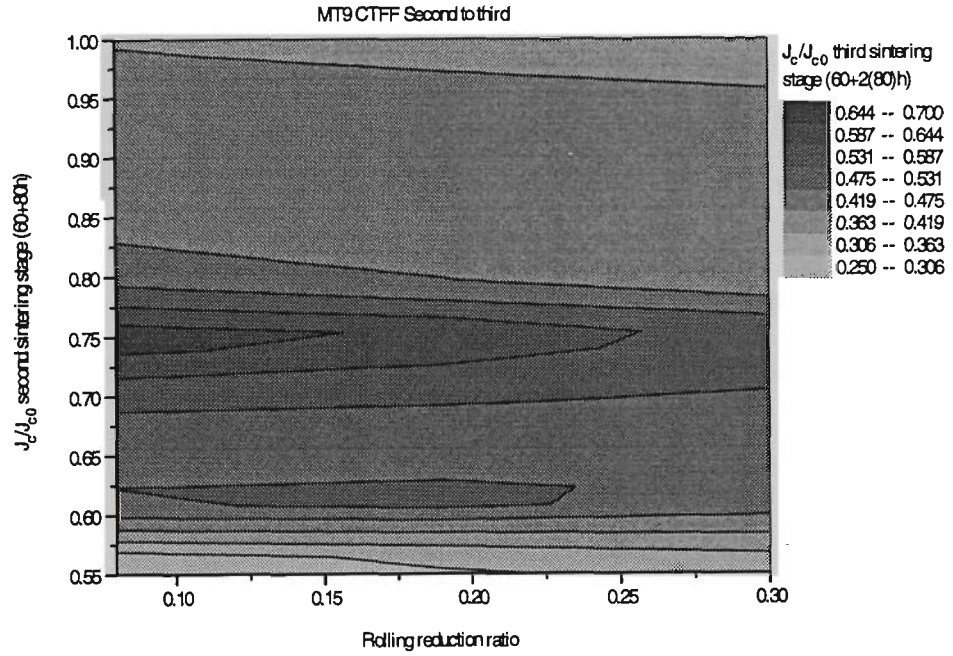

(b)

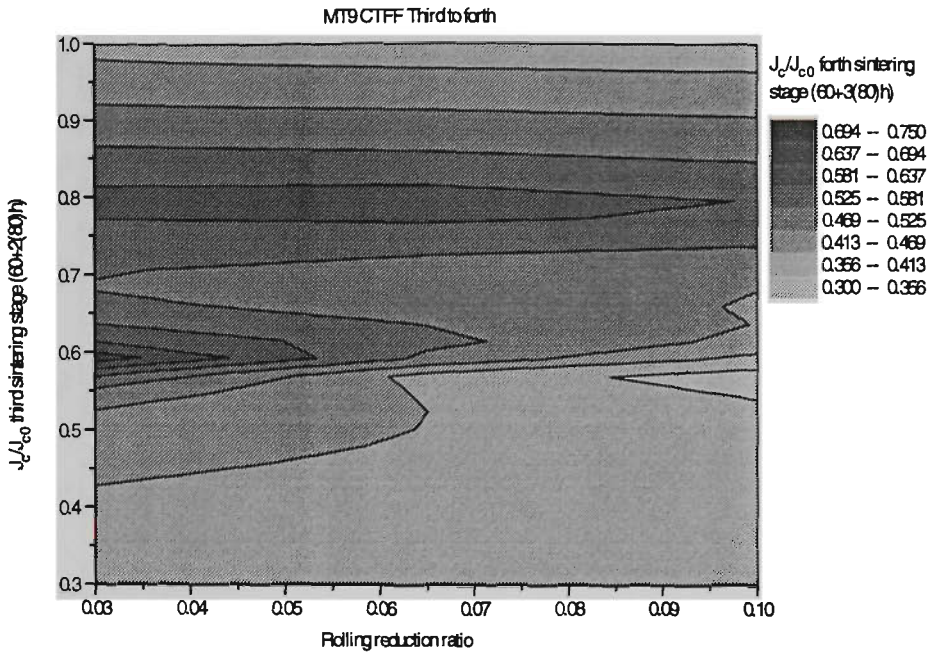

(c)

Figure 3.22 *Contour plots of J_c versus rolling reduction ratio between sintering stages for batch MT9.*

Next, transport measurements of J_c versus externally applied magnetic flux density B (normal to the tape plane) at various temperatures for two samples; one having 14 filaments (MT14) the other 37 filaments (MT37), were carried out. The two samples belong to batches of MT14 and MT37, respectively. The results are shown in Figs. 3.23(a), and (b) respectively. The self field J_c values of MT14 were measured to be ~ 86 kA/cm^2 at 4.6 K, ~ 50 kA/cm^2 at 40 K and ~ 14 kA/cm^2 at 81 K. For MT37, they were ~ 40 kA/cm^2 at 40 K and ~ 13 kA/cm^2 at 81 K. With the bias external density field attaining a value of ~ 1 T, MT14 retained ~ 33.4 and 25.6 % of its zero field values at 4.6 and 40 K while MT37 retained ~ 27.6 % at 40 K. Although both samples were treated with the same sintering conditions and processed with identical precursor powder, the difference in the J_c-B characteristics between the two samples can be attributed to variations in processing parameters such as intermediate deformation between sintering stages and their filling factors. The latter processing related property has been found in particular for batches of MT14 and MT37 to be a factor in the stability design of Bi(Pb)-2223 superconducting composite tapes - discussed in section 3.3.4.

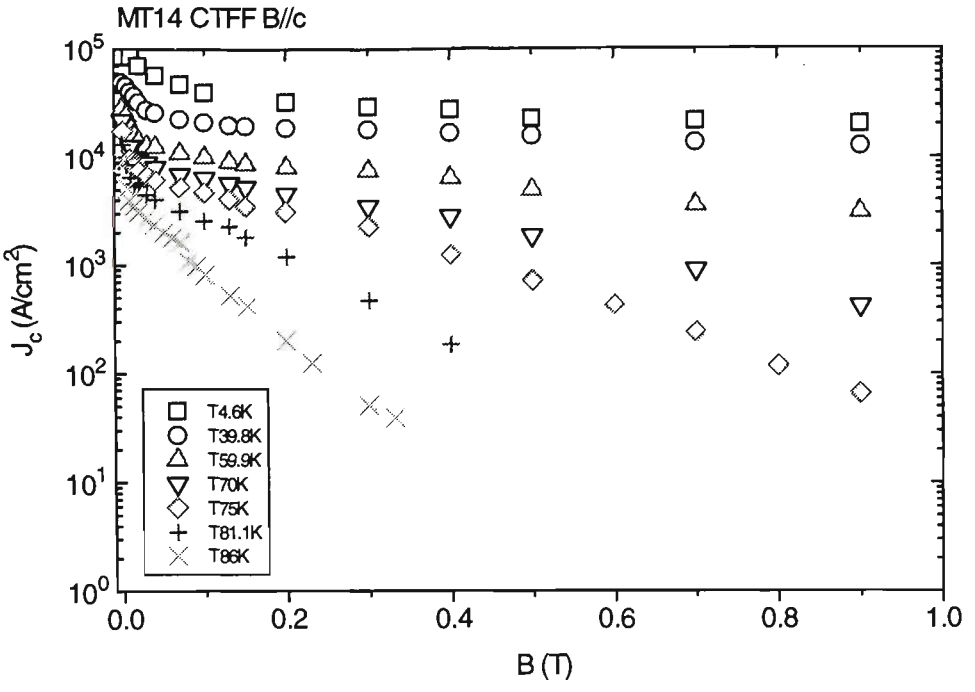
MT14 CTFF B//c
J_c (A/cm^2)
B (T)
T4.6K
T39.8K
T59.9K
T70K
T75K
T81.1K
T86K

(a)

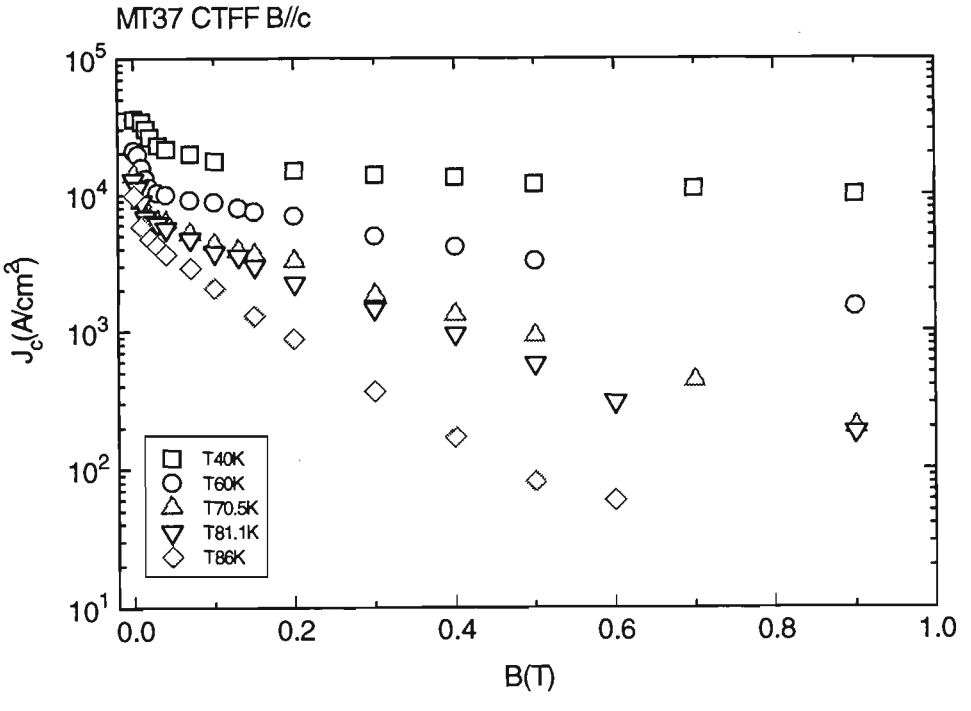
MT37 CTFF B//c
J_c(A/cm^2)
B(T)
T40K
T60K
T70.5K
T81.1K
T86K

(b)

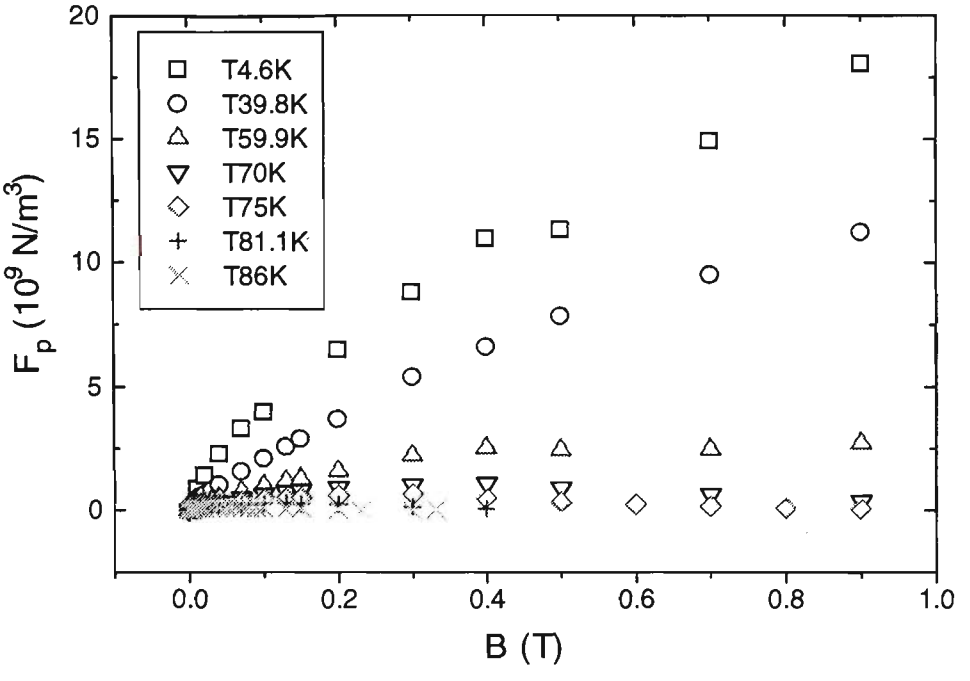

(c)

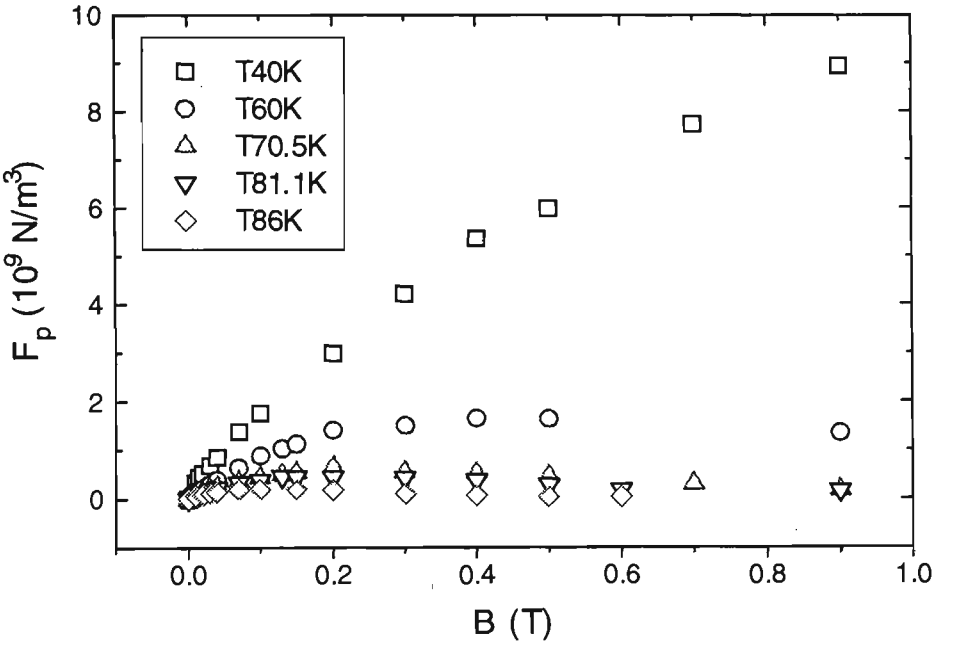

(d)

Figure 3.23 *Transport J_c versus magnetic flux density, B at various temperatures. The field is applied perpendicular to the tape, along the c-axis of the majority of grains for sample (a) MT14, and (b) MT37, with the corresponding volume density of the flux-pinning force, F_p against B, shown in (c), and (d) respectively.*

Figures 3.23(c) and (d) respectively, show the corresponding volume density of the flux-pinning force F_p against the applied magnetic flux density, B for MT14 and MT37. Here, the peaks can be observed to have shifted to the right decreasing in temperature. At similar temperatures such as ~ 40, 60, 70, 81 and 86 K, sample MT14 tends to exhibit stronger pinning forces over MT37. Again, this indicates that the higher J_c is being responsible which in turn depends largely on the processing aspects. It is speculated that problems such as filamentary bridging due to excessive deformation can degrade the samples performance under the influence of external field.

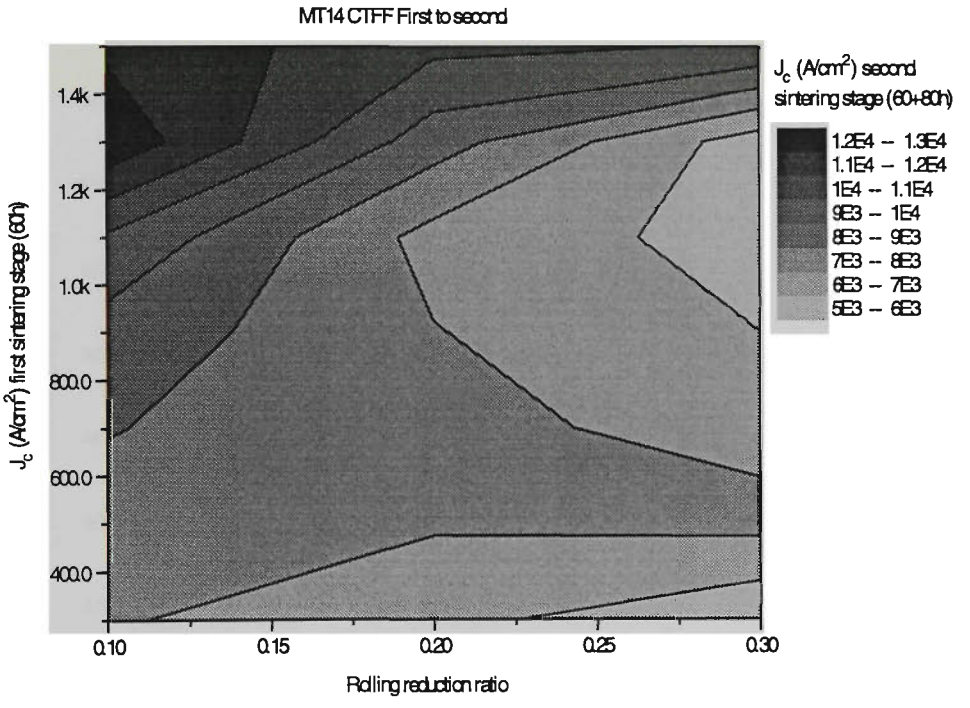

(a)

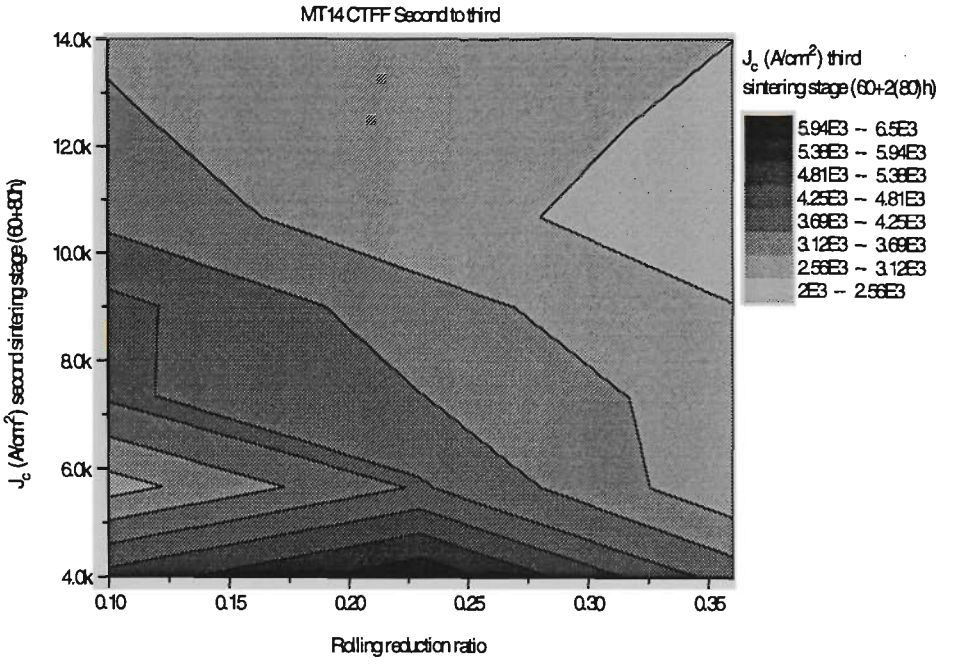

(b)

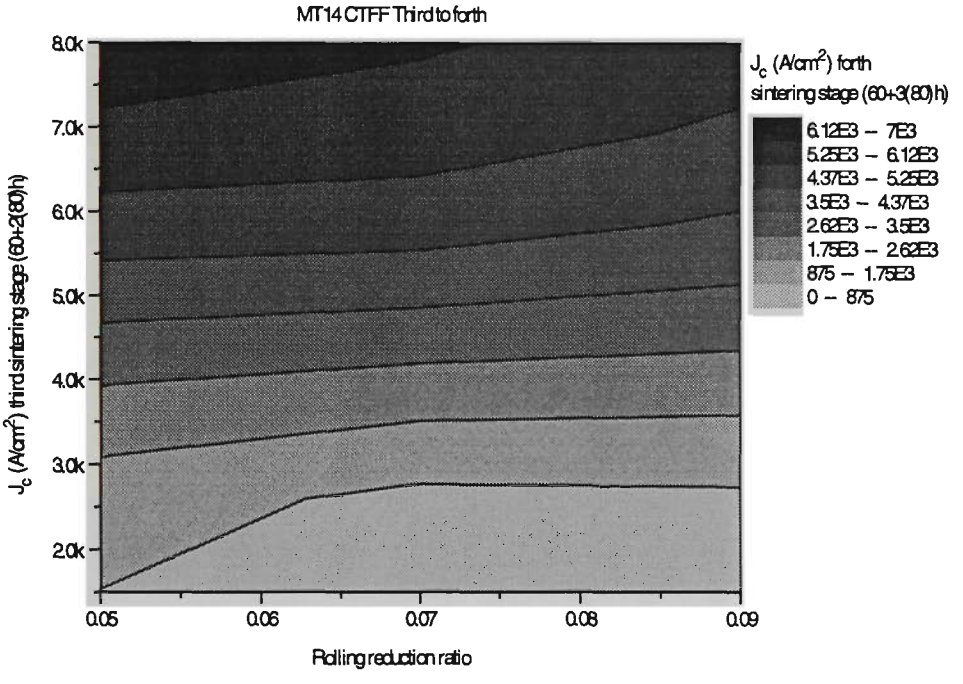

(c)

Figure 3.24 *Surface contour plots of J_c versus rolling reduction ratio in between sintering stages for batch MT14.*

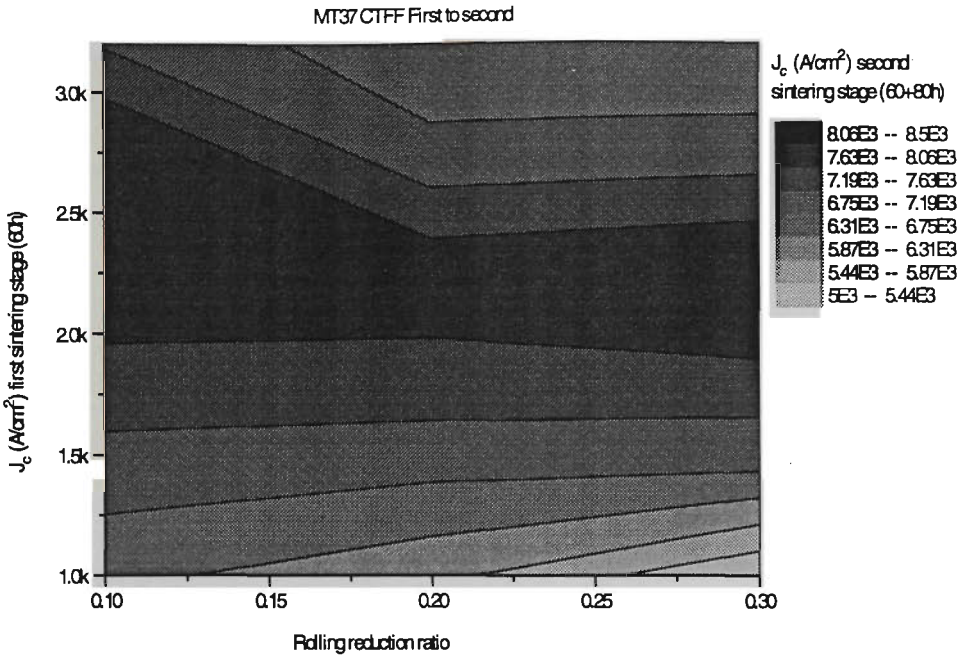
MT37 CTFF First to second
J_c (A/cm^2) second sintering stage (60+80h)
8.06E3 -- 8.5E3
7.63E3 -- 8.06E3
7.19E3 -- 7.63E3
6.75E3 -- 7.19E3
6.31E3 -- 6.75E3
5.87E3 -- 6.31E3
5.44E3 -- 5.87E3
5E3 -- 5.44E3
J_c (A/cm^2) first sintering stage (60h)
3.0k
2.5k
2.0k
1.5k
1.0k
0.10
0.15
0.20
0.25
0.30
Rolling reduction ratio

(a)

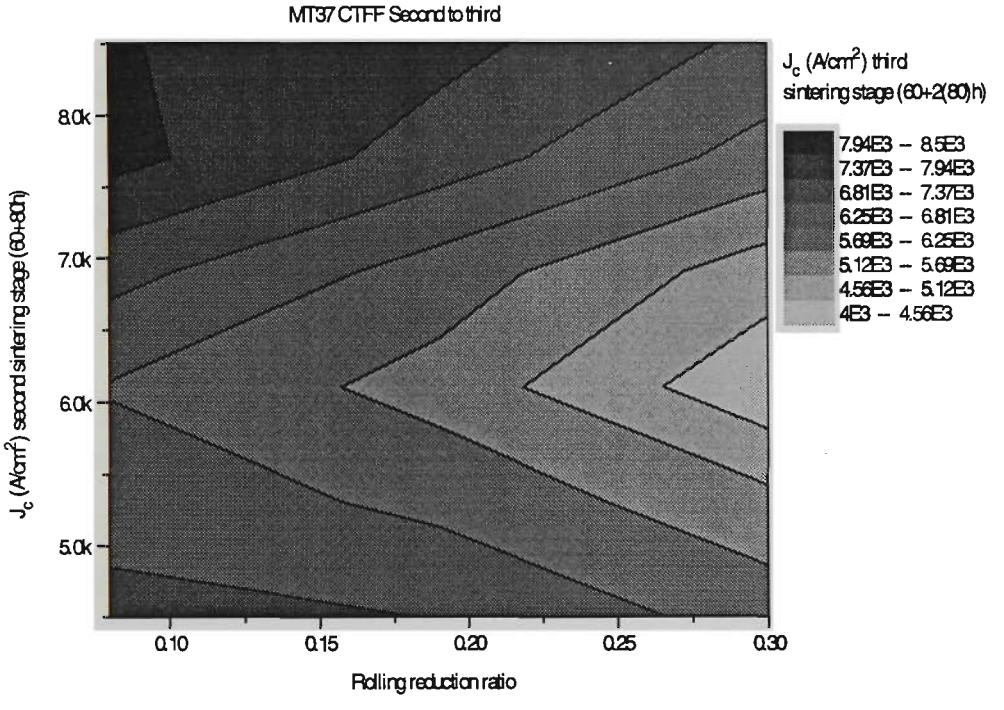
MT37 CTFF Second to third
J_c (A/cm^2) third sintering stage (60+2(80)h)
7.94E3 -- 8.5E3
7.37E3 -- 7.94E3
6.81E3 -- 7.37E3
6.25E3 -- 6.81E3
5.69E3 -- 6.25E3
5.12E3 -- 5.69E3
4.56E3 -- 5.12E3
4E3 -- 4.56E3
J_c (A/cm^2) second sintering stage (60+80h)
8.0k
7.0k
6.0k
5.0k
0.10
0.15
0.20
0.25
0.30
Rolling reduction ratio

(b)

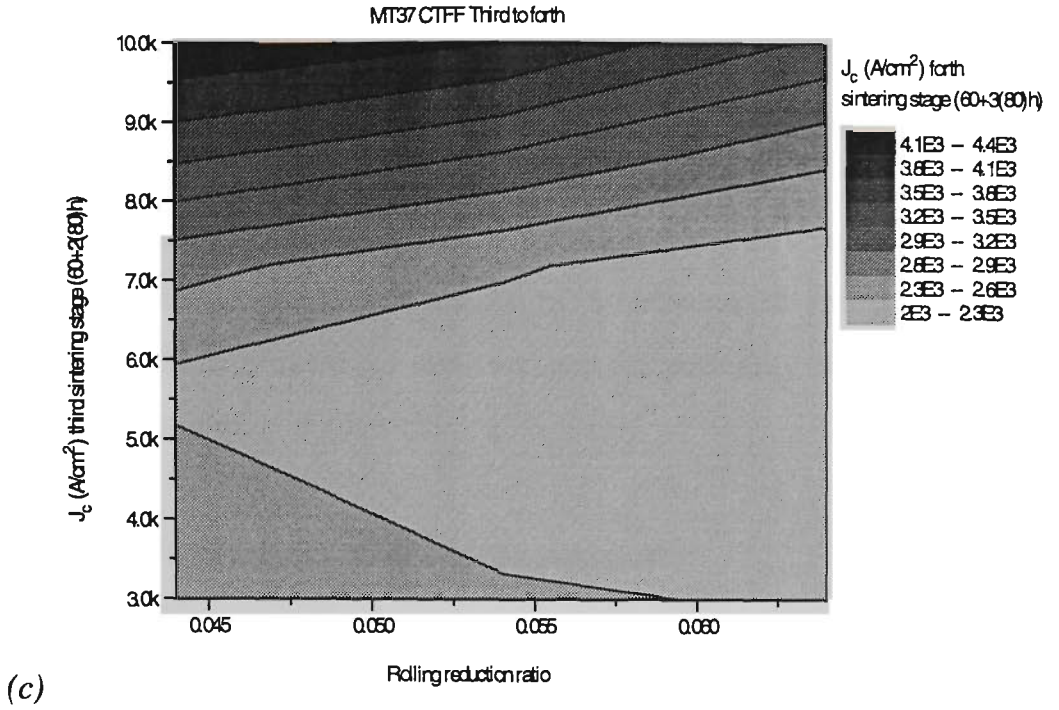

(c)

Figure 3.25 *Surface contour plots of J_c versus rolling reduction ratio in between sintering stages for batch MT37.*

The 2-D contour plots of J_c versus rolling reduction ratio between sintering stages made from measurements obtained for the processed batch samples of MT 14 and MT37 are shown in Figs. 3.24(a)-(c), and 3.25(a)-(c). The contour plots once again show how the J_c values of MF tapes vary over sintering time, with different amount of intermediate reduction induced between sintering periods. This certain amount of deformation or critical reduction zone between the first and second sintering stages are up to ~ 12 % for batch MT14 and up to ~ 30 % (perhaps more) for batch MT37. Between the second and third sintering stages, this window increases to ~ 20-25 % for MT14 while MT37 shows a decrease in the reduction zone ~ less than 10 %.

Finally the window between the third and fourth (last) sintering stages drops in either case to ~ less than 7 % and ~ less than 5 % for MT14 and MT37, respectively, suggesting any further cycle of deformation and heat treatment would only degrade the J_c of the tapes. The difference in reduction zones between the two batches can be explained in terms of (1) the

phase composition (which depends on intermediate deformation ratio), (2) the effect of filamentary behaviour such as inter-filamentary bridging, and (3) the filling and stacking factors which can decide the thickness of the filaments themselves.

Based on the gradual reduction in deformation approach, PIT and CTFF composite tapes of Bi(Pb)-2223 with reproducible values of J_c between 15 and 20 kA/cm^2 have been achieved. It should be pointed out however, that the generality of the result may be limited to the particular overall stoichiometry.

3.3.3 Phase Formation, and Microstructure

To see why certain degree of rolling reduction adversely affects the final J_c of Bi(Pb)-2223 tapes, the relative amount of high- (2223) and low- (2212) T_c phases were studied in conjunction with SEM images on the surfaces of rolled samples, prior to their next sintering step. Figures 3.26(a), and (b) contain XRD patterns of relative intensities obtained from 'fractured' surfaces of T (thin wall) samples before and after rolling, after 60 (for 5 samples) and 240h (for 6 samples) respectively. All tape samples were sintered with a 60 h period. Indicated on the left side of each pattern is the relative amount of 2212 to 2223 using intensity peaks at 2θ of ~ 23.20^0 (hkl = 008 & 1110) for the 2212 phase and ~ 23.92^0 (hkl = 0010) for the 2223 phase, since there are no overlapping peaks at these reflections [277]. The XRD patterns vertically aligned on the left are for tapes after sintering, while those on the right represent the diffraction patterns of the same corresponding tape but after being rolled with a particular reduction ratio (labelled between the two columns of XRD patterns), with no further heat treatment. The influence of rolling on the relative amount of low to high-T_c phases is apparent. This relative value appears to increase with increasing reduction ratio for 'T-60' samples (shown in Fig. 3.26(a)). The relative percentage of 2212 to 2223 has certainly been altered immediately after rolling. One explanation for the apparent increase would be due to the disruption of morphology of grains on the surface of the ceramic core from which rolling has incurred. Plate-like grains of 2223 could be fractured or pushed deeper into the pores and cavities of the BPSCCO core due to the rolling process. After only 60 h of sintering time, not only the

core hasn't been fully densified, the 2223 phase itself has still not fully reacted. This explanation is strongly supported by the *two*-dimensional nucleation (one nuclei per grain) or random-growth mechanism of the 2223 grains [278]. For 'T-240' samples, the reduction ratios applied to the tapes were much less on average. Reduction ratios below about 20 % showed an increase in the relative amount of 2223 phase, as shown in Fig. 3.26(b), and around 30 % and above, the same trend with the 'T-60' samples was noticed. Indeed, after 240 h (four cycles of heat treatment) the phase development of 2223 has been almost fully reacted. Further deformation can only result in fracturing of the B(P)SCCO core since the core density is quite high after the forth sintering step. Not shown here are the J_c values measured for 'T-240' samples before and after rolling. As expected, it was found that the electrical property of the 'T-240' samples plummeted even with the smallest amount of deformation applied, with no further sintering. Thus improving the relative amount of 2223 due to deformation alone does not necessarily mean better J_c since the microstructure of the superconductor has been damaged. Additional heat treat is thus essential to heal the mechanically induced cracks.

To see the effect of rolling on the microstructure of the Bi(Pb)-2223 tapes, SEM images of the transverse cross-sections of samples of 'T-60' and 'T-240' were taken. Large cracks due to rolling alone, as shown in Figs. 3.27(a) and (b), were revealed. Each SEM image is labelled correspondingly to the XRD patterns of Fig. 3.26. With 'T-60' samples (Fig. 3.27(a)), large reduction as high as ~ 37 % (reduction ratios shown in Fig. 3.27(b)) has caused the surface induced cracks to become more visible, especially at the silver-core interface. Any reduction ratio higher than this however, would result in the onset of or actual splitting of the tape (as found with a reduction ratio of 43.1 %. Note SEM image is not included for this reduction ratio due to splitting of the tape.). This can be understood with the following reasons; there is relatively a large amount of 2212 and liquid phases present, and that the expansion of the tape itself is high after the first heat treatment while the core density is relatively low. In contrast, a reduction ratio as low as 4.1 % still inflict serious cracks to the microstructure of 'T-240' tapes, as indicated in Fig. 3.27(b).

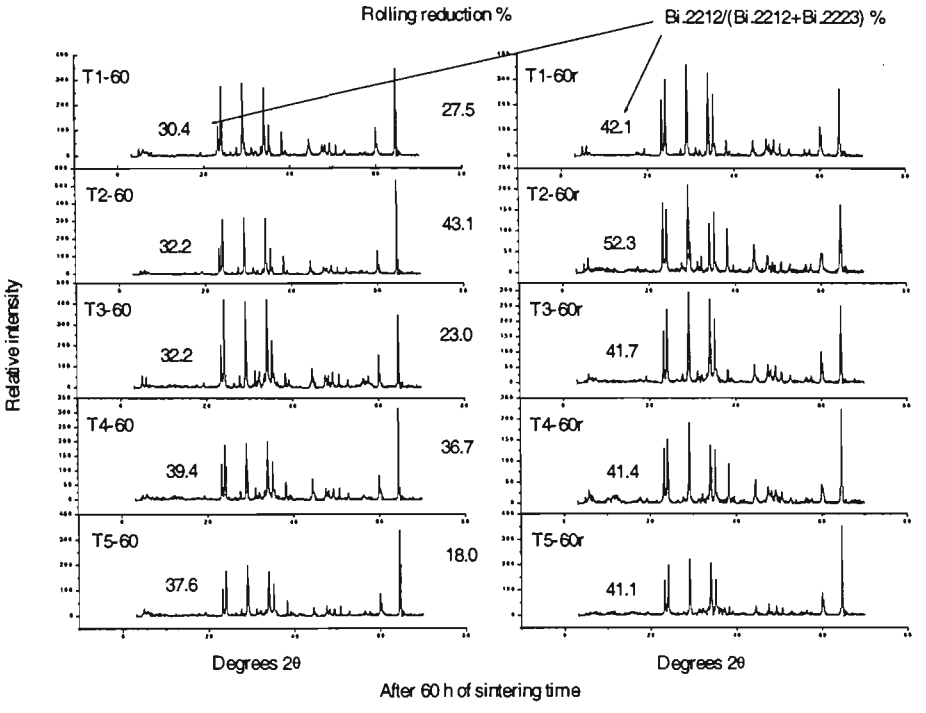

(a)

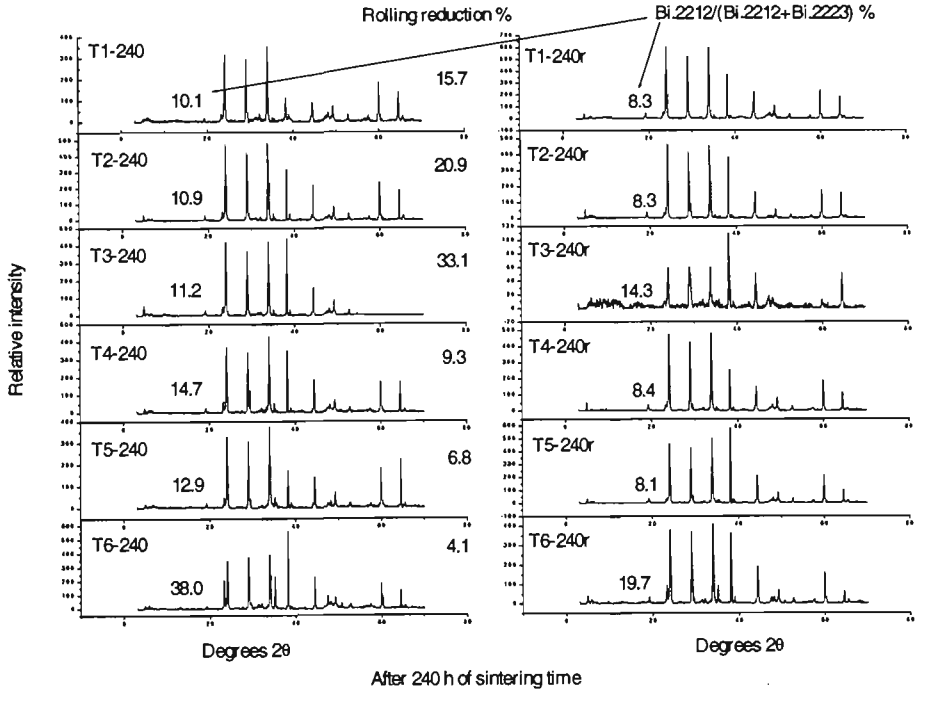

(b)

Figure 3.26 *XRD patterns of (a) 60 h sintered and (b) 240 h sintered T tapes before (left column) and after (right column) rolling. Reduction ratios are indicated between the columns.*

Once again, the damage can be understood in terms of the brittleness and plate-like nature of the 2223 grains. It must be emphasized that these visible cracks are not due to polishing nor thermal cycle of J_c measurements. With regard to rolling, the deformation path of the material during the procedure normally results in the extension of the tape in the longitudinal direction (or direction of rolling) due to shear stress [230]. This would promote cracks which are aligned in the direction transverse to the direction of current flow. From SEM images of 'T*n*-240r' cross-sections (where n = 1,2,3..), the lifting of the silver sheath and large opening of cracks along the direction of rolling are consistent with the picture of the shearing force at work (in particular are images of 'T1-240r' and 'T4-240r'). With moderate to small rolling reduction ratios (say less than 15 % of the tape's thickness) the width strain and shearing stress of the tape can be approximated to zero. However, when large reduction is used, the compressive force induced by the rollers may cause a finite width strain and shearing stress which may fracture the core longitudinally. If the breakage is too great, any subsequent heat treatment may then not be enough to recover the crack. The SEM micrograph of 'T2-240r' shown in Fig. 3.27(b) demonstrates this effect, where the reduction ratio employed was ~ 20.9 %. In summary, results drawn thus far would then suggest that rolling (at room temperature in particular) affects not just the microstructure of Bi(Pb)-2223 tapes alone, but influences greatly on the rate of phase formation as well.

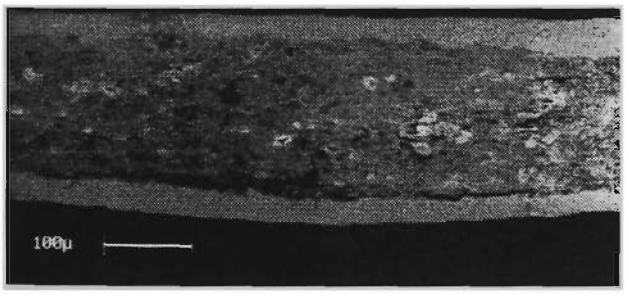

T1-60

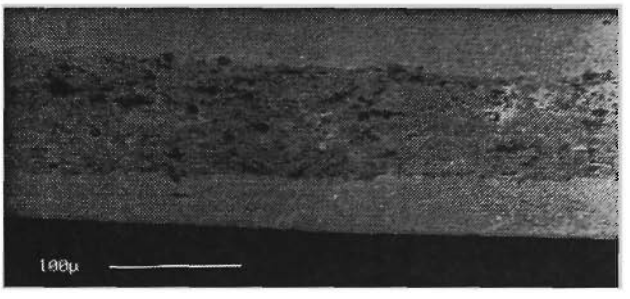

T1-60r

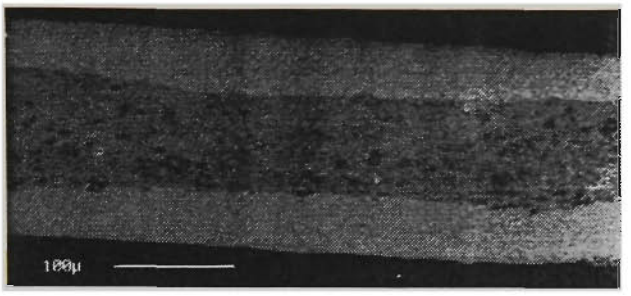

Blank *T3-60r*

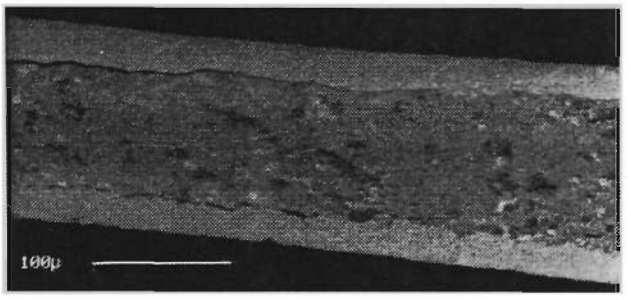

Blank *T4-60r*

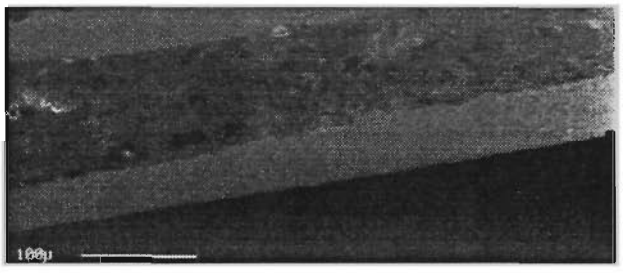

Blank *T5-60r*

(a)

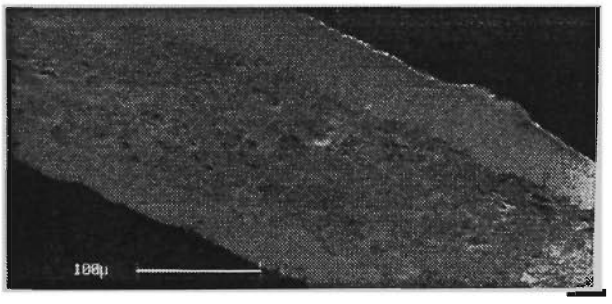

T1-240

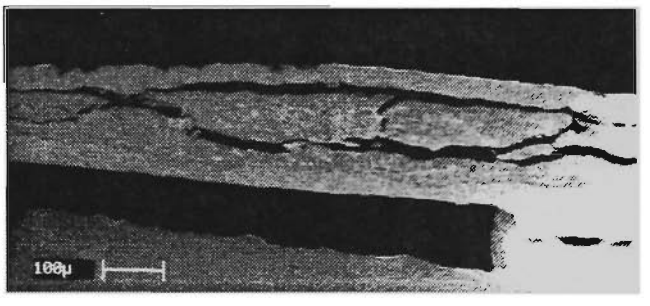

T1-240r

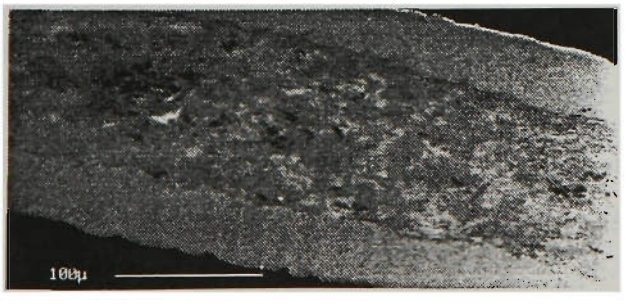

T2-240

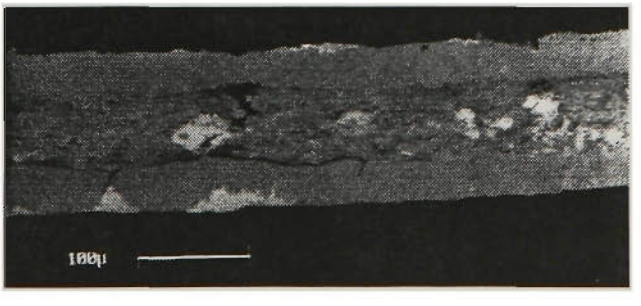

T2-240r

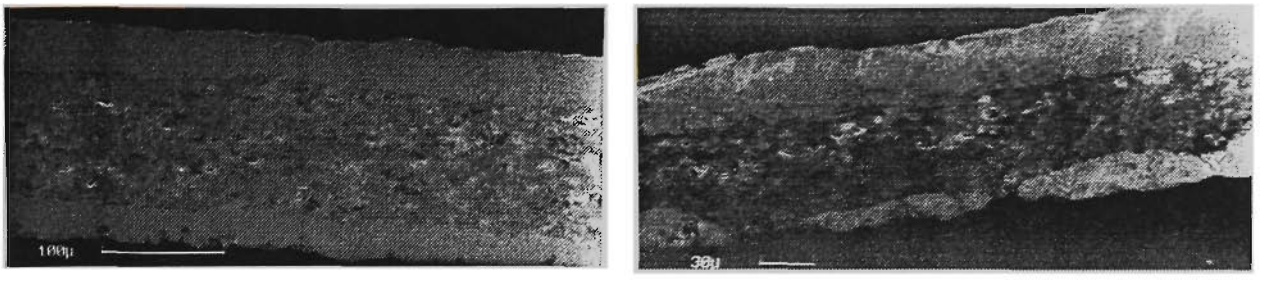

T3-240 *T3-240r*

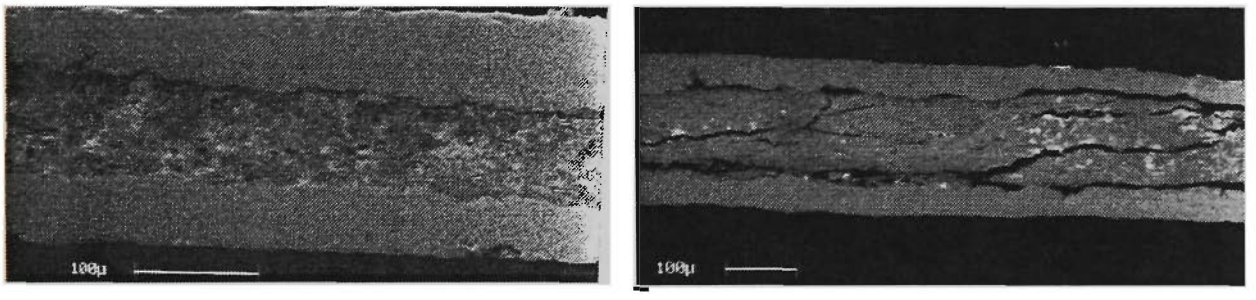

T4-240 *T4-240r*

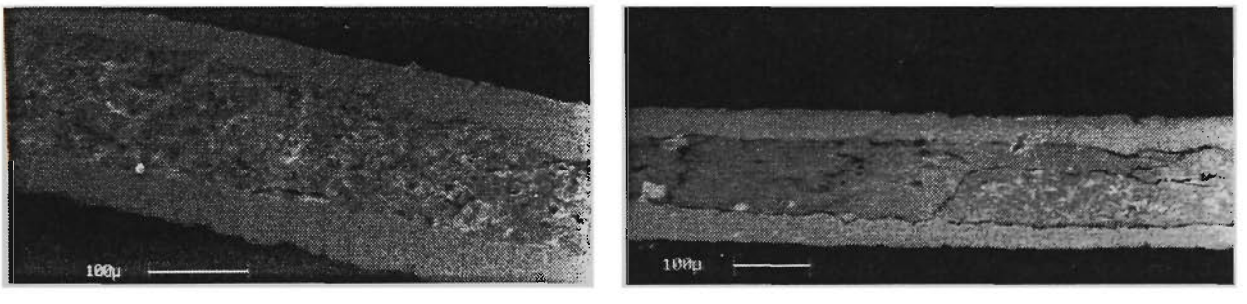

T5-240 *T5-240r*

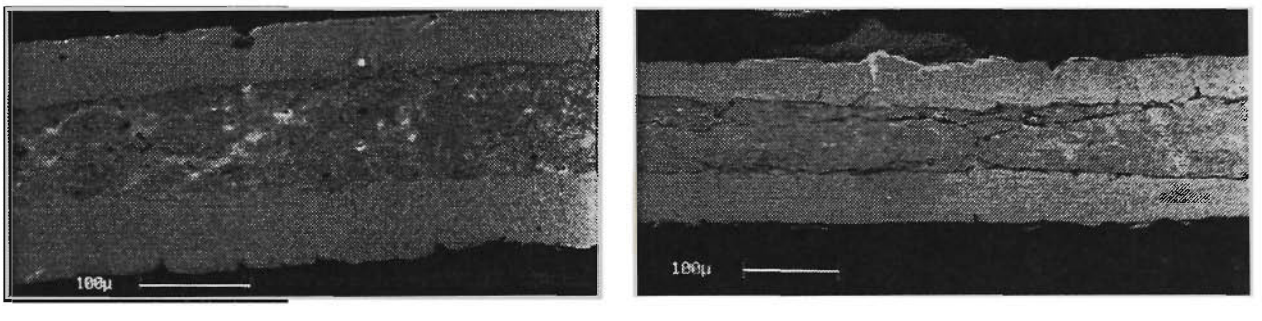

T6-240 *T6-240r*

(b)

Figure 3.27 *SEM images of (a) 60 h sintered, and (b) 240 h sintered T tapes, corresponding to those with reduction ratios labelled in Fig. 3.26.*

For completeness, further measurements were obtained (as graphed in Figs. 3.28(a)-(c) for T samples, and the combined results for CTFF MF tapes in Figs. 3.29(a)-(c)) for the relative percentages of low- to high-T_c phase, plotted against rolling reduction and

sintering time. The evidence gathered from these results show strong support to the notion of rolling having an effect on the rate of phase development. Firstly, the XRD results obtained for T samples (Fig. 3.28(a)), after the first 100 h and second 80 h of sintering periods have indicated a negative growth of 2223 when reduction ratio was approximately 40 % or higher. Below this value, an increase in the development of 2223 phase on average can be observed on the graph of Fig. 3.28(a). Secondly, XRD analysis of D samples after 2×40 h and 2×40+60 h has suggested a positive growth of 2223 when the applied reduction ratio was approximately 20 % or less, as shown in Fig. 3.28(b). With U samples, this positive growth of 2223 occurred for any reduction ratio around 25 % or less (Fig. 3.28(c)). Indeed, there appears to be a similar reduction 'zone' or 'window' within which optimal results can be achieved for Bi(Pb)-2223 tapes in terms of their microstructure, the rate of reaction for phase transformation, and current carrying capacity.

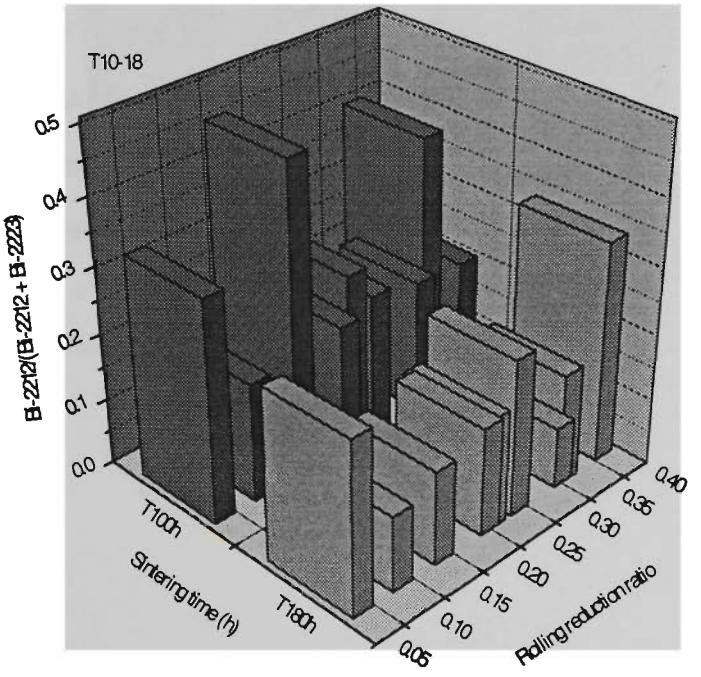

(a)

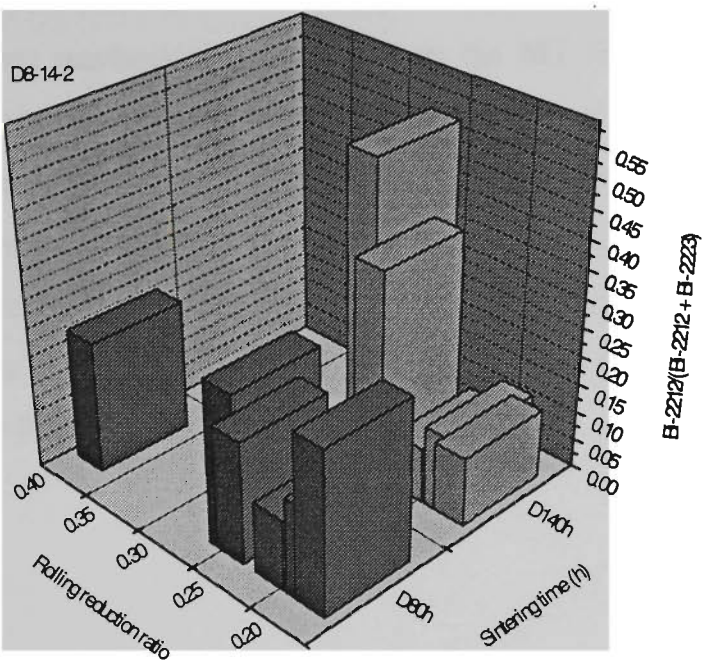

(b)

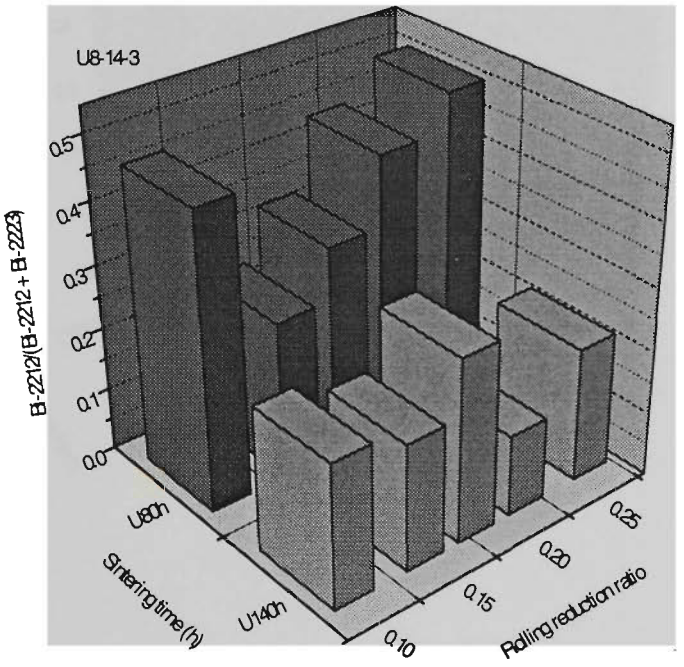

(c)

Figure 3.28 *Compositional phase of 2212 as a fraction of 2223 versus sintering time and rolling reduction ratios.*

The determination of the relative amount of 2212 phase been used to provide feedback on the effect of intermediate mechanical deformation on the MT Bi(Pb)-2223/Ag tapes as shown in Fig. 3.29. These bar graphs reveal the importance of gradually reducing the amount of intermediate reduction with progressing sintering stages for tapes requiring several cycles of sinter-deformation-sinter (SDS). With good agreement to the trends observed from these graphs (and results obtained from XRD analysis), the formation of 2212 and 2223 phases has indeed been found to be dependent on the mechanical deformation applied for Bi(Pb)-2223 composite tapes.

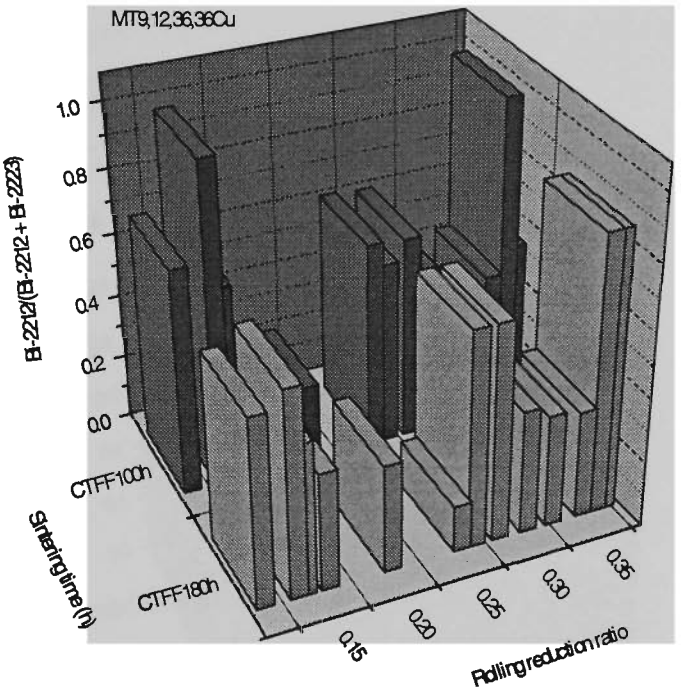

(a)

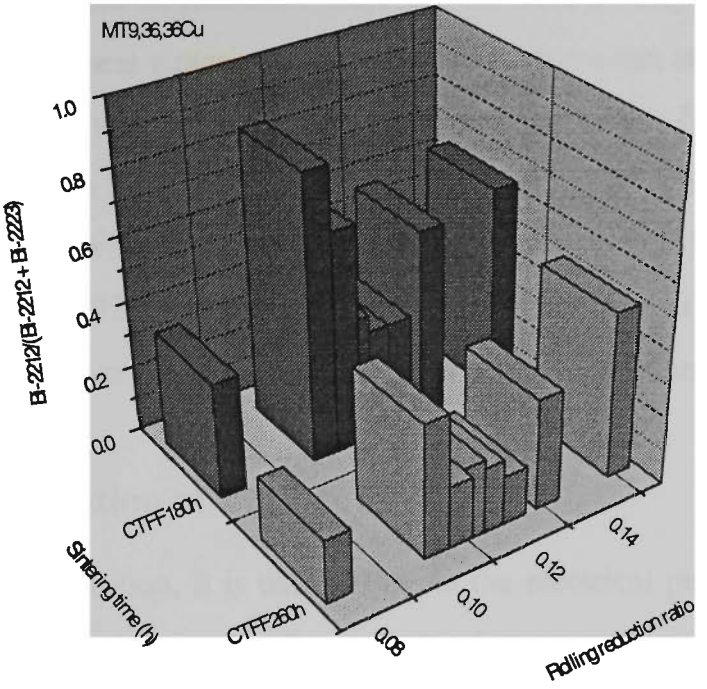

(b)

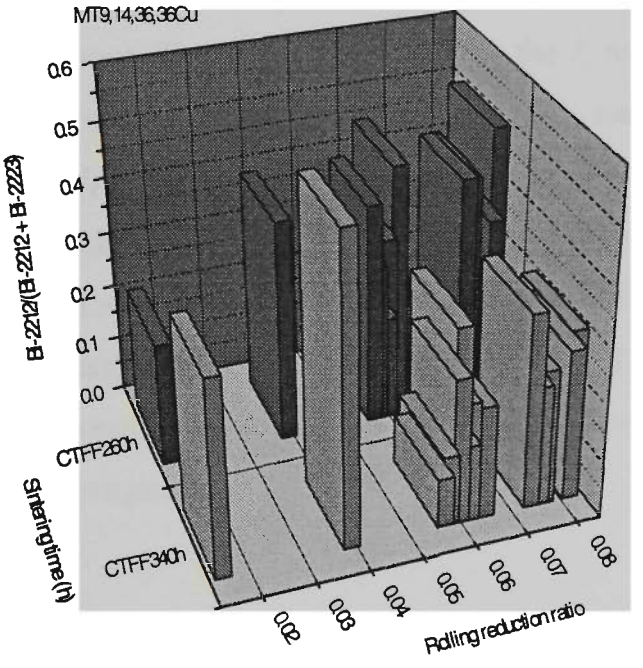

(c)

Figure 3.29 *Relative low to high-T_c phase vs rolling reduction ratio over progressive sintering time.*

Although a large amount of reduction increases the core density and assists grain growth (occurs during subsequent sintering stages), this axial force can at the same time introduce 'late-forming' cracks which can remain right through to the final sintering stage. The apparent 'increasing in 2212 'content' especially observed for the two last sintering stages can be explained in terms of the 2212 'nucleation growth' [278] or 'sandwhich layers of Bi-2212 between Bi-2223' [279] where mechanically induced cracks are likely to expose more of the 2212 seed-crystals upon which the aligned 2223 grains epitaxially grown.

3.3.4 The Implication of Fill Factor

For commercial application, it is usual to quote the electrical performance of a device in terms of the engineering or conductor critical current density, J_e. This leads to a convenient parameter called 'filling factor' (or just fill factor), correctly defined as the volume fraction of superconductor to conductor, but is define here as the ratio of the transverse cross-sectional area of the superconducting core to the total transverse cross-sectional area of the conductor. Thus by optimizing both the J_c and fill factor, the current carrying capability for specified conductor dimensions can be maximized and consequently maximizing J_e itself. Extensive studies have been conducted by Hillmann *et al* in the investigation on the geometry of superconducting 'flat cables' (or tapes) with useful deductions relating the fill factor, and aspect ratio (ratio of the width or breadth of the conductor to its thickness) to the number of filaments [280]. The results presented here however, are limited to certain tube (of Ag) sizes which were used to process the composite tapes under investigation.

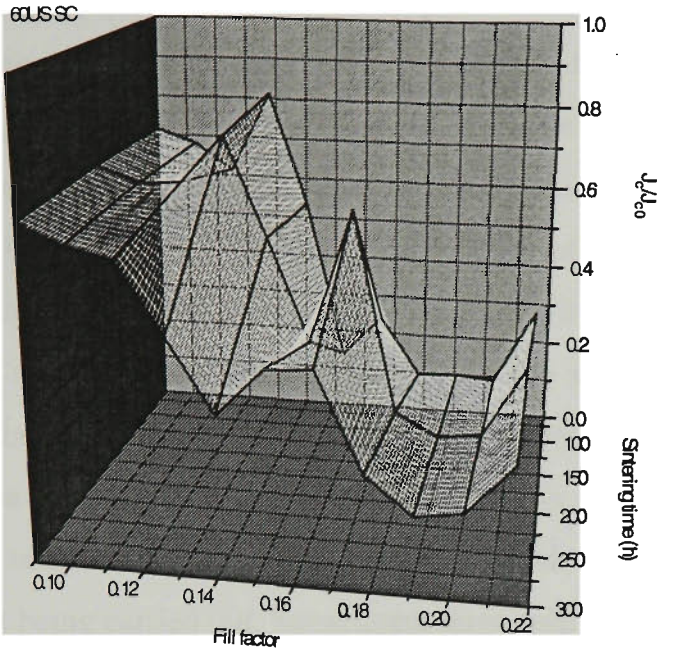

(a)

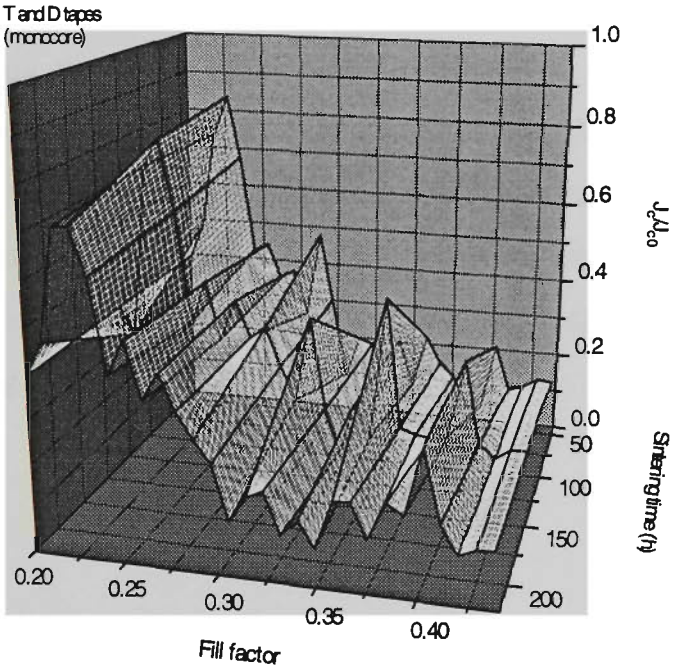

(b)

Figure 3.30 *3D surface representation of fill factor, normalized J_c, and sintering time for (a) U (b) T and D SF Bi(Pb)-2223 tapes.*

By determining the fill factor, and J_c values for all tapes made from precursors with the same nominal composition after each different sintering period, it was possible to see any significant variation in J_c (normalized) over a range of fill factor values against sintering time. Figure 3.30(a) reveals two peaks for U samples. The one with larger normalized J_c lies between 12 and 13 % fill factor region, after about 200 h of sintering time (note the data represented here has been gridded and correlated into a 3D surface, hence the extension of the plot to zero time for certain data set, on the *sintering time*-axis). The second peak is located between 16 and 17 % fill factor after approximately 180 h of sintering time. The reason for this was due to different reduction ratios employed between sintering steps since all samples (from the same batch) started with the same fill factor before any heat treatment being carried out. Subsequent large rolling reduction ratios (refer to Table 3.5) may well increase the fill factor significantly as the silver sheath would stretch more than the brittle B(Pb)SCCO core itself. This observation can be also seen in Fig. 3.30(b) where more peaks appear more frequently for T and D samples. The highest peak in this 3D graph lies roughly between 22 and 23 % along the *fill factor*-axis after about 180 h of sintering time. For increasing fill factor (as a result of large rolling reduction ratios), the normalized J_c values show a gradual drop for any fill factor value of greater than say 24 %. Again, the increase in fill factor in this case was subsequently due to large rolling reduction ratios, which not only would cause a thinning of the silver sheath (hence less cross-sectional area) but could damage the ceramic core as pointed out earlier from SEM images of Fig. 3.27(b).

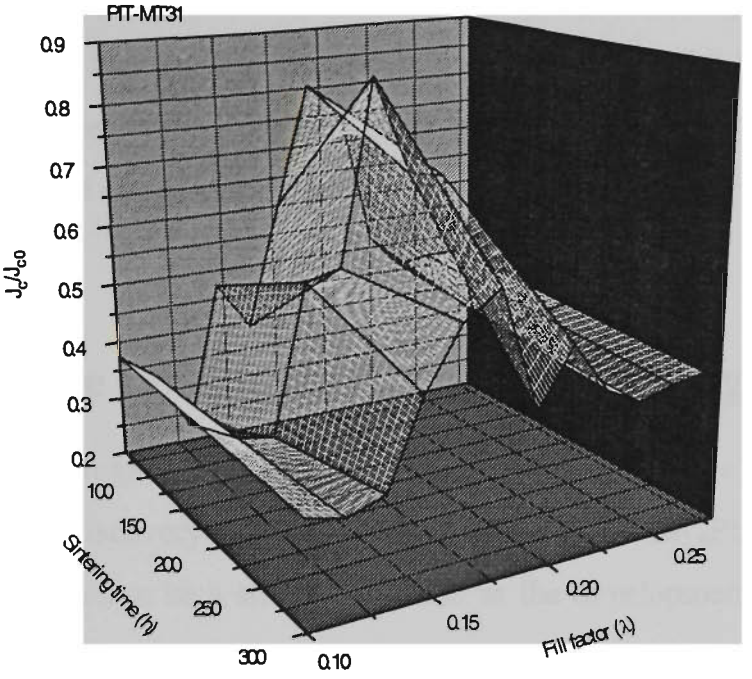

(a)

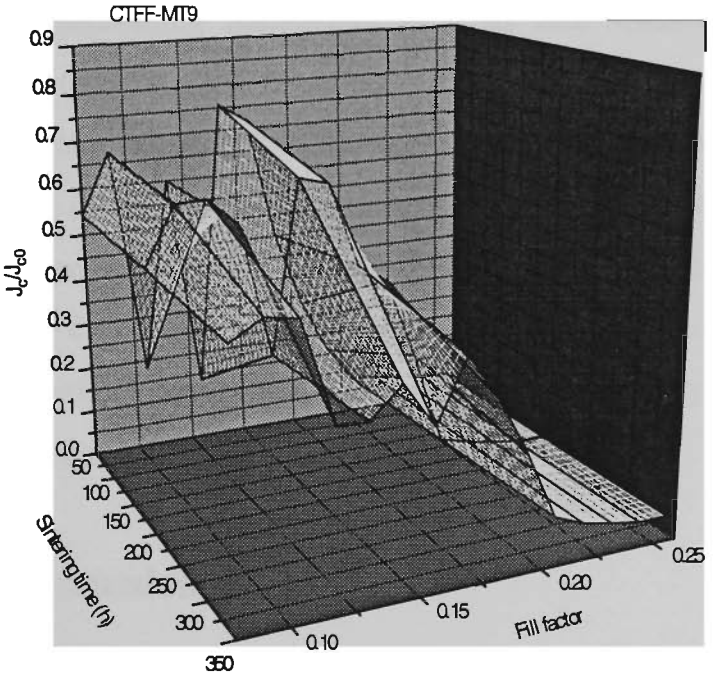

(b)

Figure 3.31 *3D surface representation of fill factor, normalized J_c, and sintering time for (a) PIT MT31, and (b) CTFF MT9.*

As for MF PIT (MT31), and CTFF (MT9) tapes, the 3D surface plots, shown in Fig. 3.31(a), and (b), reveal two characteristic peaks corresponding to fill factor values of ~ 10 and 15 % for the former, and giving a λ range between 16 and 18 % within which the highest J_c values can be obtained for the latter.

3.4 Temperature Control and Related Processing Issues

There has been rapid progress in numerous engineering applications of the so called 'high-T_c SCs' since their discovery in 1986 [31]. Among these $Bi_{1.6}Pb_{0.4}Sr_2Ca_2Cu_3O_{10}$ (or Bi(Pb)-2223) has proven to be a strong contender in the development of composite tapes (due to its flake-like grains) over an extended temperature range under high fields [281-284]. Besides the manipulation of the microstructure (grain size, boundaries, orientation, etc.), achieving high J_c from high quality precursor powders requires a combination of good material science and processing control. This normally involves the monitoring and/or optimization of processing parameters such as heat treatment (section 3.2), mechanical deformation (section 3.3), filament configuration and mechanical property (section 3.5), cladding materials, etc. This section therefore attempts to address some of the remaining processing related parameters such as temperature control, and the initial compositional phase of precursor powders, based on experimental findings, as well as present data obtained for CTFF and PIT MF Bi(Pb)-2223 tapes concerning the 'critical-intermediate-rolling-reduction-zone' (CIRRZ) whose topic has already been discussed in detailed in the previous section (3.3).

3.4.1 Results and Discussion

Details on sample preparation of CTFF and PIT composite tapes can be found in section 2.1. As an extension of Fig. 2.36 (now including powders U, and B), and for comparison purposes, the XRD patterns of precursor powders S, T, D, U, and B are shown in Fig. 3.32, with information related to their compositional phase listed in Table 3.6.

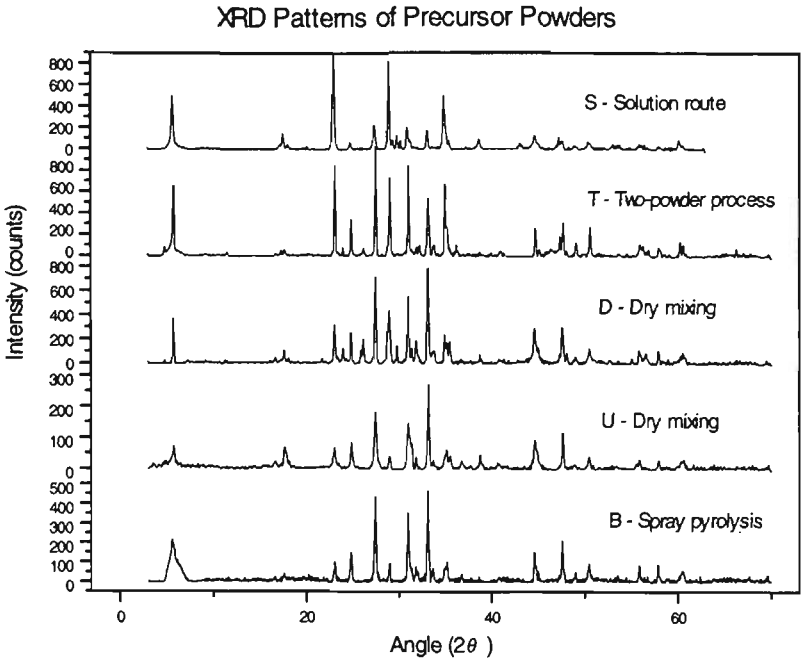

Figure 3.32 *X-ray diffraction patterns of precursor powders S, T, D, U and B.*

TABLE 3.6 *Precursor powder initial phase composition.*

Powder ID	**S**	**T**	**D**	**U**	**B**
Initial 2212 phase	high	high	high	high	high
Initial content of Ca_2PbO_4	low	very low	moderate	moderate	very low
Unreacted phases	low	high	high	low	low

For the precursor powders of Fig. 3.32, it was found that a significant improvement in the electrical transport property, and 2223 phase transformation rate when reduced sintering temperature (of ΔT amount) during the second sintering period of heat treatment was made, using a two-sinter process. One analogy towards explaining this effect would be in 'the cooking of rice' - whereby the cooking temperature is turned down once the water boils to allow for grain growth ! The amount of temperature reduced was found to depend

on the type of powder used and hence its synthesis route. Details on the ΔT drop with sintering temperature and duration used for each type of powder are given in Table 3.7. The extent of the drop appeared to be larger for precursor powders with a relatively higher sintering temperature. This correlation can further be linked to the initial amount of plumbate phase present in the precursor powder (refer to Table 3.6, and Fig. 3.32), since the results strongly suggest that increasing amount of Ca_2PbO_4 tends to decrease the optimal sintering temperature.

TABLE 3.7 *Sintering temperature & dwelling time obtained for tapes prepared from various precursor powders.*

Powder type	**S**	**T**	**D**	**U**	**B**
T1 (±1 ^{0}C)	834	838	832	832	841
P1 (h)	~ 25	~ 25	Σ[#]	Σ	~ 25
P2 (h)	~ 40	~ 40	Σ	Σ	~ 40
ΔT (±1 ^{0}C)[*]	~ 15	~ 15	~ 10	~ 5	~ 15

[*] *ΔT=0 ^{0}C => optimal sintering period of ~ 60 h,* [#] *Σ=P1+P2 ≈ 60 h.*

The appropriate time during the second heat treatment at which the temperature drop was made, has also been investigated, with P1 and P2 respectively, chosen to represent the sintering duration (or dwelling time) before and after the drop. For powders S, T and B, the respective dwelling time of P1 and P2 has been determined to be ~ 25, and 40 h. Altering P1 and keeping P2 constant (and vice versa) was found to degrade the J_c of composite tapes when durations other than the aforementioned values were used. This was tested on MF samples prepared from the various powders. For composite tapes prepared from powders of D and U (namely by dry-mixing), the dwelling time of P1 and P2 has not been investigated, but is expected to be such that their sum equals ~ 60h as indicated in Table 3.7.

Since the objective was to eventually produce long lengths of composite tapes for the construction of coils and magnets, flat-rolling was employed as the intermediate

deformation between sintering stages. As discussed in section 3.3, the degree of intermediate rolling (IR) was found to be crucial in determining the performance of the final tape and indeed was shown that the evolution and development of 2223 and the transport property of Bi(Pb)-2223/Ag compoiste tapes were governed by the extent of deformation induced. Based on these findings, it was necessary to determine approximately the range or window of amount of IR within which an optimal value of J_c could be achieved. This required a systematic study of short samples from numerous batches of MF tapes, and was carried out for samples prepared from both methods of OPIT and CTFF (all unreacted tapes had an initial thickness of ~ 0.32 mm).

TABLE 3.8 *Critical-intermediate-rolling-reduction zone (CIRRZ as a %) for MF Bi(Pb)-2223 tapes.*

Filaments	1st CIRRZ	2nd CIRRZ	3rd CIRRZ
60+3×(80) h			
9 (CTFF)	16-30 >	17 <	3.5 <
12 (CTFF)	27-30 >	16-21	8 <
14 (CTFF)	12 <	18-25	7.5 <
36 (CTFF)	27 >	15 <	7-8 >
37 (CTFF)	30 >	10 <	5.5 <
36Cu (CTFF)	13 <	8 <	5.5 <
31 (OPIT)	15-30 >	15-23	3-5
100+3×(80) h			
9 (CTFF)	16 <	10.5 <	9 <
12 (CTFF)	16 <	13-13.5	7-9 >
14 (CTFF)	37 >	11.7-13.7	6.5-8.5
36 (CTFF)	15-33	11.6-12.5	6.4 <
36Cu (CTFF)	23 <	10 <	3 <

The procedural schematic for the process is shown on the following page. The ID window, or more informatively, the 'critical-intermediate-rolling-reduction-zone' (CIRRZ) for each batch of MF Bi(Pb)-2223/Ag and Ag-alloy (viz. Ag-7 at. % Cu) is listed in Table 3.8, shown as reduction percentages of the tapes' thickness. The shaded regions indicate maximal J_c attained after the subsequent sintering period. This suggests the complexity involves controlling the processing parameters such as intermediate deformation, and filamentary design and preparation.

In summary, apart from the conclusive existence of an optimal sintering period, precursor powders of Bi(Pb)-2223 were found to react much quicker when a temperature drop was incorporated into the second sintering period with the extent of the drop being dependent on the precursor synthesis route, as well as the initial amount of 2212, plumbate and impurity phases. With flat-rolling as the intermediate mechanical deformation between sintering periods, it was conclusively shown the existence a critical-intermediate-rolling-reduction-zone within which superior performance of Bi(Pb)-2223/Ag and alloy of Ag composite tapes can be produced. This reduction zone was found to depend on filamentary characteristics and sample preparation methods.

INTERMEDIATE-ROLLING-REDUCTION SCHEMATIC

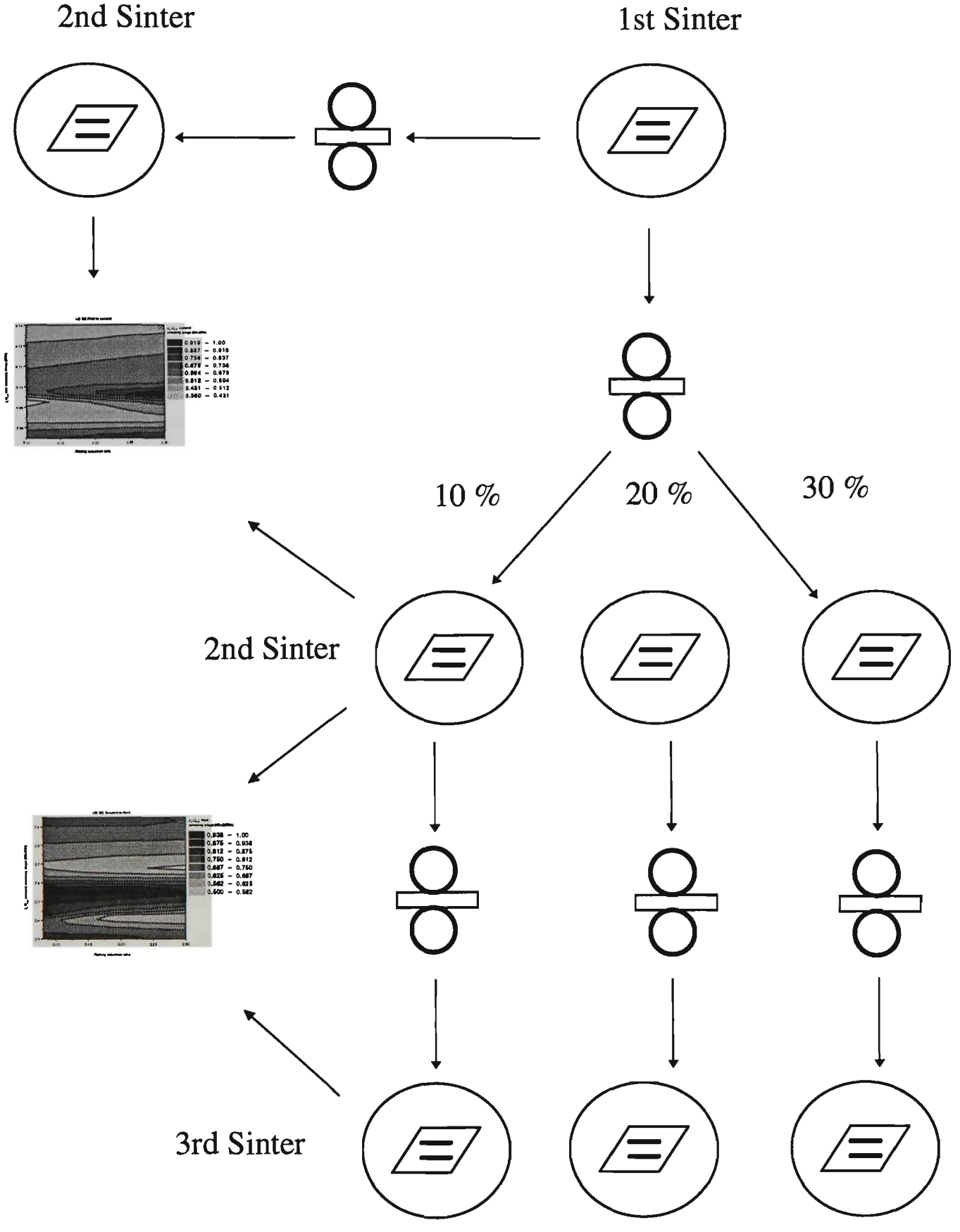

3.5 Mechanical Property and Filamentary Configuration

With high field applications, the requirements for optimization in processing parameters is quite demanding to improve the overall J_e, and minimum propagation zone (MPZ) parameters (such as normal zone propagating velocity, MPZ length, and energy) in HTSCs. Details on the caluclated MPZ parameters for Bi(Pb)-2223 composite tapes are given in chapter 4. This section summarizes the investigation conducted to determine the effect of fill factor, and filamentary geometry on the mechanical and electrical properties of composite Bi(Pb)-2223 tapes prepared by methods of CTFF, and PIT.

3.5.1 Experimental Details

The details on sample preparation and thermomechanical treatment of CTFF and PIT composite tapes can be found in section 2.1. A surface strain tolerance double bend test was carried out by measuring the I_c (determined by pressing the four point contacts on the tape surface with a 1 cm gauge length) of the sample at 77 K, obtained after each cycle of bending/straightened/reverse-bending, using pre-curved metal strips. The bend strain being defined as $\varepsilon = r_t/R$ where r_t is the tape's half thickness and R the radius of bend curvature. Images obtained for transverse and longitudinal cross-sections of the tapes were made using optical and SEM employing both secondary and backscattered electrons (SE, BSE), some of which are given in sections 2.1.2.1, and 2.2.2.

Vickers microhardness (H_V) tests were conducted using the LECO M-400-H1 Hardness Testing Machine (shown in Fig. 3.33) with a 25 g load applied to all samples. As in earlier sections, plots of 3-D surface were made by gridding and corelating the raw J_c, fill factor and sintering time values (hence giving a smaller than should be values of J_c on the axes).

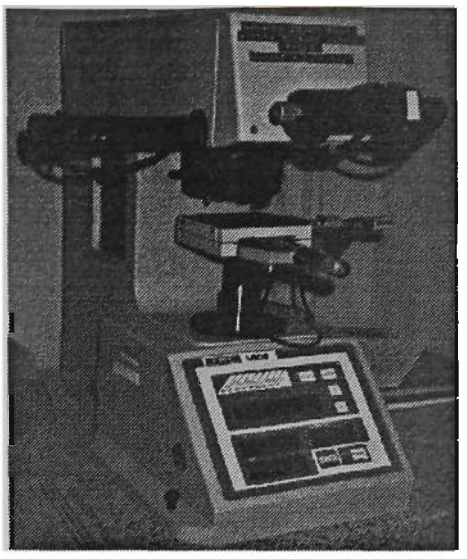

Figure 3.33 *Leco Microhardness Testing Machine M-400-H1, Akashi Corp. Japan.*

3.5.2 Results and Discussion

Apart from the distinctive difference in morphology between the reacted (micaceous) and unreacted (fine agglomerate powder) forms of Bi(Pb)-2223, the volume fraction of this HTSC material to that of the matrix used (most of the time being Ag) was found to varied with processing (during deformation to be more precise). This therefore makes controlling the fill factor λ quite difficult. Nevertheless, optimizing λ is necessary for the improvement in mechanical property as well as quench protection consideration in issues related to conductor design of Bi(Pb)-2223 composite tapes, as discussed in chapters 1, and 4.

Table 3.9 lists the fill factor values obtained for each MT wire and tape at different processing stages, details of which are given in section 2.1.2. The changing in fill factor values across the table indicates a processing dependent nature. For Ag/AgCu, Vickers microhardness tests gave ~ 102/112H_V after work-hardening by rolling to wire form, and ~ 38/64H_V in red tape form (fully treated). For Bi(Pb)-2223 in PIT/CTFF composites, the Vickers microhardness results were ~ 92/103H_V for the packed precursor powders in unreacted form at the wire stage. For the reacted superconducting ceramic of Bi(Pb)-2223, the tests gave ~ 56/195H_V with the applied load (i.e., mechanical indentation onto the

surface) parallel/perpendicular to the *ab*-plane. This suggests that although both powder and matrix have similar hardness prior to the heat treatment stage, their physical properties showed a large change after sintering; some 40-60 % drop in Vickers hardness for the matrix in contrast with an ~ 100 % increase in H_V for the core itself. As expected, variations in fill factors can be attributed to the difference in hardness and ductility between superconductor and matrix which varies with heat treatment and loading (i.e. the amount of rolling reduction applied), as well as non-uniformity along the direction of deformation ('sausaging effect').

TABLE 3.9 *Fill factor values for Bi(Pb)-2223 composite wires and tapes (unreacted -> 'green', and reacted -> 'red'). Refer also to Fig. 2.10 in section 2.1.2.1.*

Sample ID	Wire form	Green tape	Red Tape
MT9	0.233	0.347	0.200
MT12	0.218	0.187	0.126
MT14	0.197	0.254	0.163
MT19	0.297	0.205	0.196
MT31	0.257	0.292	0.187
MT36	0.210	0.209	0.198
MT36Cu	0.154	0.145	0.151
MT37	0.184	0.224	0.154
MT40~	0.130	0.104	0.111
MT50~	0.106	0.093	0.110

~ *Double stacked.*

For samples produced by the double stacking of the strands or filaments (e.g. MT40 and MT50), the matrix content was found to increase (as expected, since the core reduces in size, which was being replaced by the accompanied matrix itself), as well as the complexity in controlling the fill factor ratio. Figure 3.34 shows SEM backscattered

images of cross-sections of single (MT37) and double stacking (MT50) of CTFF MF Bi(Pb)2223/Ag wires and tapes obtained at different processing stages.

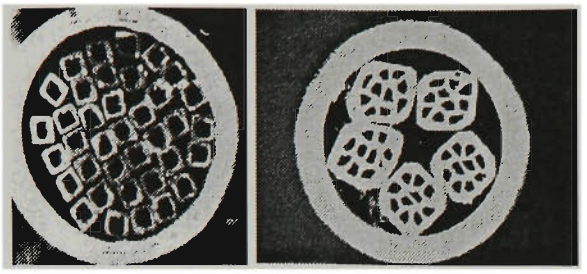

(a) Tube form with ID/OD = 8/10 mm.

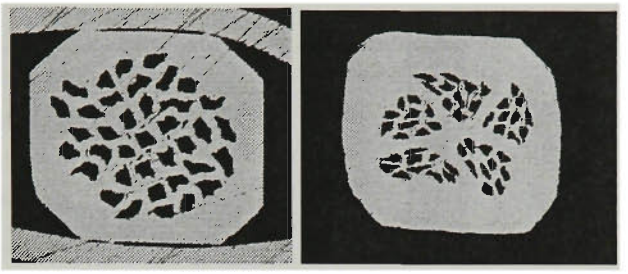

(b) Wire form, ~ 2.2×2.2 and 3.2×3.2 mm^2 for MT37 and MT50 respectively.

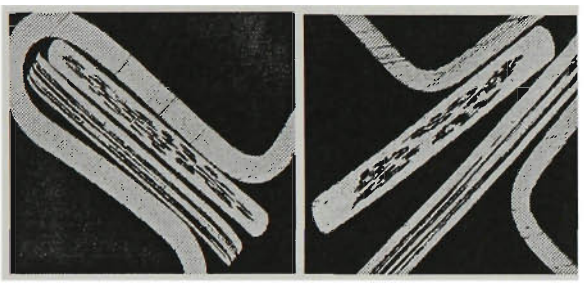

(c) Green tape form (unreacted) of thickness ~ 0.35 and 0.45 mm for MT37 and MT50 respectively.

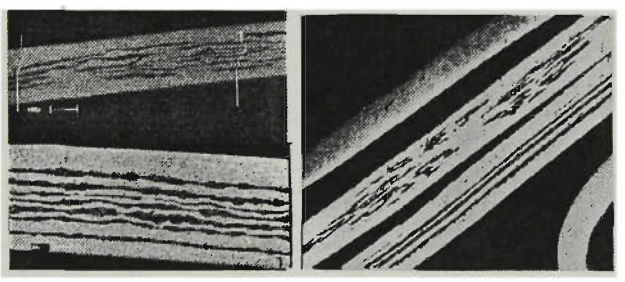

(d) Red tape form (reacted) of thickness ~ 0.24 and 0.37 mm for MT37 and MT50 respectively.

Figure 3.34 *Optical (a)-(c), and SEM (d) (BSE for MT37 red tape) images of cross sections of MF Bi(Pb)-2223/Ag in tube, wire and tape form for MT37 (single stacked) and MT50 (double stacked).*

By arranging symmetrical shaped objects such as hexagons (as shown in Fig. 2.9, section 2.1.2.1), an expression representing the total number of filaments can be derived to be $1+3m(m+1)$ where $m = n-1$, n denoting the number of layers with the central object being regarded as the first layer. The filamentary arrangement from this simple expression theoretically gives the highest fill factor for any multifilamnetary wire. However, in practice, the bundle of filaments is normally circumscribed inside a circle (as that of a circular tube) the overall fill factor then reduces to $\leq 3\sqrt{3}/2\pi \approx 82.7$ % [22]. The fill factor can be improved by removing corner filaments (reducing the space factor) as suggested in a scheme devised by Hillmann [280]. Ideally, the stacking of filaments is often

accomplished with positioners containing preset holes to give maximum number density. Fig. 3.34(a) shows such a configuration with n = 3 (MT37).

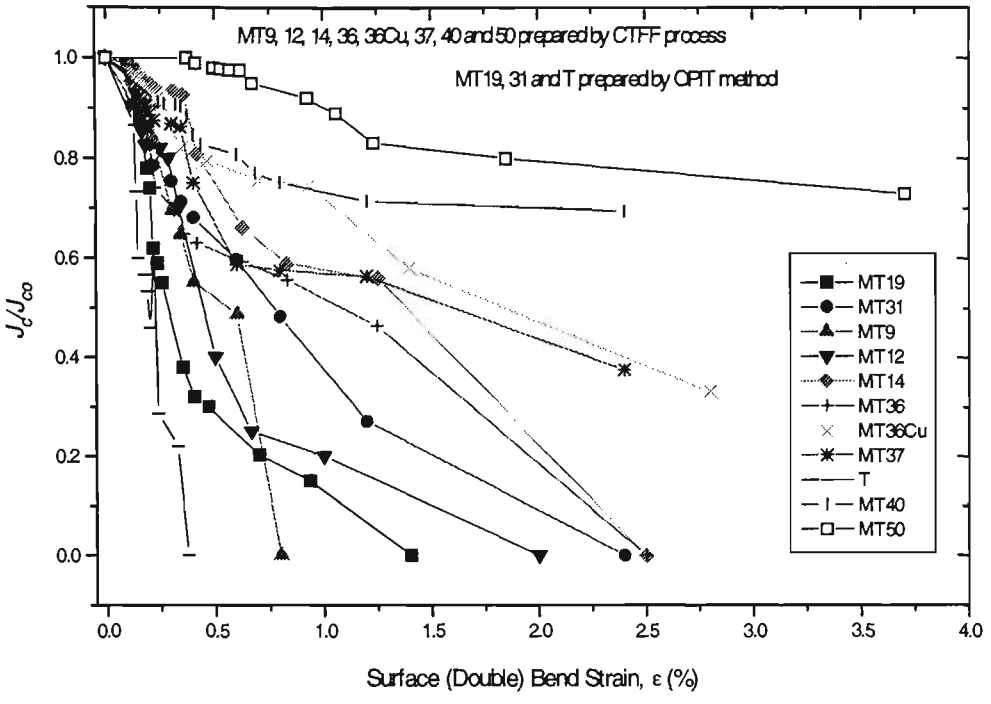

Figure 3.35 *Variations in normalized J_c with respect to surface tensile strain using a double bend test procedure for Bi(Pb)-2223/Ag (and Ag-Cu) composite OPIT, and CTFF tapes, with sample T being a monocore.*

Surface bend strain tests were conducted for MT samples (processed with similar thermo-mechanical treatment) of different thickness containing different number of filaments (Fig. 3.35). The critical strain tolerance (taken here as the strain at which the J_c dropped below ~ 95 % of the original value, as opposed to the strain at which the onset of the lost of supercurrent occurred - as with the results plotted in Fig. 3.6, of section 3.1) together with the fill factor determined for each tape are listed in Table 3.10. For comparable filamentary thickness, the critical strain was found to increase with number of filaments (e.g. for singly stacked samples of MT12 and MT37 with average filamentary width of ~ 15-25 μm and the doubly stacked of MT40 and MT50 with average filamentary width of ~ 7-14 μm), consistent with that found by Masur *et al* [285] and Sato *et al* [111].

TABLE 3.10 *MF tapes' thickness, fill factor and critical bend strain prepared by OPIT and CTFF.*

Sample ID (Preparation method)	Thickness (mm)	Fill Factor (A_{sc}/A_T)*	Critical Bend Strain (%)
MT9 (CTFF)	0.24	0.200	0.2
MT12 (CTFF)	0.20	0.126	0.12
MT14 (CTFF)	0.25	0.163	0.36
MT36 (CTFF)	0.25	0.198	0.18
MT36Cu# (CTFF)	0.28	0.151	0.25
MT37 (CTFF)	0.24	0.154	0.17
MT40 (CTFF) - double stacked	0.24	0.111	0.34
MT50 (CTFF) - double stacked	0.37	0.110	1.06
MT19 (OPIT)	0.28	0.196	0.15
MT31 (OPIT)	0.24	0.187	0.16
T (OPIT)	0.18	0.529	0.12

* *A_{sc} = superconductor area, A_T = area of core plus matrix.*

\# *Silver cladded filaments stacked in sterling silver tube of Ag:Cu ~ 93:7.*

The variation in critical bend strain, as listed in Table 3.10 for MF tapes of different thickness can be attibuted to several factors. The first being the fill factor as pointed out by Osamura *et al* [286], although this was investigated for monofilamentary Bi(Pb)-2223/Ag composites. The second factor being filamentary geometry where poorly located filaments (unevenly spaced) together with a high λ, can result in interfilamentary bridging, which subsequently may have a negative effect on the tape's strain tolerance [287]. The third factor has to do with the superconductor's morphology; phase composition, core density or porosity, the amount and extent of microcracks present, and the different stress and strain states between core and matrix. This last factor implies a well controlled (optimized) thermo-mechanical procedure. Although variation in critical bend strain exists among these MF tapes, it can be observed, from Fig. 3.35 that the higher number of filamentary

tapes tend to retain a much greater percentage of their original I_c with increasing strain. The results shown in Table 3.10 are also suggesting an existence of a critical thickness (of filament and hence of tape) for a particular number of filaments below which the strain tolerance of the tape degrades. This can be understood in terms of the extra flexibility support which the matrix provides in between filaments. Lastly, tests of H_V and strain tolerance show that Ag-Cu alloy improves the overall mechanical property (strength and flexibility) of the tape conductor, an important consideration in conductor design for high field applications.

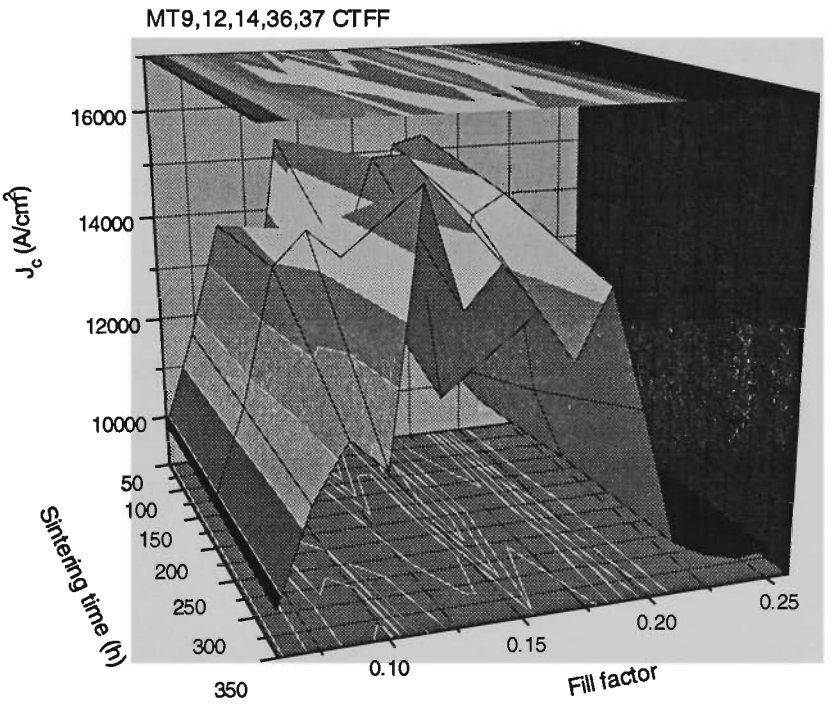

Figure 3.36 *Combined results of J_c versus fill factor and sintering time for batches of MT9, 12, 14, 36 and 37 CTFF tapes.*

As a result of the extensive work performed on many batches of composite Bi(Pb)-2223/Ag and Ag-Cu tapes, it was possible to plot the J_c dependence on fill factor and sintering time for each separate batch (i.e. for a particular number of filaments). Figure 3.36 is a combined 3-D surface plot correlating the results obtained for batches of MT9, 12, 14, 36 and 37 CTFF short tapes. The surface reveals several characteristic peaks (each belonging to a different batch). For a peaking in values of J_c the fill factor is shown to lie

between 0.10 and 0.20. Indeed, as discussed in sections 3.3, and 3.4, an existance of a fill factor range or window was found, within which high values of J_c (but not necessarily I_c) were achieved. This interval of fill factor values corresponded to a particular processing procedure which optimizes the final electrical, mechanical and magnetic properties of the tapes.

Thus in brief, a systematic approach in determining the best thermo-mechanical procedure is necessary each time a HTSC tape is made from different raw materials of precursor powder and the cladding matrix. There is a direct link between the fill factor and the processing procedure which can be utilized to enhance the performance of Bi(Pb)-2223/Ag and Ag-alloy composite tapes. The roll of the matrix using as a cladding material has been shown to be partially responsible for the improving of mechanical property of these tape conductors as the arrangement or geometry of the filaments themselves must be taken into account. Processing parameters such as filamentary size, number of filaments, tape thickness, sheathing materials, intermediate deformation, sintering periods and temperature can all be optimized to maximize the J_c which in turns meet the quench protection requirements (discussed in chapter 4), necessary to improve the performance of these tapes in high field applications.

Chapter 4

Stability Consideration and the Development of Class II Bi(Pb)-2223 Coils and Magnets

4.1 Conductor Design with Bi(Pb)-2223/Ag Composite Tapes

Apart from providing the critical temperature, T_c and upper critical field, H_{c2} for HTSCs, which inherently are intrinsic parameters, practical application purposes require the specification of extrinsic parameters which vary with processing technique and conductor design. Such parameters might include the physical shape and size of the conductor, critical current, matrix stabilization material, and mechanical property. Like many high-T_c oxides, Bi(Pb)-2223 when heat treated correctly crystallizes into a micaceous morphology which is most useful in tape form where the grains can be aligned by means of pressing or rolling for greater performance [288-251, 182, 247].

The discovery of a 90 K superconductor with the general formula of $RBa_2Cu_3O_7$ (where R indicates Y or a rare earth element) by Chu *et al* [290] and subsequently superconductivity at higher temperatures in the Bi-Sr-Ca-Cu-O (BSCCO) and Tl-Ba-Ca-Cu-O (TBCCO) by Maeda *et al* [33], and Herman *et al* [34] respectively has made superconductor applications possible at LN temperature. Since then many conductor designers have evaluated the performance of $Y_1Ba_2Cu_3O_{7-x}$ (YBCO or 123) over a wide range of temperatures (e.g., at 20 K and 77 K [132-133], 4.2 K and 77 K [291] and 4 K, 20 K and 80 K [142, 144, 292]), but relatively few results have been reported on the Bi(Pb)-2223 (or BPSCCO) system, primarily perhaps due to the lack of published data on its cryophysical property.

This section is set out to discuss the inter-relationship between issues concerning the stability and processing of Bi(Pb)-2223/Ag MF, based on measurements and calculations obtained for two particular CTFF MF short tapes, (MT14, and MT37). Also data obtained from their respective batches, and combining with information on cryostability property data gathered from recent studies made by other researchers [131, 22, 129], to provide further insight into conductor design at 77 K (with liquid nitrogen as a coolant). The batch processing details for these samples are given in section 2.1.2.

4.1.1 Stability Parameters for Bi(Pb)-2223/Ag MF Tapes

Some stability parameters were calculated for MF Bi(Pb)-2223/Ag tapes to evaluate their performance at 77 K and to show a direct connection with the mechanical processing of the tapes. Most of the expressions quoted have been slightly modified after Iwasa [131] to account for the multifilamentary layout of tapes. Magneto-resistivity and transport measurements together with mechanical property and processing parameters such as filling factors of the two tapes MT14 and MT37, were examined in conjunction with their calculated stability parameters. Table 4.1 shows a summary of the cryophysical property data which were used to calculate the desired parameters.

The theories behind flux-jump stability and cryostability are given in section 1.3.3. Values for a_{ad} (or $d_{ad}/2$ - eqn. (1.31)), and a_{dyn} (or $d_{dyn}/2$ - eqn. (1.32)) evaluated from temperature dependence data given in Table 4.1 are listed in Table 4.2 together with the corresponding actual tape width and equivalent filament and conductor diameters. The parameters obtained for Bi(Pb)-2223/Ag MF tape conductors have shown that they are flux jump stabled at 77 K, even in adiabatic mode of operation as predicted by Iwasa for high-T_c superconductors [130].

TABLE 4.1 *Temperature dependence of physical properties of Bi(Pb)-2223 MF tapes.*

Property	Symbol	Unit	T (K)	Value	Ref
Specific Heat Capacity of BPSCCO	c_p	J g^{-1} K^{-1}	120	~ 0.192	(a)
Density of BPSCCO	γ_{sc}	g cm^{-3}	300	~ 4.35	(b)
Specific Heat of BPSCCO	C_{psc}	J cm^{-3} K^{-1}	120	~ 0.835	
			77	~ 0.8	
Specific Heat of Ag	C_{pAg}	J cm^{-3} K^{-1}	77	~ 1.7	(c)
Thermal Conductivity of BPSCCO	K_{sc}	W cm^{-1} K^{-1}	77	~ 1.9×10^{-2}	(d)
Thermal Conductivity of Ag	K_{Ag}	W cm^{-1} K^{-1}	77	~ 4.3	(e)
Electrical Resistivity of Ag[#]	ρ_{Ag}	Ω cm	77	~ 3×10^{-7}	(f)
Heat Transfer Coefficient	h_q	W cm^{-2} K^{-1}	77	~ 0.77	(g)
Filling Factor[*] of MT14	λ_{14}	-	300	~ 0.163	
Filling Factor of MT37	λ_{37}	-	300	~ 0.154	
Critical Current Density of SC-MT14	J_{c14}	A cm^{-2}	77	~ 1.58×10^{4}	
Critical Current Density of SC-MT37	J_{c37}	A cm^{-2}	77	~ 1.10×10^{4}	
Critical Current Density of Ag[&]-MT14	J_{ag14}	A cm^{-2}	77	~ 3.83×10^{3}	
Critical Current Density of Ag-MT37	J_{ag37}	A cm^{-2}	77	~ 2.45×10^{3}	
Effective Specific Heat[@] of MT14	C_{cd14}	J cm^{-3} K^{-1}	77	~ 1.553	
Effective Specific Heat of MT37	C_{cd37}	J cm^{-3} K^{-1}	77	~ 1.561	

(a) [131] pp. 399, (b) ibid., (c) [131] pp. 386, (d) [131] pp. 399, (e) [131] pp. 385, (f) [292], (g) [142], [129] pp. 93.

[#] *A function of magnetic flux density.*

[*] *Filling factor:* $\lambda \cong A_{sc}/(A_{sc}+A_{Ag})$

[&] *Critical current density of Ag:* $J_{Ag} \cong J_c(A_{sc}/A_{Ag})$

[@] *Effective or average specific heat:* $C_{av} \cong \lambda\, C_{psc} + (1-\lambda)\, C_{pAg}$

It is also possible to derive and expression involving R_s, the matrix to superconductor ratio, and D, the equivalent wire diameter for fully cryostabled operations [22]. The values of D for MT14 and MT37 (if they were in wire form) are included in Table 4.3 for comparison purposes. Quantities calculated from eqns. (1.34)-(1.36), and (1.38) are listed in Table 4.3.

TABLE 4.2 *Intrinsic-Stability Parameters for Bi(Pb)-2223/Ag MF tapes.*

Parameter	**Symbol**	**Unit**	**MT14**	**MT37**
Adiabatically stable half width of conductor[#]	a_{ad}	mm	~ 16.5	~ 24.5
Dynamically stable half width of conductor[*](zero field)	a_{dyn}	mm	~ 28.7	~ 53.7
Measured half width of conductor	a_{mea}	mm	~ 1.33	~ 1.85
Measured thickness of conductor	t_{mea}	mm	~ 0.25	~ 0.24
Actual equivalent filament diameter	d_{fil}	mm	~ 0.088	~ 0.059
Actual equivalent conductor diameter	d_{str}	mm	~ 0.92	~ 1.06

[#] *The composite nature of the conductor has been incorporated in the expression for adiabatic stability.*

[*] *The theory derived is for single core tapes. The composite nature of the conductor designated* λ_s *for monocore tapes has been replaced by* λ *for multifilamentary tapes.*

Thus with Bi(Pb)-2223/Ag MF tapes, coils and magnets can operate cryostably at LN temperature. In comparison to other HTSC such as YBCO in wire form at 80 K [142, 144], the critical MPZ zones for Bi(Pb)-2223/Ag MF tapes are relatively large. However, mechanical disturbances such as fixer cracking (e.g. epoxy, slurry, etc.) or conductor sliding motion due to the low strength property of the insulating material (e.g. Teflon or alumina paper used in the react-and-wind (R&W) procedure) are still major problems to be addressed. As a result normal zones larger than the MPZ can cause burn out in the winding due to the large concentration of energy at the point source initiating the disturbance as well as the 'inherently' small expansion rate. With the wind-and-react (W&R) procedure where the insulating material used covers most of the tape, the coil (usually solenoidal) can behave adiabatically, which can make matters worse due to insufficient cooling.

TABLE 4.3 *Cryostability parameters.*

Parameter	Symbol	Unit	MT14	MT37	Ref
Total conductor perimeter[%]	P_{cd}	cm	~ 8.53	~ 8.74	
Fraction of P_{cd} exposed to cryogen[#]	f_p	-	~ 2/3	~ 2/3	
Silver/BPSCCO ratio	R_s	-	~ 5.12	~ 5.49	
Area of BPSCCO	A_{sc}	cm^2	~ 8.54×10^{-4}	~ 1.02×10^{-3}	
Area of BPSCCO plus silver	A_{tot}	cm^2	~ 5.23×10^{-3}	~ 6.62×10^{-3}	
Stekly stability parameter[*]	α_{sk}		~ 9.27×10^{3}	~ 1.67×10^{4}	(a)
Conductor diameter (full cryostability)	D	mm	~ 8.7	~ 20.9	(b)
MPZ length (1-D)	l_{MPZ}	cm	~ 134.8	~ 323.8	(c)
NZP velocity (1-D)	v_{ad}	$cm\ s^{-1}$	~ 0.723	~ 0.460	(d)
MPZ triggering energy[&]	E_{MPZ}	J	~ 32.8	~ 100.4	(e)

(a) [131], (b) [22] pp. 274, in wire form only, (c) [131], (d) ibid., (e) [142, 144, 131].

[%] *P_{cd} = 2(w+l), assuming each tape (MT14 and MT37) of length ~ 4 cm.*

[#] *$f_p \approx 2/3$ assuming insulation obscuration of ~ 1/3, [129] pp. 103. This fraction is an approximation for pancake coils where only the edge of the tape conductor is exposed to the cryogen bath. It is much less for solenoidal coils.*

[*] *Values for α_{sk} evaluated at I_c. The coil or magnet does not have to be operated at its utmost limit. A safety margin can be introduced such as $I_{op} < I_{co} = I_c(T_{op})$. The percentage of I_{op} over I_c (for persistent mode operation) can be determined from calculating the index number n from I-V curves. Values of A_m is slightly larger where coils have been fabricated by co-wounding the tapes.*

[&] *ΔE_h predicted for HTS magnets ≥ order of 10 J. [131] pp. 258, 231.*

4.1.2 Magnetoresistivity and Transport Measurements

Magnetoresistivity measurements were made for MT14 and MT37 with the applied field both normal and parallel to the tape plane. The zero field resistivity curve gave a T_c of ~110 K, onset, and ~ 107 K, midpoint, for these tapes. Broadening effect has been observed in curves with increasing field. From these curves the pinning potentials at various field values were obtained by determining the gradient of the tangent to each Arrhenius plot of $\ln R_c$ versus $1/T$ for each tape separately as shown in Fig. 4.1.

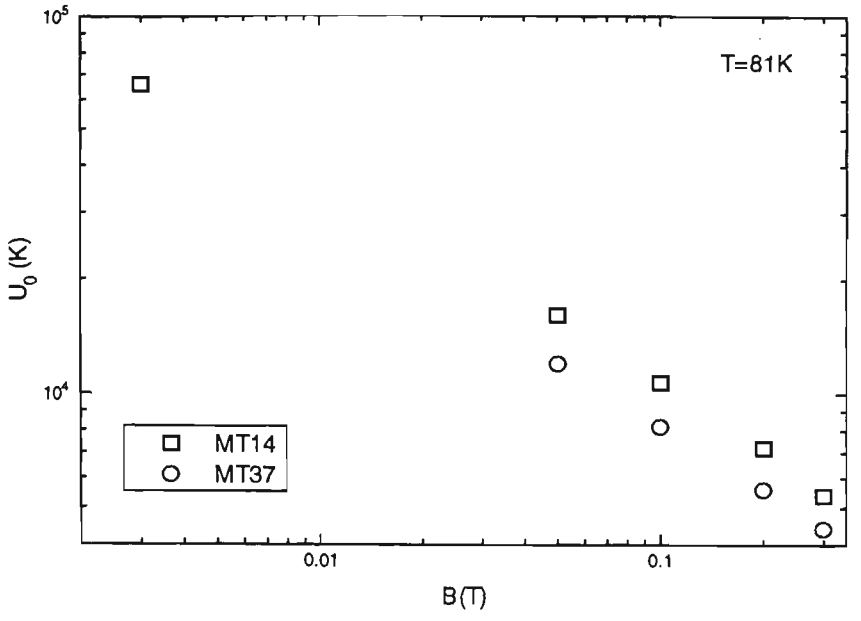

Figure 4.1 *Pinning potentials of MT14 and MT37 in DC field with flux density up to 1 T, at a temperature of 81 K.*

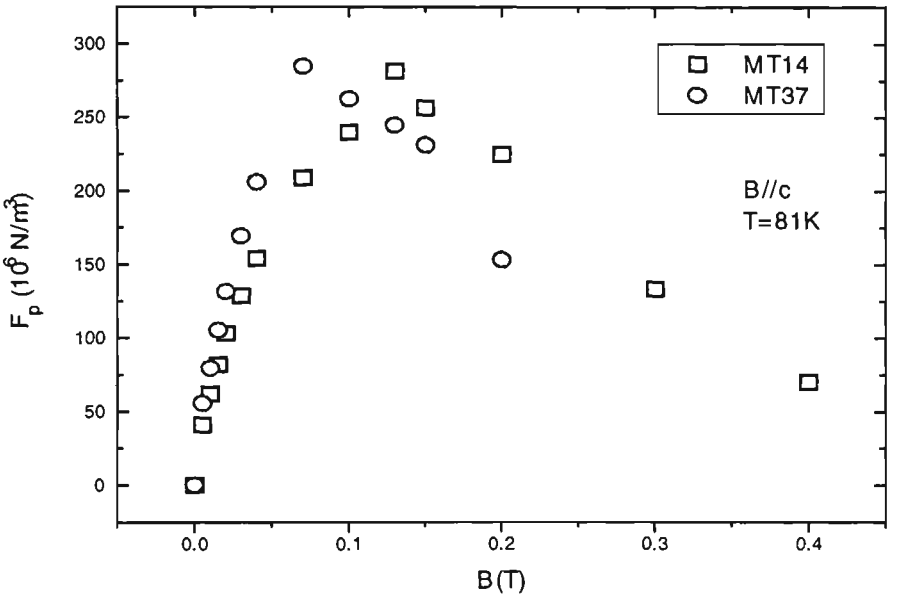

Figure 4.2 *Plots of macroscopic pinning forces versus magnetic flux density with the field applied normal to the tape plane for samples MT14 and MT37 at 81 K.*

Clearly MT14 exhibits greater pinning potential than MT37. In addition, the dependence of J_c in fields with flux density up to 1 T were performed. From these transport measurements the macroscopic pinning force was calculated for each tape with results agreeing to those found from magnetoresistive curves with sample MT14 revealing greater pinning strength, deduced from the apparent shifting of its peak towards the higher flux density regime. This is shown in Fig. 4.2.

A comparison of the J_c-H behaviour between the two tapes were also carried out, shown in Fig. 4.3. Here, MT14 again retained a larger percentage of its zero field J_c value in flux density greater than ~ 100 mT.

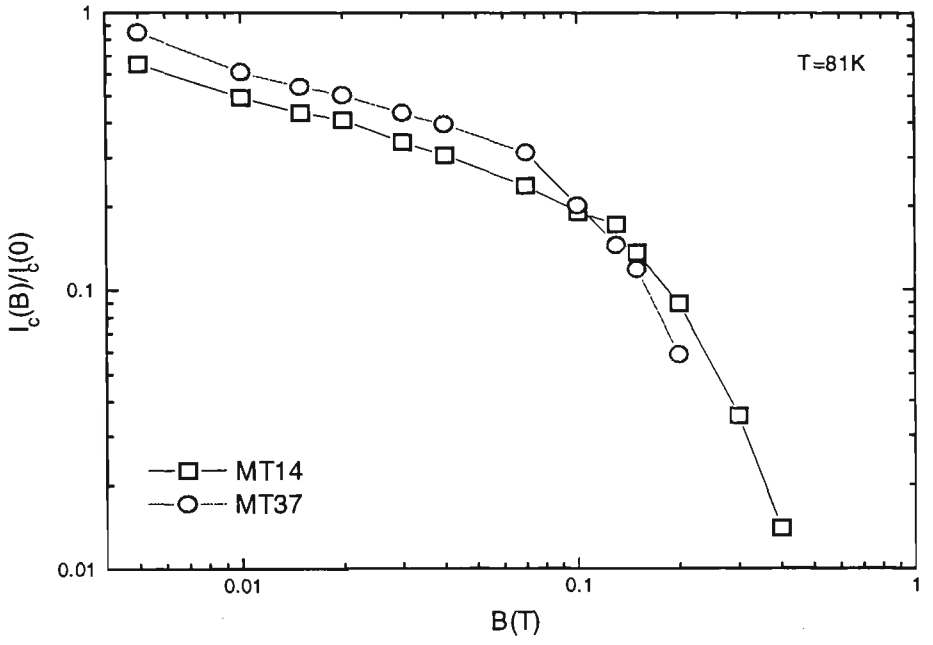

Figure 4.3 *Comparison of the J_c-B behaviour between MT14 and MT37.*

4.1.3 Mechanical Property

A double bend strain tolerance (bend/straighten/reverse/bend/straighten/remeasured) test was conducted at 77 K for MT14 and MT37, shown in Fig. 4.4. The curves show a contrary result to what has been expected in that the critical bend strain for MT14 was

found to be about the same as that of MT37. In fact, MT14 retained on average a higher percentage of its initial I_c than MT37 up to a strain of about 1.25 %.

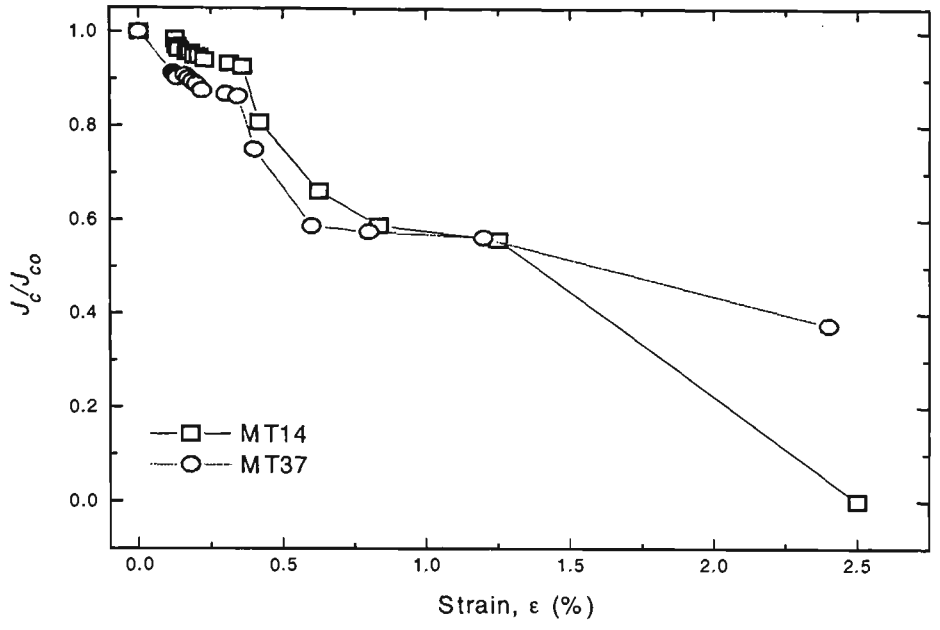

Figure 4.4 *Double bend strain tolerance test at 77 K for MT14, and MT37, each with different filling factor.*

It has been pointed out by Sato *et al* [111] that although the strain tolerance of BSCCO/Ag composites can be increased by increasing the number of filaments, the filling factor might not remain constant which can pose a problem in filament size consideration (stability, and the onset of sausaging). The result from Fig. 4.4 was indeed quite unexpected since the measured filling factors for MT14 and MT37 were found to be (from Table 4.1), 0.163, and 0.154 respectively, which according to the work of Osamura *et al* [286], based on SF silver composite tapes, suggests that higher strain tolerance favours a smaller filling factor. An explanation for this can be found from optical images of MT14, and MT37 (Fig. 4.5) where inter-filamentary microstructural cross-over or bridging was found to occur more frequent in the latter image. This is the result when too much deformation was committed to a MF tape. Indeed, initial filamentary size and tape thickness, dictate the amount of deformation beneficial to the performance of the tape conductor.

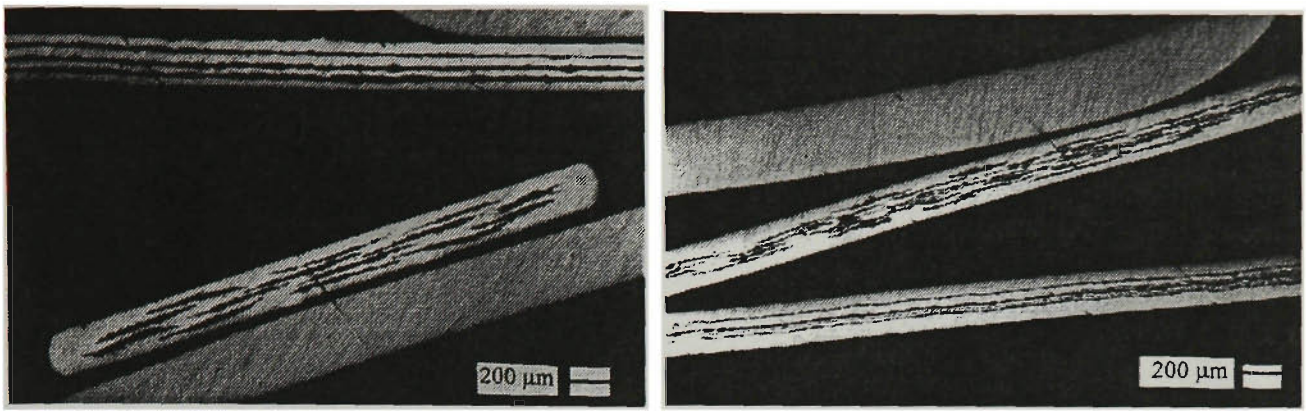

(a) *(b)*

Figure 4.5 *Optical microimages of the transverse, and longitudinal cross-sections of (a) MT14, and (b) MT37.*

4.1.4 Deformation, Fill Factor, and Stability

Three dimensional phase space of critical current density, sintering time and fill factor was generated, based on measurements obtained from a batch processing of some dozen samples of MT14 and MT37 separately. The tapes produced from each batch started out with a given value of fill factor. A systematic deformation procedure was performed to show the inter-relationship between intermediate deformation, fill factor and electrical property of the MF tapes. The 3-D contour curves of Fig. 4.6 for batches of MT14 and MT37 tapes reveal the existence of a window on filling factors outside which the tape's performance degrades. This degradation of J_c can be understood from effects such as bridging (which can be controlled during the intermediate deformation process), and stability issues (which was shown to depend on factors such as R_s, the ratio of matrix/superconductor, and λ, the fill factor).

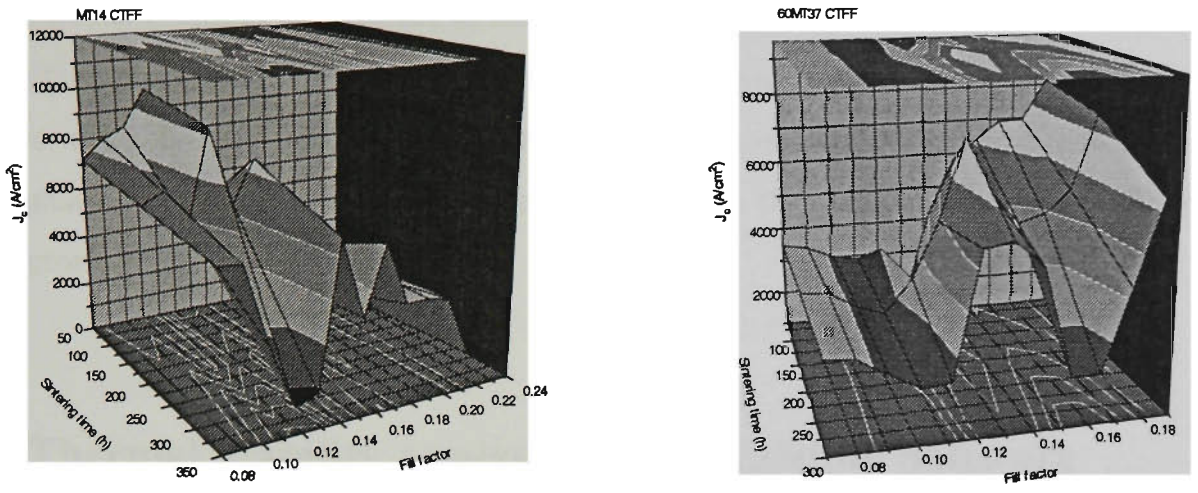

(a) *(b)*

Figure 4.6 *Critical current density-sintering time-filling factor surface plots of processed batch samples of (a) MT14 and (b) MT37.*

4.1.5 Present Status of Bi(Pb)-2223 MF Tapes

Stability issues on conductor design with multifilamentary Bi(Pb)-2223/Ag tapes was addressed. Due to Bi(Pb)-2223/Ag being available as tape, the dynamic stability criterion is applicable to edge-cooled (in cryogen bath), or force-cooled (stream of cold gas such as helium) coils and magnets. These tape conductors are unlikely to experience any flux jump instability when using LN as a coolant. Bi(Pb)-2223/Ag MF tapes were found to be able to sustain superconductivity (at 77 K), perhaps better than other HTSC such as YBCO in wire form even in the presence of a quench-causing disturbance by virtue of their large critical normal zone length based on the theory of MPZ. The expansion rate of the normal front however was found to be comparable to those found for other HTSC suggesting cryostability could only be achieved as long as sufficient cooling was provided in the case of a quench. The concentration of the triggering energy was determined to be relatively large (as predicted), nearly an order in magnitude in comparison to YBCO wire. This prompts further improvement on the tape processing aspect with the need to optimize processing parameters such as R_s and λ to further increase the normal front velocity to avoid the formation of hot-spots. In general, the processing side of conductor design was found to be related to issues of stability. Parameters such as R_s, and λ can ultimately

determine the extent of the stability of the tape and although difficult to maintain constant during tape processing, they are controllable if the processing of tapes and fabricating of devices can be fully automated. Additionally, intermediate deformation and initial filamentary size were also found to be influential to the performance of these tape conductors.

4.2 Thermal Stability Analysis with Simulation Software

Based on the extensive research in materials processing and the design and construction of Bi(Pb)-2223 coils and magnets, this section embarks on issues concerning the thermal stability of Bi(Pb)-2223/Ag pancake-shaped coils, from a processing point of view, with the use of a numerical analysis software simulation package which implements the method of three-dimensional finite elements. Details on tape preparation and coil production are given in sections 2.1.2, and 2.1.3 respectively.

4.2.1 Software Simulation

The thermal analysis of one of the test coils (Coil ID 7, refer to Appendix C) was conducted by means of a computer simulated software using the method of three-dimensional finite elements. In the finite-element model, the actual continuum or body of matter is divided into an assemblage of subdivisions called finite elements. The elements are interconnected along the elemental boundaries at specific joints common to two or more elements (nodes or nodal points). The larger the number of nodes for each element, the more sophisticated the element will be. The actual variation of the field variables (e.g., displacement, stress, temperature, pressure, velocity, etc.) inside the continuum is not known and is approximated by a simple function, obtained in terms of these variables at the nodes for a particular element. Combinations of appropriate boundary conditions and considerations on equilibrium and compatibility are determined for the elements to give a set of constraints. As a consequence of these operations, a set of finite linear equations is obtained in terms of the unknown field variables for each element. The simulation attempts to solve the heat flow equation (as given by the first law of thermodynamics on

the conservation of energy) by considering the temperature variation with thermal conductivity and the effect of the convection coefficient from the surface of the coil (edge-cooled). The step-by-step approach of the finite- element method (both in steady-state and transient) can be summarized as follows:

1. Formulate governing equations and boundary conditions
2. Discretize and select element types
3. Select interpolation functions
4. Determine elemental properties
5. Assemble global equations
6. Solve global equations
7. Interpret results
8. Verify results

4.2.2 Coil Modeling and Simulation

The coils used in the simulation analysis were derived from an actual HTSC Bi(Pb)-2223/Ag pancake-shaped test coil made using the procedure of R&W with an overall J_c before and after winding of ~ 7, and 4 kA/cm^2 (77 K) respectively, shown in Fig. 4.7(a), together with SEM (backscattered) microimages of the transverse, and longitudinal cross-sections of the MT tape used for winding, shown in Fig. 4.7(b).

The two types of coils simulated were the monolayer (singly wound superconductor) and multilayer (two layers of co-wound tapes) coils. The fill factor for the MF tape was determined to be ~ 0.15. For the actual test coil, three layers of teflon tape each of thickness ~ 0.03 mm were used as the insulating material between each of 12 turns consisting of two layers of co-wound MF tapes, each of thickness ~ 0.34 mm. The schematic is shown in Fig. 4.7(c) with the assumption that the designated total area of the superconductor is an aggregate of each filamentary area to reduce computation complexity.

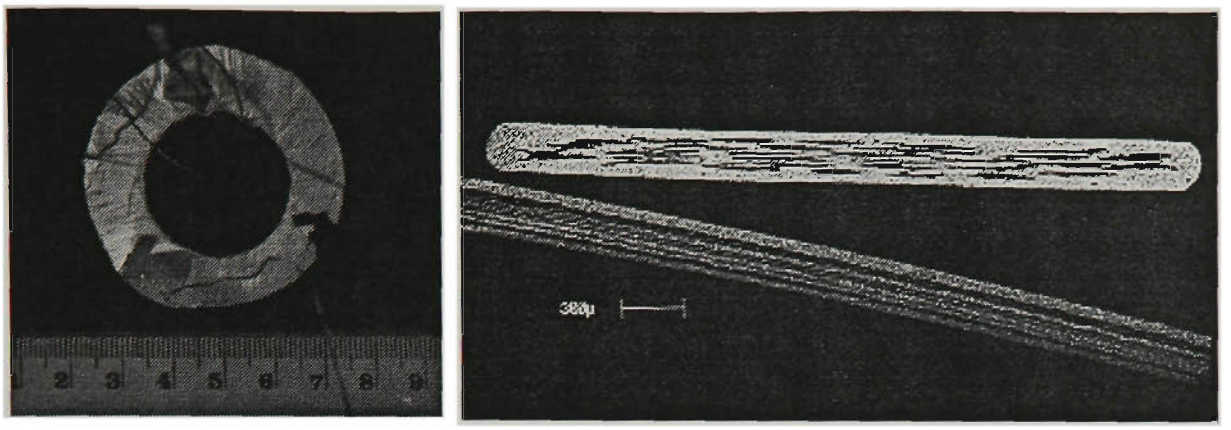

(a) (b)

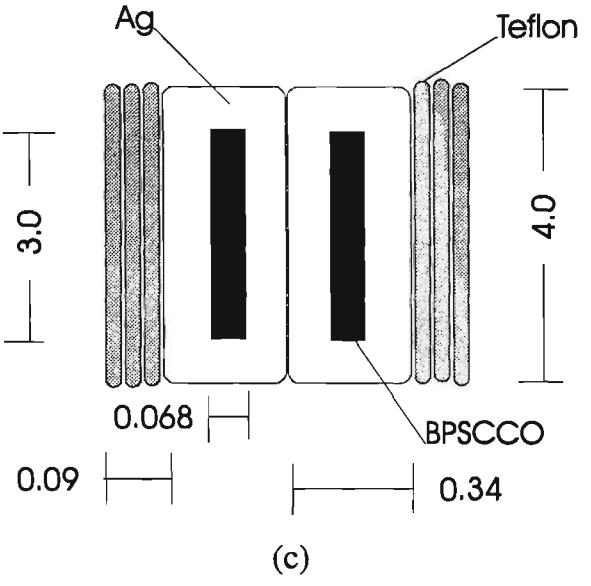

(c)

Figure 4.7 *(a) Bi(Pb)-2223/Ag pancake-shaped test coil (R&W procedure), (b) SEM (backscattered) micro images of the transverse and longitudinal cross-sections of the 31-filamentary tape used for winding, (c) Schematic of cross-section of the multilayer coil.*

The material properties relevant to thermal analysis include density, thermal conductivity and specific heat capacity. The physical constants for silver, teflon and BSCCO are listed in Table 4.4. The density of BSCCO was taken as ~ 3.157 g/cm^3 at the time of the simulation; a more accurate value would be ~ 4.350 g/cm^3 for BPSCCO with corresponding heat capacity of ~ 0.192 Jg^{-1}K^{-1}, see [131] pp. 399. The dependence of the thermal and normal electrical properties of each material on temperature was neglected as

the temperature change in the simulation is not sufficiently high to influence results significantly.

TABLE 4.4 *Physical properties for thermal analysis.*

Material	Density (gcm^{-3})	Thermal Conductivity ($Wcm^{-1}K^{-1}$)	Specific Heat Capacity ($Jg^{-1}K^{-1}$)
BSCCO	~ 3.157	~ 1.02×10^{-2}	~ 0.172
Ag	~ 10.49	~ 4.31	~ 0.151
Teflon	~ 2.302	~ 2.91×10^{-3}	~ 19.37
air	~ 2.783×10^{-3}	~ 7.62×10^{-5}	~ 1.032

4.2.3 Thermal Analysis

In this analysis, different values of heat generation rates were input into the software simulation to obtain their effect on temperature. The aim was to determine the cryothermal stability (at 77 K) for the entire superconducting coil, as a result of an onset of a temperature rise on part of the superconducting tape (by studying a cake-slice of the coil). For comparison purposes, two values of the film boiling heat transfer rate (film coefficient) of LN were assumed, 0.3 and 1.0 W/cm^2K, although a value of ~ 0.6 W/cm^2K is normally used [136]. Conventionally, it is assumed that the superconducting coil fails if the temperature of any part of the coil rises by more than ~ 5^0 above LN temperature. For an edge-cooled pancake-shaped coil, depending on how well the matrix can avert hot-spot formation (matrix's resistivity and fill factor) and whether sufficient cooling is available, the onset of a temperature rise in any part of the coil can also act as a heat-dissipating source to the adjacent layer of the tape (whether co-wound or singly wound). This ohmic heating can result in a domino effect with more sections of tape failing until ultimately the entire coil fails.

When part of the coil becomes nonsuperconducting, the current will be shunted into the silver matrix and dissipate heat. Knowing the cross-sectional areas of BPSCCO (~

0.00204 cm^2 for two co-wound tapes), the Ag matrix (~ 0.0231 cm^2 combined), the critical current I_c (~ 8.16 A) and the resistivity, ρ, of Ag, (~ 2.89×10^{-7} Ωcm), the heat generation rate (calculated from the current passing through the superconductor just before it failed) for a single node (as $I^2R/63$ per node) was determined to be ~2.673 μW. This generation rate was input in the simulation for both the mono- and multilayer coils for two different values of film coefficients. The resulting temperature rise is summarized in Table 4.5. Comparing the temperatures for the four cases with the initial temperature of 77.35 K, it appears that there is no significant change in the temperature of the coil itself and no thermal gradient exists in the coil.

TABLE 4.5 *Thermal analysis results for the simulated coils with a fill factor of ~ 0.15.*

Coil Type	**Film Coefficient (W/cm^2K)**	**Temperature Rise (K)**
Mono-layer	0.3	~ 77.358
	1.0	~ 77.351
Multi-layer	0.3	~ 77.370
	1.0	~ 77.365

It can be shown that the fill factor (λ), and heat generation rate (with Joule heating as the major dissipative source) are related as follows:

$$P = \frac{I^2 \rho l}{A_{BPSCCO}\left(\frac{1}{\lambda} - 1\right)}, \tag{4.1}$$

where l is the unit length of the conductor under consideration.

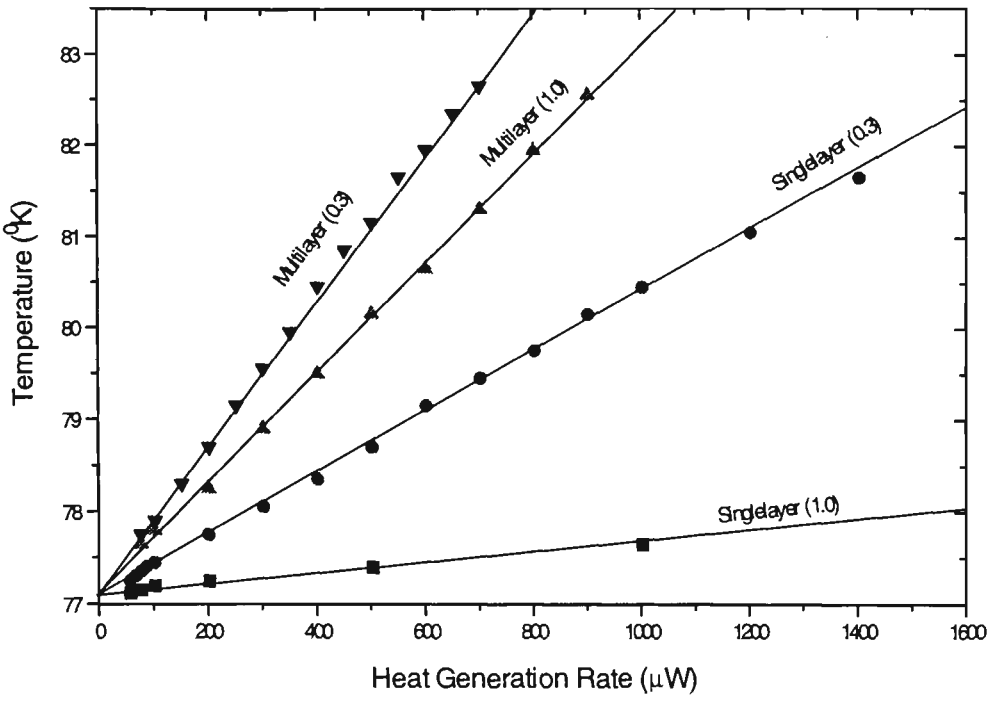

Figure 4.8 *Plots of temperature versus heat generation rate.*

It was then possible to vary λ and obtain plots of temperature versus heat generation rate; the results are shown in Fig. 4.8. Table 4.6 lists values of P (for corresponding values of λ using the two different values of film coefficients) required to increase the temperature from 77.35 to 78.35 K and from 77.35 to 82.35 K for the two coil type. To raise the temperature by 5 K, the maximum permissible fill factors were found to be 0.991 and 0.999 for the monolayer, and 0.977 and 0.983 for the multilayer coil with film coefficients of 0.3, and 1.0 W/cm^{2}K, respectively. The fill factor required to raise the temperature by 1 K was found to be 0.958, 0.995, 0.896, and 0.920, respectively. From Fig. 4.8, and Table 4.6, the amount of heat generation needed to raise the temperature whether by 1 or 5 K is greater for the monolayer coil than for the multilayer one. In other words, the value of fill factor can be increased to a greater extent in the case of the monolayer coil in comparison with the multilayer one. In the latter situation there would be more dissipation involved due to the greater possibility of a domino effect between adjacent tapes in the event of the onset of a thermal runaway, which would require a much greater amount of matrix

available for diverting the nonsupercurrent from a larger (in aggregate) core of BPSCCO ceramic.

TABLE 4.6 *Results for a 1 and 5 K temperature increase.*

Coil Type	**Film Coefficient** (W/cm^2K)	**Heat Generation** P **(mW)**	**Fill Factor** (λ)
Mono-layer (1 K ↑)	0.3	~ 0.34	~ 0.958
	1.0	~ 3.06	~ 0.995
Multi-layer (1 K ↑)	0.3	~ 0.13	~ 0.896
	1.0	~ 0.17	~ 0.920
Mono-layer (5 K ↑)	0.3	~ 1.70	~ 0.991
	1.0	~ 15.0	~ 0.999
Multi-layer (5 K ↑)	0.3	~ 0.65	~ 0.977
	1.0	~ 0.86	~ 0.983

Furthermore, by increasing the film coefficient or cooling rate (e.g., also with cryocooler-cooled coils and magnets) from 0.3 to 1.0 W/cm^2K, the heat generation rate (and hence fill factor) increases by nearly an order for the single-layer coil. Multilayer pancakes are normally preferred as greater amount of current and strength can be achieved [118, 80, 123]. However, an increase in the number of co-wound tapes would require a counter balance in the reduction of the fill factor value per tape necessary for thermal stability. The amount of BPSCCO core can thus only be increased at the expense of the extra cost required to increase the cooling rate for the edge-cooled coils.

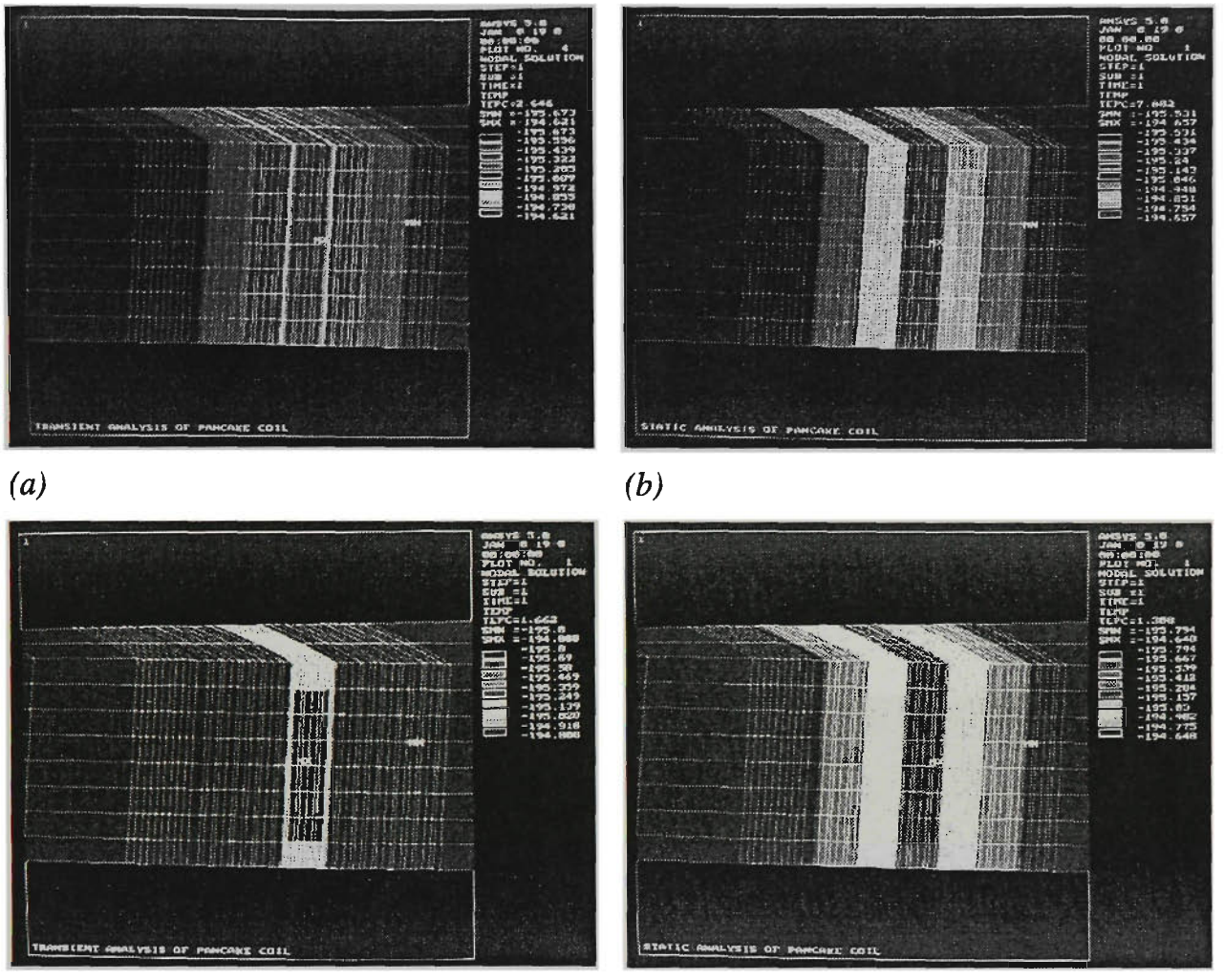

(a) *(b)*

(c) *(d)*

Figure 4.9 *Temperature distribution with film coefficient of 0.3 W/cm^{2}K for (a) monolayer, (b) multilayer, and of 1.0 W/cm^{2}K for (c) monolayer, and (d) multilayer coil.*

To see the difference in temperature distribution between the two types of coils, photographs were obtained from simulation (cake-slices) comparisons of the mono- and multilayer coils respectively, with film coefficients of 0.3 W/cm^{2}K (Figs. 4.9(a),(b)) and 1.0 W/cm^{2}K (Figs. 4.9(c), (d)). As expected, for equal values of fill factor, the advantage of increasing the heat transfer coefficient for the single-layer coil is most apparent where edge-cooling is much more effective (Fig. 4.9(c)). Similarly for the heat flux distribution, the degree of effectiveness of heat removal from the failed section of the tape (hot-spot

formation) is shown as contour plots in Figs. 4.10(a)-(d). Again, an increase in cooling was found to be more beneficial to the monolayer coil (Figs. 4.10(c) and (d)).

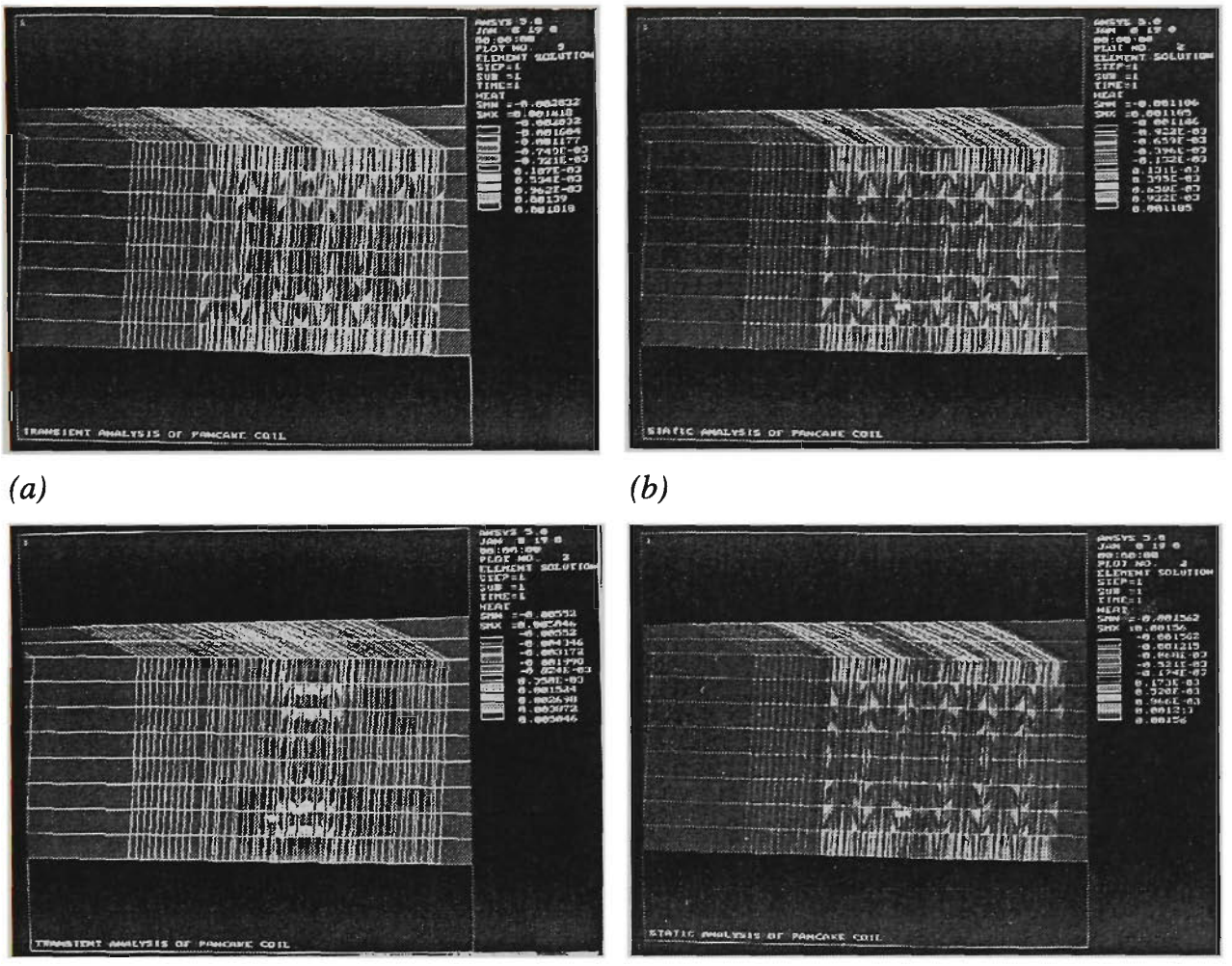

(a) *(b)*

(c) *(d)*

Figure 4.10 *Heat flux distribution with film coefficient of 0.3 W/cm^{2}K for (a) monolayer, (b) multilayer and of 1.0 W/cm^{2}K for (c) monolayer and (d) multilayer coil.*

4.2.4 Concluding Remarks

Processing related issues, and the thermal stability design of Bi(Pb)-2223/Ag pancake-shaped coils were discussed in detail. To achieve optimal current capability, a gradual reduction in the amount of intermediate deformation between sintering periods was determined for MF Bi(Pb)-2223/Ag tapes. This corresponded to a particular value of the

fill factor which played a crucial role in the thermal stability of the processed pancake-shaped coils. Although multilayer pancake-shaped edge-cooled coils normally can normally achieve larger critical currents, and greater mechanical integrity in comparison to the monolayer ones, they tend to require greater cooling, and are limited to a certain amount of superconductor, and matrix present depending on the number of co-wound tapes, in order to sustain an equivalent thermal stability as would be achieved by their monolayer counterparts.

4.3 Development of Bi(Pb)-2223/Ag Pancake-Shaped and Solenoidal Coils

With the highest critical temperature (T_c of ~ 110 K onset, or ~ 107 K mid-point), and excellent magnetic-field-dependent critical current densities, $J_c(B)$, from 4.2 to ~ 30 K [281, 293, 283, 284] among the Bi-based superconducting compounds, Bi(Pb)-2223 stands as the most likely candidate for high field magnet applications. In zero applied background field, Bi(Pb)-2223/Ag and Ag-alloy magnets have reached self generating fields of ~ 2.6 T (10 pancake coils, each made from ~ 3×16 m co-wound tapes - W&R and R&W) [118] and ~ 2.4 T (17 double pancakes each consisted of ~ 3×23 m co-wound tapes - R&W) [122] at 4.2 K, and ~ 0.36 T [118] and ~ 0.24 T [122] at 77 K. The overall combined field can be much greater (about one order) when these Bi(Pb)-2223 coils are used as insert magnets.

As mentioned in earlier chapters, practical purposes, and due to its morphology, Bi(Pb)-2223 superconducting ceramic comes in the form of a tape which requires repeated cycles of sintering-deformation-sintering to improve the grain alignment, growth, texture, connectivity and core density [294-298, 271]. Fabricating coils and magnets then requires the tape to be wound which can have a detrimental effect on the ceramic core microstructure of the composite conductor. With technical advances in tape production and coil making however, MF tapes, using the method of wind-react (W&R)

have been employed successfully to produce high performance superconducting coils and magnets [118, 122].

In this section, the fabricating of Bi(Pb)-2223/Ag pancake-shaped (both in single, and double format) and solenoidal coils from MF tapes using both the R&W, and W&R procedures is presented. In addition, some recent J_c data obtained for Bi(Pb)-2223 double pancake-shaped (DP) coils at 77 K, fabricated from silver- and silver-alloy sheathed composite tapes prepared by the novel methods of wire-in-tube (WIT), continuous-tube-forming/filling (CTFF) and the standard method of powder-in-tube (PIT), are also given and discussed.

4.3.1 Experimental Details

The fabrication of the 31-filamentary tape (precursor powder U), used to produce single pancake-shaped (with ID 14-18), and solenoidal coils (IDs 24, and 31) is given in section 2.1.2. After the final sintering step two 50 cm long samples were obtained from the long length MF tape, tested using a '50-probe' instrument developed to determine the uniformity of J_c along the longitudinal direction of the tape. Variations in J_c was found to be within the ~ 12 % margin, due to factors such as sausaging and processing induced defects along the tape (consult Fig. 2.52, of section 2.2.6 also).

Figure 4.11 shows both the transverse and longitudinal cross-section images of the tape (left) obtained from optical microscopy. The long length MF tape was divided roughly into two halves one for fabricating the five pancake-shaped coils and the other used for making two solenoidal coils. With the R&W procedure used to fabricate coil 24, an alumina ceramic tube was used for the final sintering stage, also depicted in Fig. 4.11.

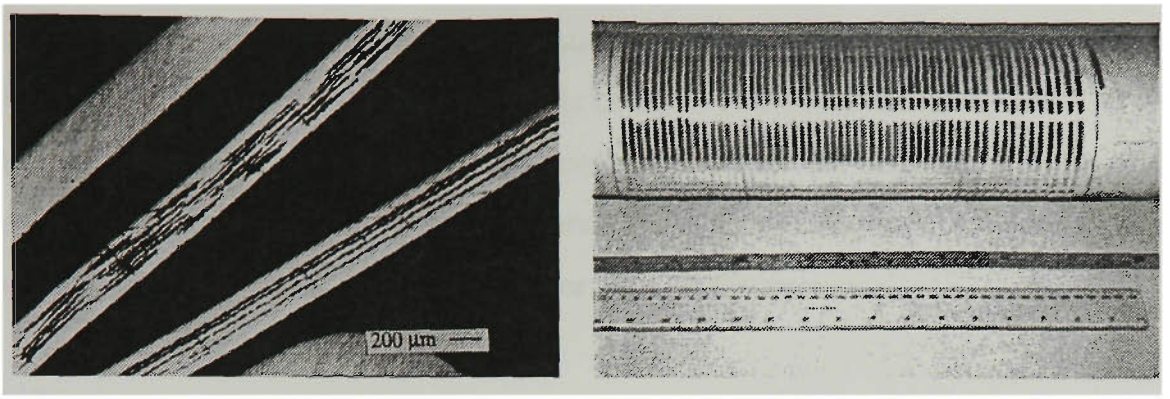

Figure 4.11 *Optical micro-images of the transverse and longitudinal cross-sections of the 31-filamentary tape (left). Partially reacted long length MF tape wound on an alumina ceramic tube used during high temperature heat treatment (right).*

For the DP coils, two alloys of silver used were: Ag-7 at.% Cu, and Ag-0.02 at.% Mg. These composite alloys of silver were processed into tape using the standard PIT method. The processing of composite tapes and fabrication procedure of pancake-shaped coils can be found in section 2.1.2-3. Final thickness of the composite tapes were 0.28, 0.29, 0.35, and 0.14 mm used in the winding of DP35, 36, 25 and 37 respectively. All DP coils were fabricated through the use of a W&R procedure. For short sample testing, the standard four-probe technique was used to detect resistive voltages. The transport current for which a resistive voltage of 1 µV appeared across voltage taps separated by 10mm corresponding to a resistive electric field of 1 µV/cm was chosen to be the I_c. The normalized J_c *vs* B characteristics of the short samples (applied field parallel and normal to the *c*-axis) were obtained from transport measurements conducted with external magnetic flux densities up to 1 T generated from a 90 mm bore water-cooled magnet (Fig. 2.55, section 2.2.6). Critical transport measurements for the DP coils were calculated based on the 10^{-11} Ω-cm criterion, using the I_c (1 µV/cm) value measured from a short section of the coil.

4.3.2 Single Pancakes and Solenoidal Coils

The making of pancake coils can be said to have evolved from the fact that it is easier to produce shorter lengths of tape than long ones especially on a laboratory scale. Besides, if

one of the pancake coils in a magnet construction happens to break down for some reasons (e.g. due to mechanical disturbances), it is better to substitute the faulty pancake coil than to replace the entire magnet as the case may be if a solenoidal coil was used. One major set back with pancake coils however is the problem of connecting them together (less so with double-pancakes) which in itself is another topic of discussion.

TABLE 4.7 *Physical properties of the fabricated SP, and solenoidal coils.*

Coil ID	Type[@]	Powder type	Filaments	Tape thickness[#]	Layers
14	P, W&R	U	31	0.32	2
15	P, W&R	U	31	0.32	2
16	P, W&R	U	31	0.32	2
17	P, W&R	U	31	0.32	2
18	P, W&R	U	31	0.32	2
24	S, R&W	U	31	0.34	1
31	S, W&R	U	31	0.32	1

[#]Dimensions in mm, [@] SP: single pancake, ~ 2 m long, S: Solenoidal,
coil 24 ~ 7 m, coil 31 ~ 14 m, refer to Appendix C for more details.

The five single pancake (SP) coils, and two solenoidal coils present here are identified accordingly as shown in Table 4.7, together with the information on their physical dimensions. Photographs of the actual coils themselves are shown in Fig. 4.12. The SP coils (ID 14-18) were fabricated using the W&R procedure by co-winding two layers of tape together. The winding took place after the second to last sintering stage when some 20 m length of MF tape was deformed by rolling for the last time, cut up into strips of tape ~ 2 m long, then co-wound two at a time with a thin coat of an alumina based slurry of ~ 100 μm thick applied to one side of one of the tapes. A final heat treatment was then performed after setting and curing of the coils to complete the fabrication process.

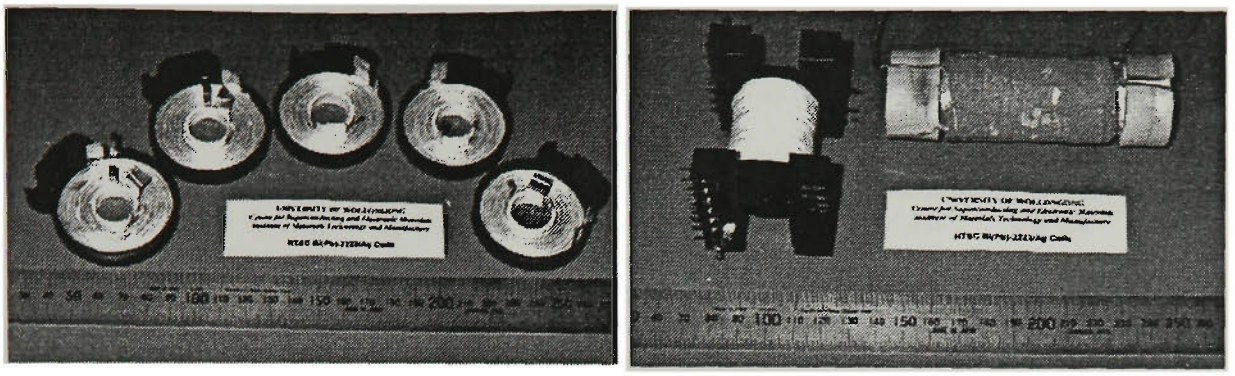

Figure 4.12 *SP coils made using the W&R procedure from a total combined length of ~ 20 m of MF tape, each generates a field of ~ 5 mT at 77 K in zero background field (left). Solenoidal coils made using the R&W and W&R procedure from a total combined length of ~ 20 m of MF tape. The R&W coil (~ 400 ampere-turns on the left) generates a field of ~ 12 mT, while the W&R coil (~ 973 ampere-turns) generates ~ 19 mT, both at 77 K in zero background field (right).*

The reason for using MF tapes and co-winding them is of two fold. The first is for extra mechanical flexibility which is crucial especially with the R&W procedure and also to reduce the risk of damaging the tapes during the handling operation. The second reason is related to issues of stability and losses. These issues have already been addressed in other sections (2.1, 3.5, and 4.1). For the solenoids (in particular S 31), the methodology used was very much the same to that used to produce the SP colis, with the exception of it being singly-wound. Solenoid 24 (~ 400 ampere-turns) however, was made using the R&W procedure with the insulating material being teflon. The critical bend strain from a double bend tolerance strain test was determined to be ~ 0.15 % after the final heat treatment, measured from a short sample obtained from the long length.

Electrical and magnetic properties of these coils at liquid nitrogen temperature of 77 K are tabulated in Table 4.8. The I_c for each coil was obtained using the $10^{-13}\Omega$m criterion. The J_c, and J_e were calculated by determining the transverse cross-sectional areas (of two tapes for the pancake coils) of the superconductor and of the conductor (matrix plus core) respectively.

TABLE 4.8 *Electrical and magnetic measurements obtained at 77 K for the fabricated coils.*

ID	Turns	I_c (A)	J_c (kA/cm^2)	J_e (kA/cm^2)	Field (mT)	ID/OD[&] (mm)
14	18.4	7	3.5	0.63	5.06	20/48
15	18.2	9	4.5	0.83	6.44	20/48
16	18.5	8	4.0	0.83	5.89	20/47
17	18.7	8	4.0	0.83	6.02	20/46
18	18.0	7	3.5	0.63	5.01	20/47
24	100	4	2.55	0.48	12.0	20/30
31	139[*]	7	7.0	1.25	18.8	29/36

[*]*4×(15+16)+15=139 turns,* [&]*height: each pancake ~ 4 mm, coil 24 ~ 42 mm and coil 31 ~ 65 mm.*

In particular, the J_c obtained for solenoid 31 made from some 14 m long MF tape is ~ 7 kA/cm^2. This is approximately 97 % of the measured short sample (on part of the coil itself) at 77 K using the 1 μV/cm criteria. The calculated field for each coil was determined from simple expressions derived for solenoidal and pancake coils (refer to section 2.2.6). From the figures of Table 4.8, it can be understood that it is perhaps 'better' to fabricate solenoidal coils if there are means to produce long lengths of tape since the best combining field from five pancakes can be no more than ~ 36.7 mT at 77 K (limited by the joints between the coils) by using the simple expression ('long solenoidal approximation'):

$$B_{total} = \frac{\mu_0 NI}{L} \approx 36.7\ mT \tag{4.2}$$

where the calculation was based on a series connection with an overall critical current, I_c of ~ 7 A, the total number of turns $N = \Sigma\, n_i \approx 91.8$ turns and the height of this hypothetical five-pancake magnet $L = \Sigma\, l_i \approx 5(4)$mm + 2mm gap (allowance between coils) ≈ 22 mm.

TABLE 4.9 *Resistive loss due to index number n, and corresponding operating current under persistent mode for each coil. The heat treatment sequence and insulating material type are also listed.*

Coil ID	Index no. (n) fitted/calculated	I_{op}/I_c (%)^	Heat treatment & Sintering time	Insulation type
14	~ 3.4 / 4.7-5.2	~ 8-10	60/80/60h 832-835^{0}C	Slurry A
15	~ 8.3 / 13.2-49.5	~ 40-75	60/80/60h 832-835^{0}C	Slurry A
16	~ 3.7 / 1.5-2.5	~ 5-7	60/80/60h 832-835^{0}C	Slurry A
17	~ 3.1 / 7.2-8.5	~ 20-25	60/80/60h 832-835^{0}C	Slurry A
18	~ 3.1/1.4-2.5	~ 5-7	60/80/60h 832-835^{0}C	Slurry A
24	~ 1.8/-	~ 3-	60/80/110h 832-835^{0}C	Insulator T
31	~ 3.7/-	~ 8-	60/60/60h 832-835^{0}C	Slurry A

^ *Persistent mode of operation.*

Practical superconducting magnets (SM) sometimes are required to operate in a persistent mode whereby the field decay rate must be kept below a certain value. For this reason an *index number, n* has been introduced to give conductor designers an idea of the nonzero resistance of these SM [55]. Both the fitted (from *V-I* curves) and calculated values of *n* are listed in Table 4.9. These values have been determined based on selecting the operating current I, at the critical current I_c (using 1 μV/cm criteria). The calculated values of *n* were obtained from the following expression:

$$n = \frac{\ln(E_2 / E_1)}{\ln(I_2 / I_1)}, \tag{4.3}$$

where E_1 = 0.1 μV/cm, and E_2 = 1.0 μV/cm. In practice, it is usual to have the SM operating at chosen currents not too close to the I_c. When this happens, the calculated values n can sometimes be found to increase [131] pp. 308, as the case with coil 15 shown in Table 4.9 where n reaches a value of ~ 49.5 at $I/I_c \approx 0.49$. Some recent studies made by Warnes *et al* [299] and Williams *et al* [300] have shown that the variation in n can be attributed to processing induced nonuniformity of the conductor along its length ('sausaging effect'). For each coil listed in Table 4.9, the corresponding recommended operating current (for persistent mode of operation) range is also indicated as well as the heat treatment sequence and the material insulating type.

4.3.3 WIT, CTFF, PIT, and Ag-Alloy Double Pancakes

The J_c for DP37 (using the WIT procedure - Fig. 4.13(a)-(c)), fabricated from a ~ 2.2m tape produced by drawing, has reached a J_c of ~ 12,500 A/cm^2 at LN temperature (~ 77.3 K). It was found that higher I_c was possible with MgAg (Ag-0.02 at.% Mg) samples (~ 17 A over entire tape length), although only ~ 0.13m of tape was used to fabricate DP36 (Mg-Ag, prepared by the PIT method) - due to limited resource. The relatively higher J_c found for the WIT DP was attributable to the generally lower value λ of ~ 0.08 (compared with PIT, and CTFF samples, which generally contain λ in the range of 0.1 to 0.5, refer to section 3.5), as well as from the strong evidence of high-J_c regions near the silver interface [77, 301]. In comparison with the singly stacked MF tapes, it was found that by using the doubly stacked configuration for CTFF composites (such as the 40-filamentary CTFF tape used in the production of DP25), the processing of long length tapes prepared by the method of CTFF had a higher success rate in terms of retainability of J_c before and after winding them into coils.

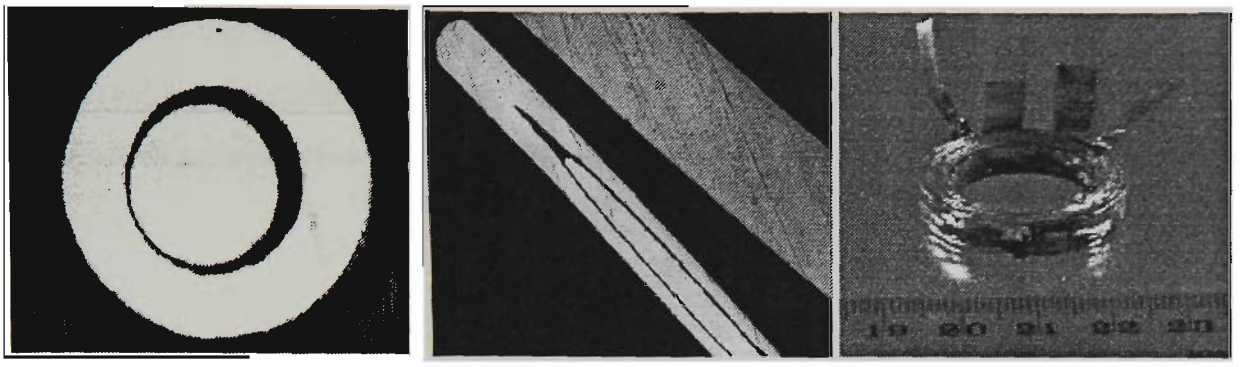

(a). Transverse cross-section of WIT wire, ϕ_{outer} ~ 2.01 mm

(b). Transverse cross-section of WIT tape, thickness ~ 0.14 mm.

(c). WIT DP37r.

Figure 4.13 *The three stages of WIT.*

TABLE 4.10 *Filamentary configuration, precursor powder type and dimensions of double pancakes.*

Coil ID[#]	Filament-Powder	ID/OD/Height[@] (mm)	Length/Turns (m)
DP35 (Ag-Cu)	MT37-B	~ 20/45/9	~ 6.6/62
DP36 (Mg-Ag)	MT21-B	~ 21/23/10	~ 0.13/2
DP25 (DS CTFF)	MT40-U	~ 20/30/9	1.5/17.4
DP37r	WIT-B	~ 20/28/7	~ 2.2/60

[#] where DP = Double Pancake, DS = Double Stacked, MT = Multifilamentary Tape, [@] gap ~ 1 mm. r = extended sintering.

For DP35 (the cladding matrix of the filaments is of pure Ag with the conductor sheath of Cu-Ag alloy), shown in Fig. 4.14, a significant improvement was noticed in the tapes mechanical strength (with the Vicker's microhardness test results: Ag-7 at.% Cu ≈ $64H_V0.025$, Ag-0.02 at.% Mg ≈ $44H_v0.025$, and Ag ≈ $38H_v0.025$, determined from fully

heat-treated tapes, refer to section 2.1.2.4), and superconductor microstructural uniformity (observable via optical images, again see section 2.1.2.4). Table 4.10 gives the dimensions, preparation method and filamentary configuration for each DP.

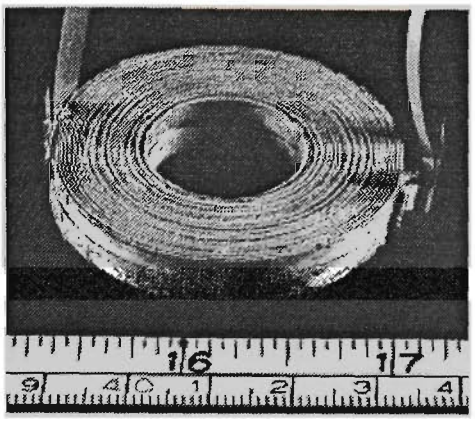

Figure 4.14 *DP35 of Ag-Cu alloy.*

The *V-I* traces for the three DP coils obtained from in-house developed software were used to calculate as well as for fitting curves to give the index number n (the exponent appearing in the *V-I* relationship near I_c: $V \propto (I/I_c)^n$). These values of n still require much improvement in order for the coils to sustain higher supercurrent especially under persistent mode of operation [242]. To give an example, for n = 5, 10, and 15, the corresponding allowable operating current (relative to the I_c of the coil) in persistent mode would be ~ 10, 30, and 45 % respectively. Table 4.11 contains the relevant measured electrical properties for the aforementioned coils.

Figure 4.15 presents a typical set of normalized J_c *vs* B plots with the externally applied magnetic field both parallel and perpendicular to the c-axis (normal to the tape plane) for various composite Bi(Pb)-2223/Ag tapes prepared by three distinct different methods: PIT (monocore samples of S, T and D), CTFF (sample MT37), and WIT (sample W). The processing details for these samples can be found in sections 2.1.2, and 2.2.

TABLE 4.11 *Critical current, self field and index number of double pancakes at 77 K.*

Coil ID	J_c (kA/cm^2, 10^{-11} Ω-cm)	Field (mT) (Calc.)	Index no. (n) fitted/calculated[8]
DP35 (Ag-Cu)	~ 4.11	~ 9.42	~ 3.0/8.9
DP36 (Mg-Ag)	~ 11.3	~ 1.48	~ 8.1/4.2
DP25 (DS CTFF)	~ 2.61	~ 2.66	~ 1.8/-
DP37r (WIT)	~ 12.5	~ 14.85	~ 4.0/5.7

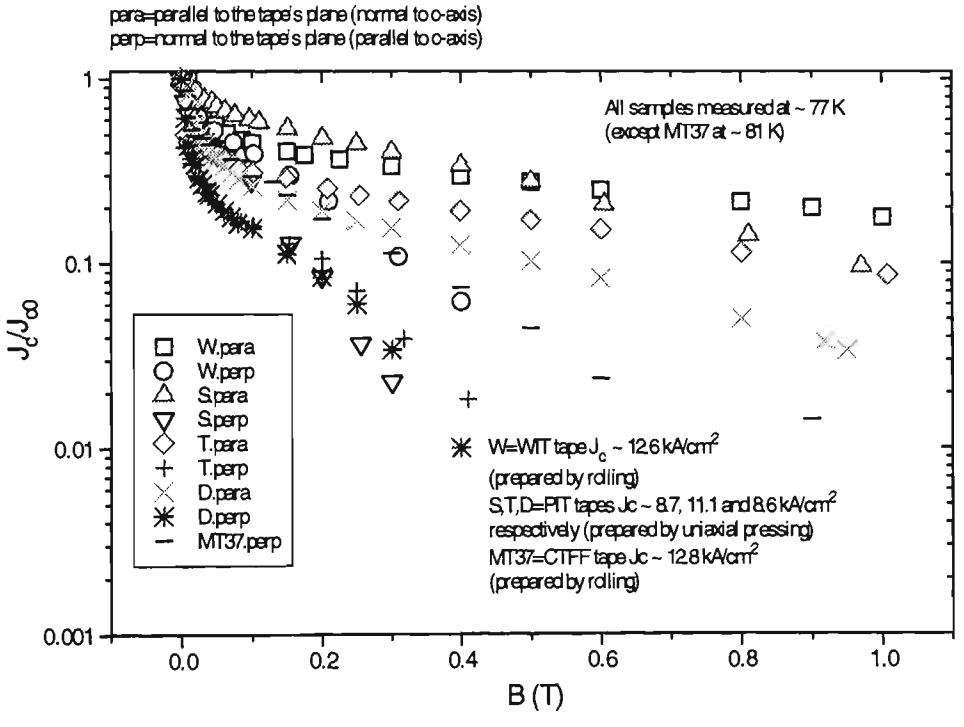

Figure 4.15 *Normalized J_c Vs B for samples with different preparation methods.*

The hysteretic behaviour for Bi(Pb)-2223/Ag composite (mostly for MF) tapes, discussed in section 2.2.5, was found to be small at ~ 77 K, but increases with decreasing in temperature, down to ~ 4.2 K (the measurements were performed using SQUID magnetometry at *Ames Laboratory, Iowa State University*). The set of plots shown in Fig.4.15 indicates that the WIT, and CTFF samples sustain their superconductivity perhaps better in the presence of magnetic field. This is apparent especially with the applied flux density normal to the tape plane where greatest anisotropy occurs. These results are also quite encouraging for composite tapes prepared with flat-rolling employed as the intermediate deformation step.

4.4 Construction and NZP Analysis of Bi(Pb)-2223/Ag Class II Coils and Magnets

High-T_c superconducting Bi(Pb)-2223/Ag composite tapes with J_c well over the 10,000 A/cm^2 minimum requirements for industry application and of lengths approaching and beyond the 1 km mark have been reported [112, 113]. However, to maintain the same level of performance for these tapes in the production of commercially viable products would be the next challenging step and it is this final obstacle (as well as for economical reasons) that's been preventing these HTSCs in many areas of application to exist more as an enabling rather than a replacing technology [131]. This section presents some recent study on the production of Bi(Pb)-2223/Ag pancake-shaped coils and magnets on a laboratory scale, in particular on the constructional aspect, and also reports results for some quench propagation parameters.

4.4.1 Physical Properties

All coils presented here have been fabricated by means of the wind-react (W&R) procedure with the application of a thin layer (~ 100 μm) of alumina based slurry (with a volume weighted mean particle size diameter, D[4,3] of ~ 37.7 μm) having a thermal conductivity of ~ 7.9×10^{-3} W/cm-K, further details can be obtained from section 2.1.3.

Table 4.12 lists some physical properties; including filamentary configuration, precursor powder type, and dimensions of the coils and magnets.

TABLE 4.12 *Physical properties of Bi(Pb)-2223/Ag coils & magnets.*

Coil ID[#]	Filament & Powder	ID/OD/Height (mm)	Length/Turns (m)
SP15	MT31-U	~ 20/48/4	~ 2/18.2
SP16	MT31-U	~ 20/47/4	~ 2/18.5
SP17	MT31-U	~ 20/46/4	~ 2/18.7
SP18	MT31-U	~ 20/47/4	~ 2/18.0
DP13	MT37-B	~ 20/50/8	~ 5/44
DP14	MT37-B	~ 20/50/8	~ 5/44
MG-Ag	MT37-B	~ 20/50/17[@]	~ 10/88
MG-SC	MT37-B	~ 20/50/17	~ 10/88
MG-SC&strap	MT37-B	~ 20/50/17	~ 11/89

[#] *where SP = Single Pancake, DP = Double Pancake, MG = Magnet, SC = Superconductor of Bi(Pb)-2223/Ag.* [@] *Air gap ~ 1 mm.*

As before, I_c measurements for the coils and magnets were made using the Keithley (->10 A), and HP (->100 A) power supplies with the 10^{-11} Ω-cm criterion determined from *I-V* curves generated by in-house developed software. Normal-zone-propagation (NZP) parameters (viz. the longitudinal, V_l, and turn-to-turn, V_t velocities) were calculated from results obtained during the batch processing stage of MF Bi(Pb)-2223/Ag and Ag-alloy tapes (refer to section 1.3.3 for theoretical treatment).

4.4.2 Construction and Testing

The importance in superconducting joint technology has been recognized [55] and studied by various research groups [302, 303, 126], where attempts have been made to directly

connect and fuse the superconductor together during the subsequent sintering stage. These methods have been tested with the coils presented here for connection but failed due to their lack of strength. Instead, two types of joints were chosen - tapes of pure silver and of superconducting (SC) Bi(Pb)-2223/Ag, with indium metal used for soldering contacts (low melting point).

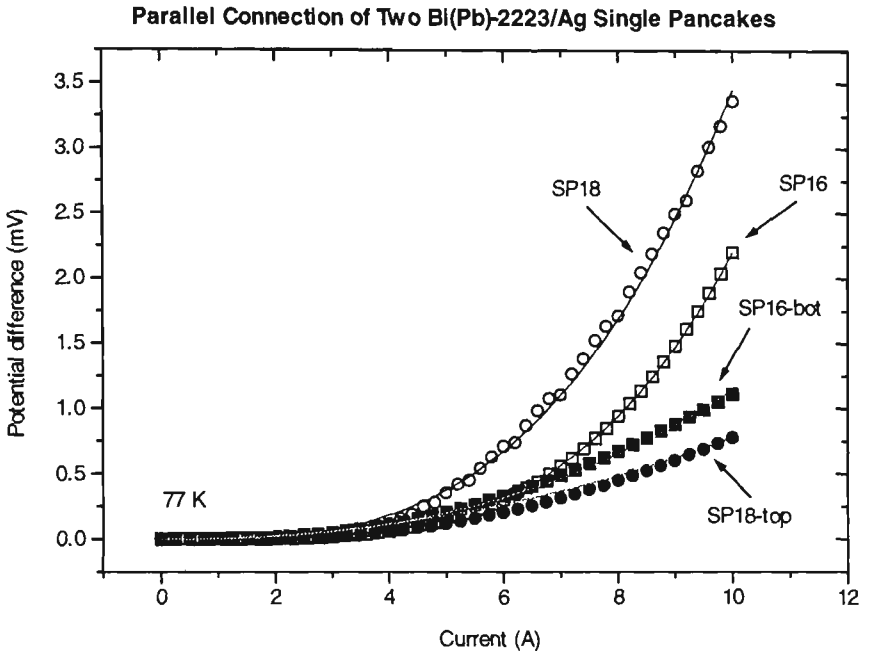

Figure 4.16 *I-V curves of SP16 and 18 before and after the parallel connection.*

Figure 4.16 contains the *I-V* curves (measured, and fitted) for single-pancake (SP) coils SP16 and 18, before and after a parallel connection was made (the joints were made of SC tapes - see Fig. 4.19, left). Similarly, Fig. 4.17 shows the *I-V* curves for the separate SP15 and 17, and the curve obtained after a series connection was made between the two (also with SC joints - shown in Fig. 4.19, right). Since each SP have similar characteristics by virtue of the same thermo-mechanical treatment, a direct comparison can be made for the two types of connection.

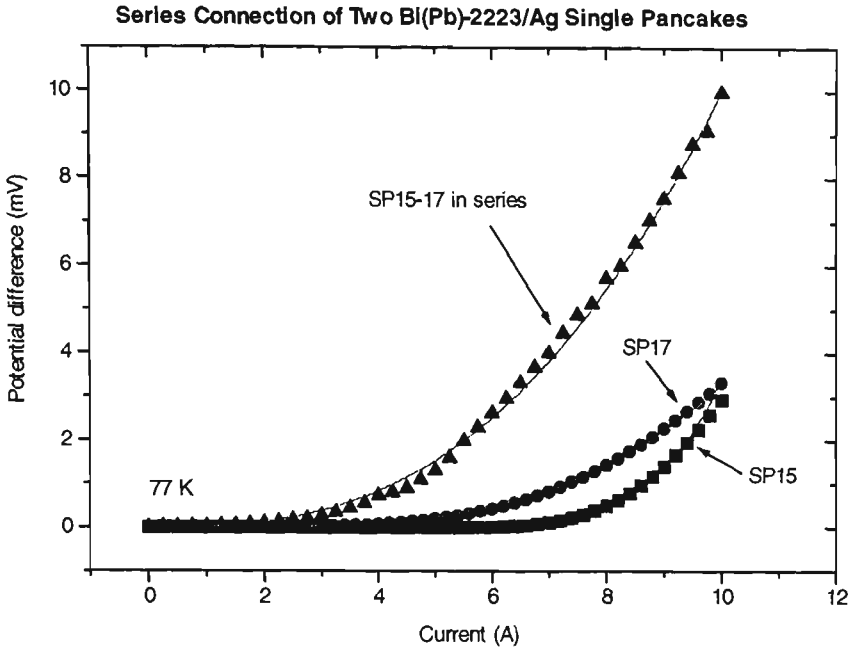

Figure 4.17 *I-V curves of SP15 and 17 before and after the series connection.*

From Table 4.13, it is clear that the series connection of the SP coils is preferable (more turns, greater self field, and higher indices).

Next, comparisons between Ag, and Ag-SC composite joints were studied by constructing two double-pancake coils (DP13 and 14) in series to form a magnet (MG - as depicted in Fig. 4.19, middle). Again, the index number (n) was obtained by fitting each I-V curve of the magnet for each joint type (Fig. 4.18) and is listed in Table 4.13. Although the results indicate similar fitted indices for the three joints, connections made using 'SC&strap' improves (or better in retaining) the overall current carrying capacity and thus enables higher self field. This can be attributed to the additional channel provided by the strap for diverting some current and assists in averting hot spot formation.

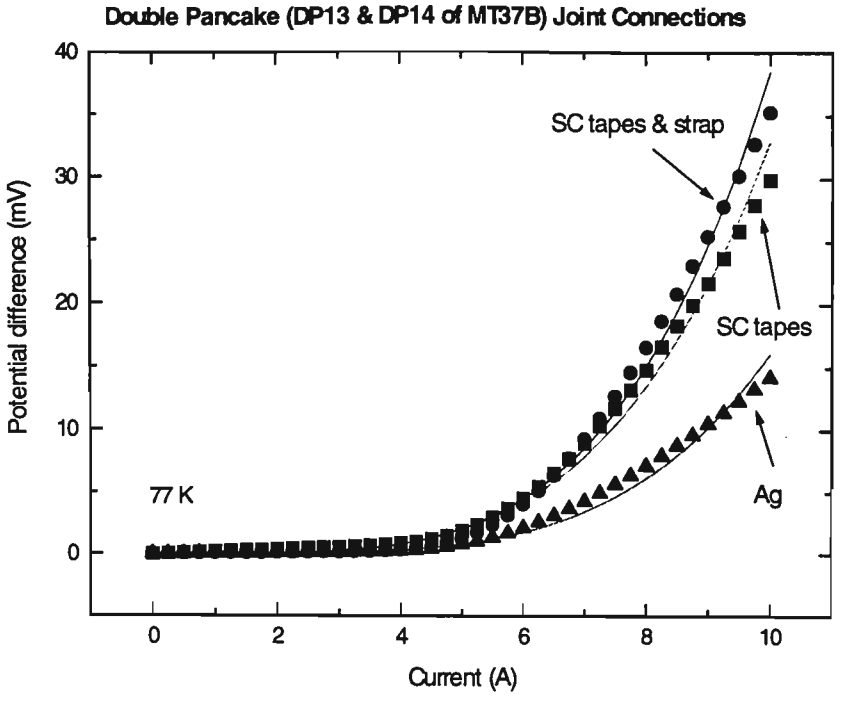

Figure 4.18 *I-V curves for the different joint type implemented in the construction of the MG.*

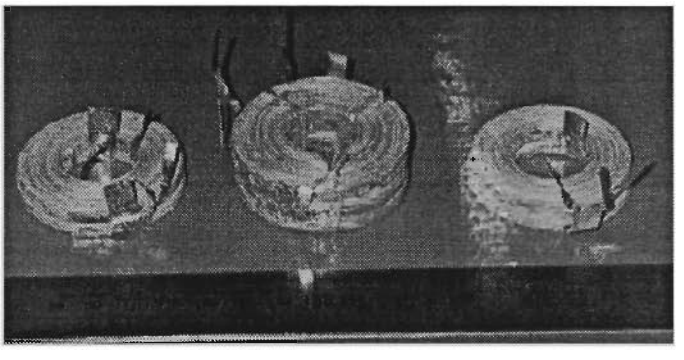

Figure 4.19 *Photographs of a parallel connection between SP16, and 18 (left), and a series connection between SP15, and 17 (right). The construction of the MG using SC&strap connecting DP13, and 14 in series is shown at the center of the picture.*

TABLE 4.13 *Critical current, self field, and index number of Bi(Pb)-2223 coils and magnets.*

Coil ID	I_c (A) (LN) 10^{-11} Ω-cm	Field (mT) (Calc.)	Index no. (n) fitted/calculated
SP15	~ 9	~ 6.44	~ 8.3/13.2-49.5
SP16	~ 8	~ 5.89	~ 3.8/1.5-2.5
SP17	~ 8	~ 6.02	~ 3.7/7.2-8.5
SP18	~ 7	~ 5.01	~ 3.2/1.4-2.5
SP-parallel	~ 4-4.25	~ 5.99	~ 2.1-2.5/-
SP-series	~ 5.5	~ 8.00	~ 2.7/-
DP13	~ 7	~ 11.82	~ 5.4/1.86
DP14	~ 7	~ 11.82	~ 5.2/1.86
MG-Ag	~ 5	~ 16.89	~ 4.3/-
MG-SC	~ 5.8	~ 19.59	~ 4.0/-
MG-SC&strap	~ 6.2	~ 20.94	~4.2/-

4.4.3 Normal Zone Propagation Analysis

The stability consideration of superconducting coils, and magnets is of great importance in conductor design as well as for operational purposes. The concept of minimum propagating zone (MPZ) is one that relates issues of conductor stability to the cooling environment [304, 79, 252]. The coils, and magnets examined in this chapter are partially edge-cooled, with most of the windings buried under the slurry, and so the analysis can approximate adiabatic conditions as derived from the theory of MPZ [131]. Two parameters, the normal zone propagation (NZP) longitudinal and turn-to-turn velocities, V_l and V_t respectively were calculated from the following expressions, as given in section 1.3.3, repeated here for convenience:

$$V_t = \frac{J_m}{C_{cd}} \sqrt{\frac{\rho_m k_m}{\left(T_t' - T_{op}\right)}} \tag{4.4}$$

and

$$V_t = \frac{J_m}{\tilde{C}_{cd}} \sqrt{\frac{\rho_m k_i \delta_{cd}}{2\delta_i \left(T_t' - T_{op}\right)}} \tag{4.5}$$

where J_m, ρ_m, k_m are the matrix's critical current density, resistivity and thermal conductivity respectively, $T_t' = (T_{cs} + T_c)/2$, with T_{cs} the current sharing temperature $T_{cs} \equiv T_c(I)$, T_{op} as the operating temperature, C_{cd} and $\tilde{C}_{cd}$ are the volumetric average of SC's and matrix's heat capacities at 77 K, and over the temperature range of interest respectively, δ_i and k_i are the insulator's thickness and thermal conductivity and δ_{cd} is the thickness of the SC tape.

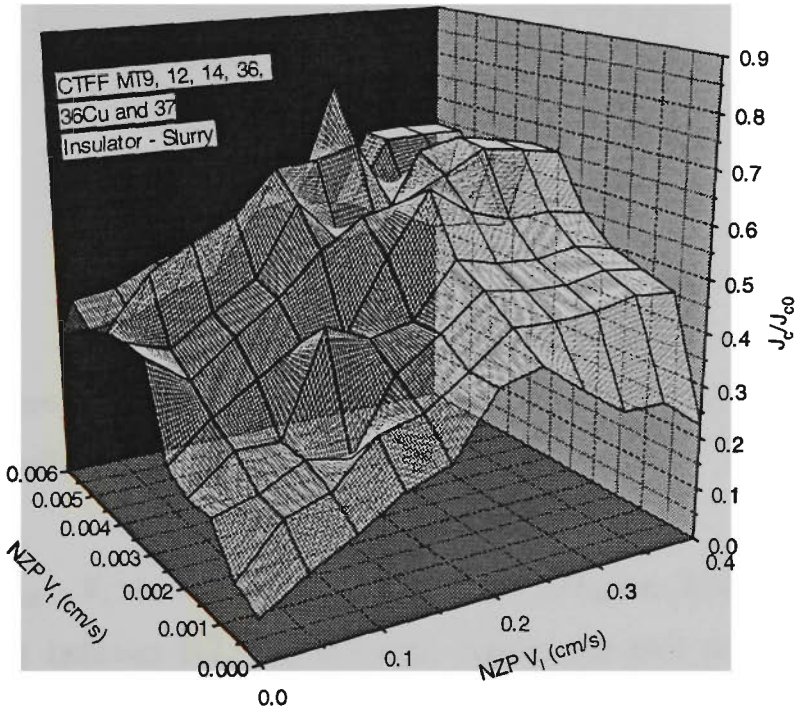

Figure 4.20 *3-D surface plot of NZP velocities against normalized J_c.*

These parameters were then used to generate the three dimensional surface plots, as shown in Figs. 4.20-4.22. Figure 4.20 depicts the normalized J_c (against J_{c0}) of batch processed MF tapes versus V_l, and V_t. The accumulated results indicate significantly higher V_l, and V_t for samples with higher J_c.. With V_l however, this is not absolutely true against J_c/J_{c0}, as a peak can be seen in the plot. The fill factor of the tapes is the underlying explanation in this case (see Fig. 4.22). For V_l and V_t., the two most influential parameters are C_{cd} (or $\tilde{C}_{cd}$) and ρ_m.

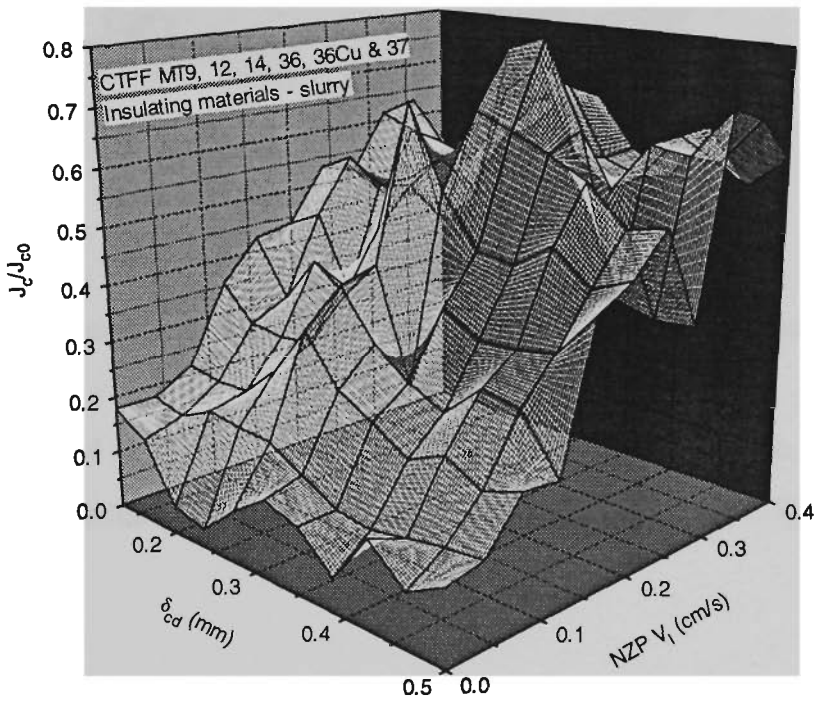

Figure 4.21 *3-D surface plot of sample thickness and NZP V_l against normalized J_c.*

Figure 4.21 relates δ_{cd} , V_l and normalized J_c. Here, the J_c/J_{c0} was found to peak for MF samples of thickness between 0.2, and 0.3 mm. Again, the plot reveals higher V_l is favoured for samples with higher J_c. Figure 4.22 contains the information which explains the nature of Fig. 4.20. In Fig. 4.22, not only samples with higher J_c but those with a relatively low fill factor value exhibit larger V_l..

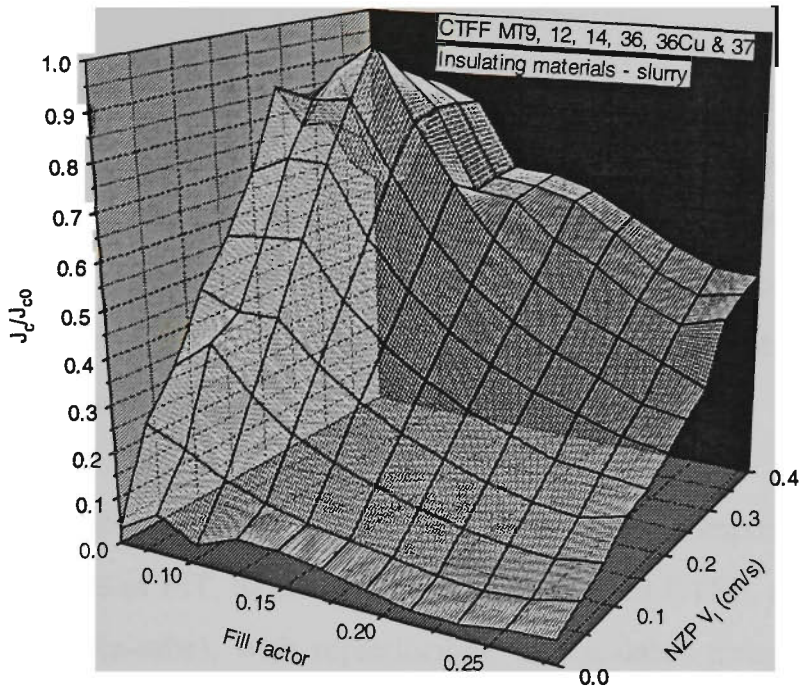

Figure 4.22 *3-D surface plot of fill factor and NZP V_l against normalized J_c.*

The results presented and discussed so far have been confirmed with Teflon used as an insulating materials with a different thermal conductivity (~2.91×10^{-3} W/cm-K).

Summary and Conclusions

By adopting a systematic approach in the optimization procedure on the processing related parameters of Bi(Pb)-2223 silver, and silver alloy composite tapes, high-T_c superconducting Bi(Pb)-2223 coils, and magnets have been successfully developed on a laboratory scale. Leading up to this objective, the following studies were conducted in the quest of extending the current knowledge on materials processing, and science of Bi(Pb)-2223 composite tapes:-

The processing of Bi(Pb)-2223 short, and long length composite tapes (from the standard procedure of PIT, to the conventional method of CTFF, and the novel format of WIT, or wire-in-tube), with reproducible, and scalable transport critical current densities between 15, and 20 kA/cm^2 (77 K, self field, 1μ V/cm) using intermediate cold-rolling was achieved. The characterization on their physical, chemical, electrical, and magnetic properties by means of measurements were also performed. The implemented techniques include; Vickers microhardness tests (H_VT), particle size analysis (PSA), X-ray diffraction (XRD), differential thermal and thermo-gravimetric analysis (DTA/TG), scanning electron microscopy with energy-dispersive spectrometry (SEM/EDS), electrical transport, ac-susceptibility, and the SQUID (superconducting quantum interference device) magnetometry.

The effect of initial packing density of OPIT method on the mechanical and electrical transport properties, and phase formation of Bi(Pb)-2223 monocore superconducting tapes was investigated. A thinner core was found to give slightly more flexibility and better mechanical performance, with more tolerance to surface bend strain. Low initial packing density monocore short tapes were found to give a low overall critical current. In addition, higher initial packing density of monocore short tapes reacted quicker, converting greater amount of low- (2212) to high-T_c (2223) phase for the same thermomechanical and heat treatment process. SEM images of SF Bi(Pb)-2223 tapes revealed that for higher initial packing density, grain alignment, connectivity and growth in more than one instance, improved notably as well. Indeed, better uniformity can be achieved especially for long length, but this was found to depend on other parameters such as the smoothness of the interior surface of the silver tube, and

smallness of particle size. Despite the low overall critical current achieved, the use of a device such the vibrator for PIT purposes was found to give better structure unformity along the longitudinal direction, with better mechanical performance and hence reproducibility and predictability in the terms of materials processing of Bi(Pb)-2223 composite tapes.

The effect of sintering periods on the microstructure, phase development, electrical transport and magnetic properties of Bi(Pb)-2223 monocore superconducting tapes was investigated. The results gave conclusive evidence that there was an optimal sintering period for precursor powders with a particular stoichiometric composition. Sintering period of approximately 60 h was found to be most suitable for precursor with a stoichiometry of Bi:Pb:Sr:Ca:Cu = 1.84:0.35:1.91:2.05:3.05, independent of powder processing route and particle size characteristics. This sintering period indeed gave better electrical transport property and microstructural morphology, to the treated Bi(Pb)-2223 composite tapes.

Long sintering periods (of duration $\geq$ 100 h) were found to give better preferential growth of grains, but greater grain misalignment and porosity, while shorter sintering periods (of duration ~ 40 and 60 h) showed a more densely processed core. Nevertheless, sintering periods which were too short (as with the 40 h ones) were found to inhibit grain growth and the recovery of mechanically induced microcracks. In addition, the average percentage value of fill factor was found to increase with increasing duration of sintering for powders with the same stoichiometry, but different processing routes and particle size, primarily due to high porosity, with the added presence of voids, and microcracks in the superconducting cores of tapes treated with sintering periods $\geq$ 100 h. Furthermore, it was concluded that the average conversion rate of 2212 to 2223 phase after approximately 100 h of sintering time was very similar for different sintering sequences of tapes prepared from differently processed powders with the same stoichiometric composition.

The roll of sintering period was certainly shown to aid in the development of the 2223 phase. Substantial improvement in J_c, in regions of high field was achieved by increasing the oxide core density (by eliminating voids, and microcracks), and

homogeneity (such as other secondary phases), which in turn gave better grain connectivity and interfacial microstructure. Resistivity measurements of activation energy for monocore short tapes with different precursor powders indicated that the ~ 60 h sintering period sample exhibited greater flux pinning strength, approximately two to three fold over those with sintering periods of ~ 40 or 100 h.

The effect of intermediate cold-rolling at room temperature on the microstructure, phase formation and electrical transport property of Bi(Pb)-2223 composite tapes were investigated. Conclusive results indicated that there was indeed a 'deformation window' within which optimal microstructure, transformation rate of 2223 phase and the electrical property were optimized. A gradual decrease in rolling reduction was found to be necessary in conjunction with progressive sintering steps to achieve high J_c values. This deformation window was found to vary between sintering periods. The rolling reduction ratios were found to lie approximately within 25-30 % between the first and second sintering periods, about 15-20 % between the second and third sintering periods, and roughly 5-10 % between the third and forth sintering periods. With large reduction ratios, especially after the second or third sintering period, fracturing of the ceramic core running longitudinally may result due to a finite width strain and shearing stress created by the compressive force induced by the rollers. Any subsequent heat treatment may then not be enough to recover the crack. The gradual decrease in reduction window size, as found in the subsequent intermediate rolling stages, was necessary to prevent the negative growth of the 2223 grains, and breaking of the ceramic core (due to the lack of liquid phase present), as well as for increasing in core density, and physical hardness. The fill factor for tapes made from two precursor powders with different stoichiometric compositions was found to be affected by the amount of intermediate deformation imposed on them. The increase in fill factor was caused by large rolling reduction made between late sintering periods; as there was an increasing in the mismatching of the physical property between matrix and core. For Bi(Pb)-2223 tapes prepared by OPIT from a precursor with nominal composition of Bi:Pb:Sr:Ca:Cu = 1.84:0.35:1.91:2.05:3.06, silver tube with inner and outer diameters of 4.5/6.5 mm, initial packing density between 60 and 65 % of the theoretical value, the optimal fill factor was determined to be within the range of ~ 16 and 17 %. Similarly for samples made from another powder with nominal composition of

1.84:0.35:1.91:2.05:3.05, initial packing density between 65 and 70 % of the theoretical value, with the same silver tube thickness, the optimal fill factor was determined to lie between 22 and 23 %.

The effect of implementing a two-sinter heat treatment procedure with a temperature drop during sintering in the latter period on Bi(Pb)-2223/Ag MF tapes was investigated. The amount of drop in sintering temperature was found to depend on the phase assemblage, such as the plumbate, 2212, and impurities phases. Rapid 2223 formation was found in MF tapes treated using the two-sinter process. One analogy towards explaining this effect would be in 'the cooking of rice' - whereby the cooking temperature is turned down once the water boils to allow for grain growth !

Stability issues on conductor design with MF Bi(Pb)-2223/Ag tapes were also addressed. Stability parameters obtained for these tape conductors showed that they are cryostabled, and that they are unlikely to experience any flux jump instability when using LN as a coolant. Bi(Pb)-2223/Ag MT tapes were found to be able to sustain 'SC' (at 77 K) perhaps better than other HTSC such as YBCO in wire form, even in the presence of a quench-causing disturbance by virtue of their large critical normal zone lengths based on the theory of *minimum propagating zone* (MPZ). The expansion rate of the normal front however was determined to be comparable to those found for other HTSCs, suggesting cryostability can only be achieved as long as sufficient cooling is provided in the case of a quench. The concentration of the triggering energy was found to be relatively large (as predicted), nearly an order in magnitude in comparison to YBCO wire. This prompts further improvement in the tape processing side, with the need for optimization in processing parameters such as R_s, and λ, to further increase the normal front velocity in order to avoid the formation of hot-spots.

The thermal stability of Bi(Pb)-2223 coils at 77 K was investigated. It was found that the extent of thermal stability of Bi(Pb)-2223/Ag pancake-shaped coils, at 77 K can be determined by controlling the amount of matrix and superconducting materials during processing. The intermediate deformation step between sintering stages was found to be crucial in optimizing the performance of the processed composite tapes, as well as governing the thermal stability of the subsequently produced pancake-shaped coils.

Results obtained from numerical analysis by the finite element method showed that monolayer coils produced from Bi(Pb)-2223/Ag composite tapes are thermally very stable, with high values of fill factor. Increasing the number of co-wound tapes however (for reasons of achieving higher current carrying capacity, and improving in mechanical integrity of the coil, or magnet system), was found to require either a reduction in the fill factor, or an increase in cooling rate, for thermal stability to be sustained as would otherwise be achieved with the metallurgically same single tape.

In brief, a systematic approach in determining the best thermo-mechanical procedure was found to be necessary each time a HTSC tape is made from different raw materials, including precursor powder and the matrix used. There is a direct link between the fill factor and the processing procedure which can be utilized to enhance the performance of Bi(Pb)-2223/Ag and Ag-alloy composite tapes. The role of the matrix using as a cladding material has been shown to be partially responsible for the improving of mechanical property of these tape conductors as the arrangement or geometry of the filaments themselves must be taken into account. The processing parameters such as filamentary size, number of filaments, tape thickness, sheathing materials, intermediate deformation, sintering period, temperature and duration can all be optimized to maximize the quench protection requirements which are necessary for improvement in the performance of these tapes for high field applications.

Finally, the development of Bi(Pb)-2223 class-II coils and magnets was investigated. By using the method W&R, it was possible to retain up to ~ 97 % of the J_c obtained from short sample, on a solenoid made from a length of ~ 14 m of MF tape. Although pancake-shaped coils proved to be easier to fabricate, their performance was limited ultimately by the joints connecting them together. The resistive loss due to n found to vary slightly over the fabricated pancake coils indicated some nonuniformity in the MF tape, attributable to processing parameters. A novel W&R solenoidal coil (reaching ~ 973 ampere-turns) wound on an alumina ceramic tube generated a dc-field of ~ 19 mT, at 77 K was produced together with five pancake-shaped coils, each generated an average of ~ 5 mT at 77 K, destined for magnet construction with a possible combined calculated field of ~ 0.04 T at 77 K (with liquid nitrogen as a coolant). Critical currents of superconducting silver and silver-alloy composite double pancake coils of Bi(Pb)-

2223 were measured at liquid nitrogen temperature. A critical current density of ~ 12.5 kA/cm^2 was obtained for a coil fabricated from Bi(Pb)-2223/Ag composite tape of length ~ 2.2 m (~ 342 Ampere-turns) using the WIT method. For coils made from alloys of silver (e.g. ~ 0.02% magnesium), higher critical currents (~ 17 A) were achieved over those fabricated with tapes processed with pure silver matrix. Transport measurements of normalised J_c *vs* B in fields up to 1T showed encouraging results for WIT, and CTFF composite tapes prepared from intermediate rolling. New methods of joining between double pancake-shaped coils were also investigated, together with the determination of some quench propagation parameters. The implementation of the superconducting joint with strap produced a laboratory test magnet constructed from two double pancake-shaped coils (total length of ~ 20 m, or ~ 552 Ampere-turns) gave a self dc-field of ~ 21 mT, at 77 K.

Appendix A

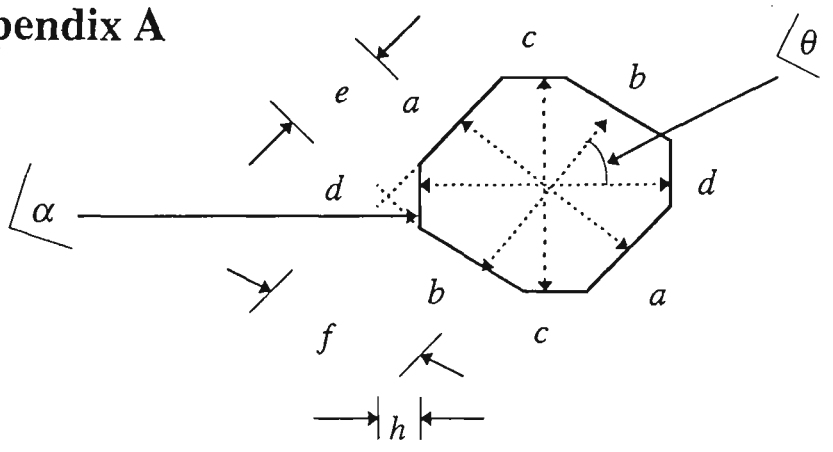

Groove-rolling area and percentage reduction calculations

Assumption: $\alpha = \theta = 45^0$

$e = a/2 \tan\theta = a/2$

$f = b/2 \tan\theta = b/2$

$$\tan\theta = \frac{f}{\frac{a}{2}} \& \sin\theta = \frac{\frac{b}{2}}{\left(h + \frac{d}{2}\right)}$$

$$\Rightarrow h = \frac{\left(b\sqrt{2} - d\right)}{2}$$

Area of little triangle at corner of octagon:

A = ½ (2g) $h = h^2$ {g is the ½ baselength of corner triangle = h}

Let $L = (a+b)/2$ and $D = (c+d)/2$ {average lengths}

The required area of octagon:

$= 2e \times 2f - 4A$

$= L^2 - 2(L\sqrt{2} - D)$

Percentage reduction in area of subsequent groove:

$$= \left[1 - \frac{L_2^2 - 2\left(L_2\sqrt{2} - D_2\right)}{L_1^2 - 2\left(L_1\sqrt{2} - D_1\right)}\right] \times 100$$

Appendix B

By arranging filaments in a manner similar to that of the 'nut-model' (as Fig. 2.9 of chapter 2) to achieve the highest packing possible, counting the total number of filaments gives 1, 7, 19, 37, 61, 91, 127, etc. each time a layer is added.

This can be expressed as: 1, 1+6, 1+18, 1+36, 1+60, 1+90, 1+126, etc. which is 1, 1+6, 1+6+2(6), 1+6+2(6)+3(6), 1+6+2(6)+3(6)+4(6), 1+6+2(6)+3(6)+4(6)+5(6), etc. This recurrence expression is = 1+6(1+2+3+4+5+6+.....), which is

$1+6\left[\frac{1}{2}m(m+1)\right]$ *i.e.* $1+3m(m+1)$ as required

(using the formula for the arithmetic series).

Appendix C

Information on measurements, and physical property of Bi(Pb)-2223 coils.

Coil ID	Type	Precursor powder	Filaments	Tape thickness (mm)	Layers	Length (m)	Turns	I_c (A)	J_c (kA/cm^2)	J_e (kA/cm^2)	Field (mT) LN	ID/OD (mm)	Height (mm)	Heat treatment & Sintering time
1	Pancake W&R	U	1	0.15	3	3.5	30	1.5	1.33	0.23	1.73	20/50	3.5	60/80/80h 832-835°C
2	Pancake W&R	U	1	0.15	3	4.0	28.2	-	-	-	-	33/62	3.5	60/80/80h 832-835°C
3	Pancake W&R	U	1	0.15	3	4.0	32.5	2	1.75	0.31	2.24	20/60	3.5	80/80/80h 832-835°C
4	Pancake W&R	T	1	0.2	3	3.5	26.2	6	1.25	0.56	5.43	20/60	4.5	80/80/80h 832-835°C
5	Pancake W&R	T	1	0.2	3	1.5	15	5	1.04	0.47	3.10	20/44	4.5	80/80/80h 832-835°C
6	Pancake W&R	T	1	0.2	3	1.0	10.2	4	0.83	0.37	1.88	20/38	4.5	80/80/80h 832-835°C
7	Pancake R&W	U	31	0.34	2	0.8	12	8	4.0	0.42	4.21	40/52	4.0	100/120h 832-835°C
8	Pancake R&W	U	1	0.15	1	2.5	25	1	2.9	0.47	1.12	18/41	3.5	60/80/110h 832-835°C
9	Pancake W&R	T	1	0.2	3		9	-	-	-	-	21/40	4.5	60/80/90h 832-835°C
10 Breakthru'	Pancake W&R	U (9/8/95)	1	0.15	2	< 1.0	8	3	4.3	0.7	1.32	20/26	3.5	60/80/80h 832-835°C
11	Pancake R&W	U	31	0.34	1	<1.0	8.7	7	4.5	0.83	3.57	20/23	4.0	100/120h 832-835°C
12	Pancake W&R	U	31	0.32	2	1.0	10.4	9	4.5	0.81	4.32	20/36	4.0	60/80/60h 832-835°C
13	Pancake W&R	U	31	0.32	2	1.0	10.6	8	4.0	0.72	4.40	20/29	4.0	60/80/60h 832-835°C
14	Pancake W&R	U	31	0.32	2	2.0	18.4	7	3.5	0.63	5.06	20/48	4.0	60/80/60h 832-835°C
15	Pancake W&R	U	31	0.32	2	2.0	18.2	9	4.5	0.83	6.44	20/48	4.0	60/80/60h 832-835°C
16	Pancake W&R	U	31	0.32	2	2.0	18.5	8	4.0	0.83	5.89	20/47	4.0	60/80/60h 832-835°C
17	Pancake W&R	U	31	0.32	2	2.0	18.7	8	4.0	0.83	6.02	20/46	4.0	60/80/60h 832-835°C
18	Pancake W&R	U	31	0.32	2	2.0	18.0	7	3.5	0.63	5.01	20/47	4.0	60/80/60h 832-835°C
19	Pancake W&R	CTFF	36Cu	0.28	1	1.0	13	0.3	0.3	0.05	0.20	20/29	2.5	60/80/60h 832-835°C

Coil ID	Type	Precursor powder	Filaments	Tape thickness (mm)	Layers	Length (m)	Turns	I_c (A)	J_c (kA/cm^2)	J_e (kA/cm^2)	Field (mT)	ID/OD (mm)	Height (mm)	Heat treatment & Sintering time
20	Pancake W&R	CTFF	12	0.2	1	1.15	16.7	0.2	0.35	0.043	0.17	20/30	2.5	60/80/60h 832-835°C
21	Pancake W&R	CTFF	36	0.25	1	1.7	21	1	0.90	0.18	1.02	20/33	3.0	60/80/60h 832-835°C
22	Pancake W&R	CTFF	14	0.25	1	2.3	26.4	2	2.34	0.38	2.44	20/36	2.5	60/80/60h 832-835°C
23	Pancake W&R	CTFF	9	0.24	1	2.0	26.2	2	1.95	0.39	2.46	20/35	2.0	60/80/60h 832-835°C
24	Solenoidal R&W	U	31	0.34	1	7.0	100	4	2.55	0.48	12.0	20/30	42	60/80/110h 832-835°C
25	Solenoidal W&R	U	31	0.34	1	0.95	9.3	2	1.23	0.24	0.9	29/30.5	26	60/80/60h 832-835°C
26	Pancake R&W	U	31	0.32	1	1.0	21	-	-	-	-	22/42	5	60/80/60h 832-835°C
27	Pancake W&R	U	31	0.32	1	0.75	9	2	2.0	0.36	1.01	20/25	4.5	60/80/60h 832-835°C
28	Pancake W&R	U	19	0.28	1	1.2	15	6	3.15	0.62	4.51	20/31	5	60/80/60h 832-835°C
29	Pancake W&R	U	31	0.32	3	0.28	3	7	2.33	0.45	1.11	20/28	4.5	60/80/60h 832-835°C
30	Pancake W&R	U	31	0.32	2	1.15	12.5	2	1.0	0.18	1.17	20/37	4.0	60/60/60h 832-835°C
31	Solenoidal W&R	U (30/10/95)	31	0.32	1	14	139	7	7.0	1.25	18.8	29/36	65	60/60/60h 832-835°C
A (32)	Pancake W&R	U	37	0.24	3	2.98	21.9	2	0.65	0.10	1.48	20/62	4.0	60/60/60h 832-835°C
B (33)	Pancake W&R	U	37	0.24	3	2.65	21.2	2	0.65	0.10	1.51	20/57	4.0	60/60/60h 832-835°C
C (34)	Pancake W&R	U	37	0.24	3	3.00	22.2	3.5	1.14	0.18	2.66	20/61	4.0	60/60/60h 832-835°C
35	Pancake W&R	U	31	0.32	1	0.65	8.6	6.2	6.2	1.11	2.86	21/26	3.5	60/60/60h 832-835°C

[#] Alumina based slurry, modified version of Aron Ceramic D, from Toagosei Co. Ltd., Japan.
[@] Teflon tape, thickness ~ 0.03 mm.
[$] Epoxy resin (Araldite, or Acryfix).
[%] Mylar tape, thickness ~ 0.2 mm.
[*] Fine (0.1-1μm size) alumina mixed with sodium silicate (water glass).

Appendix D

Particle size characteristics of precursor powders, and alumina based slurries.

MALVERN MASTERSIZER

Result: Sieve BS 410:1986 Report

Sample Details

Sample ID: NVVO-S-Precursor
Sample File: NVVO-5
Sample Path: C:\SIZERS\DATA\
Sample Notes:

Run Number: 3
Record Number: 1

Measurement Date: Tue, Nov 07, 1995 7:59PM
Analysis Date: Tue, Nov 07, 1995 7:59PM
Result Source: Analysed

System Details

Range Lens: 300RF mm
Presentation: 3OHD
Analysis Model: Polydisperse
Modifications: None

Beam Length: 2.40 mm
[Particle R.I. = (1.5295, 0.1000); Dispersant R.I. = 1.3300]

Sampler: None

Obscuration: 12.4 %
Residual: 1.148 %

Result Statistics

Distribution Type: Volume
Mean Diameters:
D [4, 3] = 20.82 um

Concentration = 0.0144 %Vol
D (v, 0.1) = 3.72 um
D [3, 2] = 8.40 um

Density = 1.000 g / cub. cm
D (v, 0.5) = 16.13 um
Span =2.580E+00

Specific S.A. = 0.7144 sq. m / g
D (v, 0.9) = 45.33 um
Uniformity = 8.185E-01

Mesh No	Aperture um	Volume In%	Volume Below%
10	2000	0.00	100.00
12	1700	0.00	100.00
14	1400	0.00	100.00
16	1180	0.00	100.00
18	1000	0.00	100.00
20	850	0.00	100.00
25	710	0.00	100.00
30	600	0.00	100.00
35	500	0.00	100.00
40	425	0.00	100.00
45	355	0.00	100.00
50	300	0.00	100.00
60	250		100.00

Mesh No	Aperture um	Volume In%	Volume Below%
60	250	0.00	100.00
70	212	0.00	100.00
80	180	0.00	100.00
100	150	0.00	100.00
120	125	0.00	100.00
140	106	0.00	100.00
170	90	0.04	99.96
200	75	1.89	98.06
230	63	3.45	94.62
270	53	4.87	89.75
325	45	6.41	83.34
400	38		

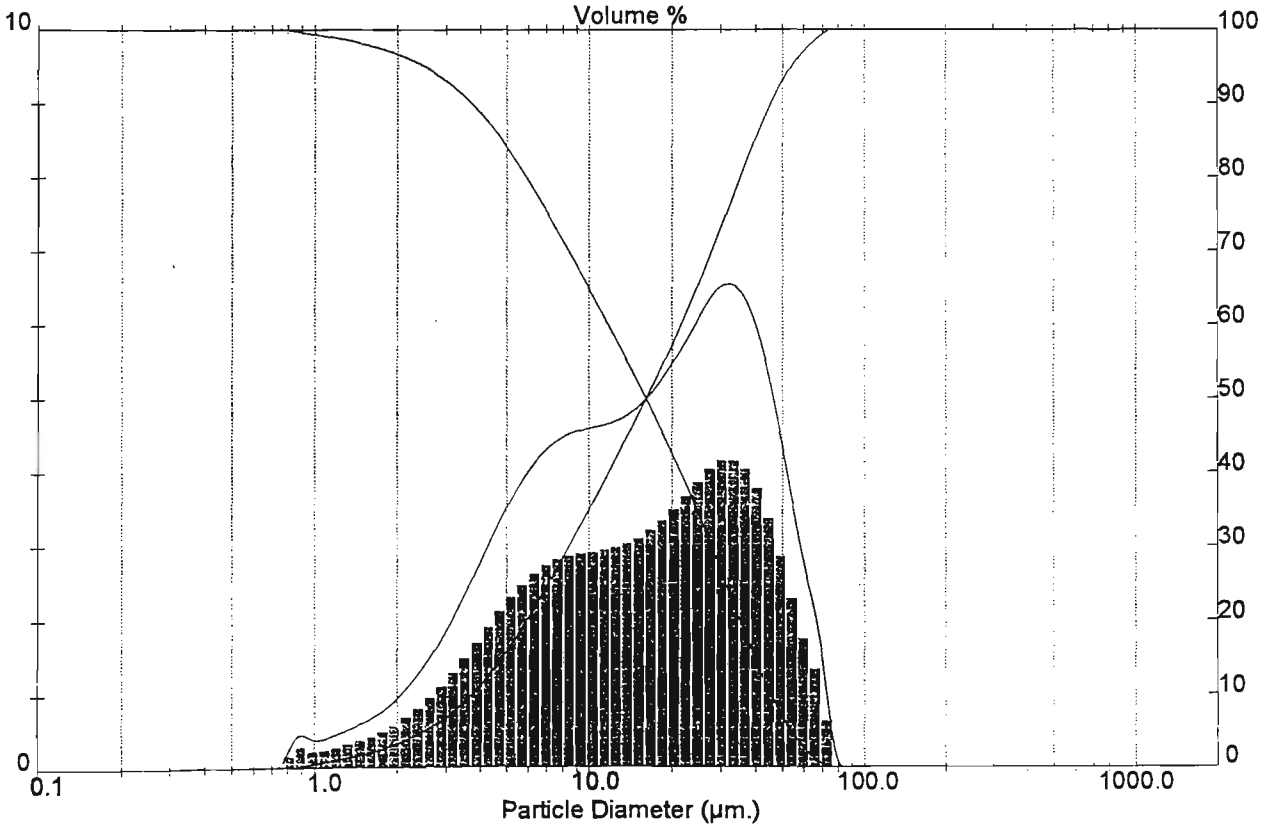

Malvern Instruments Ltd.
Malvern, UK
Tel:0684 892456 Fax:0684 892789

Mastersizer S Ver. 2.11
Serial Number: 32734-21

07 Nov 95

MALVERN INSTRUMENTS

MASTERSIZER

Result: Sieve BS 410:1986 Report

Sample Details

Sample ID: NVVO-T-Precursor
Sample File: NVVO-2
Sample Path: C:\SIZERS\DATA\
Sample Notes:

Run Number: 2
Record Number: 1

Measurement Date: Tue, Nov 07, 1995 7:13PM
Analysis Date: Tue, Nov 07, 1995 7:13PM
Result Source: Analysed

System Details

Range Lens: 300RF mm
Presentation: 3OHD
Analysis Model: Polydisperse
Modifications: None

Beam Length: 2.40 mm
[Particle R.I. = (1.5295, 0.1000); Dispersant R.I. = 1.3300]

Sampler: None

Obscuration: 19.2 %
Residual: 0.575 %

Result Statistics

Distribution Type: Volume
Mean Diameters:
D [4, 3] = 29.00 um

Concentration = 0.0341 %Vol
D (v, 0.1) = 5.97 um
D [3, 2] = 12.20 um

Density = 1.000 g / cub. cm
D (v, 0.5) = 21.80 um
Span =2.505E+00

Specific S.A. = 0.4919 sq. m / g
D (v, 0.9) = 60.60 um
Uniformity = 8.010E-01

Mesh No	Aperture um	Volume In%	Volume Below%
10	2000	0.00	100.00
12	1700	0.00	100.00
14	1400	0.00	100.00
16	1180	0.00	100.00
18	1000	0.00	100.00
20	850	0.00	100.00
25	710	0.00	100.00
30	600	0.00	100.00
35	500	0.00	100.00
40	425	0.00	100.00
45	355	0.00	100.00
50	300	0.00	100.00
60	250		100.00

Mesh No	Aperture um	Volume In%	Volume Below%
60	250	0.00	100.00
70	212	0.02	100.00
80	180	0.23	99.98
100	150	0.78	99.75
120	125	1.11	98.97
140	106	1.50	97.86
170	90	2.33	96.37
200	75	3.18	94.03
230	63	4.30	90.86
270	53	5.22	86.55
325	45	6.47	81.34
400	38		74.87

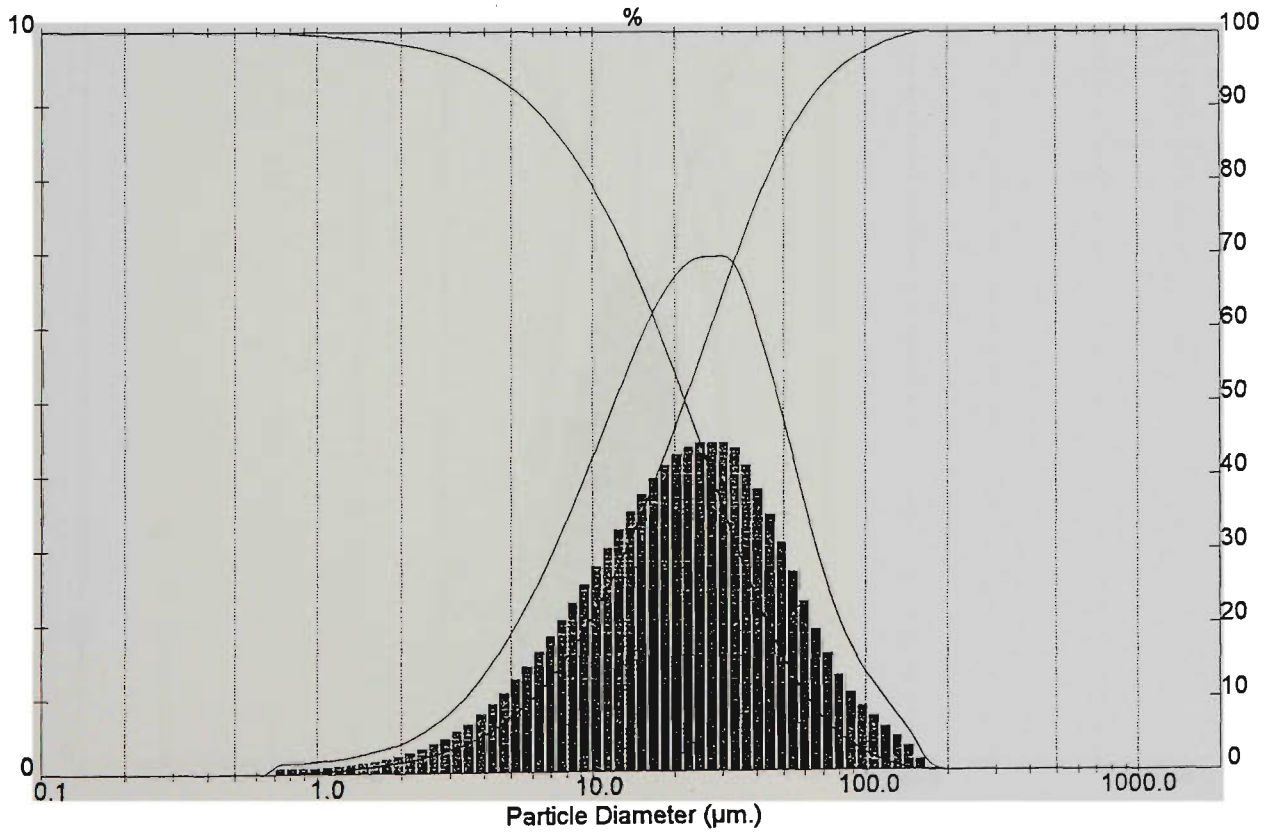

Malvern Instruments Ltd.
Malvern, UK
Tel:0684 892456 Fax:0684 892789

Mastersizer S Ver. 2.11
Serial Number: 32734-21

07 Nov 95 19

MASTERSIZER

Result: Sieve BS 410:1986 Report

Sample Details

Sample ID: NVVO-D-Precursor
Sample File: NVVO-4
Sample Path: C:\SIZERS\DATA\
Sample Notes:

Run Number: 2
Record Number: 1

Measurement Date: Tue, Nov 07, 1995 7:46PM
Analysis Date: Tue, Nov 07, 1995 7:46PM
Result Source: Analysed

System Details

Range Lens: 300RF mm
Presentation: 3OHD
Analysis Model: Polydisperse
Modifications: None

Beam Length: 2.40 mm
[Particle R.I. = (1.5295, 0.1000); Dispersant R.I. = 1.3300]

Sampler: None

Obscuration: 10.8 %
Residual: 6.259 %

Result Statistics

Distribution Type: Volume
Mean Diameters:
D [4, 3] = 11.02 um

Concentration = 0.0118 %Vol
D (v, 0.1) = 4.59 um
D [3, 2] = 8.00 um

Density = 1.000 g / cub. cm
D (v, 0.5) = 9.59 um
Span =1.566E+00

Specific S.A. = 0.7500 sq. m / g
D (v, 0.9) = 19.61 um
Uniformity = 4.832E-01

Mesh No	Aperture um	Volume In%	Volume Below%
10	2000	0.00	100.00
12	1700	0.00	100.00
14	1400	0.00	100.00
16	1180	0.00	100.00
18	1000	0.00	100.00
20	850	0.00	100.00
25	710	0.00	100.00
30	600	0.00	100.00
35	500	0.00	100.00
40	425	0.00	100.00
45	355	0.00	100.00
50	300	0.00	100.00
60	250		100.00

Mesh No	Aperture um	Volume In%	Volume Below%
60	250	0.00	100.00
70	212	0.00	100.00
80	180	0.00	100.00
100	150	0.00	100.00
120	125	0.00	100.00
140	106	0.00	100.00
170	90	0.00	100.00
200	75	0.00	100.00
230	63	0.00	100.00
270	53	0.00	100.00
325	45	0.05	100.00
400	38		99.95

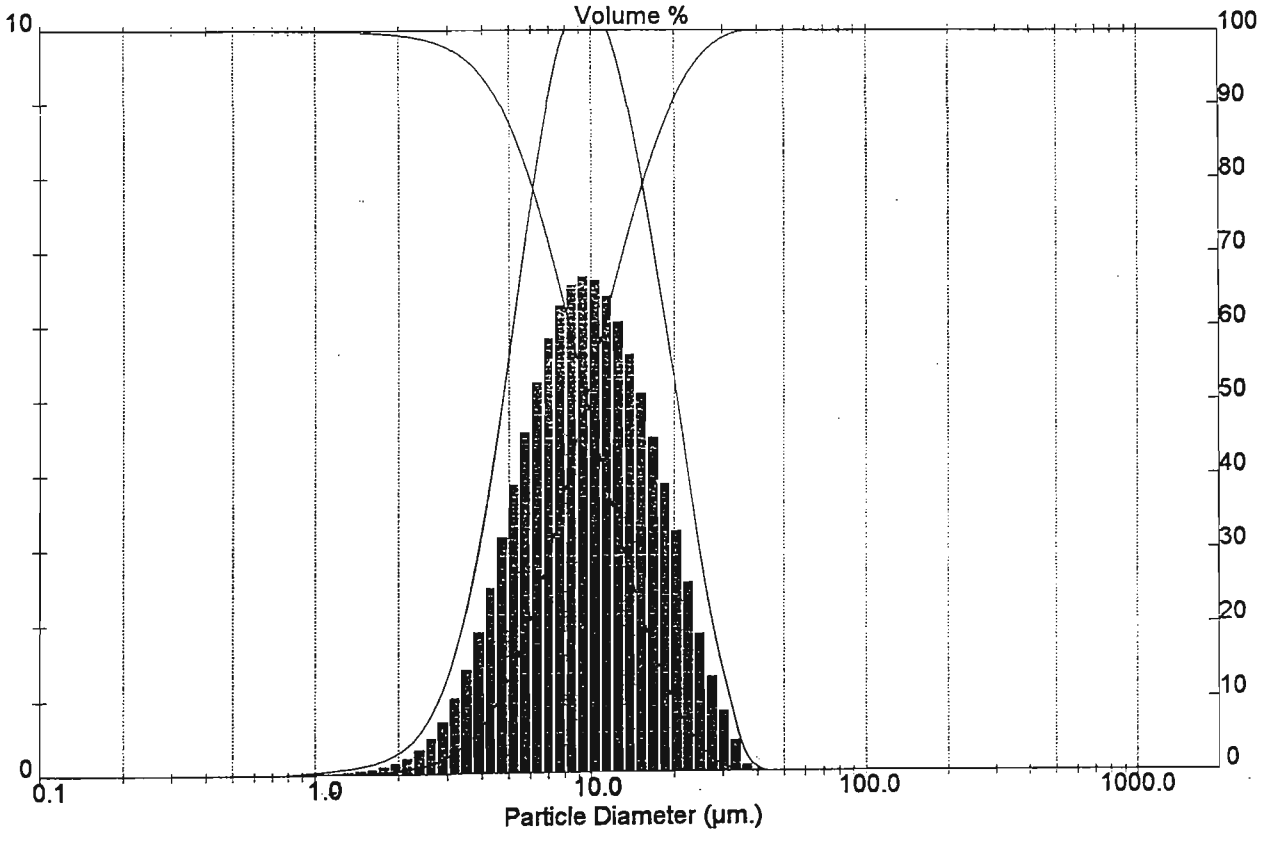

Malvern Instruments Ltd.
Malvern, UK
Tel:0684 892456 Fax:0684 892789

Mastersizer S Ver. 2.11
Serial Number: 32734-21

07 Nov 95 19:51

MALVERN MASTERSIZER

Result: Sieve BS 410:1986 Report

Sample Details

Sample ID: NVVO-U-Precursor
Sample File: NVVO-3
Sample Path: C:\SIZERS\DATA\
Sample Notes:

Run Number: 1
Record Number: 1

Measurement Date: Tue, Nov 07, 1995 7:32PM
Analysis Date: Tue, Nov 07, 1995 7:32PM
Result Source: Analysed

System Details

Range Lens: 300RF mm
Presentation: 3OHD
Analysis Model: Polydisperse
Modifications: None

Beam Length: 2.40 mm
[Particle R.I. = (1.5295, 0.1000); Dispersant R.I. = 1.3300]

Sampler: None

Obscuration: 14.4 %
Residual: 3.589 %

Result Statistics

Distribution Type: Volume
Mean Diameters:
D [4, 3] = 5.09 um

Concentration = 0.0070 %Vol
D (v, 0.1) = 1.87 um
D [3, 2] = 3.54 um

Density = 1.000 g / cub. cm
D (v, 0.5) = 4.63 um
Span =1.534E+00

Specific S.A. = 1.6936 sq. m / g
D (v, 0.9) = 8.96 um
Uniformity = 4.715E-01

Mesh No	Aperture um	Volume In%	Volume Below%
10	2000	0.00	100.00
12	1700	0.00	100.00
14	1400	0.00	100.00
16	1180	0.00	100.00
18	1000	0.00	100.00
20	850	0.00	100.00
25	710	0.00	100.00
30	600	0.00	100.00
35	500	0.00	100.00
40	425	0.00	100.00
45	355	0.00	100.00
50	300	0.00	100.00
60	250	0.00	100.00

Mesh No	Aperture um	Volume In%	Volume Below%
60	250	0.00	100.00
70	212	0.00	100.00
80	180	0.00	100.00
100	150	0.00	100.00
120	125	0.00	100.00
140	106	0.00	100.00
170	90	0.00	100.00
200	75	0.00	100.00
230	63	0.00	100.00
270	53	0.00	100.00
325	45	0.00	100.00
400	38		100.00

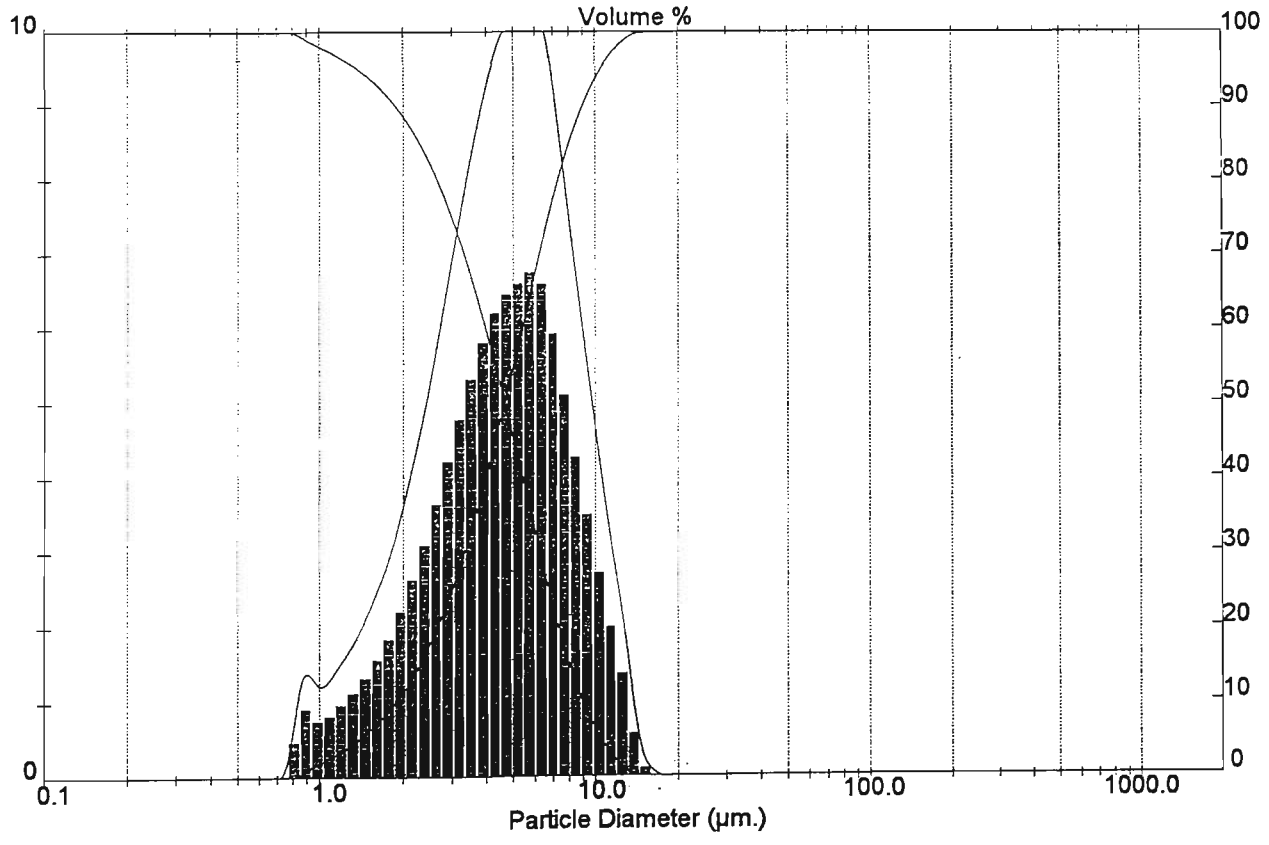

Malvern Instruments Ltd.
Malvern, UK
Tel:0684 892456 Fax:0684 892789

Mastersizer S Ver. 2.11
Serial Number: 32734-21

07 Nov 95 19:38

MALVERN MASTERSIZER

Result: Sieve BS 410:1986 Report

Sample Details

Sample ID: NVVO-B-Precursor
Sample File: NVVO-9
Sample Path: C:\SIZERS\DATA\
Sample Notes:

Run Number: 1
Record Number: 2

Measurement Date: Wed, Nov 08, 1995 10:57AM
Analysis Date: Wed, Nov 08, 1995 10:57AM
Result Source: Analysed

System Details

Range Lens: 300RF mm
Presentation: 3OHD
Analysis Model: Polydisperse
Modifications: None

Beam Length: 2.40 mm
[Particle R.I. = (1.5295, 0.1000); Dispersant R.I. = 1.3300]

Sampler: None

Obscuration: 14.0 %
Residual: 5.243 %

Result Statistics

Distribution Type: Volume
Mean Diameters:
D [4, 3] = 8.76 um

Concentration = 0.0084 %Vol
D (v, 0.1) = 2.14 um
D [3, 2] = 4.23 um

Density = 1.000 g / cub. cm
D (v, 0.5) = 5.84 um
Span =3.184E+00

Specific S.A. = 1.4183 sq. m / g
D (v, 0.9) = 20.75 um
Uniformity = 9.104E-01

Mesh No	Aperture um	Volume In%	Volume Below%
10	2000	0.00	100.00
12	1700	0.00	100.00
14	1400	0.00	100.00
16	1180	0.00	100.00
18	1000	0.00	100.00
20	850	0.00	100.00
25	710	0.00	100.00
30	600	0.00	100.00
35	500	0.00	100.00
40	425	0.00	100.00
45	355	0.00	100.00
50	300	0.00	100.00
60	250		100.00

Mesh No	Aperture um	Volume In%	Volume Below%
60	250	0.00	100.00
70	212	0.00	100.00
80	180	0.00	100.00
100	150	0.00	100.00
120	125	0.00	100.00
140	106	0.00	100.00
170	90	0.00	100.00
200	75	0.00	100.00
230	63	0.00	100.00
270	53	0.00	100.00
325	45	0.32	100.00
400	38		99.68

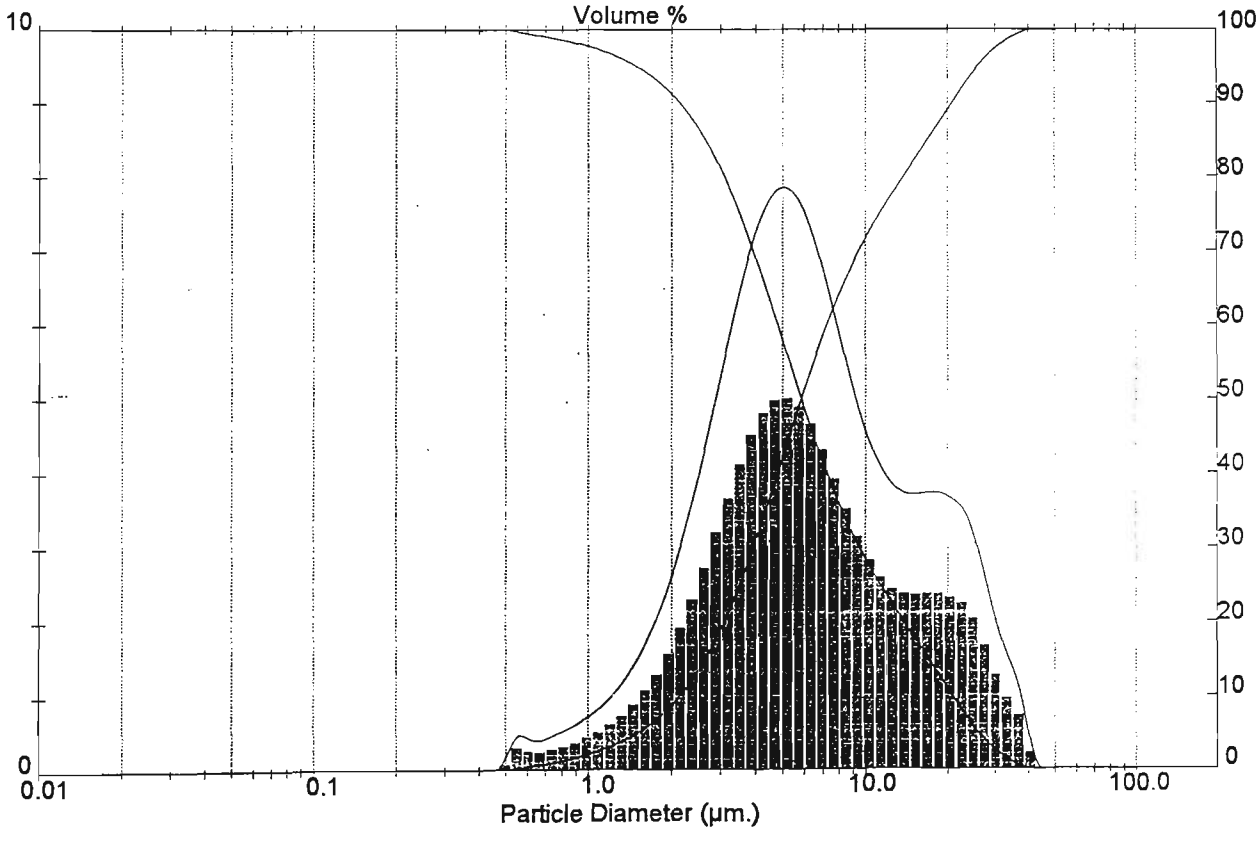

Malvern Instruments Ltd.
Malvern, UK
Tel:0684 892456 Fax:0684 892789

Mastersizer S Ver. 2.11
Serial Number: 32734-21

p.
08 Nov 95 11:0

MALVERN MASTERSIZER

Result: Sieve BS 410:1986 Report

Sample Details

Sample ID: NVVO-Aron-Ceramic-D
Sample File: NVVO-6
Sample Path: C:\SIZERS\DATA\
Sample Notes:

Run Number: 4
Record Number: 1

Measurement Date: Tue, Nov 07, 1995 8:08PM
Analysis Date: Tue, Nov 07, 1995 8:08PM
Result Source: Analysed

System Details

Range Lens: 300RF mm
Presentation: 3OHD
Analysis Model: Polydisperse
Modifications: None

Beam Length: 2.40 mm
[Particle R.I. = (1.5295, 0.1000); Dispersant R.I. = 1.3300]

Sampler: None

Obscuration: 11.9 %
Residual: 0.340 %

Result Statistics

Distribution Type: Volume
Mean Diameters:
D [4, 3] = 37.68 um

Concentration = 0.0050 %Vol
D (v, 0.1) = 0.38 um
D [3, 2] = 1.32 um

Density = 1.000 g / cub. cm
D (v, 0.5) = 17.52 um
Span =5.925E+00

Specific S.A. = 4.5579 sq. m / g
D (v, 0.9) = 104.18 um
Uniformity = 1.991E+00

Mesh No	Aperture um	Volume In%	Volume Below%
10	2000	0.00	100.00
12	1700	0.00	100.00
14	1400	0.00	100.00
16	1180	0.00	100.00
18	1000	0.00	100.00
20	850	0.00	100.00
25	710	0.00	100.00
30	600	0.00	100.00
35	500	0.00	100.00
40	425	0.00	100.00
45	355	0.00	100.00
50	300	0.03	100.00
60	250		99.97

Mesh No	Aperture um	Volume In%	Volume Below%
60	250	0.52	99.97
70	212	1.04	99.46
80	180	1.87	98.42
100	150	2.78	96.55
120	125	3.37	93.77
140	106	4.10	90.40
170	90	5.26	86.30
200	75	5.38	81.04
230	63	5.26	75.67
270	53	4.57	70.40
325	45	4.10	65.83
400	38		61.73

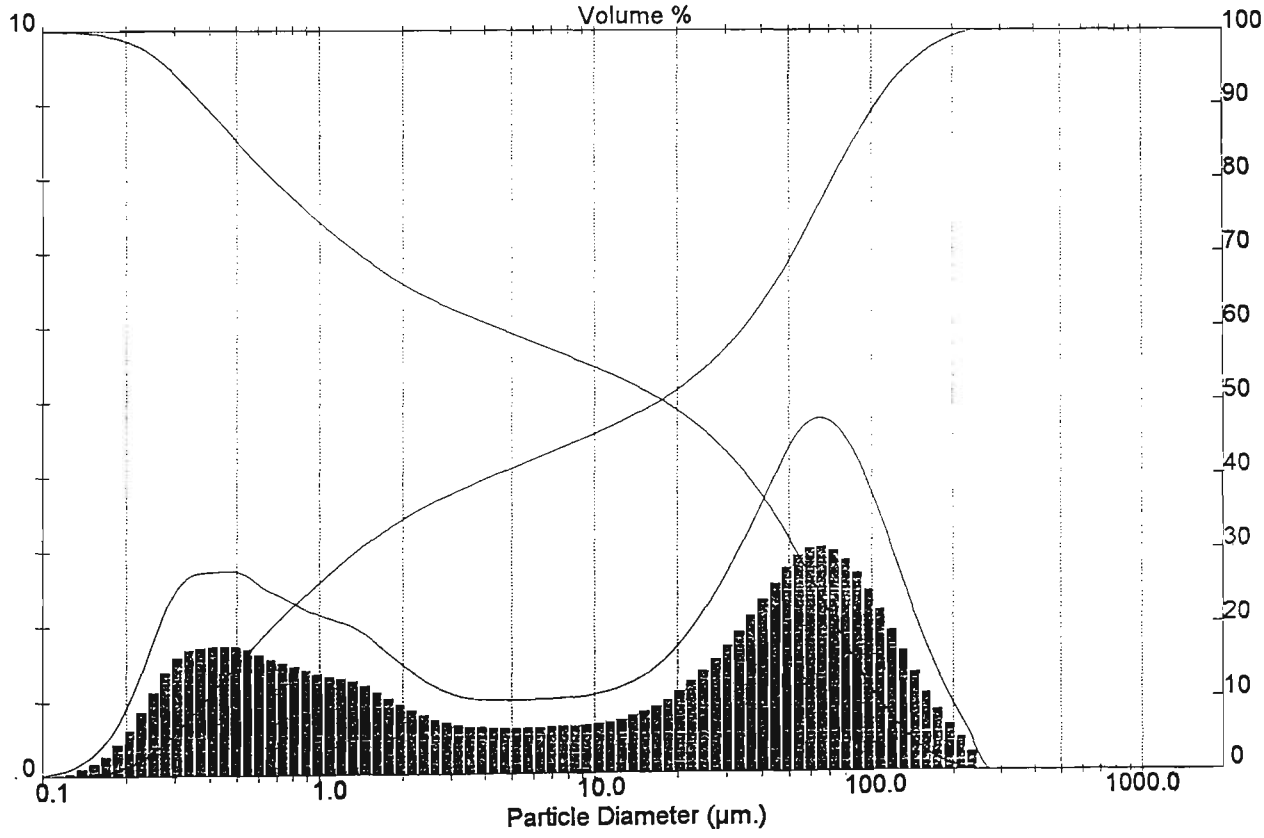

Malvern Instruments Ltd.
Malvern, UK
Tel:0684 892456 Fax:0684 892789

Mastersizer S Ver. 2.11
Serial Number: 32734-21

07 Nov 95 20:11

MALVERN MASTERSIZER

Result: Sieve BS 410:1986 Report

Sample Details

Sample ID: NVVO-1micron-Alumina
Sample File: NVVO-8
Sample Path: C:\SIZERS\DATA\
Sample Notes:

Run Number: 1
Record Number: 2

Measurement Date: Wed, Nov 08, 1995 10:23AM
Analysis Date: Wed, Nov 08, 1995 10:24AM
Result Source: Analysed

System Details

Range Lens: 300RF mm
Presentation: 3OHD
Analysis Model: Polydisperse
Modifications: None

Beam Length: 2.40 mm
[Particle R.I. = (1.5295, 0.1000); Dispersant R.I. = 1.3300]

Sampler: None

Obscuration: 15.4 %
Residual: 2.302 %

Result Statistics

Distribution Type: Volume
Mean Diameters:
D [4, 3] = 0.89 um

Concentration = 0.0028 %Vol
D (v, 0.1) = 0.22 um
D [3, 2] = 0.45 um

Density = 1.000 g / cub. cm
D (v, 0.5) = 0.58 um
Span =3.009E+00

Specific S.A. = 13.2550 sq. m / g
D (v, 0.9) = 1.98 um
Uniformity = 9.473E-01

Mesh No	Aperture um	Volume In%	Volume Below%
10	2000	0.00	100.00
12	1700	0.00	100.00
14	1400	0.00	100.00
16	1180	0.00	100.00
18	1000	0.00	100.00
20	850	0.00	100.00
25	710	0.00	100.00
30	600	0.00	100.00
35	500	0.00	100.00
40	425	0.00	100.00
45	355	0.00	100.00
50	300	0.00	100.00
60	250		100.00

Mesh No	Aperture um	Volume In%	Volume Below%
60	250	0.00	100.00
70	212	0.00	100.00
80	180	0.00	100.00
100	150	0.00	100.00
120	125	0.00	100.00
140	106	0.00	100.00
170	90	0.00	100.00
200	75	0.00	100.00
230	63	0.00	100.00
270	53	0.00	100.00
325	45	0.00	100.00
400	38		100.00

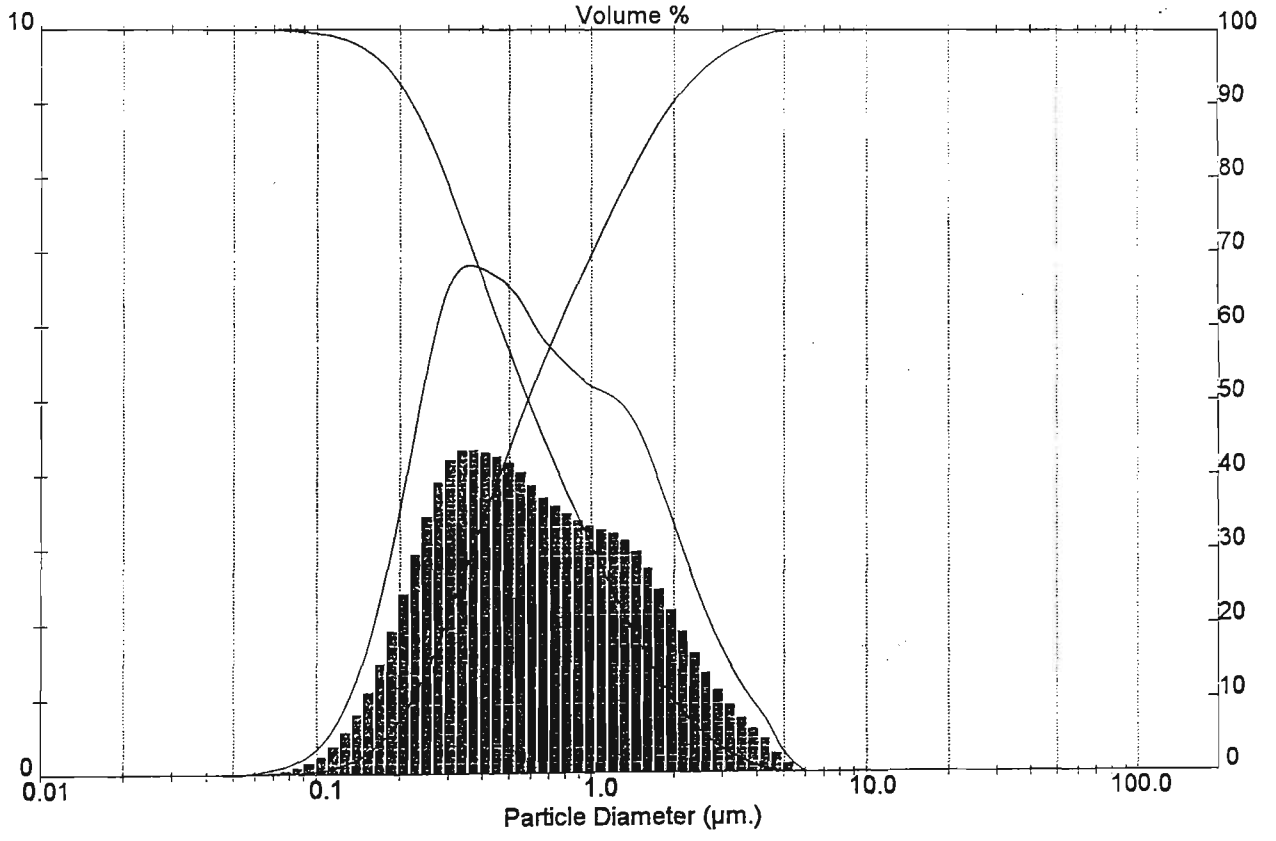

Malvern Instruments Ltd.
Malvern, UK
Tel:0684 892456 Fax:0684 892789

Mastersizer S Ver. 2.11
Serial Number: 32734-21

Appendix E

DTA/TG of precursor powders, and green tapes of Bi(Pb)-2223.

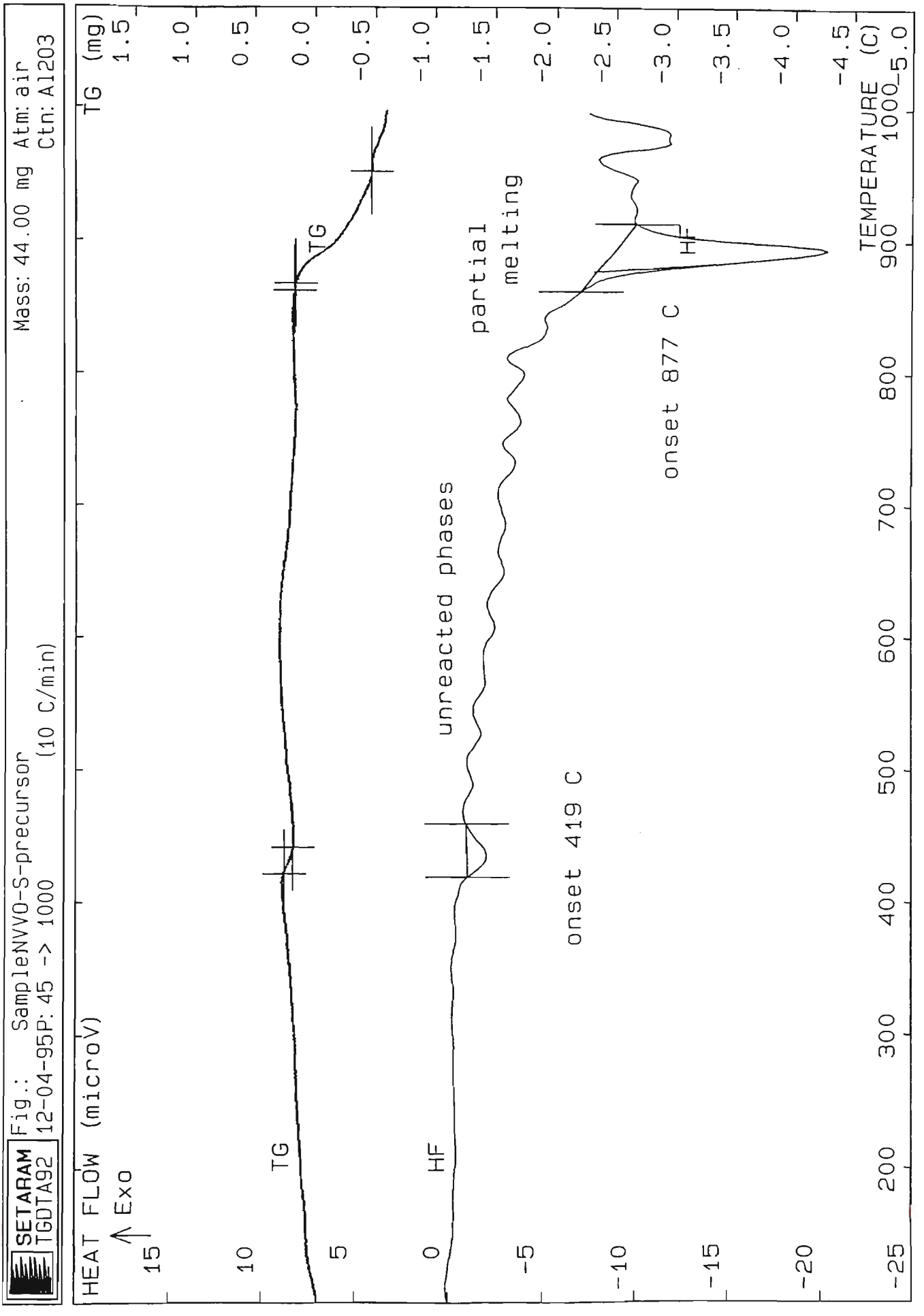

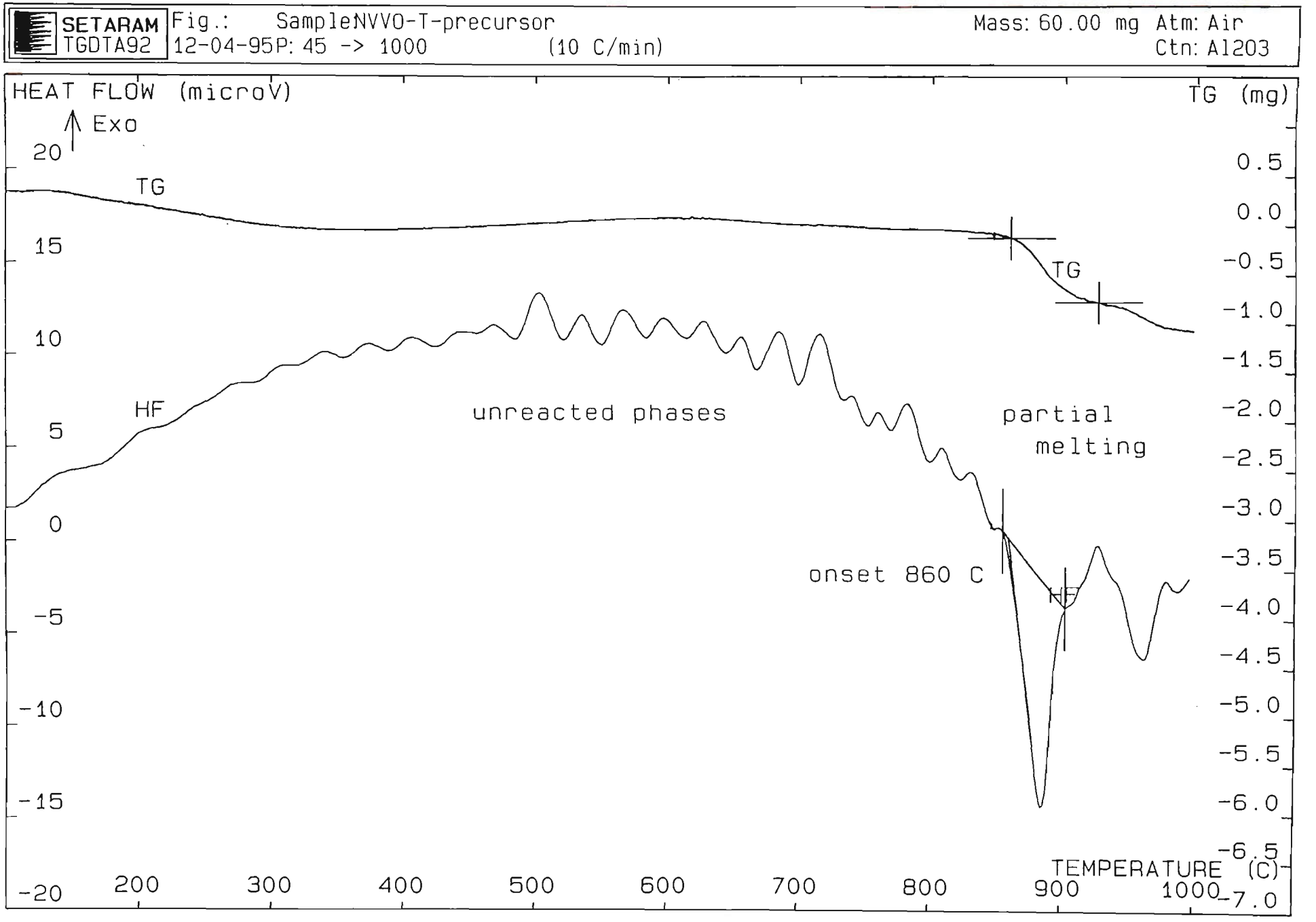
SETARAM
TGDTA92
Fig.: SampleNVVO-T-precursor
12-04-95P: 45 -> 1000 (10 C/min)
Mass: 60.00 mg Atm: Air
Ctn: Al203
HEAT FLOW (microV)
Exo
TG (mg)
TG
TG
HF
unreacted phases
partial
melting
onset 860 C
HF
TEMPERATURE (C)
20
15
10
5
0
-5
-10
-15
-20
200
300
400
500
600
700
800
900
1000
0.5
0.0
-0.5
-1.0
-1.5
-2.0
-2.5
-3.0
-3.5
-4.0
-4.5
-5.0
-5.5
-6.0
-6.5
-7.0

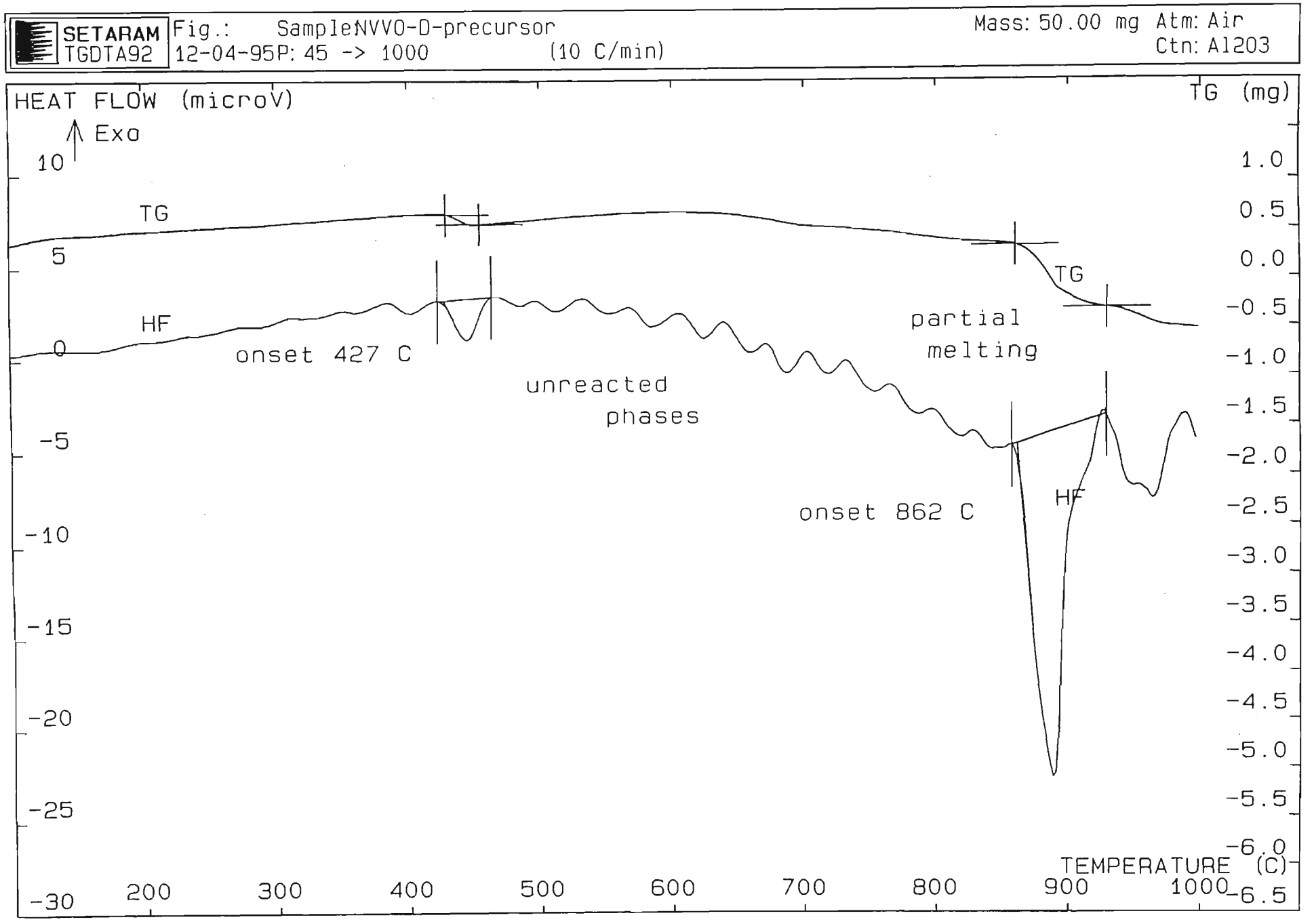
SETARAM
TGDTA92
Fig.: SampleNVVO-D-precursor
12-04-95P: 45 -> 1000 (10 C/min)
Mass: 50.00 mg Atm: Air
Ctn: Al203
HEAT FLOW (microV)
Exo
TG (mg)
TG
HF
onset 427 C
unreacted
phases
partial
melting
TG
onset 862 C
HF
TEMPERATURE (C)

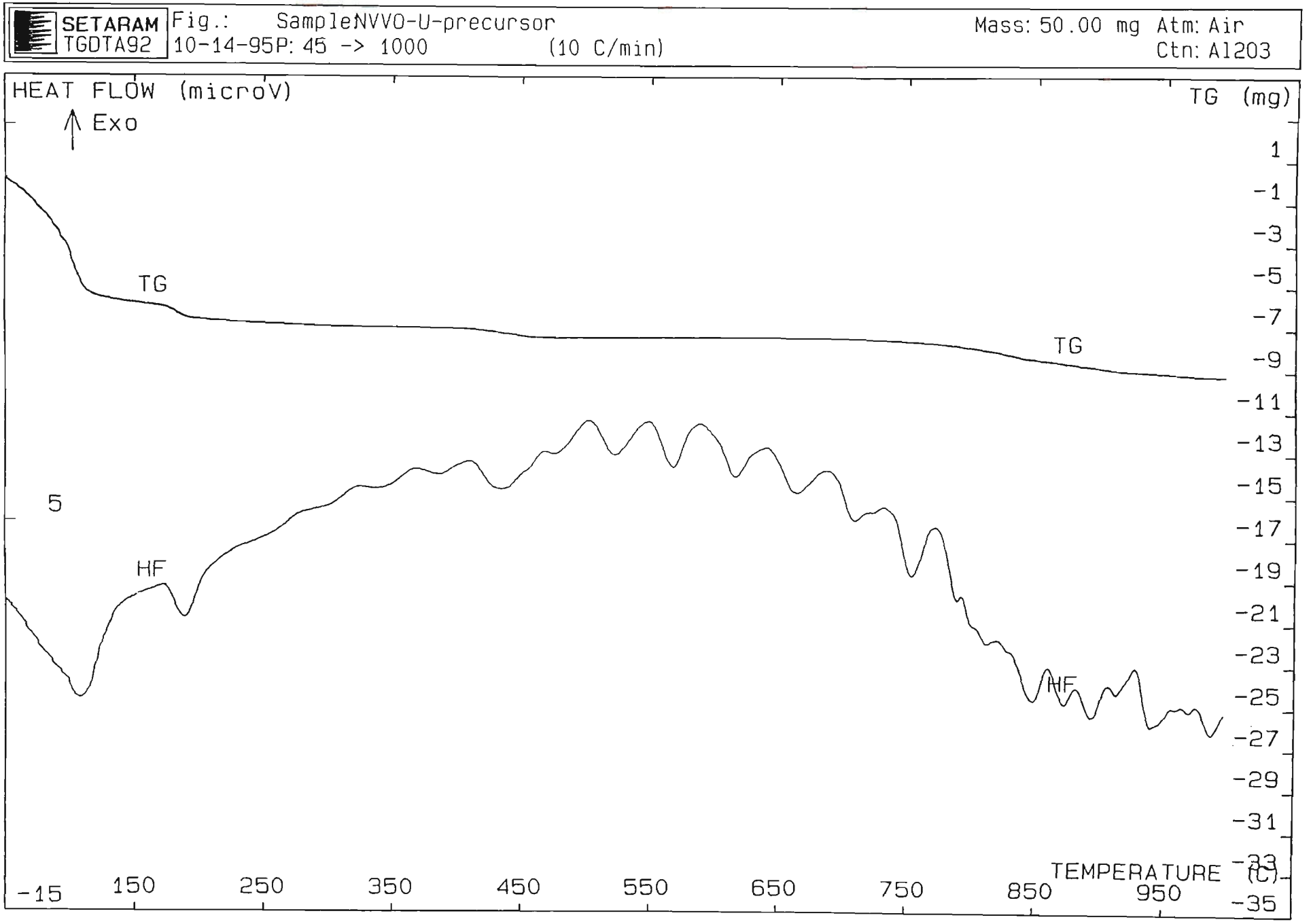
SETARAM
TGDTA92
Fig.: SampleNVVO-U-precursor
10-14-95P: 45 -> 1000 (10 C/min)
Mass: 50.00 mg Atm: Air
Ctn: Al203
HEAT FLOW (microV)
Exo
TG (mg)
TG
TG
5
HF
HF
1
-1
-3
-5
-7
-9
-11
-13
-15
-17
-19
-21
-23
-25
-27
-29
-31
-33
-15
150
250
350
450
550
650
750
850
950
TEMPERATURE (C)

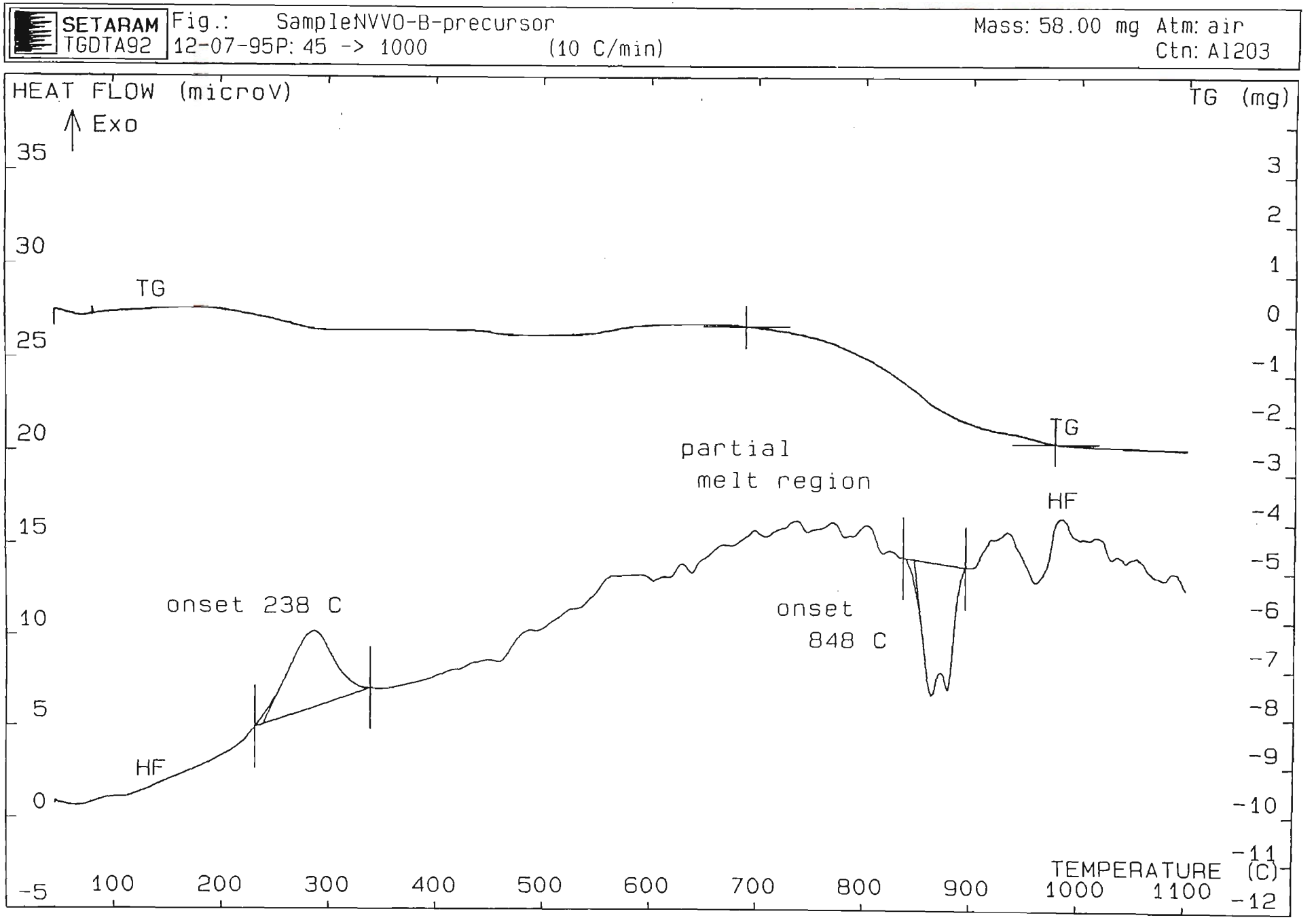
SETARAM
TGDTA92
Fig.: SampleNVVO-B-precursor
12-07-95P: 45 -> 1000 (10 C/min)
Mass: 58.00 mg Atm: air
Ctn: A1203
HEAT FLOW (microV)
Exo
TG (mg)
TG
TG
partial
melt region
HF
HF
onset 238 C
onset
848 C
TEMPERATURE (C)
35
30
25
20
15
10
5
0
-5
3
2
1
0
-1
-2
-3
-4
-5
-6
-7
-8
-9
-10
-11
-12
100
200
300
400
500
600
700
800
900
1000
1100

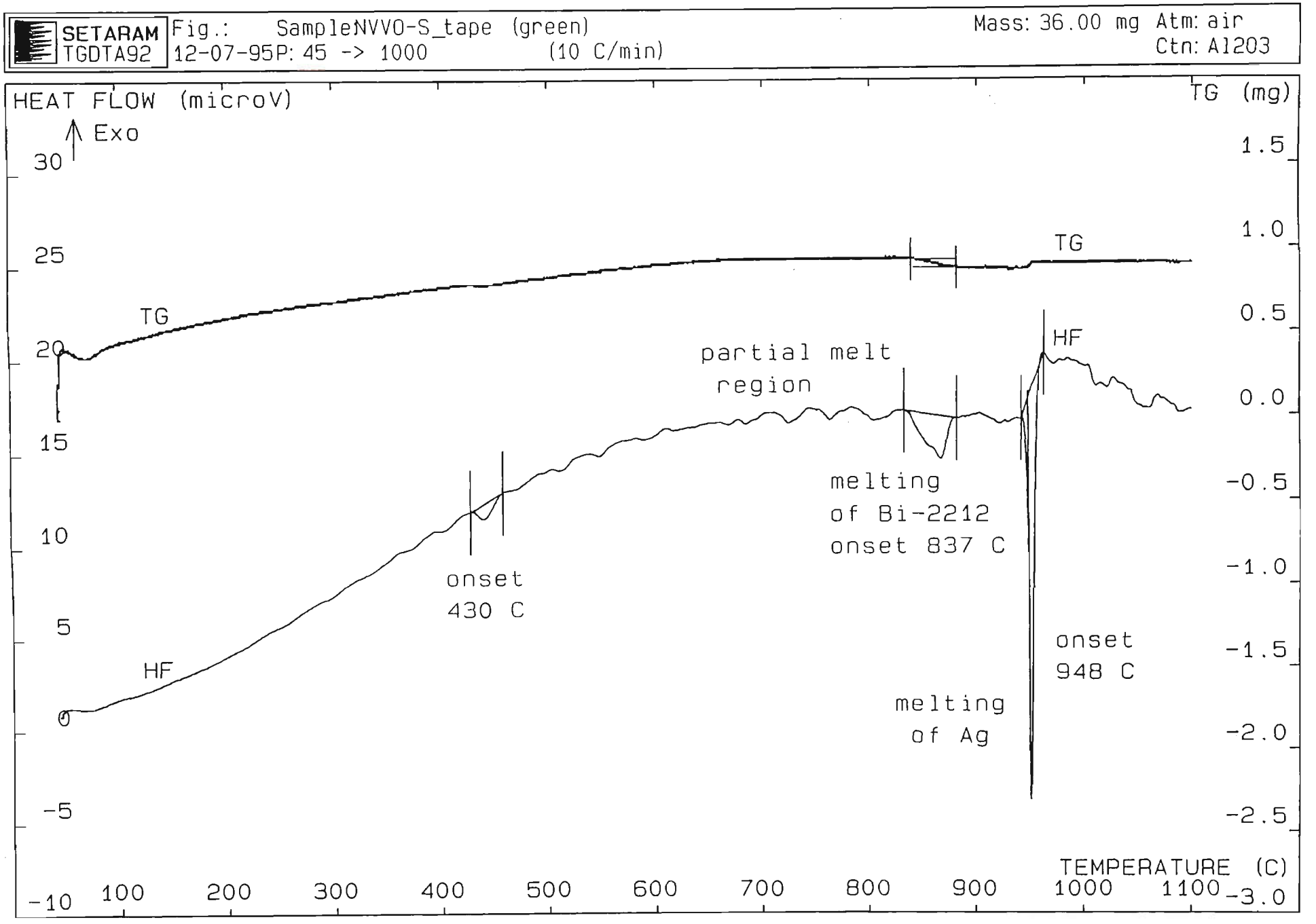
SETARAM
TGDTA92
Fig.: SampleNVVO-S_tape (green)
12-07-95P: 45 -> 1000 (10 C/min)
Mass: 36.00 mg Atm: air
Ctn: Al203
HEAT FLOW (microV)
Exo
TG (mg)
TG
TG
HF
HF
partial melt
region
melting
of Bi-2212
onset 837 C
onset
430 C
onset
948 C
melting
of Ag
TEMPERATURE (C)
30
25
20
15
10
5
0
-5
-10
100
200
300
400
500
600
700
800
900
1000
1100
1.5
1.0
0.5
0.0
-0.5
-1.0
-1.5
-2.0
-2.5
-3.0

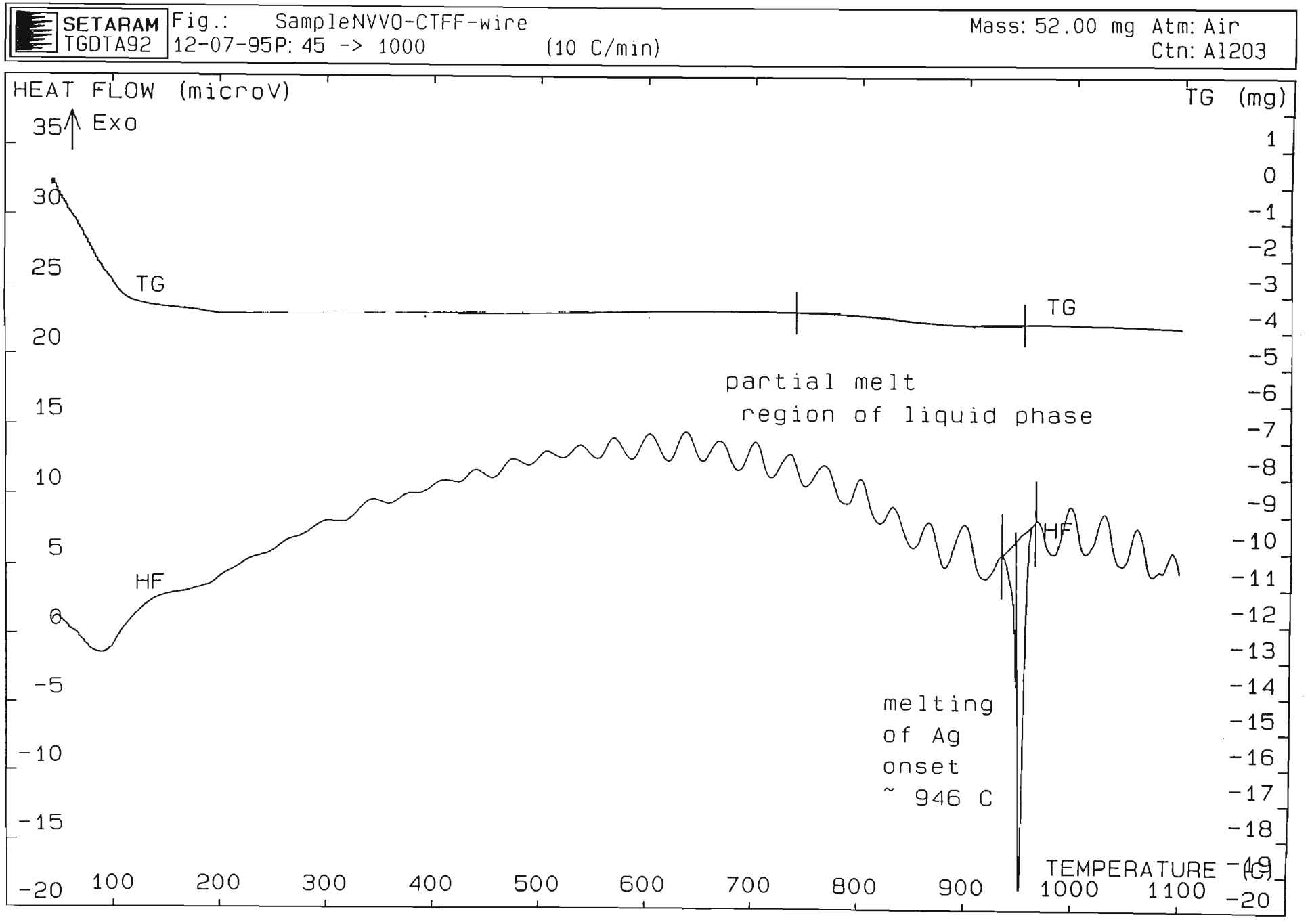
SETARAM
TGDTA92
Fig.: SampleNVVO-CTFF-wire
12-07-95P: 45 -> 1000 (10 C/min)
Mass: 52.00 mg Atm: Air
Ctn: Al203
HEAT FLOW (microV)
Exo
TG (mg)
TG
TG
partial melt
region of liquid phase
HF
HF
melting
of Ag
onset
~ 946 C
TEMPERATURE (C)

Appendix F

DC magnetization curves obtained using SQUID magnetometry.

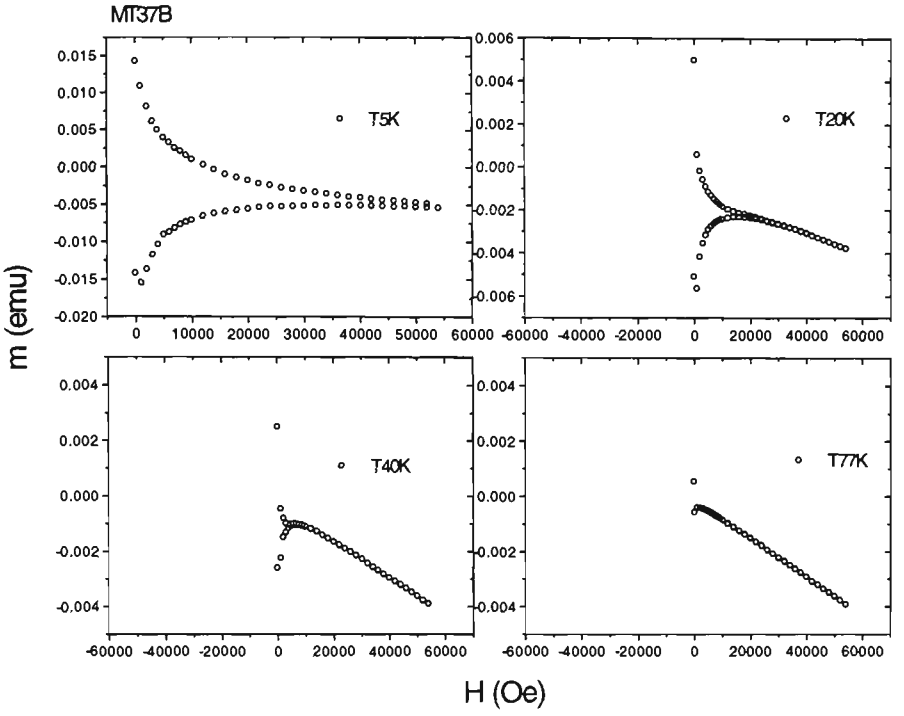

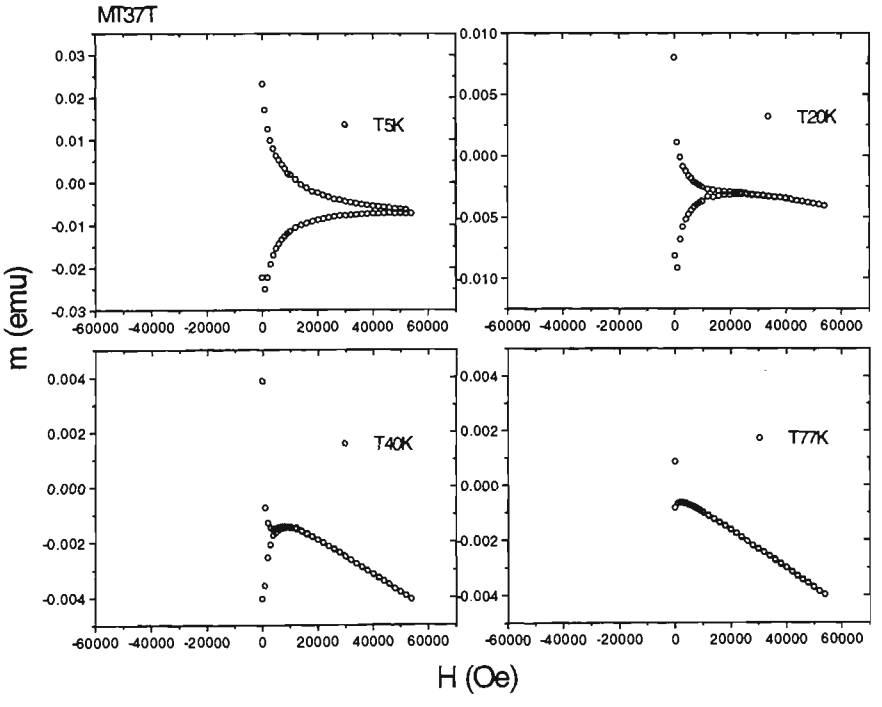

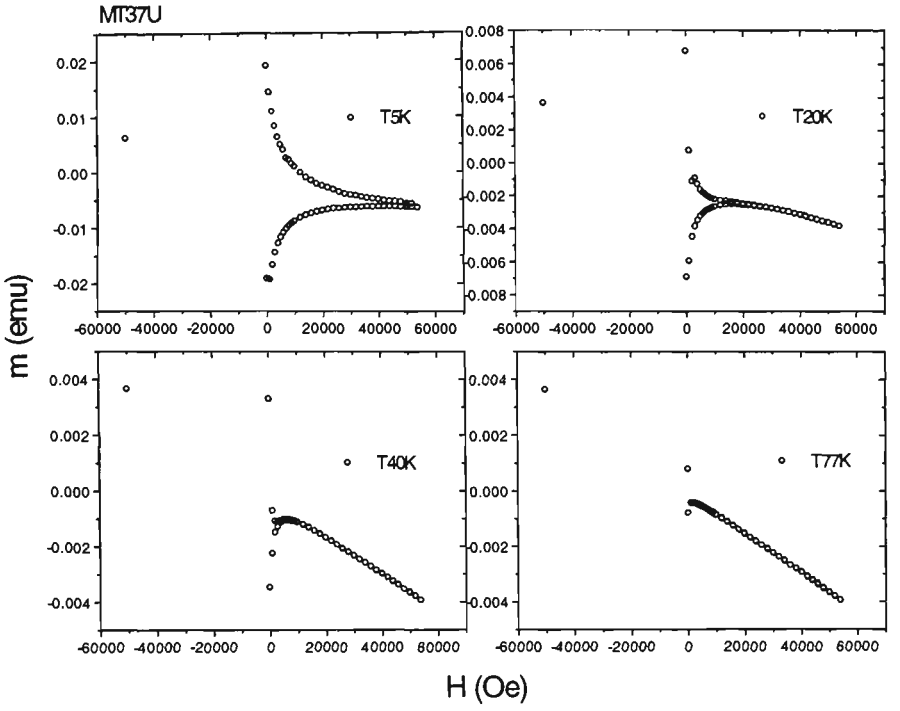
MT37U
T5K
T20K
T40K
T77K
m (emu)
H (Oe)

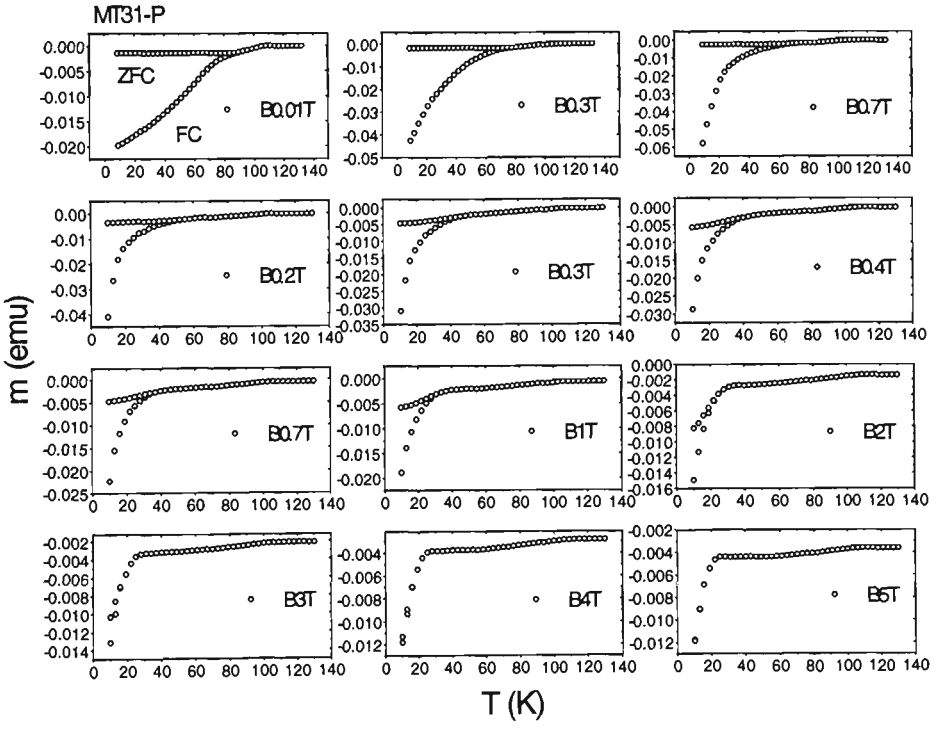
MT31-P
ZFC
FC
B0.01T
B0.3T
B0.7T
B0.2T
B0.3T
B0.4T
B0.7T
B1T
B2T
B3T
B4T
B5T
m (emu)
T (K)

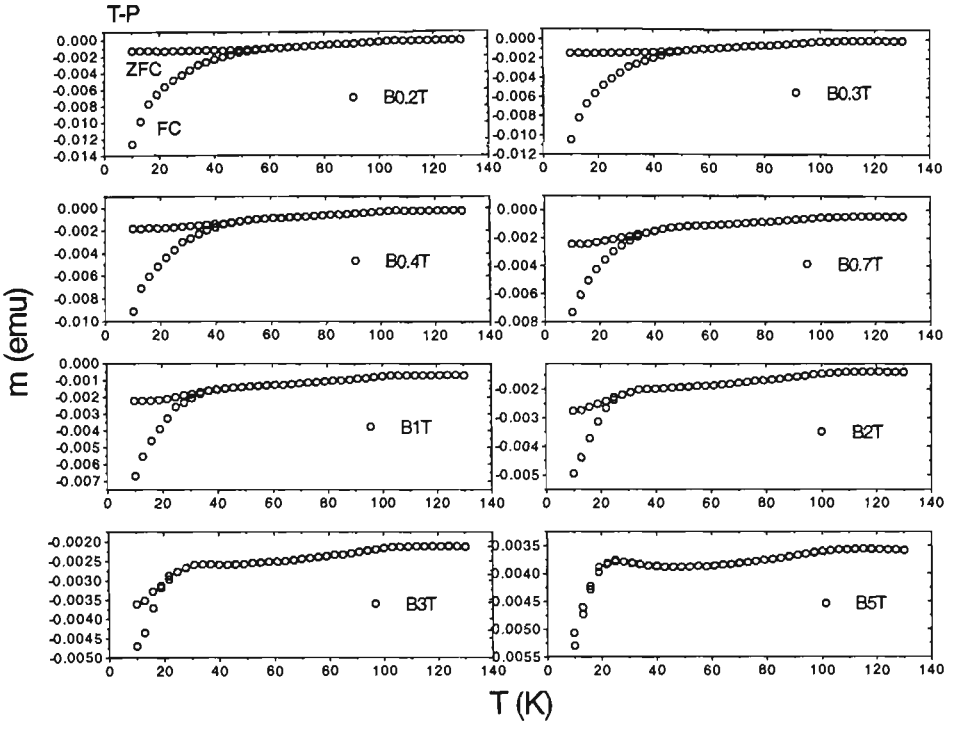
T-P
ZFC
FC
B0.2T
B0.3T
B0.4T
B0.7T
B1T
B2T
B3T
B5T
m (emu)
T (K)

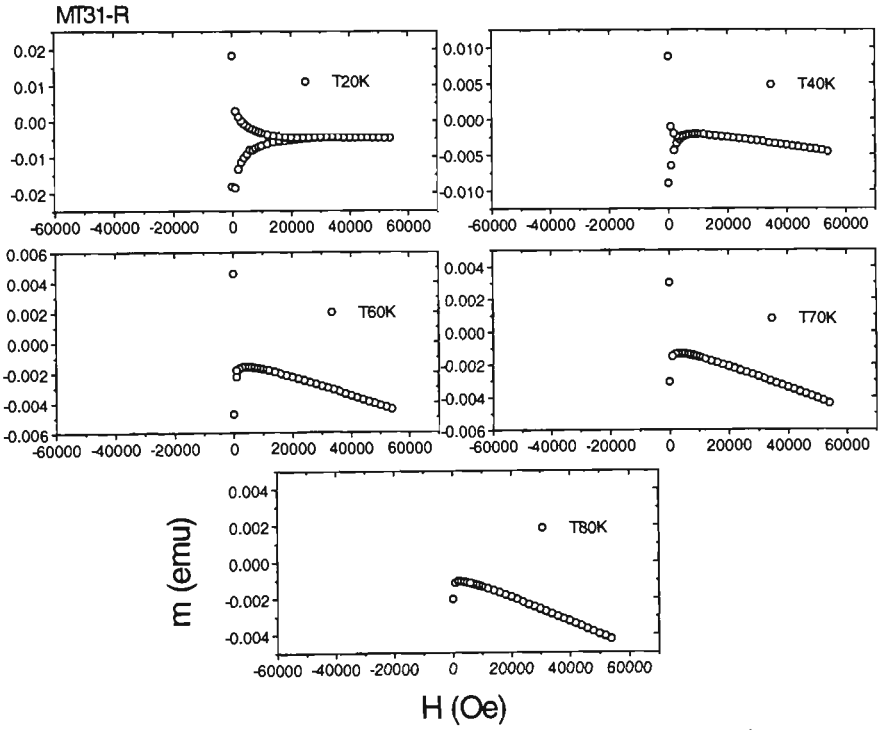
MT31-R
T20K
T40K
T60K
T70K
T80K
m (emu)
H (Oe)

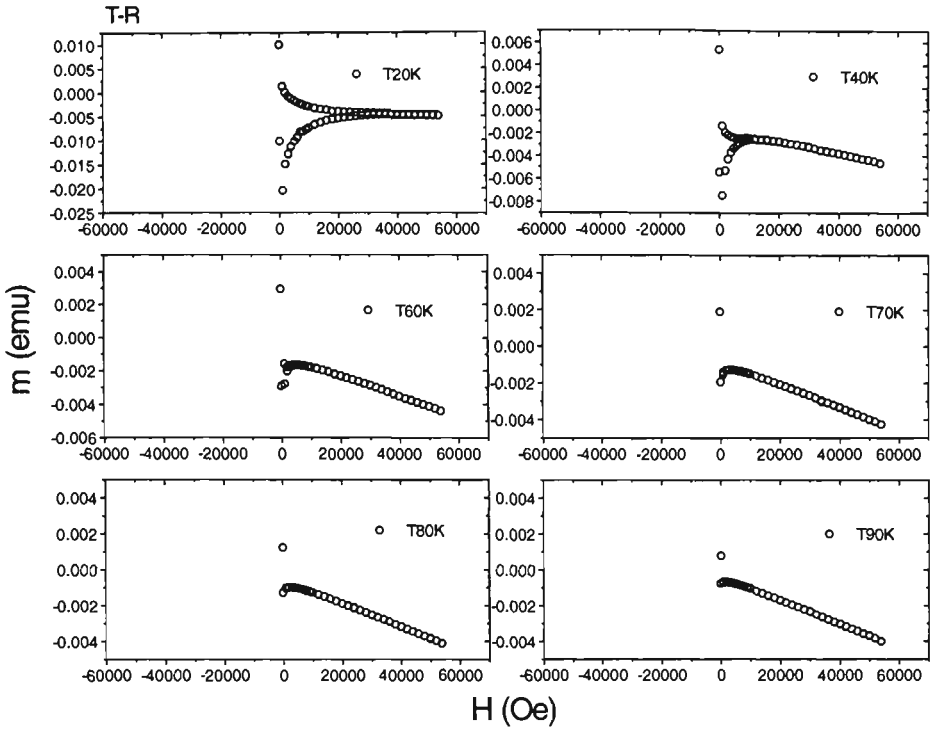
T-R
T20K
T40K
T60K
T70K
T80K
T90K
m (emu)
H (Oe)

List of Figures

Page no. given at the end of each caption.

List of Tables

Page no. given at the end of each caption.

Publications

Refereed Papers

1. N.V.Vo, S.X. Dou, and H. K. Liu,
'The Effect of Initial Packing Density of OPIT Method on The Phase Formation, Electrical Transport and Mechanical Properties of Bi-(Pb)-Sr-Ca-Cu-O Monocore Superconducting Tapes',
Physica C **250**, (1995) 139-152.

2. N.V. Vo, H. K. Liu, and S. X. Dou,
'Effect of Sintering Periods on The Microstructure and Electrical Transport Properties of High-T_c Superconducting Bi-(Pb)-Sr-Ca-Cu-O Tapes',
J. Mater. Res. **11** 5 (May 1996) 1101-1107.

3. N.V. Vo, H.K. Liu, and S.X. Dou,
'Effect of Sintering Periods on the Pinning Force, Activation Energy and Microstructure of High-T_c Superconducting Bi-(Pb)-Sr-Ca-Cu-O Tapes',
Supercond. Sci. Technol. **9** (1996) 104-112 .

4. N.V. Vo, S. X. Dou, and H. K. Liu,
'Effect of Rolling Reduction on The Transport Property, Microstructure, Phase Formation and Fill Factor of High-T_c Superconducting Bi-(Pb)-Sr-Ca-Cu-O Tapes',
Cryogenics **36** (1996) 903-913.

5. J. Horvat, N.V. Vo, and S.X. Dou,
'V-I Characteristics of Ag-sheathed Bi-Pb-Sr-Ca-Cu-O Superconductors: gap in pinning energy',
Physica C, accepted for publication 1995.

6. N.V. Vo, H.K. Liu, S.X. Dou, and I. Kusevic,
'Conductor Design With High-T_c Superconducting Bi(Pb)-2223/Ag Multifilamentary Tapes',
Mater. Sc. Eng. **B40** (1996) 217-223.

7. N.V. Vo, S.X. Dou, and H.K. Liu,
'Development of Bi(Pb)-2223/Ag Pancake-Shaped and Solenoidal Coils',
IEEE Trans. Appl. Super. **6** 2 (Jun 1996) 102-105.

8. N.V. Vo, C.C. Neo, A.J. Bourdillon, S.X. Dou, and H.K. Liu,
'Thermal Stability In High-T_c Coil and Magnet Design By Processing Control of Bi(Pb)-2223/Ag Multifilamentary Tapes',
J. Supercond. **9** 6 (1996) 607-616.

9. N.V. Vo, H.K. Liu, and S.X. Dou
'Critical Current Densities of High-T_c Bi(Pb)-2223 Wire-In-Tube, Continuous-Tube-Forming/Filling and Silver-Alloy Double-Pancake Coils at 77 K',
Appl. Supercond. Int. - Solid-State Electronics, submitted in July 1996 - accepted.

Conference Papers

1. N.V. Vo, S.X. Dou, and H.K. Liu,
'Phase Development and Microstructural Effect of Sintering Periods on Uniaxially Pressed High-T_c Superconducting Bi(Pb)-Sr-Ca-Cu-O Tapes',
TMS, 4-8 February 1996, Warrendale, Pennsylvania, US.

2. N.V. Vo, S.X. Dou, and H.K. Liu,
'Processing and Fabrication of Ag-Clad Bi(Pb)-2223 Mono and Multifilamentary Tapes For Small Scale Coils Application',
ANZIP 20th CMPM, 30 Jan - 2 Feb. 1996, Wagga Wagga, NSW, Australia.

3. S.X. Dou, M. Ionescu, W.G. Wang, Y.C. Guo, N.V.Vo, B. Zeimetz, H.K. Liu, I. Kusevic, and E. Babic,
'Advances In Development of Ag-Clad Bi-Based Superconducting Tapes',
ANZIP 20th CMPM, 30 Jan - 2 Feb. 1996, Wagga Wagga, NSW, Australia.

4. N.V. Vo, H.K. Liu, S.X. Dou, and E.W. Collings
'Dependence of Mechanical and Electrical Properties af Multifilamentary Bi(Pb)-2223/Ag Tapes Prepared By A Continuous Process on Fill Factor and Filament Distribution',
PACRIM 2, 15-17 July 1996, Cairns, Queensland, Australia.

5. N.V. Vo, S.X. Dou, H.K. Liu, and E.W. Collings
'Advances In The Fabrication of Multifilamentary Bi(Pb)-2223/Ag Tapes',
ICEC/ICMC, 20-24 May 1996, Kitakyushu, Japan.

6. M.D. Sumption, N.V. Vo, S.X. Dou, and E.W. Collings,
'Eddy Current and Creep-Based Loss In CTFF Type Bi:2223 Multifilamentary Tapes',
ICEC/ICMC, 20-24 May 1996, Kitakyushu, Japan.

7. S.X. Dou, W.G. Wang, B. Zeimetz, N.V. Vo, Y.C. Guo, H.K. Liu,
I. Kusevic, and E. Babic,
'Improvement In Electromagnetic Properties of Ag-Clad
Bi-Based Superconducting Tapes Through Process Control',
ICEC/ICMC, 20-24 May 1996, Kitakyushu, Japan.

8. Y.C. Guo, J.N. Li, M. Yavuz, H.K. Liu, N.V. Vo, E. R. Vance, and S.X. Dou,
'Effect of Precursor Powder on The Properties of
Silver-Clad Bi-2223 Superconducting Wires and Tapes',
ICEC/ICMC, 17-21 July 1995, Ohio, Columbus, US.

9. N.V. Vo, I. Kusevic, J.E. Ostenson, E. Babic, S.X. Dou, and H.K. Liu, 'Processing Related Issues on The Enhancement of Critical Current Density of Bi(Pb)-2223/Ag Multifilamentary Tapes', *8th IWCC,* 27-29 May 1996, Kitakyushu, Japan.

10. N.V. Vo, H.K. Liu, and S.X. Dou, 'Issues Involving The Processing and Fabrication of Bi(Pb)-2223/Ag Mono and Multifilamentary Tapes for Coil and Magnet Applications', *ASC*, 25-30 Aug., 1996, Pittsburgh, PA, US.

11. N.V. Vo, H.K. Liu, and S.X. Dou, 'Construction and Normal Zone Propagation Analysis of High-T_c Superconducting Bi(Pb)-2223/Ag Class II Coils and Magnets', *ASC*, 25-30 Aug., 1996, Pittsburgh, PA, US.

References

[1] M. Sittig, *Cryogenics Research and Applications*, D. Van Nostrand Co. Inc. New Jersey, 1963.

[2] A.C. Rose-Innes, *Low Temperature Techniques*, Eng.Univ. Press Ltd., 1964.

[3] H. Kamerlingh Onnes, *Leiden Comm.*, No. 1206 (1911) 1226.

[4] W. Meissner, and R. Ochsenfeld, *Naturwissenschaften*, **21** (1933) 787.

[5] T.P. Orlando, and K.A. Delin, *Foundations of Applied Superconductivity*, Addison-Wesley Pub. Co. Inc., 1991.

[6] F. London, and H. London, *Physica*, **2** (1935) 341.

[7] C.J. Gorter and H.G.B. Casimir, *Phys. Z*, **35** (1934) 963.

[8] F. London, *Superfluids*, vol. 2, John Wiley & Sons Inc., New York, 1954.

[9] A.B. Pippard, *Physica*, **19** (1953) 765.

[10] V.L. Ginzburg, and L.D. Landau, *Zh. Eksp. Teor. Fiz.*, **20** (1950) 1064 [English translation: *Men of Physics*, eds. L.D. Landau and D. ter Haar, vol. 1, Pergamon Press, Oxford, 1965].

[11] H. Frohlich, *Proc. Phys. Soc.* (London) **63**, 778 *Phys. Rev.* **79** (1950) 845.

[12] A.D.C. Grassie, *The Superconducting State*, Sussex Univ. Press, 1975.

[13] J. Bardeen, *Phys. Rev.*, **79** (1950) 813.

[14] L.N. Cooper, *Phys. Rev.*, **104** (1956) 1189.

[15] J. Bardeen, L.N. Cooper, and J.R. Schrieffer, *Phys. Rev.*, **108** (1957) 1175.

[16] B.D. Josephson, *Phys. Lett.*, **1** (1962) 25.

[17] A.A. Abrikosov, *Zh. Eksper. Teor. Fiz.*, **32** (1957) 1442.

[18] M. Cyrot and D. Pavuna, *Introduction to Superconductivity and High-T_c Materials*, World Scientific, 1992.

[19] C.P. Poole, Jr.T. Datta, and H.A. Farach, *Copper Oxide Superconductors*, John Wiley & Sons Inc., New York, 1988.

[20] E.W. Collings, *Applied Superconductivity, Metallurgy, and Physics of Titanium Alloys*, vol. 1, Plenum Press, New York, 1986.

[21] V. Illingworth, *The Penguin Dictionary of Physics*, Penguin Books, 1991.

[22] E.W. Collings, *Applied Superconductivity, Metallurgy, and Physics of Titanium Alloys*, vol. 2, Plenum Press, New York, 1986.

[23] G. Burns, *High-Temperature Superconductivity; An Introduction*, Academic Press Inc., 1992.

[24] B.W. Roberts, *Handbook of Chemistry and Physics*, 61st ed., E-87, 1980.

[25] B.T. Matthias, *Superconductivity in d and f Band Metals*, AIP Conf. Proc., No. 4, ed. D.H. Douglass, New York, 1972.

[26] B.T. Matthias, *Phys. Rev.*, **92** (1953) 874.

[27] C. Hammond, *Introduction to Crystallography*, Oxford Univ. Press, 1990.

[28] J.R. Gavaler, *Appl. Phys. Lett.*, **23** (1973) 480.

[29] R. Simon, and A. Smith, *Superconductors; Conquering Technology's New Frontier*, Plenum Press, 1988.

[30] N.N. Greenwood, and A. Earnshaw, *Chemistry of The Elements*, MMIE, Pregamon Press, 1989.

[31] J.G. Bednorz, and K.A. Muller, *Z. Phys. B*, **64** (1986) 189.

[32] M.K. Wu, J.R. Ashburn, C.J. Torng, *et al.*, *Phys. Rev. Lett.*, **58** (1987) 908.

[33] H. Maeda, Y. Tanaka, M. Fukutomi, *et al.*, *Japan J. Appl. Phys.*, **27** (1988) L209.

[34] Z.Z. Sheng, and A.M. Herman, *Nature*, **332** (1988) 55.

[35] T.P. Sheahen, *Introduction to High-Temperature Superconductivity*, Plenum Press, 1994.

[36] C.C. Sorell, *Tomorrow's Materials*, ed. K. Easterling, 2^{nd} *Edn. Inst. Of Metals*, London, pp112.

[37] J. Evetts, *Concise Encyclopedia of Magnetic and Superconducting Materials*, Pergamon Press, 1992.

[38] V.Z. Kresin, and S.A. Wolf, *Fundamentals of Superconductivity*, Plenum Press, 1990.

[39] I. Kusevic, E. Babic, M. Prester, *et al.*, *Solid State Comm.*, **88** 3 (1993) 241.

[40] A.C. Rose-Innes, and E.H. Rhoderick, *Introduction to Superconductivity*, 2nd ed., Pergamon, 1994.

[41] R.A. Hein *et al.*, *Magnetic Susceptibility of Superconductors and Other Spins Systems*, Plenum Press, New York, 1991.

[42] K. Sato, T. Hikata, and Y. Iwasa, *Appl. Phys. Lett.*, **57** (1990) 1928.

[43] B.H. Bransden, and C.J. Joachain, *Introduction to Quantum Mechanics*, Longman Scientific and Technical, 1989.

[44] D. Saint-James, G. Sarma, and E.J. Thomas, *Type-II Superconductivity*,

Pergamon Press, Oxford, 1969.

[45] J.C. Phillips, *Physics of High-T_c Superconductors*, Academic Press, New York, 1989.

[46] P.H. Kes, J. van den Berg, *Studies of High Temperature Superconductors*, edited by A.V. Narlikar, Nova Science Publ., New York, 1989.

[47] J. Li, *Flux Pinning Phenomena in High-T_c Superconductors*, Ph.D. Thesis, 1992, Univ. of Amsterdam, Holland.

[48] J. Bardeen, and M.J. Stephen, *Phys. Rev.*, **A140** (1965) 1197.

[49] P.W. Anderson, *Phys. Rev. Lett.*, **9** (1962) 309.

[50] M.R. Beasley, R. Labusch, and W.W. Webb, *Phys. Rev.*, **181** (1969) 682.

[51] D. Dew-Hughes, *Cryogenics*, **28** (1988) 674.

[52] M. Nikolo, and R.B. Goldfarb, *Phys. Rev. B*, **39** (1989) 6615.

[53] K.A. Muller, M. Takashige, and J.G. Bednorz, *Phys. Rev. Lett.*, **58** (1987) 1142.

[54] Y. Yeshuran and A.P. Malozemoff, *Phys. Rev. Lett.*, **60** (1988) 2202.

[55] Y. Iwasa, *Phase Transitions*, **41** (1993) 87.

[56] E.W. Collings, and M.D. Sumption, *IEEE Trans. on Magnetics*, **28** 1 (Jan. 1992) 156.

[57] C. Rossel, E. Sandvold, M. Sergent, *et al.*, *Physica C*, **165** (1990) 233.

[58] A. Nishida, and K. Horai, *Solid State Commun.*, **74** (1990) 947.

[59] J.J. Lin, E.L. Benitez, S.J. Poon, *et al., Phys. Rev.*, **B38** (1988) 5095.

[60] D.E. Farrell, S. Bonham, J. Foster, *et al., Phys. Rev. Lett.*, **63** (1989) 782.

[61] Y. Iye, T.Tamegai, T. Sakakibara, *et al., Physica C*, **26** (1988) 153.

[62] S.X. Dou, H.K. Liu, Q.Y. Hu, *et al., Physica B*, **194-196** (1994) 1829.

[63] N.V. Vo, S.X. Dou, and H.K. Liu, *High Temperature Superconductors: Synthesis, Processing, and Large-Scale Applications*, pp 53, ed. U. Balachandran, P.J. McGinn, and J.S. Abell.,*TMS* 4-8 Feb. 1996, Warrendale, PA, US.

[64] P.M. Grant, *Nature*, **375** (May 11, 1995) 107.

[65] R.S. Service, *Science*, **268** (May 5, 1995) 644.

[66] D. Caplin, *Nature*, **335** (Sep 15, 1988) 204.

[67] P. Haldar, and L. Motowidlo, *JOM*, (Oct 1992) 54.

[68] D.C. Larbalestier, and M.P. Maley, *MRS Bulletin*, (Aug 1993) 50.

[69] K. Sato, K. Hayashi, K. Ohkura, *et al., Proceedings of 16th Cryogenic*

Engineering Conference and International Cryogenic Materials Conference, (ICEC16/ICMC), May 20-24, 1996, Kitakyushu, Japan.

[70] K.H. Sandage, G.N. Riley, Jr., and W.L. Carter, *JOM*, (Mar 1991) 21.

[71] N.V.Vo, H.K. Liu, S.X. Dou, and I. Kusevic, *Mater. Sci. & Eng.* **B40** (1996) 217.

[72] P. Kovac, I. Husek, and W. Pachla, *1997 IEEE Trans. Appl. Supercond. The 1996 Applied Superconductivity Conference (ASC96)*, 25-30 Aug., 1996, Pittsburgh, PA, US.

[73] N.V.Vo, C.C. Neo, A.J. Bourdillon, S.X. Dou and H.K. Liu, *J. Supercond.*, **9** 6 (1996) 607.

[74] C. Michel, M. Hervieu, M.M. Borel, *et al.*, *Z. Phys. B,* **68** (1987) 421.

[75] J.M. Tarascon, Y. LePage, P. Barboux, *et al.*, *Phys. Rev.*, **B37** (1988) 9382.

[76] C.C. Torardi, M.A. Subramanian, I.C. Calabrese, *et al., Phys. Rev.*, **B38** (1988) 225.

[77] D.C. Larbalestier, X.Y. Cai, H. Edelman, *et al.*, *J. Metals*, **46** 12 (1994) 20.

[78] R.M. Hazen, C.T. Prewitt, R.J. Angel, *et al., Phys. Rev. Lett.*, **60** (1988) 1174.

[79] P.W. Eckels, *Cryogenics*, **29** (June 1989) 625.

[80] C.H. Rosner, M.S. Walker, P. Haldar, and L.R. Motowidlo, *Cryogenics* **32** 11 (1992) 940.

[81] S.A. Sunshine, T. Siegrist, L.F. Schneemeyer, *et al.*, *Phys. Rev.*, **B38** (1988) 893.

[82] Y. Yamada, and S. Murase, *Jpn. J. Appl. Phys.*, **27** 6 (June 1988) L996.

[83] P. Bordet, J.J. Capponi, C. Chaillout, *et al., Studies of High Temperature Superconductors*, **2**, ed. A. Narlikar, Nova Science Inc., New York, 1989.

[84] B. Raveau, and C. Michel, *Ann. Rev. Mater. Sci.*, **19** (1989) 319.

[85] K. Easterling, and J. Niska, *Sci. Progress Oxford*, **74** (1990) 69.

[86] F. Izumi, and E. Takayama-Muromachi, *Crystal Structures and Phase Equilibria*, pp 81, ed. Donglu Shi, *High-Temperature Superconducting Materials Science and Engineering, New Concepts and Technology*, Pergamon, G.B. 1995.

[87] N. Kijima, H. Endo, J. Tsuchiya, *et al.*, *Jpn. J. Appl. Phys.*, **28** (1989) L787.

[88] E.T. Muromachi, Y. Uchida, Y. Matsui, *et al.*, *Jpn. J. Appl. Phys.*, **27** 4 (Apr 1988) L556.

[89] S. Ochiai, K. Hayashi and K. Osamura, *Cryogenics*, **32** 9 (1992) 799.

[90] M. Satou, Y. Yamada, S. Murase, *et al.*, *Appl. Phys. Lett.* **64** 5 (Jan 31, 1994) 640.

[91] L.N. Bulaevskii, L.L. Daemen, M.P. Maley, and J.Y. Coulter, *Phys. Rev.*, **B48** 18 (Nov 1, 1993) 13798.

[92] A.D. Caplin, *et al.*, *Physica C*, **209** (1993)167.

[93] Y. Matsui, H. Maeda, Y. Tanaka, *et al., Jpn, J. Appl. Phys.*, **27** (1988) L827.

[94] Y. Matsui, S. Takekawa, H. Nozaki, *et al., Jpn, J. Appl. Phys.*, **27** (1988) L1241.

[95] Z. Xu, P.D. Han, L. Chang, *et al.*, *J. Mater. Res.*, **5** (1990) 39.

[96] R. Ramesh, G. Thomas, S. Green, *et al., Phys. Rev.*, **B38** (1988) 7070.

[97] M. Wilhem, and O. Eibl, *Solid State Comm.*, **70** (1989) 137.

[98] D.J. Werder, C.H. Chen, S. Jin, and R.C. Sherwood, *J. Mater. Res.*, **4** (1989) 748.

[99] S. Hu *et al., Phys. Rev.*, **B43** (1991) 2878.

[100] H. Krauth *et al.*, *Proceedings of the 3rd Int. Symp. on Superconductivity*, 6-9 Nov. 1990, Sendai, Japan.

[101] J.W. Ekin, *et al.*, *Appl. Phys. Lett.*, **59** (1991) 360.

[102] L.N. Bulaevskii, J.R. Glazman, and A.P. Malozemoff, *Phys. Rev.*, **B45** (1992) 2545.

[103] J. Mannhart, and C.C. Tsuei, *Z. Phys. B*, **77** (1989) 53.

[104] B. Hensel, J.-C. Grivel, A. Jeremie, *et al., Physica C,* **205** (1993) 329.

[105] Y. Feng, Y.E. High, D.C. Larbalestier, *et al.*, *Appl. Phys. Lett.*, **62** (1993) 1553.

[106] *'Low Temerature Superconductors'*, pp 982, *Appl. Supercond. Conf.*, 23-28 Aug., 1992, Chicago Illinois, US, *IEEE Trans. Appl. Supercond.*, Mar 1993.

[107] G.N. Riley, presented at the *DOE Annual Review*, July 19-20, 1994.

[108] K. Sato, K. Ohkura, K. Hayashi, *et al., Physica B*, **216** (1996) 258.

[109] D.M. Buczek, L.J. Masur, P.K. Miles, *et al, 1997 IEEE Trans. Appl. Supercond. The 1996 Applied Superconductivity Conference (ASC96), 25-30 Aug., 1996, Pittsburgh, PA, US.*

[110] E.W. Collings, *private communication.*

[111] K. Sato, T. Hikata, H. Mukai, *et al., IEEE Trans. Magn.* **27** (1991) 1231.

[112] G.N. Riley Jr, J.J. Gannon Jr, P.K. Miles, and D.R. Parker, *Appl. Supercond.* **2** ¾ (1994) 155.

[113] J. Fujikami, N. Shibuta, K. Sato, *et al., Appl. Supercond.* **2**, ¾ (1994) 181.

[114] P. Haldar, and J.G. Hoehn Jr., *I.G.Corp., Oral, 1996 Applied Superconductivity Conference (ASC96)*, 25-30 Aug., 1996, Pittsburgh, PA, US.

[115] W.E. Brockenborough, *A.S.Corp., private communication, 1996 Applied Superconductivity Conference (ASC96)*, 25-30 Aug., 1996, Pittsburgh, PA, US.

[116] K. Chen, C.H. Tai, Y.T. Huang, *et al., J. Supercond.*, **9**, 1 (1996) 73.

[117] L. Bigoni, L. Martini, E. Varesi, *et al., 1997 IEEE Trans. Appl. Supercond. The 1996 Applied Superconductivity Conference (ASC96), 25-30 Aug., 1996, Pittsburgh, PA, US.*

[118] U. Balachandran, A.N. Iyer, P. Haldar, *et al., Appl. Supercond.* **2** ¾ (1994) 251.

[119] N.V. Vo, S.X. Dou, and H.K. Liu, *IEEE Trans. Appl. Supercond.* **6** 3 (June 1996) 102.

[120] N.V. Vo, H.K. Liu, and S.X. Dou, LSB-9, *1997 IEEE Trans. Appl. Supercond. The 1996 Applied Superconductivity Conference (ASC96), 25-30 Aug., 1996, Pittsburgh, PA, US.*

[121] T. Kitamura, T. Hasegawa, and H. Ogiwara, *IEEE Trans. Appl. Supercond.*, **3** 1 (1993) 939.

[122] K. Ohkura, K. Sato, M. Ueyama, *et al., Appl. Phys. Lett.*, **67** 13 (Sept 25, 1995) 1923.

[123] U. Balachandran, A.N. Iyer, P. Haldar, *et al., 4th World Congress on Superconductivity*, Orlando, FL, June 27-July1, 1994.

[124] K. Chen, C.H. Tai, and L. Horng, *J. Supercond.*, **9** 3 (1996) 289.

[125] H.-G. Lee, I.-H. Kuk, G.-W. Hong, *et al., Physica C*, **259** (1996) 69.

[126] H.K. Liu, R. Bhasale, and S.X. Dou, *Proceedings of the 15th Cryogenic Engineering Conference and International Cryogenic Materials Conference (15ICEC/ICMC)*, Columbus, OH , 1995.

[127] P.V. Shoaff Jr., Y.S. Hascicek, *et al., 1997 IEEE Trans. Appl. Supercond. The 1996 Applied Superconductivity Conference (ASC96), 25-30 Aug., 1996, Pittsburgh, PA, US.*

[128] H. Brechna, *Superconducting Magnet Systems*, Springer-Verlag New York, 1973.

[129] M. Wilson, *Superconducting Magnets*, Clarendon-Press Oxford, 1983.

[130] Y. Iwasa, *IEEE Trans. Magn.* **24** (1988) 1211.

[131] Y. Iwasa, *Case Studies in Superconducting Magnets, Design and Operational Issues*, Plenum Press, New York, 1994.

[132] T. Ogasawara, *Cryogenics*, **29** (Jan 1989) 3.

[133] T. Ogasawara, *Cryogenics*, **29** (Jan 1989) 6.

[134] C.P. Bean, *Phys. Rev. Lett.*, **8** (1962) 250.

[135] H.T. Coffey, *Cryogenics*, **7** (1967) 73.

[136] E.W. Collings, *Cryogenics*, **28** (Nov 1988) 724.

[137] E.W. Collings, *Adv. Cryo. Eng. Mater.*, ed. A.F. Clark, and R.P. Reed, **34** (1988) 639.

[138] A.R. Kantrowitz, and Z.J.J. Stekly, *Appl. Phys. Lett.*, **6** (1965) 56.

[139] Z.J.J. Stekly, R. Thome, and B. Strauss, *J. Appl. Phys.*, **40** (1969) 2238.

[140] A.P. Martinelli, and S.L. Wipf, *Proceedings of 1972 Applied Supoerconductivity Conference* (1972) 331.

[141] H.L. Laquer, F.J. Edeskuty, W.V. Hassenzahl and S.L. Wipf, *IEEE Trans. Magn.*, **25** 2 (Mar 1989) 1516.

[142] E.W. Collings, *Advances in Supercond. II, Proceedings of the 2nd International Symposium on Superconductivity (ISS '89)*, Nov. 14-17 1989, Tsukuba, Japan.

[143] L. Bottura, and O.C. Zienkiewicz, *Cryogenics*, **32** 8 (1992) 719.

[144] E.W. Collings, *2nd Int. SAMPE Symp. and Exhib.*, Dec. 11-14, 1991, Chiba, Japan.

[145] S.X. Dou, H.K. Liu, C.C. Sorrell, *et al., Mater. Forum*, **14** (1990) 92.

[146] H.S.W. Chang, S.R. Sheen, D.H. Chen, *et al., Mater. Lett.*, **16** (1993) 342.

[147] K-H. Song, H.K. Liu, S.X. Dou, and C.C. Sorrell, *J. Am. Ceram. Soc.*, **73** 6 (1990) 1771.

[148] Y.E. High, Y. Feng, Y.S. Sung, *et al., Physica C*, **220** (1994) 81.

[149] Y. Zhang, Z. Fang, M. Muhammed, *et al., Physica C*, **157** (1989) 108.

[150] S.E. Dorris, B.C. Prorok, M.T. Lanagan, *et al., Synthesis of Highly Pure Bismuth-2223 By a Two-Powder Process, Physica C*, in press.

[151] T.G. Holesinger, K.V. Slazar, D.S. Phillips, *et al., J. Mater. Res.*, **11**, 1 (Jan 1996) 28.

[152] H. Medelius, and D.J. Rowcliffe, *Materials Sci. Eng.*, **A109** (1989) 289.

[153] Y. Wadayama, K. Kudo, A. Hagata, *et al., Jpn. J. Appl. Phys.*, **27** (1988) L1221.

[154] Y.C. Guo, *Investigation of Silver-Clad (Bi, Pb)$_2$Sr$_2$Ca$_2$Cu$_3$O$_{10+x}$ High-T_c Superconducting Composites*, Ph.D. Thesis, 1994, Univ. of N.S.W., Australia.

[155] A.J. Bourdillon, and N.X.T. Bourdillon, *High Temperature Superconductors: Processing and Science*, Academic Press Inc., 1994.

[156] M. Yavuz, S.X. Dou, E.R. Vance, and H.K. Liu, *Proceedings of 1994 International Ceramics Conference (Austceram 94)*, **1** 2 (1994) 1159.

[157] E.E. Hellstrom, pp 383, ed. Donglu Shi, *High-Temperature Superconducting Materials Science and Engineering, New Concepts and Technology*, Pergamon, G.B. 1995.

[158] K. Sato, N. Shibuta, H. Mukai, *et al., Physica C*, **190** (1991) 50.

[159] Y. Yamada, B. Obst, and R. Flukiger, *Supercond. Sci. Technol.*, **4** (1991) 165.

[160] S.X. Dou, H.K. Liu, Y.C. Guo, and C.C. Sorrell, *Supercond. Sci. Technol.*, **5** (1991) S471.

[161] L. Martini, V. Ottoboni, S. Zannella, *et al.*, pp 565, *Proceedings of the 7th International Workshop on Critical Currents in Superconductors (7th IWCC)*, Austria, 24-27 Jan, 1994.

[162] M. Lelovic, P. Krishnaraj, N.G. Eror, *et al., Supercond. Sci. Technol.*, **9** (1996) 201.

[163] N.V. Vo, H.K. Liu, and S.X. Dou, *Applied Superconductivity*, Pergamon, 1996, in press.

[164] N.V. Vo, S.X. Dou, and H.K. Liu, *Physica C*, **250** (1995) 139.

[165] R.B. Poeppel, editor, *Applied Superconductivity*, Pergamon, **2** ¾ (Mar/Apr, 1994).

[166] *Private communication, Appl. Supercond. Conf.*, 25-30 Aug., 1996, Pittsburgh, PA, US.

[167] S. Jin, *Present and Future Wire Fabrication...*, pp 3, ed. U. Balachandran, E.W. Collings, and A. Goyal, *Proceedings of the Symposium on Processing of Long Lengths of Superconductors, TMS*, Oct. 17-21, 1993, Pittsburgh, PA, US.

[168] N.V. Vo, H.K. Liu, S.X. Dou, and E.W. Collings, *Proceedings of the 2nd International Meeting of Pacific Rim Ceramic Societies (PACRIMII)*, July15-17, 1996, Cairns Australia.

[169] Y.C. Guo, P.A. Bain, H.K. Liu, *et al., Proceedings of 15th Cryogenic Engineering Conference and International Cryogenic Materials Conference, (15ICEC/ICMC)*, 1995, Columbus OH , US.

[170] R.N. Wright, *et al., 'Mechanical Considerations...', presented at the TMS Annual Meeting*, 18-22 Feb., 1990, Anaheim, CA, U.S.

[171] S.X. Dou, H.K. Liu, M. Ionescu, *et al., Physica B*, **216** (1996) 255.

[172] B. Zeimetz, A. Pan, and S.X. Dou, *Physica C*, **250** (1995) 170.

[173] W.G. Wang, H.K. Liu, Y.C. Guo, *et al., Appl. Supercond.*, **3**, 11/12 (1995) 599.

[174] J.O. Willis, R.D. Ray II, T.G. Holesinger, *et al., Proc. of the 7th US/Japan Workshop on HTSC*, 22-24 Oct. 1995, Tsukuba, Japan.

[175] S.J. Guo, *Bi-Based High T_c Superconductors and Enhancement of Critical Current Density,* Ph.D. Thesis, Lulea University of Technology, 1991.

[176] R.J. Arsenault ed., *Treatise On Materials Science and Technology - Plastic Deformation of Materials*, **6**, Academic Press, 1975.

[177] Y. Yamada, M. Satou, S. Murase, *et al., Proceedings of the 5th International Symposium on Superconductivity (ISS'92)* 1992, 717.

[178] Y. Kamisada, T. Koizumi, M. Satou, and Y. Yamada, *IEEE Trans. Magn.*, **30** (1994) 1675.

[179] B. Ullmann, A. Gabler, M. Quilitz, and W. Goldacker, *1997 IEEE Trans. Appl. Supercond. The 1996 Applied Superconductivity Conference (ASC96), 25-30 Aug., 1996, Pittsburgh, PA, US.*

[180] W. Goldacker, E. Mossang, M. Quilitz, and M. Rikel, *1997 IEEE Trans. Appl. Supercond. The 1996 Applied Superconductivity Conference (ASC96), 25-30 Aug., 1996, Pittsburgh, PA, US.*

[181] J. Yoo, H. Chung, J. Ko, and H. Kim, *1997 IEEE Trans. Appl. Supercond. The 1996 Applied Superconductivity Conference (ASC96), 25-30 Aug., 1996, Pittsburgh, PA, US.*

[182] Y. Tanaka, T. Asano, T. Yanagiya, *et al., Jpn. J. Appl. Phys.*, **31** (1992) L235.

[183] J. Tenbrink, M. Wilhelm, K. Heine, and H. Krauth, *IEEE Trans. Magn.*, **3** (1993) 1123.

[184] K. Nomura, T. Sasaoka, J. Sato, *et al., Appl. Phys. Lett.*, **64** (1996) 422.

[185] J. Sato, K. Nomura, and S. Kuma, *Proceedings of 16th Cryogenic Engineering Conference and International Cryogenic Materials Conference, (ICEC16/ICMC),* May 20-24, 1996, Kitakyushu, Japan.

[186] M. Ishizuka, Y. Tanaka, and H. Maeda, *Physica C*, **252** (1995) 339.

[187] O. Dur, S. Nakamae, J. Schwartz, and Y.S. Hascicek, *1997 IEEE Trans. Appl. Supercond. The 1996 Applied Superconductivity Conference (ASC96), 25-30 Aug., 1996, Pittsburgh, PA, US.*

[188] L.G. Lewis, *AMInc.* Oak Ridge, TN, and J.E. Ostenson, *AMES Lab*, Iowa, U.S.,

private communication.

[189] H. Jones, and R.G. Jenkins, pp 259, ed. Donglu Shi, *High-Temperature Superconducting Materials...*, Pergamon, G.B. 1995.

[190] P.F. Smith, M.N. Wilson, and A.H. Spurway, *Appl. Phys.*, **3** (1970) 1561.

[191] R.E. Hintz, *Adv. Cryo. Eng.*, **13**, ed. K.D. Timmerhaus, Plenum Press, NY, 1968, pp51.

[192] K. Kuroda, *Cryo. Eng.* (Tokyo) **10** (1975) 222.

[193] R.W. Fast, W.W. Craddock, M. Kobayashi, and M.T. Mruzek, *Cryogenics*, **28** (1988) 7.

[194] MasterSizer S, *User Manual*, Nov. 1994, Malvern Instruments Ltd.

[195] British Standard BS2955:1993.

[196] J.I. Goldstein, D.E.Newbury, P. Echlin, *et al., Scanning Electron Microscopy and X-ray Microanalysis*, Plenum Press, New York, 1981.

[197] Y.C. Guo, *private communication*, data courtesy of R.K. Wang.

[198] T. Hatano, K. Aota, H. Hattori, *et al., Cryogenics*, **30** (Jul 1990) 611.

[199] Y-T. Huang, W-N. Wang, S-F. Wu, *et al., J. Am. Ceram. Soc.*, **73** 11 (1990) 3507.

[200] A. Oota, K. Ohba, A. Ishida, *et al., Jpn. J. Appl. Phys.*, **28 7** (Jul 1989) L1171.

[201] F. Chen, N. Li, W. Zhang, *et al., Proceedings of 1992 Interantional Workshop on Supercond.*, June 23-26, 1992, Honolulu, US.

[202] S.E. Dorris, B.C. Prorok, M.T. Lanagan, *et al., Physica C,* **212** (1993) 66.

[203] P.E.D. Morgan, J.D. Piche, and R.M. Housley, *Physica C*, **191** (1992) 179.

[204] T.N. Blanton, C.L. Barnes, and M. Lelental, *Physica C,* **173** (1991) 152.

[205] Y.B. Huang, G.F. de la Fuente, A. Larrea, and R. Navarro, *Supercond. Sci. Technol.* **7** (1994) 759.

[206] J.M. Yoo, and K. Mukherjee, pp 131, ed. U. Balachandran, E.W. Collings, and A. Goyal, *Proceedings of the Symposium on Processing of Long Lengths of Superconductors, TMS*, Oct. 17-21, 1993, Pittsburgh, PA, US.

[207] F.K. Lotgering, *J. Inorg. Nucl. Chem.*, **9** (1959) 113.

[208] Y. Yamada, K. Jikihara, T. Hasebe, *et al., Cryogenics Eng.*, **25** (1990) 82.

[209] Y. Yamada, T. Graf, E. Seibt, and R. Flukiger, *IEEE Trans. Magn.* **27** 2 (March 1991) 1495.

[210] J-C. Grivel, A. Jeremie, B. Hensel, and R. Flukiger, pp 359, ed. J. Etourneau,

J.B. Torrance, and H. Yamauchi, *Superconducting Materials*, ICMAS 1993.

[211] M. Takano, K. Takada, K. Oda, *et al., Jpn. J. Appl. Phys.*, **27** (1988) L1476.

[212] B.C. Prorok, S.E. Dorris, R.B. Poeppel, *et al., TMS Proceedings* Oct. 17-21, 1993, Pittsburgh, Pennsylvania, USA. 39-49.

[213] D.X. Chen, and R.B. Goldfarb, *J. Appl. Phys.*, **66** (1989) 2489.

[214] T. Staiger, G. Fuchs, P. Verges, *et al., 1997 IEEE Trans. Appl. Supercond. The 1996 Applied Superconductivity Conference (ASC96), 25-30 Aug., 1996, Pittsburgh, PA, US.*

[215] R.A. Hein, and R.L. Falge Jr., *Phys. Rev.*, **123** (1961) 407.

[216] H.K. Liu, Y.C. Guo, S.X. Dou, *et al., Physica C* **213** (1993) 95.

[217] M.B. Elzinga, and C. Uher, *Phys. Rev.*, **B 32** (1985) 88.

[218] R.B. Goldfarb, A.F. Clark, A.I. Braginski, and A.J. Panson, *Cryogenics*, **27** (1987) 475.

[219] J.R. Cave, A. Fevrier, H.G. Ky, and Y. Laumond, *IEEE Trans. Magn.*, **23** (1987) 1732.

[220] R.B. Goldfarb, M. Lelental, and C.A. Thompson, pp 49, ed. R.A. Hein *et al.*, *Magnetic Susceptibility of Superconductors and Other Spins Systems*, Plenum Press, New York, 1991.

[221] I. Kusevic, E. Babic, J. Ivkov, *et al., Solid State Comm.*, **92** 9 (1994) 735.

[222] S.X. Dou, and H.K Liu, *Supercond. Sci. Technol.* **6** (1993) 297.

[223] Y. Yamada, B. Oberst, and R. Flukiger, *Supercond. Sci. Technol.* **4** (1991) 165.

[224] S.X. Dou, H.K. Liu, M.H. Apperley, *et al., Supercond. Sci. Technol.* **3** (1990) 138.

[225] S.X. Dou, Y.C. Guo, and H.K. Liu, *Physica C* **194** (1992) 343.

[226] Q. Li, K. Brodersen, H.A. Hjuler, and T. Freltoft, *Physica C* **217** (1993) 360.

[227] K.H. Sandhage, G.N. Riley, Jr., and W.L. Carter, Overview (March 1991 JOM) 21.

[228] H.K. Liu, Y.C. Guo, and S.X. Dou, *Physica B* **194-196** (1994) 1931.

[229] Z. Han, and T. Freltoft, *Appl. Supercond.* **2** 3/4 (1994) 201.

[230] D.A. Korzekwa, J.F. Bingert, E.J. Podtburg, and P. Miles, Appl. Supercond. **2** 3/4 (1994) 261.

[231] M. Suzuki, T. Kimura, and T. Takeshita, The International Workshop on Superconductivity (June 23-26 1992 Honolulu) 368.

[232] Y.C. Guo, H.K. Liu, and S.X. Dou, *Mat. Sc. Eng.*, **B23** (1994) 58.

[233] Vlasko-Vlaskov, and V.I. Nikitenko, *Appl. Phys. Lett.* **66** (1995) 1270.

[234] M. Dhalle, M.N. Cuthbert, G.K. Perkins, *et al., Proceedings Of The 7th International Workshop On Critical Currents in Superconductors* Alpbach, Austria (Jan 24-27 1994) 553.

[235] D. Hughes, *Philosophical Magazine B*, **55** 4 (1987) 459.

[236] K.H. Muller, C. Andrikidis, H.K. Liu, and S.X. Dou, *Phys. Rev.*, **B50** 14, (Oct 1, 1994-II) 10218.

[237] K. Togano, H. Kumakura, H. Kitaguchi, *et al.,* The International Workshop On Superconductivity (June 23-26, 1992, Honolulu) 39.

[238] G. N. Riley Jr, J. J. Gannon Jr, P. K. Miles and D. R. Parker, *Appl. Supercond.*, **2** 3/4 (1994) 155.

[239] S.X. Dou, H.K. Liu, and Y.C. Guo, *Appl. Phys. Lett.*, **60** (1992) 2929.

[240] M. Ueyama, T. Hikata, T. Kato, and K. Sato, *Jpn. J. Appl. Phys.*, **30** (1991) L1384.

[241] Y.C. Guo, H.K. Liu, H.M. Ionescu, and S.X. Dou, *Int. Ceramic Monographs, Proc. Int. Cerm. Conf.* Aust. 94, **1** 2 (1994) 1228.

[242] Y. Iwasa, *Physica B*, **216** (1996) 186.

[243] M. Ullrich, K. Heinemann, W. Schaper, and H.C. Freyhardt, *Supercond. Sci. Technol.* **5** (1992) S228.

[244] H.K. Liu, Y.C. Guo, S.X. Dou, *et al., Physica C,* **213** (1993) 95.

[245] I. Kusevic, E. Babic, Z. Marohnic, *et al., Physica C*, **235-240** (1993) 3035.

[246] Y. H. Li, J.A. Kilner, M. Dhalle, *et al., Supercond. Sci. Technol.,* **8** (1995) 764.

[247] Q.Y. Hu, R.M. Schalk, H.W. Weber, *et al., J. Appl. Phys.* , **78** 2 (July 15, 1995) 1123.

[248] J.A. Parrell, S.E. Dorris, and D.C. Larbalestier, *Adv. Cryo. Eng.*, **40** (1994) 193.

[249] H.K. Liu, R. Bhasale, Q.Y. Hu, *et al., Proc. of the 7th Int. Workshop on 'Critical Currents In Superconductors'*, Jan 24-27, 1994, 561.

[250] Y.B. Huang, G.F. de la Fuente, M.T. Ruiz, *et al., Cryogenics,* **33** 1 (1993) 117.

[251] R.H. Arendt, M.F. Garbauskas, K.W. Lay, and J.E. Tkaczyk, *Physica C,* **194** (1992) 383.

[252] T. Ito, and H. Kubota, *Cryogenics,* **29** (Jun 1989) 621.

[253] J. Yau, N. Savvides, and C.C. Sorrell, *Int.Ceramic Monographs, Proc. Int. Cerm.*

Conf. Aust. 94, **1** 2 (1994) 1129.

[254] N.V. Vo, H.K. Liu, and S.X. Dou, *Supercond. Sci. Technol.*, **9** (1996) 104.

[255] A. Oota, H. Matsui, M, Funakura, *et al., TMS Proc.* Oct. 17-21, 1993, Pittsburgh, PA, USA, 221.

[256] N.V. Vo, S.X. Dou, and H.K. Liu, *Cryogenics,* **36** 11 (1996) 903.

[257] Z.X. Zhao, and G.C. Che, *Appl. Supercond.* **2** 3/4 (1994) 227.

[258] G.M. Zorn, R. Hornung, H.E. Gobel, *et al., Supercond. Sci. Technol.*, **8** (1995) 234.

[259] M. Xu, D.K. Finnemore, U. Balachandran, and P. Haldar, *J. Appl. Phys.*, **78** 1 (July 1, 1995) 1.

[260] H. Nobumasa, K. Shimizu, Y. Kitano, and T. Kawai, *Jpn. J. Appl. Phys.*, **27** 5 (May 1988) L846.

[261] J.S. Luo, N. Merchant, V.A. Maroni, *et al., J. Appl. Phys.* **72** 6 (Sept 1992) 2385.

[262] N.V. Vo, H.K. Liu, and S.X. Dou, *J. Mater. Res.* **11** 5 (May 1996) 1101.

[263] E.J. Kramer, *J. Appl. Phys.*, **44** (1973) 1360.

[264] G.B. Smith, J.M. Bell, S.W. Filipczuk, and C. Andrikidis, *Physica C,* **160** (1989) 333.

[265] T.T.M. Palstra, B. Batlogg, R.B. van Dover, *et al., Appl. Phys. Lett.*, **54** (1989) 763.

[266] M. Inui, P.B. Littlewood, and S.N. Coppersmith, *Phys. Rev. Lett.*, **63** (1989) 2421.

[267] S.X Dou, H.K. Liu, Q.Y. Hu, *et al., Phys. B,* **194-196** (1994) 1829.

[268] S.D. Murphy, K. Renouard, R. Crittenden, and S.M. Bhagat, *Solid State Commun.*, **69** (1989) 367.

[269] J. Ferreirinho, S.J. Lee, S.J. Campbell, and A. Calka, *J. Magn. Magn. Mater.*,**88** (1990) 281.

[270] M. Daumling, J.-C. Grivel, B. Hensel, and R. Flukiger, *Physica C*, **219** (1994) 429.

[271] S.X. Dou, Y.C. Guo, J. Yau, and H.K. Liu, *Supercond. Sci. Technol.*, **6** (1993) 195.

[272] S.X. Dou, H.K. Liu, Y.C. Guo, *et al., Physica C*, **185-189** (1991) 2493.

[273] K. Osamura, S.S. Soo, and S. Ochial, *Supercond. Sci. Technol.*, 3 (1990) 143.

[274] J.A. Parell, S.E. Dorris, and D.C. Larbalestier, *Adv. Cryo. Eng.*, **40** (1994) 193.

[275] L. Gherardi, and P. Caracino, *Proc. 7th Inter. Workshop on Critical Currents in Superconductors*, (1994) 545.

[276] Y. Yamada, M. Satou, and S. Murase, "*Microstructure and Superconducting Properties of Ag Sheathed* $(Bi,Pb)_2Sr_2Ca_2Cu_3O_x$ *Tapes*", presented at the ISS5 (1992).

[277] M. Onoda, A. Yamamoto, E. Takayama-Muromachi, and S. Takekawa, *Jap. J. Appl. Phy.*, **27** 5 (May 1988) L833.

[278] Q.Y. Hu, H.K. Liu, and S.X. Dou, *Physica C*, **250** (1995) 7.

[279] L. Chen, and R. Stevens, *J. Am. Ceram. Soc.*, **75** 5 (1992) 1150.

[280] H. Hillmann, '*Fabrication Technology of Superconducting Materials in Superconductor Materials Science: Metallurgy, Fabrication and Applications*',ed. by S. Foner and B.B. Schwartz, Plenum Press, New York, (1981) pp. 275.

[281] K. Sato, T. Hikata, and Y. Iwasa, *Appl. Phys. Lett.* **57** (1990) 1928.

[282] T. Hikata, M. Ueyama, H. Mukai, and K-I Sato, *Cryogenics*, **30** (Nov 1990) 924.

[283] D.P. Hampshire, S.S. Oh, K. Osamura, and D.C. Larbalestier, *Supercond. Sci. Technol.* **3** (1990) 560.

[284] M. Daumling, G. Grasso, A. Perin, and R. Flukiger, *Supercond. Sci. Technol.* **7** (1994) 926.

[285] L.J. Masur, E.R. Podtburg, C.A. Craven, *et al.*, JOM (1996), in press.

[286] K. Osamura, S. Ochiai, and K. Hayashi, *Adv. Cryo. Eng. Mater.*, **38** (1992) 875.

[287] E.W. Collings, and M.D. Sumptions, 7th US-Japan Workshop on High-T_c Superconductors NRIM, Tsukuba, JAPAN, Oct. 24-25,1995.

[288] O. Eibl, *Supercond. Sci. Technol.* **8** (1995) 833.

[289] G.J. Sloggett, C.D. Cook, S.X. Dou, *et al., Electrical Engineering Congress*, 24-30 Nov. 1994, 163, Sydney, Australia.

[290] M.K. Wu, J.R. Ashburn, C.J. Torng, *et al., Phys. Rev. Lett.*, **58** (1987) 908.

[291] C.L. Tien, M.I. Flik, and P.E. Phelan, *Cryogenics*, **29** (1989) 602.

[292] M.D. Sumption, and E.W. Collings, *4th World Congress on Superconductivity Marriott's Orlando World Center*, Orlando, FL, Jun. 27-Jul. 1, 1994, US.

[293] T. Hikata, M. Ueyama, H. Mukai and K-I Sato, *Cryogenics*, **30** (Nov 1990) 924.

[294] Z. Xi, and L. Zhou, *Supercond. Sci. Technol.*, **7** (1994) 908.

[295] X. Yang, and T.K. Chaki, *Supercond. Sci. Technol.*, **6** (1993) 269.

[296] Y. Yamada, M. Satou, S. Murase, *et al., Adv. in Supercond. V, proc. 5th ISS* Nov. 16-19, 1992, Kobe, Japan.

[297] N.V.Vo, S.X. Dou, and H.K. Liu, *Supercond. Sci. Technol.*, **9** (1996) 104.

[298] Y. Yamada, B. Obst, and R. Flukiger, *Supercond. Sci. Technol.*, **4** (1991) 165.

[299] W.H. Warnes, and D.C. Larbalestier, *IEEE Trans. Magn. MAG-***23**, (1987) 1183.

[300] J.E.C. Williams, E.S. Bobrov, Y. Iwasa, *et al., IEEE Trans. Magn.* **28** (1992) 627.

[301] U. Welp, D.O. Gunter, and G.W. Crabtree, *Appl. Phys. Lett.* **66** (1995) 1270.

[302] J. Fujikami, K. Sato, N. Shibuta, *et al.,* US Patent 5,358,929 (1994).

[303] H.G. Lee, I.H. Kuk, G.W. Hong, *et al., Physica C,* **259** (1996) 69.

[304] T. Ito, and H. Kubota, *Cryogenics,* **31** (Jul 1991) 533.